Application of resonant-state expansion to inhomogeneous and non-spherical optical resonators

Zoltan Sztranyovszky

A Thesis submitted to Cardiff University for the degree of Doctor of Philosophy

November 15, 2022

Abstract

Resonances determine the optical properties of an object, such as its transmittance, scattering cross-section, or local field enhancement. Resonant states (RSs) provide a physically intuitive way to describe these features and a range of related physical phenomena. In this thesis I study both the resonances of dielectric optical systems and the method called resonant-state expansion (RSE). The RSE is a perturbative approach to calculate RSs, capable of treating perturbations of arbitrary arbitrary strength. It expresses the RSs of the perturbed system in the basis of the RSs of a known, unperturbed system, transforming the problem of solving Maxwell's equation to find the resonances into a linear matrix eigenvalue problem.

I study the completeness of the eigenmodes, the convergence rate of the Mittag-Leffler (ML) expansion of the Green's function (GF), as well as the convergence of sum rules that the eigenmodes satisfy, establishing limits of validity. I investigate the modes of spherically symmetric, radially inhomogeneous resonators, and find that by appropriately engineering the permittivity gradient one can achieve quasi-degeneracy of the transverse-electric and transverse-magnetic whispering gallery modes. I derive, based on the RSE, a first-order perturbation theory that can treat material and shape changes of arbitrary resonators with the same formalism, and discover a remarkable phenomenon when all orders of the standard perturbation series can contribute linearly in the change of a small parameter. I apply the RSE to non-spherical systems, and reveal additional divergent terms in the ML expansion of the GF affecting the RSE convergence, which were previously unaccounted for. Finally, I also apply a RSE based approach, which links the GF to the scattering matrix, for calculation of the cross-section of cylindrical dielectric resonators. This method can potentially supersede the computational efficiency of many other existing methods, as it does not require to solve Maxwell's equation across all space, and it also does not require overlap volume integrals between the mode fields and the excitation wave, which are used in other methods.

Publications

Zoltan Sztranyovszky, Wolfgang Langbein, and Egor A. Muljarov. *First-order perturbation theory of eigenmodes for systems with interfaces.* Physical Review Letters, Under Review, 2022. 10.48550/ARXIV.2205.13041

Zoltan Sztranyovszky, Wolfgang Langbein, and Egor A Muljarov. *Optical resonances in graded index spheres: A resonant-state-expansion study and analytic approximations.* Physical Review A, 105(3):033522, 2022. https://doi.org/10.1103/PhysRevA.105.033522

Yisu Wang, Zoltan Sztranyovszky, Attilio Zilli, Wiebke Albrecht, Sara Bals, Paola Borri, and Wolfgang Langbein. *Quantitatively linking morphology and optical response of individual silver nanohedra.* Nanoscale, 14:11028 – 11037, 2022. https://doi.org/10.1039/D2NR02131E

Yisu Wang, Attilio Zilli, Zoltan Sztranyovszky, Wolfgang Langbein, and Paola Borri. *Quantitative optical microspectroscopy, electron microscopy, and modelling of individual silver nanocubes reveals surface compositional changes at the nanoscale.* Nanoscale Advances, 2:2485–2496, 2020. https://doi.org/10.1039/D0NA00059K

Presentations

First-order perturbation theory for electromagnetic eigenmodes. Antennas and electromagnetic systems (AES), Marrakech, Morocco, 25/05/2022

Spherically symmetric systems with continuous permittivity profiles solved by the resonant-state expansion. Recent advances in modal expansions for nanophotonic systems, Online symposium, 17/09/2020

Review of modal expansion methods. Theory seminar, Cardiff University, 12/11/2020

Optical harmonic oscillators for whispering-gallery modes, explored by the resonant-state expansion. Photon, Online conference, 04/09/2020

Quasi-degeneracy of TE and TM whispering gallery modes in graded permittivity index spherical resonators. Theory seminar, Cardiff University, 04/06/2020

Eigenpermittivity states in open photonic systems. Theory seminar, Cardiff University, 23/01/2020

Resonant-state expansion: Background, challenges, and applications. Postgraduate Conference, Cardiff University, 27/09/2019

Modelling the extinction cross-section of metallic nanoparticles. Theory seminar, Cardiff University, 13/06/2019

Acknowledgements

This research would not have been possible without financial support from the Engineering and Physical Sciences Research Council (grant number: EP/R513003/1).

I am grateful to both of my supervisors for guiding me through the PhD journey, answering my relentless questions, especially in the early years, and for the countless hours of heated scientific debates. I thank Egor Muljarov for teaching me to strive for mathematical rigour and I thank Wolfgang Langbein for his insightful analogies and drawing connections between various areas of physics. Thank you to my examiners Philippe Lalanne and Bernard Schutz for an engaging and lively viva.

I am also grateful for the mentorship of Richard Lewis for his help in navigating the academic landscape and his inspiring passion for teaching. I thank Paul Roche for his support, which allowed me to become a better educator. I thank all my colleagues for the fun coffee breaks, Thursday cakes, and Friday nights at The Flute & Tankard.

I thank Michael Norman, Sander Vermeulen, and Ashley Cameron for the many discussions about science, fiction, and science fiction; Marine Furet for dragging me to gym at 7am; Irene Scicluna for the challenging philosophical discussions; Márton Simon Papp for sending me songs to listen to; Ruth Hogger for throwing shapes. I am eternally grateful for the endless support of my mother, Katalin Dengelegi. Finally, the biggest thank goes to my loving wife, Dorottya Cserző, who could not deter me from embarking on a PhD to begin with.

Contents

1

Introduction

Optical cavities are important objects in physics and engineering, and their optical properties, such as scattering cross-section or local field enhancement, can be determined based on the resonance phenomenon. In this thesis we consider the resonances of open optical systems which are described by linear, second-order, partial differential equations. In this chapter we first look at the basic concept of resonances, starting from the well known example of the classical harmonic oscillator describing a point like object, then moving onto extend system, that is, cavities, and finally we review the applications and the mathematical formulation of optical eigenmodes in the literature.

1.1 Resonances

Resonances appear in many areas of nature where wave-like phenomenon, or more generally, oscillations are present. Taking for example a particle on a spring, that is, a classical harmonic oscillator in mechanics, a resonance, or free vibration with the real natural frequency, is the oscillation in the time domain without a driving or damping force present, and the displacement $x(t)$ it is described by the second-order ordinary differential equation [1]

$$\frac{\mathrm{d}^2x}{\mathrm{d}t^2} + \omega_0^2 x = 0, \tag{1.1}$$

with the real natural frequency given by $\omega_0 = K/m$, where K is the stiffness constant of the spring and m is the mass of the particle, and the well known solution is in the form $e^{-i\omega_0 t}$. When the system is damped, the equation is modified to

$$\frac{\mathrm{d}^2x}{\mathrm{d}t^2} + 2\kappa\frac{\mathrm{d}x}{\mathrm{d}t} + \omega_0^2 x = 0, \tag{1.2}$$

where $\kappa = R/(2m)$, and R is the resistance constant determining the damping. Using the ansatz $e^{-i\omega t}$ results in the complex resonance frequency $-i\omega = -\kappa \pm \sqrt{\kappa^2 - \omega_0^2}$. When the

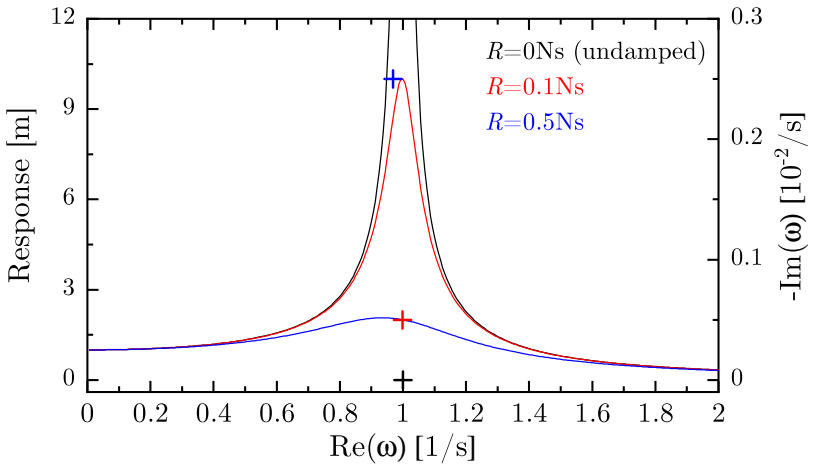

Fig. 1.1.1: Left axis (lines): amplitude with respect to the driving frequency; right axis (crosses): position of the resonance frequency in the complex plane. Mass $m = 1\,\mathrm{kg}$, driving force magnitude $F = 1\,\mathrm{N}$, stiffness constant $K = 1\,\mathrm{N/m}$, resistance constant R is indicated by the colour.

system is driven by an external force, the strongest response occurs at the natural frequency, which without damping of the system results in an oscillation with infinite amplitude, but it is kept finite if the system has damping [2]. This is illustrated on Fig. 1.1.1. The undamped system (black) shows an infinite response at the natural frequency. We can see that for a small damping parameter (red) the real part of the complex resonance is approximately at the same position as the natural frequency. As we increase the damping (blue) the imaginary part of the complex frequency grows, and the maximum of the response decreases, as well as the position of the peak shows a redshift along with the real part of the complex frequency. Note that when the system is not a point like particle, the equation of motion will be a partial differential equation, with the displacement depending not only on time but on the spatial coordinate as well.

The resonance determines the behaviour of the system. For example, when a damping is present, an underdamped oscillation occurs if the damping parameter κ is less than the natural frequency ω_0, critical damping occurs when they are equal, while overdamping occurs when the damping parameter is higher than the natural frequency [3]. The the resonance frequency of an undamped system is real, and for a damped system is complex, the real part representing the rate of oscillation, while the negative imaginary part representing the damping and the decay of the amplitude with time, assuming a $e^{-i\omega t}$ time dependence of the oscillation. The harmonic oscillator has two resonance frequencies in the complex plane, such that $\omega_1 = -\omega_2^*$, where the star * denotes the complex conjugate.

In acoustics, resonance phenomena correspond to the increase of the pressure when a

pressure wave is reflected from a surface of a cavity and a constructive interference occurs. This effect is used for enhancement of sound in instruments or loudspeakers [1]. In quantum mechanics, resonance is usually associated with a local extremum in the transmission or scattering cross-section spectra. For example, a barrier or well have quantised energy levels, and if the energy of a plane wave incident on the barrier is close to an energy level of the system a resonance occurs, manifesting in, for example, a peak in the transmission spectra. If the incoming wave is a propagating wave packet, which can be described by a collection of plane waves with different momentum components, then a sharp peak in the plane wave transmission spectra can lead to the distortion of the shape of the wave packet, as the various momentum components are reflected differently [4]. In optics, which is the main focus of the thesis, resonance phenomena have similar effects to quantum mechanics, manifesting in, for example, peaks of the transmission spectra [5].

1.1.1 Cavity resonators

The harmonic oscillator describes the behaviour of a point like particle. Extended objects are usually referred to as cavities or resonators. Resonance phenomena in cavities are conceptually the same as in case of a harmonic oscillator. Specific oscillations, also called modes, with certain frequencies, are supported when there is no source or driving; when the cavity is excited close to these frequencies, a strong response occurs. Two distinct types of cavities, or systems, can be distinguished: closed (Hermitian) and open (non-Hermitian) ones. A closed system does not interact with the surroundings, while an open one does, which means energy can leak out into the surrounding background. This can also be understood as the open system having inherent damping, which manifests again in the complex eigenfrequency of the modes. For example, a harmonic oscillator with damping in the form of air resistance would be an open system. Cavities usually have an infinite number of resonances ω_n, though there is an exception. A single δ potential in quantum-mechanics only supports one bound state, or resonance [6]. This can also be seen from the secular equation of two delta potentials [7] and decreasing the distance between them to zero, resulting in all but one of the resonances tending to infinity. Due to the vanishing extent of the cavity one could consider this system an analogue of the classical harmonic oscillator, which also has a finite number of resonances.

In case of finite structures the resonances are countable infinite. We illustrate this on Fig. 1.1.2 for two optical system. On Fig. 1.1.2a the resonance frequencies of a closed and an open 1D Fabry-Pérot cavity (a dielectric slab) is shown, along with its transmittance. The

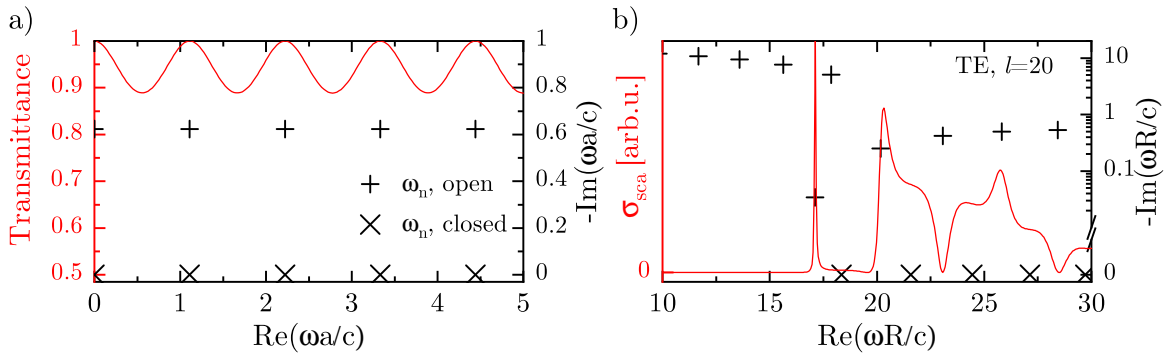

Fig. 1.1.2: a) Transmittance and eigenmodes of Fabry-Pérot cavity in a form of a dielectric slab with permittivity $\varepsilon = 2$ and width $2a$, at normal incidence for $q = 0$. b) Scattering cross-section and TE polarisation of a spherical dielectric resonator with radius R, $\varepsilon = 2$, for angular momentum $l = 20$. Note the logarithmic scale and the axis break on the right. Eigenmodes of open systems are shown with $+$, whereas for closed systems they are shown with $\times$. Both the open cavities are in vacuum background. c is the speed of light.

system is governed by the equation

$$\frac{\mathrm{d}^2E(x)}{\mathrm{d}x^2} + k^2\varepsilon(x)E(x) = 0, \tag{1.3}$$

where ε is the permittivity, and now x is the spacial coordinate while E is the electric field. On Fig. 1.1.2b the resonances of a dielectric sphere are shown for transverse-electric (TE) polarisation with angular momentum number $l = 20$, along with its partial cross-section. This system is described by the spherical Bessel differential equation

$$\frac{\mathrm{d}^2E(r)}{\mathrm{d}r^2} - \frac{l(l+1)}{r^2}E(r) + k^2\varepsilon(r)E(r) = 0, \tag{1.4}$$

where $l = 1, 2, 3...$ is an integer, and r is the distance from the origin. For closed systems we used the boundary condition that the field is zero at the cavity wall. In case of the Fabry-Pérot cavity the real part of the resonance frequencies agree for the open and closed system. This is due to that the condition for resonance, namely, that constructive interference should occur between the waves reflected at the boundaries; this gives the same wavelength of the modes in both cases due to the 1D nature of the structure. In case of a sphere the resonances of the open and closed system do not line up due to the more complicated geometry (curvature of the interface) resulting in slightly different resonance conditions for the open and the closed case. The open spherical cavity has a more varied resonance spectrum compared to the closed one, note the logarithmic scale on the right. 1D Fabry-Pérot cavities will be discussed in more detail in Chap. 2, and spherical resonators will be the subject of Chap. 3.

As we extended the system so it has infinite length along a dimension, for example an infinite planar slab with non-normal incident field, the countable infinite resonances will form a continuum. However for a good quantum number, i.e. the in plane momentum number q, there is a countable number of resonances. In addition to these, there can also be cut in the complex frequency plane, giving rise to a continuum of states, however this cut can be discretised and represented by a countable number of states [8, 9].

More details on the treatment and properties of non-Hermitian systems with examples from across the fields of physics can be found, for example, in Ref. [10].

1.1.2 Origin of resonances and their nomenclature

From a mathematical point of view, resonances are defined as the eigensolution to a second order differential equation, the wave equation in electromagnetism or the equation of motion in case of the classical harmonic oscillator, and the corresponding boundary conditions which are governing the physical problem. For linear systems the wave equation can always be cast to the Sturm-Liouville (SL) form. For a closed cavity the boundary conditions are usually Neumann, Dirichlet, or mixed, giving the value of the eigenfunction or its derivative on the surface of the cavity, and resulting in real eigenfrequencies for the SL equation [11]. For open cavities the normally adopted outgoing boundary condition expresses that the energy propagates away from the cavity to infinity, and this results in wavefunctions which outside have exponentially growing amplitude with distance from the cavity [12]. The mathematical formulation of the eigenmodes is further detailed in Sec. 1.2.1.

The eigensolutions of open systems are referred to as resonant-states (RSs) [13, 14], quasi-stationary states (QSSs) [12, 15], or quasi-normal modes (QNMs) [16, 17]. The concept of RSs is rooted in quantum mechanics and the description of the α-decay [18]. Due to their slowly decaying nature they were referred to as QSSs, while the QNM term was later adopted to highlight the difficulties associated with the definition of inner product and normalisation of the modes due to their exponentially growing amplitude outside of the system. Apart from quantum mechanics [12, 15, 18, 19], the concept of RSs has later also been adapted to gravitational waves (where they mainly referred to as QNMs [16, 20]) and to electromagnetism (where the terms RSs [14], QNMs [17], and occasionally morphology dependent resonances (MDR) are used [21], the latter name emphasises the dependence of the resonance on the shape of the cavity rather than the open character).

1.1.3 Numerical methods for calculating the response of resonators

Naturally, already many well established methods exist to calculate physical observable of systems, such as their transmission, scattering and absorption cross section, decay rate, or field enhancement. Commonly used methods include, for example, finite-element method (FEM), finite-difference time domain (FDTD), transfer matrix method (TMM), the Fourier modal method (FMM), or discrete-dipole approximation (DDA) in optics. FEM is often associated with a time independent problem, but in general, it simply means that the physical domain of interest where we want the governing differential equations solved, such as Maxwell's equations, is discretised to a mesh grid in space, and approximate solutions in terms of polynomials are found at each grid point [22]. FDTD, as the name suggest, considers time dependent problems. It discretises not only the spacial dimensions, but time as well, solving the equations in each spacial and time grid point by replacing the derivatives with differences [23]. TMM is generally used for layered structures. Considering a simple layered planar structure, where each individual layer is homogeneous, the TMM gives the exact solution of the wave equation by expressing the propagation of the incoming wave through a layer in terms of a matrix comprised of backward and forward propagating waves, and a matrix expressing the transmission and reflection effect of boundaries, with the process repeated for each individual layer in the structure [24]. FMM is usually applied for periodic gratings, and it is based on expressing the total field in terms of Floquet-Fourier series, the periodic permittivity and permeability in Fourier series, and enforcing appropriate boundary conditions at all the interfaces, repeated for each building block of the structure [25]. DDA approximates the material response of a scatterer by a set of dipoles arranged in a grid, mimicking the shape of the modelled object. The response of the system is found as the collection of the responses from the coupled dipoles [26]. Other methods also exists, such as the scattering-matrix method, which relates incoming channels of the system to the outgoing channels [27, 28], or the boundary element method, which solves an integral equation formulation of the given problem [29].

1.1.4 Eigenmode methods for calculating observables

An alternative method emerged in optics in the recent years, where the physical observables are expressed in terms of the eigenmodes of the system. This can clearly be done in case of a closed system as the eigenmodes of a regular SL equation form a complete set [11]. This property can also be shown for open quantum [30] and optical [31] systems, though in the

latter the RSs need to be complemented by static modes [32] (detailed in Sec. 1.2.1), while in case of gravitational waves completeness is not necessarily guaranteed [33].

An advantage of the eigenmode approach compared to the methods mentioned in Sec. 1.1.3 is that resonant phenomena usually directly correspond to the eigenmodes, therefore this provides the most physically intuitive explanation of various phenomena. The real part of the eigenmode wavenumber $\mathrm{Re}\,(k_n)$ corresponds to the position of the resonance, the imaginary part $\mathrm{Im}\,(k_n)$ gives the half-width at half-maximum, and also half the decay rate, and the quality factor of the mode is defined as $Q = |\mathrm{Re}\,(k_n)\,/[2\mathrm{Im}\,(k_n)]|$. In case of metallic nanoparticles (NP), which support only a few relatively high-Q modes, the response of the resonator in this spectral range can often be expressed accurately by the use of a very few RSs. For example, the optical cross-section of a gold nanorod has been calculated with only a single RS [17,34], and the transmission of a chiral gold nanodimer composed of two nanorods has been calculated with two modes only [35]. For non-metallic (e.g. dielectric) particles, or when the spectral range of interest is broad, or when a high accuracy is needed, many modes contribute to the calculation [36–38]. Apart from the cross-section, RSs can also be used to calculate the Purcell factor, that is, the change of the decay rate of a quantum emitter placed in the vicinity of a resonator [39]. Examples can be found for emitters next to gold nanorods with the use of a single RS [40, 41], or in the gap of a gold nanorod dimer with the use of two RSs [40], as well as for more complex structures, such as an emitter in the gap of a gold dimer on a photonic crystal with the use of two RSs [42], while for a broad spectral range, or for dielectric resonators, once again many modes are needed in the calculation [43, 44]. A use of a single RS is often sufficient to express first-order changes to the resonance frequency when either the surrounding medium is changed [45–48], which has important application in sensing [49], or when the shape or material of the resonator is changed [50], which allows computationally efficient design process of resonators [51]. The natural quantisation of the optical modes allows the formalism to be combined with quantum mechanics, and has been used to describe the dynamics of two spatially separated quantum emitters coupled via a gold nanorod, which is described by a single RS [52], or a quantum dot placed between a gold dimer on a photonic crystal [53] (extension of Ref. [42], here using the Jaynes-Cummings model for the quantum dot), and the approach can be used to efficiently model and design single photon sources [54]. The formalism of the RSs can be extended to treat non-linear permittivity and effects such as second harmonics generation [55, 56], as well as non-local permittivity [57]. Further application of RSs can be found in the recent review articles [58–60].

Another benefit of RSs based approaches over other methods that rely on solving the wave

equation in all space, is that once the eigenmodes are know, usually it is fast to calculate the response of the system over a range of frequencies [61], especially if only a limited number of modes contribute to the calculation, because often this just involves a simple evaluation of the RS field [38,41,62] or an an overlap integral of the mode field with an incoming wave [35–37]. While studies exist that attempt to compare the performance of various methods to calculate RSs themselves [63–65], though definite conclusions are hard to draw as the calculations with each method are often performed by different groups on different computers, detailed study on the efficiency of calculating observables with RS methods versus others, such as FEM of FDTD, to the best of our knowledge is missing.

The above examples that use one-two RSs in the calculation highlight why the modal approach is such a powerful tool in nanophotonics. However, at the same time, these examples also highlight an outstanding issue, namely, that the use of one-two modes is an approximation, and it cannot always be improved by taking into account more modes in the calculation. This is due to the completeness of the RSs, which is usually limited to the volume of the resonator [8, 31, 66, 67]. Completeness allows the expansion of other functions, such as the Green's function (GF) or the total electric field, into the basis of the RSs, and this is the core principle in all the examples listed above. Taking the calculation of the Purcell factor as an example, when there is only one dominant RSs describing the response of the resonator, the field of that mode is a good approximation of the electric field outside and it can be used to calculate the change of the decay rate of an emitter outside the resonator [40]. However the accuracy of this approximation depends on the distance of the emitter from the resonator. Far away from the resonator one needs to use a regularised field, whereas close to the surface of the resonator a single mode approximation is not enough due to the strong contribution of quasi-static terms [41]. When two RSs were used in the Purcell enhancement calculation [40, 42] the emitter was placed in the centre of the gap in the dimer. One could argue that this is in fact inside the resonator, which is comprised of the two individual parts of the dimer and the minimal convex volume surrounding them, hence in this spacial region the RSs form a complete set [68]. When many modes were used in the calculation [43, 44] the emitter was placed inside the resonator. Completeness issues outside the resonator might be circumvented by the use of artificial modes called the PML modes [58, 69]. These artificial modes will be discussed in more detail in Sec. 1.2.1 of the Introduction, but they are otherwise not used in the present work.

1.1.5 Calculating the eigenmodes

The eigenmodes of simple systems, such as slabs, infinite cylinders, or spheres can be calculated analytically, or semi-analytically via solving an appropriate secular equation approximately or numerically [70]. For more complicated geometries a secular equation determining the mode frequencies usually can not be found, and instead fully numerical methods are used, for example FEM, FDTD, or FMM [63–65]. Alternatively, perturbative methods can also be used, which means starting from the eigenmodes of a know system, then introducing a change into the system parameters, such as a change of the system boundary or the resonator material, and then finding the modes of the target system via a matrix equation or a perturbation series. Such a perturbative method is the resonant-state expansion (RSE), which solves Maxwell's equation by transforming it into a matrix eigenvalue problem [14]. The matrix equation links the eigenmodes of a basis (unperturbed) system, to the target (perturbed) system of interest (mathematical details of the RSE method will be presented in Sec. 1.2.3). The core idea is the same as in closed quantum systems, where one can also write a matrix equation for the perturbed states, from which the standard, well know perturbation series can be derived [71]. Treatment of open systems is less straight forward however, as the standard orthogonality and normalisation are no longer applicable to the eigenmodes. Nevertheless attempts have been made before the RSE both in quantum mechanics [30, 72] and in optics [70] to derive and use matrix equations to treat perturbations.

The use of RSs in optics started to become more popular with the development of a first-order perturbation theory based on the scalar equations for spherical dielectric resonators [21, 73], the establishment of the completness of the modes and the expansion of the scalar GF into the eigenmodes inside the cavity region [31], treatment of absorptive materials [74], second and third-order corrections [75, 76], and reformulation of these results to the vectorial wave equation with expansion of the transverse part of the Green's dyadic (GD) in case of dielectric spheres [66, 77, 78]. While these works laid down important foundations of the field, there were still outstanding issues with the proper normalisation [43, 69, 79], an expansion for the longitudinal part of the GD was not available, and only small perturbations were treatable.

Later the issues with the normalisation of the modes have been addressed analytically, leading to the development of the RSE, and showing on the example of a 1D slab and the TE modes of a homogeneous sphere that perturbations of arbitrary strength can be efficiently treated [14]. The RSE was later generalised to treat: 2D systems [8], waveguides [80, 81], 3D

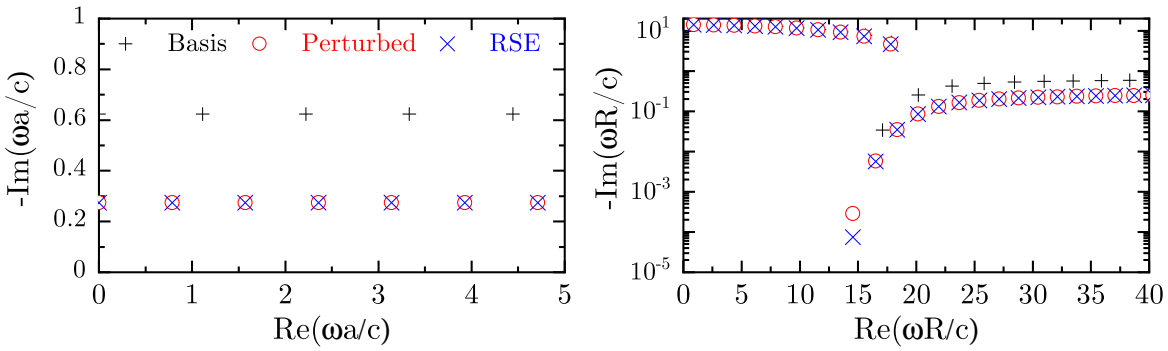

Fig. 1.1.3: Perturbation of the eigenmode with the RSE. a) 1D slab with width $2a$, basis permittivity $\varepsilon = 2$, perturbed permittivity $\varepsilon_\mathrm{p} = 4$, length $2a$. b) spherical dielectric resonator with radius R, $l = 20$, TE modes, $\varepsilon = 2$, $\varepsilon_\mathrm{p} = 4$. Both cavities have vacuum as background. $N = 100$ RSs were used in the basis.

spherical systems [63], as well as arbitrary geometries where the relevance of the static (zero-frequency) modes was identified [32], arbitrary materials including dispersive [82, 83], chiral and magnetic [68], as well as photonic crystals [9, 84]. The representation of the longitudinal part of the GD was also formulated [85]. On Fig. 1.1.3 we illustrate that the RSE can find accurately the eigenmodes of a perturbed systems when the permittivity of the resonator is changed from $\varepsilon = 2$ to $\varepsilon_\mathrm{p} = 4$, which is a 100% perturbation strength. The RSE will be the main method employed in this thesis, and it will be detailed further in the next section.

While RSs are the eigenmodes of the wave equation with the frequency or the wavenumber chosen as the eigenvalue, it is also possible to define a different set of eigenmodes, for which the permittivity constitutes as the eigenvalue [86, 87]. A perturbation method analogues to the RSE has been developed recently based on eigenpermittivity modes [88]. There are important differences compared to the RSE however. As the frequency is a real number now, the modes do not diverge outside, and the normalisation can be reduced to a simple square integral of the eigenmode over the cavity, analogous to the formalism in closed systems. Furthermore, a benefit of the use of eigenpermittivity modes is that seemingly a GD expansion across all space can be obtained in a simple manner, allowing to treat sources outside of the resonator easily. A drawback is however, that if one desires to generate spectra, the eigenmodes need to be calculated repeatedly for each frequency.

1.2 Eigenmodes, Green's dyadic, and the RSE

Here, mainly based on Ref. [60, 68, 85], we summarise the formalism of the eigenmodes and show how the RSE method, which is used throughout this thesis, is derived.

1.2.1 Eigenmodes

Resonant states

We assume a harmonic time dependence of the field in the form $e^{-i\omega t}$, where ω is the frequency of the oscillation, and it is related to the wavenumber k in vacuum as $\omega = kc$ where c is the speed of light. Assuming a harmonic time dependence allows us to separate the function describing the spacial dependence of the field, and write the time independent Maxwell's equation for the electromagnetic field as

$$\hat{\mathbb{M}}(k, \mathbf{r})\mathbb{F}(\mathbf{r}) = 0, \tag{1.5}$$

where $\mathbb{F}(\mathbf{r})$ is a six component vector field of the form

$$\mathbb{F}(\mathbf{r}) = \begin{pmatrix} \mathbf{E}(\mathbf{r}) \\ i\mathbf{H}(\mathbf{r}) \end{pmatrix}, \tag{1.6}$$

comprised of the electric field $\mathbf{E}$ and the magnetic field $\mathbf{H}$, and $\hat{\mathbb{M}}$ is a 6×6 operator defined as

$$\hat{\mathbb{M}}(k, \mathbf{r}) = k\hat{\mathbb{P}}(k, \mathbf{r}) - \hat{\mathbb{D}}(\mathbf{r})\,. \tag{1.7}$$

Here

$$\hat{\mathbb{P}}(k, \mathbf{r}) = \begin{pmatrix} \boldsymbol{\varepsilon}(k, \mathbf{r}) & \boldsymbol{\xi}(k, \mathbf{r}) \\ \boldsymbol{\zeta}(k, \mathbf{r}) & \boldsymbol{\mu}(k, \mathbf{r}) \end{pmatrix}, \tag{1.8}$$

where $\boldsymbol{\varepsilon}(k, \mathbf{r})$ ($\boldsymbol{\mu}(k, \mathbf{r})$) is the permittivity (permeability) tensor, $\boldsymbol{\xi}(k, \mathbf{r})$ and $\boldsymbol{\zeta}(k, \mathbf{r})$ are bi-anisotropy tensors, and

$$\hat{\mathbb{D}} = \begin{pmatrix} 0 & \boldsymbol{\nabla}\times \\ \boldsymbol{\nabla}\times & 0 \end{pmatrix}. \tag{1.9}$$

In this thesis we only deal with non-dispersive, isotropic, reciprocal material, so we can drop the k dependence of $\hat{\mathbb{P}}$, set $\boldsymbol{\xi}(k, \mathbf{r}) = \boldsymbol{\zeta}(k, \mathbf{r}) = 0$, and write the permittivity (permeability) as a scalar function of spacial coordinates multiplied with the identity tensor, yielding $\boldsymbol{\varepsilon}(\mathbf{r}) = \varepsilon(\mathbf{r})\mathbf{I}$ ($\boldsymbol{\mu}(\mathbf{r}) = \mu(\mathbf{r})\mathbf{I}$), and $\mathbf{I}$ is the identity tensor. We define the *system* as the finite volume V where the material tensor $\mathbb{P}_s(\mathbf{r} \subset V)$ differs from the constant homogeneous background material properties $\mathbb{P}(\mathbf{r} \not\subset V)$.

Open systems interact with the environment, and so they are considered leaky. This manifest in the boundary condition which is that there are only *outgoing waves* from the

system. The boundary condition was chosen so that it corresponds to the desired observables, for example, the scattering cross-section, which is related to the scattered waves propagating away as outgoing waves after the resonator has been excited. This condition defines the eigenmodes, or RSs, of an open system, and we denote the discrete set of RSs $\mathbb{F}_n$ at k_n with label n, which satisfy the equation

$$\hat{\mathbb{M}}(k_n, \mathbf{r})\mathbb{F}_n(\mathbf{r}) = 0\,. \tag{1.10}$$

The outgoing waves boundary condition means that the field can be written $\propto e^{ikr}/r$ in 3D (or $\propto e^{ikx}$ in 1D) far away from the system. From the outgoing wave boundary condition, and from the condition that the parallel component of the electric field and the normal component of the displacement field at the surface are continuous across the interface, for simple symmetric systems a secular equation can be found that determines the complex eigenvalues k_n. The secular equation (see for example Eq. (2.6) in Chap. 2 for a slab, or Eq. (3.1) in Chap. 3 for a spherical system) usually needs to be solved numerically, for example via Newton-Raphson method or Cauchy's argument principle method. The advantage of the latter is that all modes are guaranteed to be found in a certain spectral range [89]. It is important to note that while a spherically symmetric system can be represented as an effective 1D system, and the corresponding field given by a scalar function $u(r)$, the scalar eigenmode fields of this effective 1D system do not satisfy the Sommerfeld radiation condition [90]

$$\lim_{r\to\infty} r\left(\frac{\mathrm{d}u}{\mathrm{d}r} - iku\right) = 0\,, \tag{1.11}$$

due to the complex k eigenvalues resulting in the exponential growth of the wavefunction far away. Contrary to the claims of Ref. [41, 59, 91, 92], it was shown explicitly in Ref. [79], that the eigenmodes do not satisfy the Silver-Müller radiation condition either, which is written as [93]

$$\lim_{r\to\infty} (\hat{\boldsymbol{r}} \times \boldsymbol{\nabla} \times \mathbf{E}_n + ik_n\mathbf{E}_n) = 0\,. \tag{1.12}$$

The error in Ref. [41, 59, 91, 92] came from that the Silver-Müller radiation condition was recast into a weaker form: the sum in Eq. (1.12) was written as $A(r) - B(r)$, and it was required that $A \to B$ for $r \to \infty$, in the sense that $A/B \to 1$ for $r \to \infty$. This is clearly not identical to the actual condition, which is written as $\lim_{r\to\infty}[A(r) - B(r)] = 0$. The simplest example to show that these two conditions are not equal is taking $A = r+1$, and $B = r$, which satisfies the weak formulation, but not the actual condition. Note that the eigenmodes of a planar system at normal incidence is a special case which do satisfy Eq. (1.11) and Eq. (1.12).

The mode fields are normalised as

$$1 = \int \left(\mathbf{E}_n \cdot \boldsymbol{\varepsilon}\mathbf{E}_n - \mathbf{H}_n \cdot \boldsymbol{\mu}\mathbf{H}_n\right) \mathrm{d}V + \frac{1}{k_n} \oint \left[\mathbf{E}_n \times (\mathbf{r} \cdot \boldsymbol{\nabla})\, \mathbf{H}_n + \mathbf{H}_n \times (\mathbf{r} \cdot \boldsymbol{\nabla})\, \mathbf{E}_n\right] \cdot \hat{\boldsymbol{n}}\, \mathrm{d}S\,. \tag{1.13}$$

The first integral is over an arbitrary volume V that includes at least all inhomogeneities, and the second is an integral along the normal $\hat{\boldsymbol{n}}$ of the surface S enclosing the volume V. The normalisation can also be rewritten in terms of the electric field only as

$$1 = 2 \int \mathbf{E}_n \boldsymbol{\varepsilon} \mathbf{E}_n \mathrm{d}V + \frac{1}{k_n} \oint \left(\frac{\partial \mathbf{E}'_n}{\partial s} \cdot \mathbf{E}_n - \frac{\partial \mathbf{E}_n}{\partial s} \cdot \mathbf{E}'_n \right) \mathrm{d}S\,. \tag{1.14}$$

Here the prime denotes $\mathbf{E}'_n = (\mathbf{r} \cdot \boldsymbol{\nabla})\mathbf{E}_n / k_n$ and $\frac{\partial}{\partial s}$ is the spacial derivative along the surface normal.

Static modes

Alongside the RS solutions with $k_n \neq 0$ there are modes with $k_\lambda = 0$, which are referred to as static modes (SMs). They are irrotational fields satisfying the equation

$$\boldsymbol{\nabla} \times \mathbf{E}_\lambda(\mathbf{r}) = 0\,, \tag{1.15}$$

$$\boldsymbol{\nabla} \times \mathbf{H}_\lambda(\mathbf{r}) = 0\,, \tag{1.16}$$

therefore they can be defined as a gradient of an appropriate scalar potential. These modes are important because they also contribute to the expansion of the GD, as described in the next section. The above equations are not coupled, therefore we can define two distinct set of SMs as

$$\mathbf{E}_\lambda = -\boldsymbol{\nabla}\psi_\lambda, \qquad \mathbf{H}_\lambda = 0\,, \qquad \text{(electric)} \tag{1.17}$$

$$\mathbf{E}_\lambda = 0, \qquad \mathbf{H}_\lambda = -\boldsymbol{\nabla}\psi_\lambda\,. \qquad \text{(magnetic)} \tag{1.18}$$

There is an infinite number of different ways to define the scalar potential, which corresponds to a charge density inside the system [32, 85]. As the SMs decay outside of the system, as opposed to the RSs which diverge, they can be normalised as

$$1 = \int \left(\mathbf{E}_\lambda \cdot \boldsymbol{\varepsilon}\mathbf{E}_\lambda - \mathbf{H}_\lambda \cdot \boldsymbol{\mu}\mathbf{H}_\lambda\right) \mathrm{d}V\,, \tag{1.19}$$

with the integral over the whole space. The case of 1D planar systems is an exception, where the SMs do not decay outside of the system, and their treatment is discussed further in Chap. 2. We note that in case the material properties are dispersive the normalisation condition for SMs is modified by replacing $\boldsymbol{\varepsilon}$ with $\partial k^2 \boldsymbol{\varepsilon} / \partial k^2$. If the permittivity has a pole

at $k = 0$, then this results in vanishing field amplitude for modes with $k_\lambda = 0$. However there can also be irrotational fields, which are also known as longitudinal modes, for $k_\lambda \neq 0$ when $\mathbb{P}(k_\lambda, \mathbf{r}) = 0$ [88].

PML modes

For simple system, such as a slab or sphere [70], the eigenmodes can be calculated analytically. For more complicated systems they can be found computationally, for example with the RSE, or with other numerical techniques, such FEM which necessarily uses a perfectly matched layer (PML) [36, 51, 58, 94].

Using a PML is a method to enforce outgoing waves boundary condition in a simulation. A PML layer is added outside the physical computational domain, and via applying a complex coordinate transformation, in an ideal case the infinite PML absorbs all waves without reflecting any. In practical use however, PMLs are finite and have a some reflection (i.e. incoming waves), effectively creating a spatially closed system. The consequence of a non-ideal PML and the numerical discretisation is that, alongside the RSs and SMs, additional artificial modes, called PML modes, appear in the spectrum. PML modes usually have a small field amplitude inside resonator, and a large one inside the PML region. The PML modes are usually strongly dependent on the PML settings, so varying these will change the modes and they can be identified in the spectrum. The PML modes can be important for scattering calculations [95], especially when the background is complex, such as when a resonator is placed on a slab [36], and they can ensure completeness inside the entire simulated domain [69]. When a PML layer present, the normalisation (Eq. (1.13)) can be modified to be a simple volume integral over the entire domain (including the PML) due to the decaying nature of the modes inside the PML [40]. A unique benefit of this method of normalisation is that it is also applicable to the case when a resonator is placed on a substrate [36, 69]. While the RSE does not use a PML, we will show that for certain perturbations it can produce modes that are similar to PML modes both in behaviour inside the cavity and in functionality.

1.2.2 Green's dyadic

In case of the vectorial wave equation the GF is a tensor and will be referred to as GD. The GD of the operator $\hat{\mathbb{M}}$ satisfies the equation

$$\hat{\mathbb{M}}(k, \mathbf{r})\mathbb{G}(\mathbf{r}, \mathbf{r}'; k) = \hat{\mathbb{I}}\delta(\mathbf{r} - \mathbf{r}')\,, \tag{1.20}$$

and the same (outgoing) boundary conditions as the eigenmodes. The GD $\mathbb{G}$ can be written as 6×6 tensor, made up of four 3×3 dyadic components $\mathbf{G}$

$$\mathbb{G} = \begin{pmatrix} \mathbf{G}^{\mathrm{EE}} & \mathbf{G}^{\mathrm{EH}} \\ \mathbf{G}^{\mathrm{HE}} & \mathbf{G}^{\mathrm{HH}} \end{pmatrix}, \tag{1.21}$$

where the component $\mathbf{G}^{\mathrm{FF}'}$ can be physically interpreted as a response field F (electric E or magnetic H) due to source field F′ (electric E or magnetic H). Using the GD (or the GF for the scalar equation) it is straight forward to find the solution to a differential equation with any source term, and this approach can be used to find the observables of a system, such as the scattering matrix and cross-section [38], or the Purcell factor [82]. It is not always possible to find a simple closed analytic form of the GD, however it can always be written in terms of the eigenmodes of the system, as described in the next section. Therefore, if the eigenmodes are known, then the GD is also know, and hence all the observables are know as well. This highlights the importance of developing efficient eigenmode solvers, such as the RSE.

Mittag-Leffler expansion

The exact analytic form of the GD contains poles in the complex wavenumber plane. Inside the system GD is a meromorphic function. A meromorphic function $f(z)$ of the complex variable z is single valued and can only have finite order, isolated poles, thus can only tend to infinity as polynomial, and it can not have essential singularities [96]. Such functions can be expressed as a series called Mittag-Leffler (ML) expansion [97]. In the special case that the function $f(z)$ only has simple poles the terms in the sum will be proportional to $b_n/(z - a_n)$, where a_n is the position of the pole, and b_n is the residue, and depending on the behaviour of $f(z)$ around $z = 0$ or $z \to \infty$ the series can also contain an additional term which does not have a pole [98]. For example, in 1D planar systems for $k \to \infty$ the electric field does not vanish but it is bounded at a finite value and its ML expansion contain additional terms [99].

Inside the system volume ($\mathbf{r}, \mathbf{r}' \subset V$) the GD vanishes for large k, so $\lim_{k\to\infty} \mathbb{G} = 0$ (for the GF in 1D this is shown in Appendix A.1), which means that it can be we written as a simple ML expansion, which is also referred to as spectral representation, which has the form

$$\mathbb{G}(\mathbf{r}, \mathbf{r}') = \sum_{\nu} \frac{\mathbb{F}_\nu(\mathbf{r}) \otimes \mathbb{F}_\nu(\mathbf{r}')}{k - k_\nu} = \sum_{n} \frac{\mathbb{F}_n(\mathbf{r}) \otimes \mathbb{F}_n(\mathbf{r}')}{k - k_n} + \sum_{\lambda} \frac{\mathbb{F}_\lambda(\mathbf{r}) \otimes \mathbb{F}_\lambda(\mathbf{r}')}{k}. \tag{1.22}$$

where k_ν is a pole of the GD and $\mathbb{F}_\nu(\mathbf{r}) \otimes \mathbb{F}_\nu(\mathbf{r}')$ is the corresponding residue, n labels the RSs ($k_\nu = k_n \neq 0$) , and λ labels the static modes ($k_\nu = k_\lambda = 0$) which are used to represent

the static pole of the GD. Outside the cavity (when $\mathbf{r} \notin V$ and-or $\mathbf{r}' \notin V$) however the GD tends to infinity exponentially, therefore it can not be expressed as a ML series. From an alternative point of view, the RSs do not form a complete set outside of the cavity, therefore they are not suitable as a basis for expansion. Note that the property of completeness in Ref. [31] is also derived based on where the GF vanishes. To find the closure relation for the modes we can insert Eq. (1.22) into Eq. (1.20), compare the coefficients of terms with k, and obtain

$$\mathbb{P}(\mathbf{r}) \sum_{\nu} \mathbb{F}_{\nu}(\mathbf{r}) \otimes \mathbb{F}_{\nu}(\mathbf{r}') = \delta(\mathbf{r} - \mathbf{r}') \,. \tag{1.23}$$

We note that if the normalisation is chosen differently from Eq. (1.13), then an additional weight factor can appear in the denominator of the GD, for example a factor of 2 in Ref. [14, 63]. There are other forms of the GD available in literature. For example, one can reformulate the coupled first order differential equation for $\mathbf{E}$ and $\mathbf{H}$ (Eq. (1.5)) and obtain a second order differential equation containing only one of them; or one can also use sum rules that the eigenmodes satisfy to reformulate the GD. The link between various commonly used equation forms and corresponding GDs are considered in the next subsection.

Link between the different Green's dyadic forms

We can write Eq. (1.5) as a set of simultaneous, or coupled, first-order differential equations

$$k\boldsymbol{\varepsilon}(\mathbf{r})\mathbf{E}(\mathbf{r}) = \boldsymbol{\nabla} \times i\mathbf{H}(\mathbf{r}) \,, \tag{1.24}$$

$$k\boldsymbol{\mu}(\mathbf{r})i\mathbf{H}(\mathbf{r}) = \boldsymbol{\nabla} \times \mathbf{E}(\mathbf{r}) \,, \tag{1.25}$$

which are linear in k. Inserting Eq. (1.25) into Eq. (1.24) leads to a single, or decoupled, second-order differential equation, which contains either $\mathbf{E}$ or $\mathbf{H}$. We keep $\mathbf{E}$ here, and write the wave equation as

$$k^2\boldsymbol{\varepsilon}(\mathbf{r})\mathbf{E}(\mathbf{r}) - \boldsymbol{\nabla} \times \boldsymbol{\mu}^{-1}(\mathbf{r})\boldsymbol{\nabla} \times \mathbf{E}(\mathbf{r}) = 0 \,, \tag{1.26}$$

which is now a second-order differential equation, quadratic in k. The corresponding GD satisfies

$$k^2\boldsymbol{\varepsilon}(\mathbf{r})\mathbf{G}_{\mathrm{d}}(\mathbf{r}, \mathbf{r}') - \boldsymbol{\nabla} \times \boldsymbol{\mu}^{-1}(\mathbf{r})\boldsymbol{\nabla} \times \mathbf{G}_{\mathrm{d}}(\mathbf{r}, \mathbf{r}') = \delta(\mathbf{r} - \mathbf{r}')\mathbf{I} \,. \tag{1.27}$$

We chose subscript 'd' to denote that the GD corresponds to the decoupled differential equation. We could also write $\mathbf{G}_{\mathrm{d}}^{\mathrm{EE}'}$ instead of $\mathbf{G}_{\mathrm{d}}$ as here the GD is the electric field response E to an electric field excitation E′. The GD can be written as a sum of a resonant and a

non-resonant term, $\mathbf{G}_{\rm d} = \mathbf{G}_{\rm rs} + \mathbf{G}_{\rm nr}$, the former containing the contribution from RSs, the latter from SMs. The resonant part (with poles $k_\nu = k_n \neq 0$) of $\mathbf{G}_{\rm d}$ inside the system can be written in the well known form [14, 41, 66]

$$\mathbf{G}_{\rm rs}(\mathbf{r},\mathbf{r}') = \sum_n \frac{\mathbf{E}_n(\mathbf{r}) \otimes \mathbf{E}_n(\mathbf{r})}{k_n(k-k_n)}\,. \tag{1.28}$$

Writing the non-resonant contribution in the form

$$\mathbf{G}_{\rm nr} = \sum_\lambda \frac{\mathbf{E}_\lambda(\mathbf{r}) \otimes \mathbf{E}_\lambda(\mathbf{r})}{k^2}\,, \tag{1.29}$$

and inserting $\mathbf{G}_{\rm d} = \mathbf{G}_{\rm rs} + \mathbf{G}_{\rm nr}$ into Eq. (1.27), then comparing the coefficients of k in the equation leads to the well know sum rule [66, 82]

$$\sum_n \frac{\mathbf{E}_n(\mathbf{r}) \otimes \mathbf{E}_n(\mathbf{r})}{k_n} = 0\,. \tag{1.30}$$

In case of dispersive materials there are additional sum rules for the eigenmodes [82]. Using the sum rule Eq. (1.30), and subtracting a zero divided by k from $\mathbf{G}_{\rm rs}$, for $k \neq 0$ we can find an alternative form of the resonant part that is also often used [62, 63, 100]

$$\begin{aligned}\mathbf{G}_{\rm rs}(\mathbf{r},\mathbf{r}') &= \sum_n \frac{\mathbf{E}_n(\mathbf{r}) \otimes \mathbf{E}_n(\mathbf{r})}{k_n(k-k_n)} - \frac{1}{k}\sum_n \frac{\mathbf{E}_n(\mathbf{r}) \otimes \mathbf{E}_n(\mathbf{r})}{k_n} \\ &= \sum_n \frac{\mathbf{E}_n(\mathbf{r}) \otimes \mathbf{E}_n(\mathbf{r})}{k(k-k_n)}\end{aligned} \tag{1.31}$$

In Appendix E.2 we investigate the the validity of Eq. (1.30) and Eq. (1.31) in relation to calculating the scattering-matrix, which is the subject of Chap. 6.

Now considering the coupled wave equation (either Eq. (1.5), or Eq. (1.24) and Eq. (1.25) together) the corresponding GD, which we take in the form of Eq. (1.21), satisfies

$$\left[k\begin{pmatrix}\boldsymbol{\varepsilon}(\mathbf{r}) & 0\\ 0 & \boldsymbol{\mu}(\mathbf{r})\end{pmatrix} - \begin{pmatrix}0 & \boldsymbol{\nabla}\times\\ \boldsymbol{\nabla}\times & 0\end{pmatrix}\right]\begin{pmatrix}\mathbf{G}^{\rm EE}(\mathbf{r},\mathbf{r}') & \mathbf{G}^{\rm EH}(\mathbf{r},\mathbf{r}')\\ \mathbf{G}^{\rm HE}(\mathbf{r},\mathbf{r}') & \mathbf{G}^{\rm HH}(\mathbf{r},\mathbf{r}')\end{pmatrix} = \begin{pmatrix}\delta(\mathbf{r}-\mathbf{r}')\mathbf{I} & 0\\ 0 & \delta(\mathbf{r}-\mathbf{r}')\mathbf{I}\end{pmatrix}. \tag{1.32}$$

Multiplying out the terms leads to a set of coupled differential equations again, but this time four, which are

$$k\boldsymbol{\varepsilon}(\mathbf{r})\mathbf{G}^{\rm EE}(\mathbf{r},\mathbf{r}') - \boldsymbol{\nabla}\times\mathbf{G}^{\rm HE}(\mathbf{r},\mathbf{r}') = \delta(\mathbf{r}-\mathbf{r}')\mathbf{I}\,, \tag{1.33}$$

$$k\boldsymbol{\mu}(\mathbf{r})\mathbf{G}^{\rm EH}(\mathbf{r},\mathbf{r}') - \boldsymbol{\nabla}\times\mathbf{G}^{\rm HH}(\mathbf{r},\mathbf{r}') = 0\,, \tag{1.34}$$

$$k\boldsymbol{\mu}(\mathbf{r})\mathbf{G}^{\rm HE}(\mathbf{r},\mathbf{r}') - \boldsymbol{\nabla}\times\mathbf{G}^{\rm EE}(\mathbf{r},\mathbf{r}') = 0\,, \tag{1.35}$$

$$k\boldsymbol{\varepsilon}(\mathbf{r})\mathbf{G}^{\rm HH}(\mathbf{r},\mathbf{r}') - \boldsymbol{\nabla}\times\mathbf{G}^{\rm EH}(\mathbf{r},\mathbf{r}') = \delta(\mathbf{r}-\mathbf{r}')\mathbf{I}\,. \tag{1.36}$$

Putting Eq. (1.35) into Eq. (1.33) results in

$$k\boldsymbol{\varepsilon}(\mathbf{r})\mathbf{G}^{\mathrm{EE}}(\mathbf{r},\mathbf{r}') - \boldsymbol{\nabla}\times\boldsymbol{\mu}^{-1}(\mathbf{r})\boldsymbol{\nabla}\times\frac{\mathbf{G}^{\mathrm{EE}}(\mathbf{r},\mathbf{r}')}{k} = \delta(\mathbf{r}-\mathbf{r}')\mathbf{I}\,. \tag{1.37}$$

Clearly, $\mathbf{G}^{\mathrm{EE}}/k = \mathbf{G}_{\mathrm{d}}^{\mathrm{EE}}$. Naturally, if $\mathbf{G}^{\mathrm{EE}}$ has a simple pole at $k=0$ (static pole) then $\mathbf{G}_{\mathrm{d}}^{\mathrm{EE}}$ has a double pole at $k=0$.

1.2.3 Resonant-state expansion

Following Ref. [60, 68, 85] we now introduce a perturbation to the system described in Sec. 1.2.1, in the form

$$\Delta\hat{\mathbb{P}}(\mathbf{r}) = \begin{pmatrix} \Delta\boldsymbol{\varepsilon}(\mathbf{r}) & 0 \\ 0 & \Delta\boldsymbol{\mu}(\mathbf{r}) \end{pmatrix}, \tag{1.38}$$

where the perturbation is limited to be inside the original system volume V. The perturbed modes satisfy

$$\left(\hat{\mathbb{M}}(\tilde{k},\mathbf{r}) + \tilde{k}\Delta\hat{\mathbb{P}}(\mathbf{r})\right)\tilde{\mathbb{F}}(\mathbf{r}) = 0\,, \tag{1.39}$$

where $\tilde{\mathbb{F}}$ is the perturbed field and $\tilde{k}$ is the perturbed wavenumber. Taking the perturbation term to the other side, treating it as a source term, then using the GD of the unperturbed system to solve the equation we obtain the Lippman-Schwinger integral equation for the perturbed eigenmodes

$$\tilde{\mathbb{F}}(\mathbf{r}) = -\tilde{k}\int \mathbb{G}(\mathbf{r},\mathbf{r}';\tilde{k})\Delta\hat{\mathbb{P}}(\mathbf{r}')\tilde{\mathbb{F}}(\mathbf{r}')\mathrm{d}V'\,, \tag{1.40}$$

where the volume integral is for the primed coordinates. Using the spectral representation of the GD (Eq. (1.22)) we get

$$\tilde{\mathbb{F}}(\mathbf{r}) = -\tilde{k}\sum_{\nu}\frac{\mathbb{F}_\nu(\mathbf{r})}{\tilde{k}-k_\nu}\int \mathbb{F}_\nu(\mathbf{r}')\Delta\hat{\mathbb{P}}(\mathbf{r}')\tilde{\mathbb{F}}(\mathbf{r}')\mathrm{d}V'\,, \tag{1.41}$$

which can also be seen as the expansion of perturbed modes into the complete set of unperturbed modes as

$$\tilde{\mathbb{F}}(\mathbf{r}) = \sum_{\nu} c_\nu \mathbb{F}_\nu(\mathbf{r})\,, \tag{1.42}$$

with the expansion coefficient given as

$$c_\nu = \frac{-\tilde{k}}{\tilde{k}-k_\nu}\int \mathbb{F}_\nu(\mathbf{r}')\Delta\hat{\mathbb{P}}(\mathbf{r}')\tilde{\mathbb{F}}(\mathbf{r}')\mathrm{d}V'\,. \tag{1.43}$$

Inserting Eq. (1.42) into Eq. (1.41) we get

$$\sum_{\nu} c_\nu \mathbb{F}_\nu(\mathbf{r}) = -\tilde{k} \sum_{\nu} \frac{\mathbb{F}_\nu(\mathbf{r})}{\tilde{k} - k_\nu} \int \mathbb{F}_\nu(\mathbf{r}') \Delta\hat{\mathbb{P}}(\mathbf{r}') \sum_{\nu'} c_{\nu'} \mathbb{F}_{\nu'}(\mathbf{r}') \mathrm{d}V' \,. \tag{1.44}$$

Equating the coefficients of $\mathbb{F}_\nu$ gives us the RSE matrix equation

$$(\tilde{k} - k_\nu) c_\nu = -\tilde{k} \sum_{\nu'} V_{\nu\nu'} c_{\nu'} \,, \tag{1.45}$$

where

$$V_{\nu\nu'} = \int \mathbb{F}_\nu(\mathbf{r}) \; \Delta\hat{\mathbb{P}}(\mathbf{r}) \mathbb{F}_{\nu'}(\mathbf{r}) \mathrm{d}V \,. \tag{1.46}$$

Using the fact that $\tilde{\mathbb{F}}(\mathbf{r}) = \sum_n c_n \mathbb{F}_n(\mathbf{r}) + \sum_\lambda c_\lambda \mathbb{F}_\lambda(\mathbf{r})$, and introducing a substitution $b_n = c_n \sqrt{k_n/\tilde{k}}$ to symmetrise the matrix, we obtain a numerically more efficient symmetric RSE matrix equation

$$\sum_{n'} \frac{\delta_{nn'}}{k_n} + \frac{\overline{V}_{nn'}}{\sqrt{k_n}\sqrt{k_{n'}}} b_{n'} = \frac{1}{\tilde{k}} b_n \,, \tag{1.47}$$

where

$$\overline{V}_{nn'} = V_{nn'} - \sum_{\lambda\lambda'} V_{n\lambda} W_{\lambda\lambda'} V_{\lambda' n'} \,, \tag{1.48}$$

and W is the inverse of the matrix $\delta_{\lambda\lambda'} + V_{\lambda\lambda'}$. The static mode expansion coefficients are then

$$c_\lambda = -\sum_{\lambda'} W_{\lambda\lambda'} \sum_{n} V_{\lambda' n} c_n \,. \tag{1.49}$$

On Fig. 1.1.3 we illustrate in case of a slab and a sphere that the RSE can find the perturbed eigenmodes accurately even for larger perturbations. For practical implementations it is important to note that when the matrix equation (Eq. (1.47)) is diagonalised, a matrix of eigenvectors B is produced. This matrix of eigenvectors has to be normalised as $B^T B = I$, where ^{T} denotes the transpose, in line with Ref. [38], as opposed to $B^\dagger B = I$, where † denotes the conjugate transpose, which is often the convention in numerical algorithms.

In the limit of infinite modes in the basis the formalism gives the exact solution to the perturbed problem. In practice however, the RSE matrix is truncated to a finite size N, with the corresponding condition that only modes with $|k_n| < k_{\max}$ are taken in the basis. The size of the basis influences the accuracy of the results. Increasing the basis size has two effect: first, by taking a fixed perturbed mode $\tilde{k}$ it decreases its error, secondly, it increases the spectral range where $|\tilde{k}|$ are calculated, see for example Fig. 2.4.1 in Chap. 2. For a well behaved

perturbations, in case of a slab, or in case of permittivity (permeability) perturbation of TE (TM) modes of a sphere the error in $\tilde{k}$ is $\propto 1/k_{\text{max}}^3$ [14]. The average error of the perturbed field (Eq. (1.42)) has slower, $1/k_{\text{max}}$ convergence [101]. In case of permittivity (permeability) perturbation of TM (TE) modes of a sphere the SMs have a significant influence of the convergence rate, and it was found that using the general expansion $\sum_\lambda \mathbb{F}_\lambda(\mathbf{r}) \otimes \mathbb{F}_\lambda(\mathbf{r}')$ for the static pole residue can leads to a slower, $1/k_{\text{max}}$ convergence rate for $\tilde{k}$ [32]. It was shown in Ref. [85] that in case of a spherically symmetric basis system the residue of the static pole can be written as

$$\sum_\lambda \mathbb{F}_\lambda(\mathbf{r}) \otimes \mathbb{F}_\lambda(\mathbf{r}') = \delta(\mathbf{r}-\mathbf{r}') \begin{pmatrix} \frac{\hat{\boldsymbol{r}}\otimes\hat{\boldsymbol{r}}}{\varepsilon} & 0 \\ 0 & \frac{\hat{\boldsymbol{r}}\otimes\hat{\boldsymbol{r}}}{\mu} \end{pmatrix} + \sum_j \mathbb{F}_j(\mathbf{r}) \otimes \mathbb{F}_j(\mathbf{r}'), \tag{1.50}$$

where $\hat{\boldsymbol{r}}$ is the radial unit vector in spherical coordinates, and $\hat{\boldsymbol{r}}\otimes\hat{\boldsymbol{r}}/\varepsilon$ ($\hat{\boldsymbol{r}}\otimes\hat{\boldsymbol{r}}/\mu$) corresponds to the EE (HH) dyadic block in $\mathbb{G}$ (Eq. (1.21)) in spherical basis vectors. Using this expansion lead to a quicker, $1/k_{\text{max}}^3$ convergence rate for spherically symmetric perturbations as now the δ function which appears on the right hand side is not expanded into a set of continuous functions, the SMs. While $\mathbb{F}_j(\mathbf{r}) \neq \mathbb{F}_\lambda(\mathbf{r})$ and $\mathbb{F}_j(\mathbf{r}) \neq \mathbb{F}_n(\mathbf{r})$, the field $\mathbb{F}_j(\mathbf{r})$ can be defined in relation to the RSs and possibly SMs, and there is a range of possible forms that it can take. These are discussed in more detail in Chap. 3. Following the nomenclature of Ref. [85], we refer to Eq. (1.22) as ML1, and to Eq. (1.50) as ML3 or ML4, depending on the set of modes used for $\mathbb{F}_j(\mathbf{r})$. As $\mathbb{F}_j(\mathbf{r})$ expresses part of the static pole residue, we refer to them as static-like modes.

1.3 Thesis plan

In Chap. 2 we look at 1D examples, planar systems with waves propagating normal to the surface. We study the convergence rate of the different ML expansion of the GF, namely, with (Eq. (1.31)) and without (Eq. (1.28)) the use of a sum rule. We investigate a special case of the sum rule (Eq. (1.30)) and its validity, which has an impact on the GF convergence rate. We look at the accuracy of the RSE when the basis or perturbed system has no step like boundary. Finally we will consider a size perturbation of a slab, which results in artificial modes that can be interpreted as analogues to PML modes, in the sense that they provide completeness over the original system volume.

In Chap. 3 we consider spherically symmetric systems, which due to the symmetry can be considered as an effective 1D system. We investigate how using different functions $\mathbb{F}_j(\mathbf{r})$ in the static pole expansion impact the accuracy of the RSE. We analyse the confinement of

modes in terms of reflection from the resonator surface, and based on an effective potential picture. We consider how various continuously changing permittivity profiles, without step like boundaries, affect the spectra, and how this can give rise to quasi-degeneracy of TE and TM modes.

In Chap. 4 we develop a rigorous first-order perturbation theory for the eigenmodes based on the RSE. We investigate the contribution of static modes to the first-order results, find that all orders of the standard perturbations series can contain in fact first order contributions when the boundary of the system is changed, and finally we present a general formalism that can treat both material and shape perturbations simultaneously. We look at an example where the spherical symmetry of the system is broken.

In Chap. 5 we apply the RSE to the case of a sphere being perturbed into a cylinder, breaking the spherical symmetry. The impact of static modes on the accuracy is investigated in detail, which reveals additional divergent terms in the static pole residue.

In Chap. 6 we implement a scattering calculation method based on the RSE, and test it in case of a size and shape perturbation of the spherical basis system. The role of artificial modes in this method is exemplified, and the validity of sum rules are revisited in case of 3D.

In Chap. 7 we provide concluding remarks.

2

One dimensional planar systems

2.1 Introduction

In this chapter we investigate the convergence rate of the ML representation of the GF, and the convergence rate of the sum rule that the eigenmodes satisfy. The ML form of the GF is a core part of the RSE, as well as it can be used to calculate observables of the system, such as transmission [101], scattering cross section [38] or Purcell effect [43], therefore it is crucial to understand the properties of the series representation and its validity. As an example we use a 1D planar dielectric system, that is, a slab in a homogeneous background, with electric field propagating normal to the surface, which allows us to compare the numerical results to easily derivable analytic ones. Furthermore, 1D systems also constitutes a special case, where the sum rule of the eigenmodes is no longer equal to zero, and the static pole of the Green's function changes its order.

Previously, Ref. [101] studied the convergence rate of the ML series of the perturbed GF in case of a homogeneous slab, and it was found that when compared to the exact solution the error scaled inversely proportional to the number of basis modes N. However, this sum included error of the perturbed electric field, which was expanded into the unperturbed eigenmodes. This could obscure the true convergence rate that would be achieved if the exact perturbed eigenmode fields were used. Furthermore, the error was calculated for all coordinate combinations inside the slab, then an average was taken. The use of averaged error can hide the different convergence rates which can occur at certain coordinate combinations, as we will show later. Ref. [59] also investigated the dependence of error of the ML expansion on N for a homogeneous slab, for one set of fixed coordinates inside the resonator, at a fixed frequency, using exact eigenmodes, and also found the same convergence rate, $1/N$. Additionally, they also investigated the error when one spacial coordinate is fixed inside the resonator, and one is varied, and found that the ML sum reproduces the exact GF correctly

even in some cases when one coordinate is taken outside the resonator. This naturally follows from the analytic form of the GF (see Appendix A.1.3), which leads to the condition that for

$$\sqrt{\varepsilon_\mathrm{s}} x_< < a(1+\sqrt{\varepsilon_\mathrm{s}}) - x_> \,, \tag{2.1}$$

the GF vanishes for large k, therefore it is possible to expand it into a ML series. Here a is the slab half width, ε_s is the slab permittivity, $x_< = \min(x, x')$ and $x_> = \max(x, x')$. This is not a contradiction with the more conventional view on the completeness of eigenmodes, namely, that they are only complete inside the system, which was also derived based on the condition that the GF vanishes for large k [31, 66], but simply an extension to it. Ref. [85] investigated the error convergence rate of the ML expansion of the full Green's dyadic in a spherically symmetric system, when both coordinates are inside the resonator. It was found that the $\mathcal{G}_{11}$ dyad, which is analogues to the 1D GF, has a $1/N$ error convergence rate. It was also found that other components of the dyadic can have different convergence rates, e.g. $1/N^3$. Furthermore, the convergence rate can also depend on the form of ML representation used.

We extend on the previous works by investigating how does the error depend on the two spacial coordinates, with different combinations of them taken, such as both coordinates on the same boundary, or on opposing boundaries. This will reveal that certain forms of the ML expansion are not always correct due to the sum rule of the eigenmodes not being satisfied. In section 2.2 we will briefly review the eigenmodes and the sum rule for a 1D system. In section 2.3 we investigate the convergence of the ML representation, first in case of a homogeneous slab, then in case of a linear permittivity profile that is continuous at the boundaries, removing the step like permittivity edge. In section 2.4 we test how the RSE performs when the perturbed or the unperturbed system has the aforementioned linear permittivity profile. Finally, in section 2.5 we look at the convergence of the ML expansion of the perturbed GF when the size of the slab is changed, and investigate the role of the artificial mode generated by the RSE.

2.2 Eigenmodes, Green's function, and sum rules

Without loss of generality we take a 1D slab as a system extending from $x = -a$ to $x = a$, with permittivity $\varepsilon_\mathrm{s}(x)$ that can be arbitrary, as long as it, or one of its spacial derivatives, has a discontinuity at the surface. This condition is required for the modes to form a complete set inside the system [31, 66]. The homogeneous background to the left of the slab has the

permittivity ε_l, and to the right of the slab ε_r, giving the permittivity over all space as

$$\varepsilon(x) = \begin{cases} \varepsilon_\mathrm{l} & x < -a \\ \varepsilon_\mathrm{s}(x) & -a \le x \le a \\ \varepsilon_\mathrm{r} & a < x \end{cases} . \tag{2.2}$$

Taking the electric field polarised along $\hat{\boldsymbol{y}}$ and propagating along $\hat{\boldsymbol{x}}$ (so $\mathbf{E}(\mathbf{r}) = E(x)\hat{\boldsymbol{y}}$), the eigenmodes satisfy the differential equation

$$\left(\frac{\mathrm{d}^2}{\mathrm{d}x^2} + \varepsilon(x)k_n^2\right) E_n(x) = 0\,. \tag{2.3}$$

The outgoing wave boundary condition means that the field is $E_n \propto e^{-ik_n\sqrt{\varepsilon_\mathrm{l}}x}$ for $x < -a$, and $E_n \propto e^{ik_n\sqrt{\varepsilon_\mathrm{r}}x}$ for $a < x$. For sake of generality here we just write the eigenmode in the slab as a sum of backward (φ_b) and forward (φ_f) propagating waves, giving the field over all space as

$$E_n(x) = \begin{cases} A_\mathrm{l} e^{-ik\sqrt{\varepsilon_\mathrm{l}}x} & x < -a \\ A_\mathrm{f}\varphi_\mathrm{f}(x) + A_\mathrm{b}\varphi_\mathrm{b}(x) & -a \le x \le a \\ A_\mathrm{r} e^{ik\sqrt{\varepsilon_\mathrm{r}}x} & a < x \end{cases} . \tag{2.4}$$

where A are the amplitudes of the waves, and on the right hand side we dropped the dependence of A, φ, and k on n for brevity. In case of a 1D system with the field propagating normal to the interface Maxwell's boundary conditions (namely, that the parallel component of the electric field $\mathbf{E}$ and the magnetic field $\mathbf{B}$ are continuous across a boundary) imply that $E_n(x)$ is continuous and smooth everywhere. As the field is continuous and smooth at $x = a$, we can find

$$A_\mathrm{b} = A_\mathrm{f}\frac{ik\sqrt{\varepsilon_\mathrm{r}}\varphi_\mathrm{f}(a) - \varphi_\mathrm{f}'(a)}{\varphi_\mathrm{b}'(a) - ik\sqrt{\varepsilon_\mathrm{r}}\varphi_\mathrm{b}(r)}\,. \tag{2.5}$$

The eigenvalues k_n, for which Eq. (2.3) can be satisfied, can be found by applying Maxwell's boundary conditions at both interfaces $x = \pm a$. Alternatively one can also find k_n from the condition that the Wronskian in the denominator of the GF (Eq. (A.2) in the Appendix A.1.1) is zero at k_n, that is, the GF has a pole here. For a slab with an arbitrary permittivity profile, the secular equation is

$$\begin{aligned} ik\sqrt{\varepsilon_\mathrm{r}}\left\{-\left[ik\sqrt{\varepsilon_\mathrm{l}}\varphi_\mathrm{f}(-a) + \varphi_\mathrm{f}'(-a)\right]\varphi_\mathrm{b}(a) + \left[\varphi_\mathrm{b}'(-a) + ik\sqrt{\varepsilon_\mathrm{l}}\varphi_\mathrm{b}(-a)\right]\varphi_\mathrm{f}(a)\right\} \\ = -\left[(ik\sqrt{\varepsilon_\mathrm{l}}\varphi_\mathrm{f}(-a) + \varphi_\mathrm{f}'(-a)\right]\varphi_\mathrm{b}'(a) + \left[\varphi_\mathrm{b}'(-a) + ik\sqrt{\varepsilon_\mathrm{l}}\varphi_\mathrm{b}(-a)\right]\varphi_\mathrm{f}'(a)\,, \end{aligned} \tag{2.6}$$

where the prime denotes the derivative with respect to the spacial coordinate. In certain special cases, for example when the slab is homogeneous, k_n can be expressed explicitly, as we will show later, but otherwise the equation needs to be solved numerically.

The normalisation of the modes determining A is given by (see Appendix A.1.1 for a derivation)

$$\int_{-a}^{a} \varepsilon(x) E_n(x) E_m(x) \mathrm{d}x - \frac{\sqrt{\varepsilon_\mathrm{l}} E_n(-a) E_m(-a) + \sqrt{\varepsilon_\mathrm{r}} E_n(a) E_m(a)}{i(k_n + k_m)} = \frac{\delta_{nm}}{2} \,. \tag{2.7}$$

Here, consistent with Ref. [102], $\sqrt{\varepsilon_\mathrm{l}}$ and $\sqrt{\varepsilon_\mathrm{r}}$ appears in the surface term compared to the normalisation in Ref. [14], where vacuum was taken as a background on both sides ($\sqrt{\varepsilon_\mathrm{l}} = \sqrt{\varepsilon_\mathrm{r}} = 1$).

The GF satisfies the equation

$$\left(\frac{\mathrm{d}^2}{\mathrm{d}x^2} + \varepsilon(x) k^2 \right) G(x, x'; k) = \delta(x - x') \,, \tag{2.8}$$

with the same outgoing boundary conditions as the eigenmodes, and can be expressed as a ML sum (see Appendix A.1.2 for a derivation)

$$G_\mathrm{er}(x, x'; k) = \sum_n \frac{E_n(x) E_n(x')}{k_n (k - k_n)} + \frac{R_0}{k} \,, \tag{2.9}$$

where the first term is a sum of each pole contribution with $k_n \neq 0$, and the second term is the static pole, with the R_0 denoting the residue of the GF at $k = 0$. We chose the subscript 'er' (exact residue) to emphasize that the static pole residue is separated from the resonant part. In 1D the static pole residue is identical to the static pole residue of the background GF (G_b), and the static pole is a single pole of the GF of the decoupled wave equation. This can be seen from the Dyson equation, which can be found similarly to the integral equation for the perturbed eigenmodes (Eq. (1.40)), and it expresses the perturbed GF in terms of the unperturbed one as [14, 59]

$$G(x, x'; k) = G_\mathrm{b}(x, x'; k) - k^2 \int_{-a}^{a} G_\mathrm{b}(x, x''; k) \Delta\varepsilon(x'') G(x'', x'; k) \mathrm{d}x'' \,. \tag{2.10}$$

G_b has a single pole in k (see Appendix A.1.3). Multiplying Eq. (2.10) with k, then taking the limit $k \to 0$ will show that unless $G(x'', x'; k)$ also has a single pole in k the equation can not be satisfied. Furthermore, when the equation is satisfied the static pole residue of $G(x, x'; k)$ and $G_\mathrm{b}(x, x'; k)$ are equal, assuming that $\Delta\varepsilon$ has no pole at $k = 0$ [59]. In 1D the curl free equation defining the static modes (Eq. (1.15)) gives a constant electric field E_0. Taking $R_0 = E_0 E_0 / k_0$ to ensure the correct dimensionality, where $k_0 = 0$, the amplitude A of the static mode is proportional to $\sqrt{k}$ for $k \to 0$, which is also consistent with applying the normalisation Eq. (2.7) for the static mode.

Inserting Eq. (2.9) into Eq. (2.8) and comparing the coefficients of the terms proportional to various powers of k we obtain the following sum rules

$$\varepsilon(x)\sum_n E_n(x)E_n(x') = \delta(x-x')\,, \tag{2.11}$$

$$-\sum_n \frac{E_n(x)E_n(x')}{k_n} = R_0\,, \tag{2.12}$$

and the property $\mathrm{d}^2R_0/\mathrm{d}x^2 = 0$, which is consistent with a static mode having constant electric field. Eq. (2.11) is the closure relation well known in literature [31,66]. Eq. (2.12) is a special case of the sum rule Eq. (1.30) in 1D. For non-normal incidence the latter would give $R_0 = 0$ [14,66,80], while the actual static pole residue is still non-zero [32]. Using Eq. (2.12) we can rewrite Eq. (2.9) as

$$G_{\mathrm{sr}}(x,x';k) = \sum_n \frac{E_n(x)E_n(x')}{k(k-k_n)}\,, \tag{2.13}$$

and we chose the subscript 'sr' (sum rule) to indicate that for the residue of the static pole the sum rule (Eq. (2.12)) is used. We note that Eq. (2.13) is derived using the normalisation Eq. (2.7), which is consistent with Ref. [35,68]. If we chose the normalisation from Ref. [14, 101] then a factor of would 2 appear in the denominator of Eq. (2.13). This would also mean that we need to replace $\overline{V}$ with $\overline{V}/2$ in Eq. (1.47).

In the following sections we investigate how quickly the two different GF sums, namely Eq. (2.9) and Eq. (2.13), converge to the exact solution. To study the convergence we take all modes with $|k_n| < k_{\max}$ (i.e. a circle of radius $k_{\max}$, centred at the origin), and see how the relative error $|G_{\mathrm{ML}}/G_{\mathrm{ex}} - 1|$ of each ML representations changes with $k_{\max}$, where G_{ML} is either G_{er} or G_{sr}. We note that $k_{\max} \propto N$ in case of a 1D non-dispersive system, and we can use these quantities interchangeably in relation to the convergence rate.

2.3 Convergence of the ML sum in the unperturbed system

We investigate how the ML sum converges to the exact GF for an unperturbed system.

2.3.1 Case of a homogeneous slab

First we take the example of a homogeneous slab, with refractive index $\sqrt{\varepsilon_{\mathrm{s}}} = \sqrt{2}$, and embedded in vacuum as in Ref. [14]. For such a system $\sqrt{\varepsilon_{\mathrm{l}}} = \sqrt{\varepsilon_{\mathrm{r}}} = 1$ and

$$\varphi_{\mathrm{f}} = e^{ik\sqrt{\varepsilon_{\mathrm{s}}}x}\,, \tag{2.14}$$

$$\varphi_{\mathrm{b}} = e^{-ik\sqrt{\varepsilon_{\mathrm{s}}}x}\,. \tag{2.15}$$

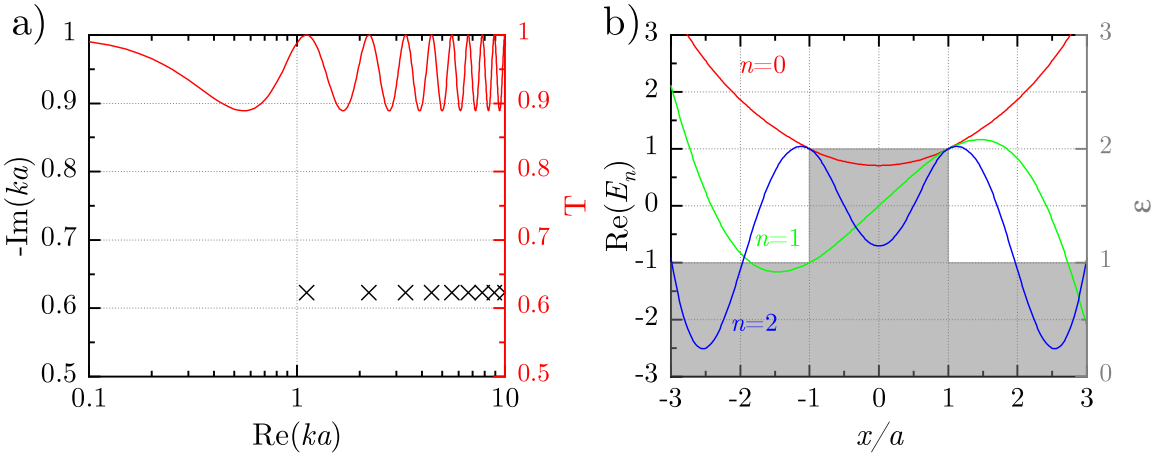

Fig. 2.3.1: Homogeneous slab in vacuum. a) eigenvalues in the complex ka plane, and the transmission coefficient T. b) real part of the electric field for the first three modes. The shading indicates the permittivity of the system and the environment.

For this case the secular equation (Eq. (2.6)) can be reduced to the explicit expression for the wavenumber

$$k_n = \frac{1}{2a\sqrt{\varepsilon_s}}(\pi n - i \ln \alpha)\,, \tag{2.16}$$

$$\alpha = \frac{\sqrt{\varepsilon_s}+1}{\sqrt{\varepsilon_s}-1}\,, \tag{2.17}$$

where $n = 0, \pm 1, \pm 2, ...$ Clearly, for a homogeneous slab k_n and a are inversely proportional. The eigenvalues are show in Fig. 2.3.1a, along with the power transmission coefficient T through the slab, illustrating that the eigenvalues correspond to peaks in the transmission spectra. In Fig. 2.3.1b we show the real part of the electric field of the first three modes. We can see that they are growing outside of the slab, and that the even and odd modes are alternating.

The GF of the system has the residue $R_0 = 1/(2i)$ at the single static pole, which can be seen from the analytic GF (Eq. (A.51) in Appendix A.1.3) or from the background GF (Eq. (A.68) in Appendix A.1.3).

To investigate the convergence of the of the ML sum to the exact GF, we take $ka = 10$, and select four spacial coordinate pairs, or points $P = (x, x')$ in the 2D spacial coordinate plane of the GF. Point $A = (0.25a, 0.5a)$ corresponds to both coordinates being inside the the resonator, point $B = (0.25a, a)$ has one coordinate on the boundary, point $C = (-a, a)$ has coordinates at opposite boundaries, and point $D = (a, a)$ has both coordinates at the same boundary. On Fig. 2.3.2 we show the error corresponding to each of these points, for both sum forms, G_{er} and G_{sr}. We can see that G_{er} converges at a rate $1/k_{max}^2$ for A, B, C,

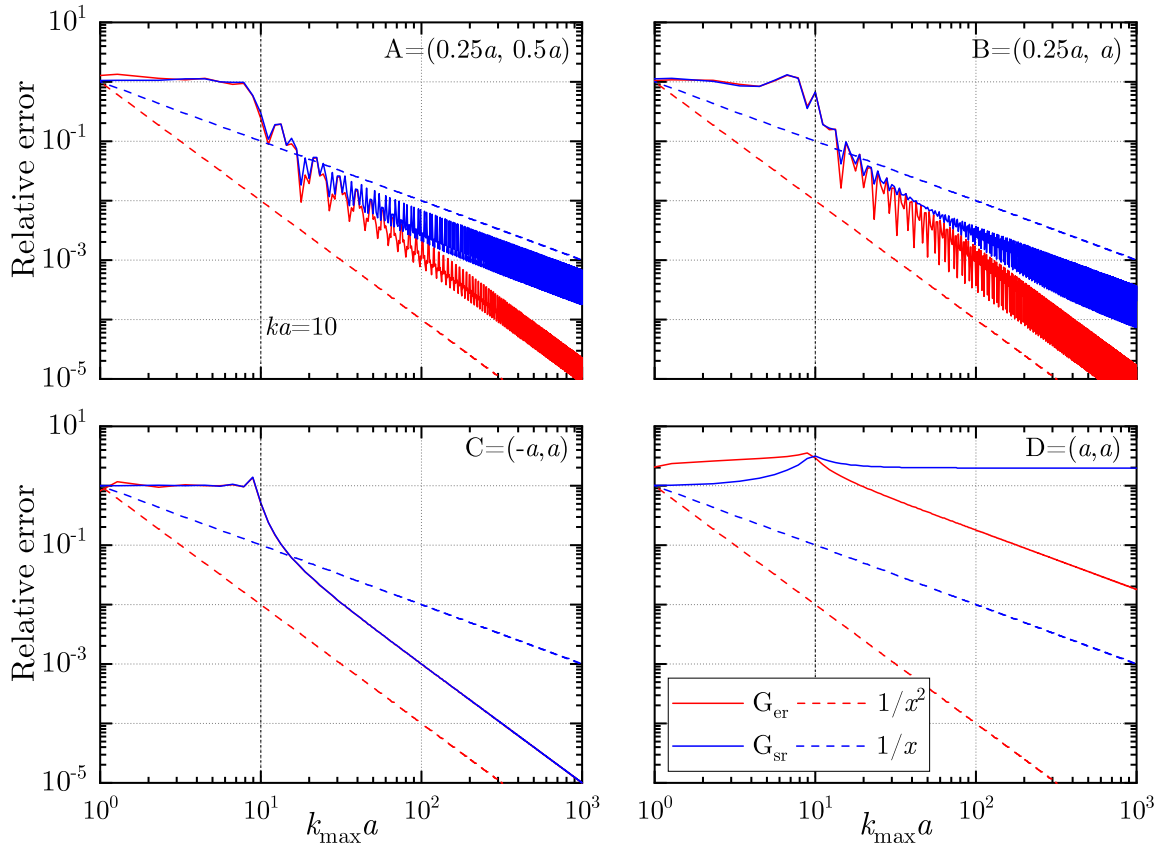

Fig. 2.3.2: Relative error of the ML expansion of the GF for a homogeneous slab, shown by solid lines. Dashed coloured lines are for reference to help estimate the error convergence rate. Slab half width is a, permittivity $\varepsilon_s = 2$, wavenuber $ka = 10$, which is indicated by the vertical dashed line.

and it has a convergence rate of $1/k_{\max}$ for D, that is, when both coordinates are at the same boundary. On the other hand, $G_{\rm sr}$ has a $1/k_{\max}$ convergence rate for A and B, when at least one point is inside the resonator, it has a $1/k_{\max}^2$ rate for C, when the spacial coordinates are at opposing boundaries, and it does not converge to the correct solution for D, when the coordinates are taken at the same boundary, albeit it does converge to a different value. It is also notable that neither of the sums start to converge to the correct value until the spectral coverage $k_{\max}$ approximately includes the appropriate k value, so until $k_{\max}a \approx 10$ in this case. This consistent with the behaviour observed in [101], where it was found that increasing N increases the radius in the complex k plane where the GF converges to the correct value.

To understand the difference between the convergence rates of $G_{\rm er}$ and $G_{\rm sr}$ we look at the sum rule for the residue, that is, Eq. (2.12). For a homogeneous system with vacuum as the background this is [14]

$$\sum_n \frac{E_n(x)E_n(x')}{ik_n} = 1\,. \tag{2.18}$$

On Fig. 2.3.3a we show how this expression converges for two different cases: when one of the

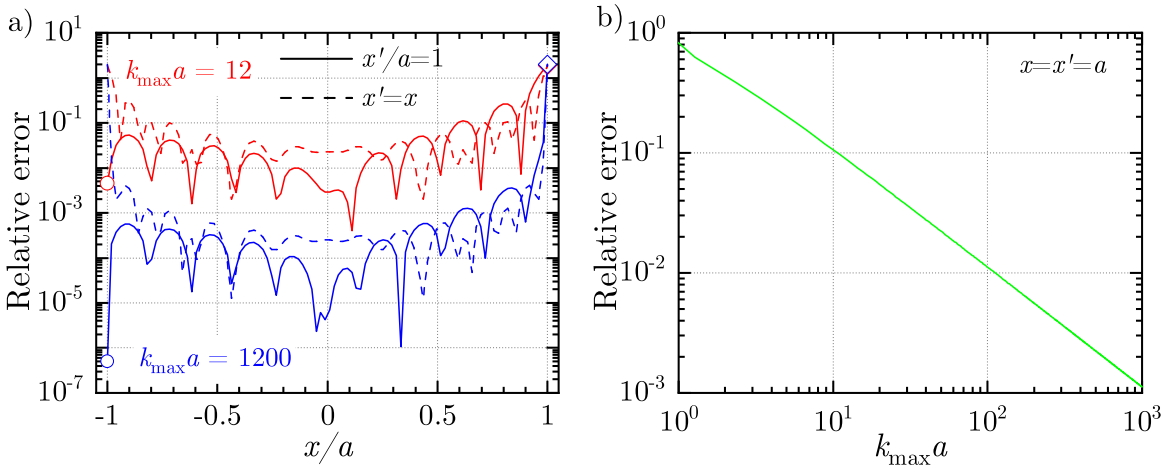

Fig. 2.3.3: a) relative error in Eq. (2.18). For the solid line the point $x = -x' = a$ is highlighted with a circle, and the point $x = x' = a$ is highlighted with a diamond. b) relative error in Eq. (2.19).

spacial coordinates is at the boundary ($x' = a$, solid line) while varying the other coordinate (x) inside the resonator, and when the two spacial coordinates are equal ($x' = x$, dashed line). We can see that generally the relative error converges as $1/k_{\max}$. For the former case, when $x' = a$, there are two significant deviations from this. First, when the two spacial coordinates are at opposing boundaries, which corresponds to the left edge of the plot, highlighted with a circle. We can see that here the expression converges as $1/k_{\max}^2$. Second, when both points are at the same boundary, on the opposite end of the plot, highlighted with a diamond, the expression does not converge to the expected solution. The dashed line shows that this is not an issue when both coordinates are equal and inside the resonator, as for $x = x' \neq \pm a$ the expression converges.

By adding the terms of the series pairs, so taking n and $-n$ together, it can be shown that when both points are inside the slab, the terms in Eq. (2.18) will take the form $\propto \sin(|n|)/|n|$, which has a convergence rate proportional to $1/N$. When the points are at opposite boundaries a similar analysis will result in terms $\propto (-1)^{|n|}/n^2$ and $\propto \cos(n)/n^2$, both of which have convergence rates of $1/N^2$. The sum G_{er} is in the latter form ($\propto 1/n^2$), for both of the aforementioned cases, which explains the better convergence rate when both points are inside the slab. When both points are at the same boundary the sum rule will take the form (see Appendix A.2.1 for details)

$$\sum_n \frac{E_n(x = x')E_n(|x'| = a)}{ik_n} = \frac{2\sqrt{\varepsilon_{\mathrm{s}}}}{\varepsilon_{\mathrm{s}} - 1} \coth(\log \alpha)\,, \tag{2.19}$$

so it no longer expresses the residue. The convergence of Eq. (2.19) is verified numerically on Fig. 2.3.3b, showing a $1/k_{\max}$ rate. We can observe that the convergence rate of the sum rule

corresponds exactly to the convergence rate of G_{sr}, and identify it as the main source of the error for that expression.

2.3.2 Case of an inhomogeneous slab without a step-like boundary

For the inhomogeneous slab we take a linear permittivity profile given as

$$\varepsilon_{\mathrm{s}}(x) = \varepsilon_{\mathrm{L}} + \frac{\varepsilon_{\mathrm{R}} - \varepsilon_{\mathrm{L}}}{2a}(x + a)\,, \tag{2.20}$$

where ε_{L} and ε_{R} are the permittivity of the slab at the left and right boundary, respectively. For a continuous permittivity profile these are equal to the background at the corresponding boundary, so $\varepsilon_{\mathrm{L}} = \varepsilon_{\mathrm{l}}$ and $\varepsilon_{\mathrm{R}} = \varepsilon_{\mathrm{r}}$. In case of a linear permittivity profile the forward and backward propagating waves are given by Bessel functions of the first (J) and second kind (Y), respectively, of order 1/3 (or alternatively, by Airy functions) [103]

$$\varphi_{\mathrm{f}} = k\sqrt{\varepsilon_{\mathrm{s}}(x)}J_{1/3}(Z)\,, \tag{2.21}$$

$$\varphi_{\mathrm{b}} = k\sqrt{\varepsilon_{\mathrm{s}}(x)}Y_{1/3}(Z)\,, \tag{2.22}$$

$$Z = \frac{2}{3\varepsilon_{\mathrm{s}}'}k[\varepsilon_{\mathrm{s}}(x)]^{3/2}\,, \tag{2.23}$$

where the prime over ε_{s} denotes the derivative with respect to the spacial coordinate.

The sum rule for the static pole residue based on the background GF is (Appendix A.1.3)

$$-\sum_n \frac{E_n(x)E_n(x')}{2k_n} = \frac{1}{i(\sqrt{\varepsilon_{\mathrm{l}}} + \sqrt{\varepsilon_{\mathrm{r}}})}\,, \tag{2.24}$$

which is consistent with Eq. (2.18), for a completely homogeneous vacuum background.

For the background permittivity we chose $\varepsilon_{\mathrm{l}} = 1$ and $\varepsilon_{\mathrm{r}} = 2$. In Fig. 2.3.4a the resulting eigenvalues and the transmission coefficient are shown. The straight dashed horizontal line is the transmission coefficient between an interface with refractive indices $\sqrt{\varepsilon_{\mathrm{l}}}$ and $\sqrt{\varepsilon_{\mathrm{r}}}$. We can see that for small k, so long wavelength, the transmission approaches this value. Intuitively, we can understand this as the incoming wave is insensitive to the thin slab between the different layers, it only "sees" a single step. At large k, so small wavelength, the permittivity does not change significantly over one wavelength, therefore no reflection occur and the transmission tends towards unity. In correlation with this, $\mathrm{Im}\,(k_n)$ increases with $\mathrm{Re}\,(k_n)$, which corresponds to the broadening of the lineshape and the consequent overlap of the peaks in the transmission spectra. Similar effects can be observed for a dispersive system, when the permittivity is described by the Drude model and the frequency independent term is equal to the background permittivity, resulting in a vanishing permittivity contrast at

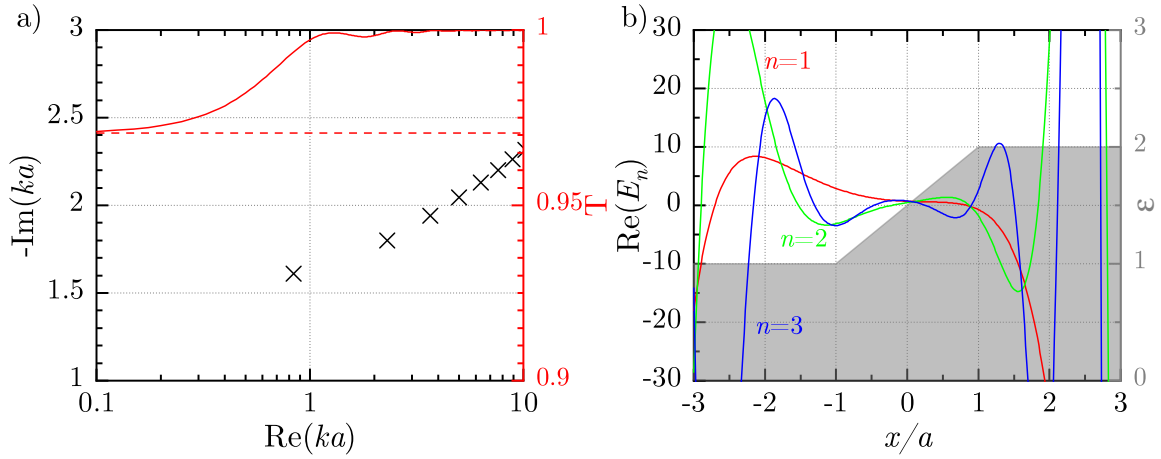

Fig. 2.3.4: Slab with a linear permittivity profile. a) eigenvalues in the complex ka plane, and the transmission coefficient T. b) real part of the electric field for the first three modes. The shading indicates the permittivity of the system and the environment.

high frequency [82]. In Fig. 2.3.4b we show the permittivity profile, as well as the first three modes which now are neither odd nor even due to the lack of symmetry of the system. The mode fields are also growing much faster outside when compared to the homogeneous case on Fig. 2.3.1b, which can be attributed to the weaker reflection at the boundary. Relation between the reflection coeffcient of a boundary (the Fresnel coefficient) and the imaginary part of the modes is described in detail in Sec. 3.2 of the next chapter.

Let us consider the convergence of the GF at the same four points as before. We choose the wavenumber $ka = 2$ this time, so that ML sum starts to converge to the correct solution for smaller $k_{\max}$. The results are shown on Fig. 2.3.5. For A and B, the rate of convergence is approximately a factor of $\sqrt{k_{\max}}$ slower than for a homogeneous slab. When both spacial coordinates are taken at opposite boundaries (C) the rate of error convergence for both sums are the same, but this time it is $1/k_{\max}$ and not $1/k_{\max}^2$. Furthermore, when both points are taken at the same boundary G_{sr} does not converge at all, and G_{er} seems to converge to the wrong value in the observed spectral range. The slower convergence can be attributed to the modes losing confinement at higher frequencies due to the reducing reflection coefficient, which is approximately inversely proportional to k for a linear profile [103]. This is exemplified on Fig. 2.3.4a by the increasing imaginary part of the modes with increasing real wavenumber.

While at a single point in parameter space, at $x = x' = a$, neither of the ML sums give the correct solution, we can conclude that overall, the ML expansion works correctly for system without a step-like boundary, even if the convergence rate might be slower. We consider this a numerical validation of the proof given in Ref. [31, 66], where it was shown that as

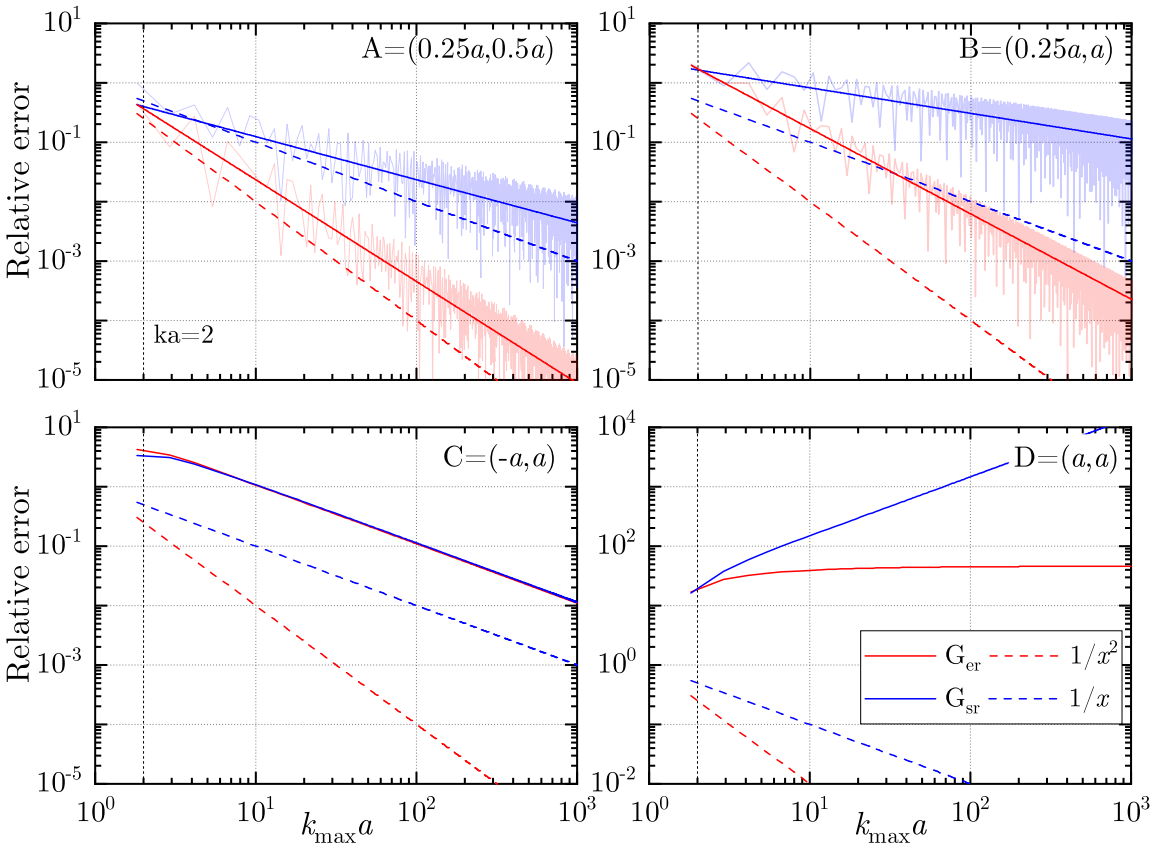

Fig. 2.3.5: Relative error of the ML expansion of the GF for a slab with a linear permittivity profile (Eq. (2.20)). For A and B a fitted line is shown, the data is shown with a faded line.

long as the permittivity, or any of its derivatives have a discontinuity, the eigenmodes form a complete set, and thus they form a suitable basis to expand the GF into. Note that if the linear profile is kept, but it is discontinuous at the boundaries, i.e. $\varepsilon_{\mathrm{L}} \neq \varepsilon_{\mathrm{l}}$ and $\varepsilon_{\mathrm{R}} \neq \varepsilon_{\mathrm{r}}$, then $\mathrm{Im}\,(k_n)$ does not grow unbounded, and the convergence rate of the ML sum will be the same as for the homogeneous slab.

2.4 Perturbation via the RSE

We investigate the error convergence rate of the RSE wavenumbers for two cases. In the first case we will look at perturbing a homogeneous slab, with different left and right background media, to a slab with a linear permittivity profile as in subsection 2.3.2. This will validate the RSE formalism for a piecewise homogeneous background, which has not been implemented before. This will also tests the convergence rate we can expect when the quality of the modes radically change, such as going from the FP modes of the homogeneous slab, with fixed $\mathrm{Im}\,(k_n)$, to the FP modes of a slab without a step-like boundary, where $\mathrm{Im}\,(k_n)$ increases

with increasing $\mathrm{Re}\,(k_n)$. In the second case we swap the systems compared to the first case: we take a slab with a continuous linear profile as basis, and perturb it to a homogeneous slab. This will show how the slow convergence rate of the GF compares with the convergence rate of the eigenvalues.

For the background medium we choose again $\varepsilon_\mathrm{l} = 1$, $\varepsilon_\mathrm{r} = 2$, but the qualitative results should not depend significantly on the combination of parameters. As the static pole residue is expressed by RSs, and the static mode itself has a vanishing amplitude, in the RSE matrix equation (Eq. (1.47)) we take $\overline{V}_{nn'} = V_{nn'} = \int_{-a}^{a} E_n(x)\Delta\varepsilon(x)E_n(x)\mathrm{d}x$.

2.4.1 Perturbation of a homogeneous slab

The backward and forward propagating waves in the slab are the same as before, given by Eq. (2.15) and Eq. (2.14), respectively. Due to the different refractive indices of the background to the left and to the right, the eigenvalues will be given by

$$k_n = \frac{1}{4\sqrt{\varepsilon_\mathrm{s}}a}(2\pi n - i\ln(\alpha))\,, \tag{2.25}$$

$$\alpha = \frac{(\sqrt{\varepsilon_\mathrm{s}}+\sqrt{\varepsilon_\mathrm{r}})(\sqrt{\varepsilon_\mathrm{s}}+\sqrt{\varepsilon_\mathrm{l}})}{(\sqrt{\varepsilon_\mathrm{s}}-\sqrt{\varepsilon_\mathrm{r}})(\sqrt{\varepsilon_\mathrm{s}}-\sqrt{\varepsilon_\mathrm{l}})}\,, \tag{2.26}$$

with again $n = 0, \pm1, \pm2....$ For the basis system we chose a slab with $\varepsilon_\mathrm{s} = 1.5$, the average of the two background permittivities. We introduce a perturbation that will results in the final permittivity to be given by Eq. (2.20). In summary, the basis permittivity is

$$\varepsilon(x) = \begin{cases} \varepsilon_\mathrm{l} = 1 & x < -a \\ \varepsilon_\mathrm{s} = 1.5 & -a \le x \le a \\ \varepsilon_\mathrm{r} = 2 & a < x \end{cases}\,, \tag{2.27}$$

and the perturbed is

$$\varepsilon_\mathrm{p}(x) = \begin{cases} \varepsilon_\mathrm{l} = 1 & x < -a \\ \varepsilon_\mathrm{l} + \frac{\varepsilon_\mathrm{r}-\varepsilon_\mathrm{l}}{2a} & -a \le x \le a \\ \varepsilon_\mathrm{r} = 2 & a < x \end{cases}\,. \tag{2.28}$$

The complex wavenumber plane and the relative error of the calculation are shown on Fig. 2.4.1. We can see that the exact solution is reproduced well, and the relative error converges as $1/k_\mathrm{max}^3$ as expected from Ref. [14, 101]. There are two modes in the complex plane at the top right (circled) that are significantly different from the exact solution. These are artificial modes, and they are produced by the RSE. They usually appear when the size

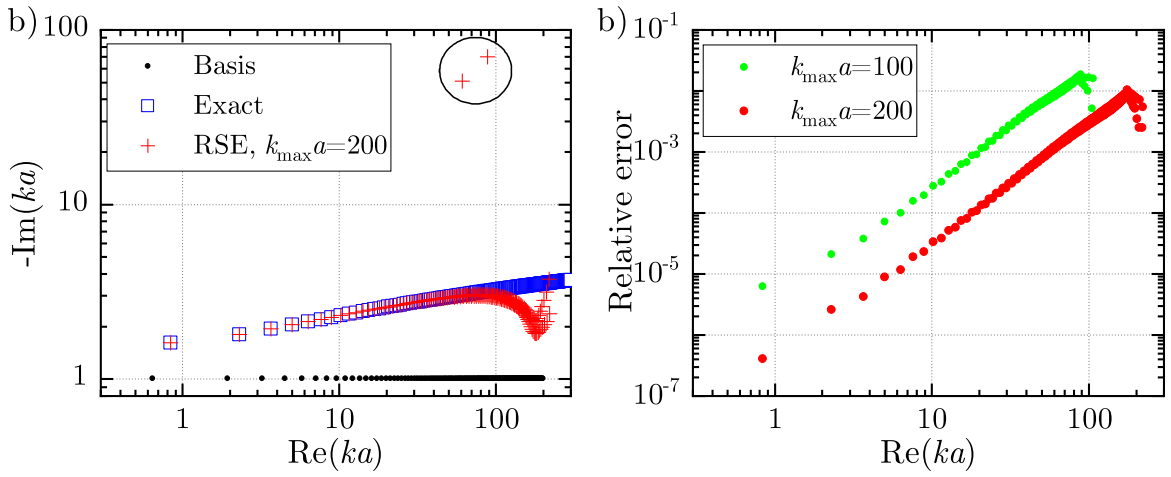

Fig. 2.4.1: Perturbing a homogeneous slab (as in Fig. 2.3.1) into a slab with a linear permittivity profile (as in Fig. 2.3.4). a) RSs wavenumbers in the complex ka plane. The circle indicates the artificial modes generated by the RSE. b) Relative error of the perturbed eigenvalues.

of the system is changed, see for example Fig.1. of Ref. [85], or Fig. 2.5.1 in Sec. 2.5. The role of these modes is to provide completeness over the original, unperturbed system volume. This will be discussed in more detail later in Sec. 2.5. In the example considered here we removed the step like boundary of the system, and this can also be interpreted as reducing the system size infinitesimally, which would lead to the formation of the artificial modes.

2.4.2 Perturbation of a slab with linear profile

Now we make reverse of the case from the previous section. We take the basis system to be the one from Sec. 2.3.2, with linear permittivity profile in the slab that is continuous at the boundaries. We introduce a perturbation that changes the inhomogeneous slab to a homogeneous one with a permittivity $\varepsilon_s = 1.5$. Therefore, the basis permittivity is

$$\varepsilon(x) = \begin{cases} \varepsilon_\mathrm{l} = 1 & x < -a \\ \varepsilon_\mathrm{l} + \frac{\varepsilon_\mathrm{r} - \varepsilon_\mathrm{l}}{2a} & -a \leq x \leq a \\ \varepsilon_\mathrm{r} = 2 & a < x \end{cases}, \tag{2.29}$$

and the perturbed is

$$\varepsilon_\mathrm{p}(x) = \begin{cases} \varepsilon_\mathrm{l} = 1 & x < -a \\ \varepsilon_\mathrm{s} = 1.5 & -a \leq x \leq a \\ \varepsilon_\mathrm{r} = 2 & a < x \end{cases}. \tag{2.30}$$

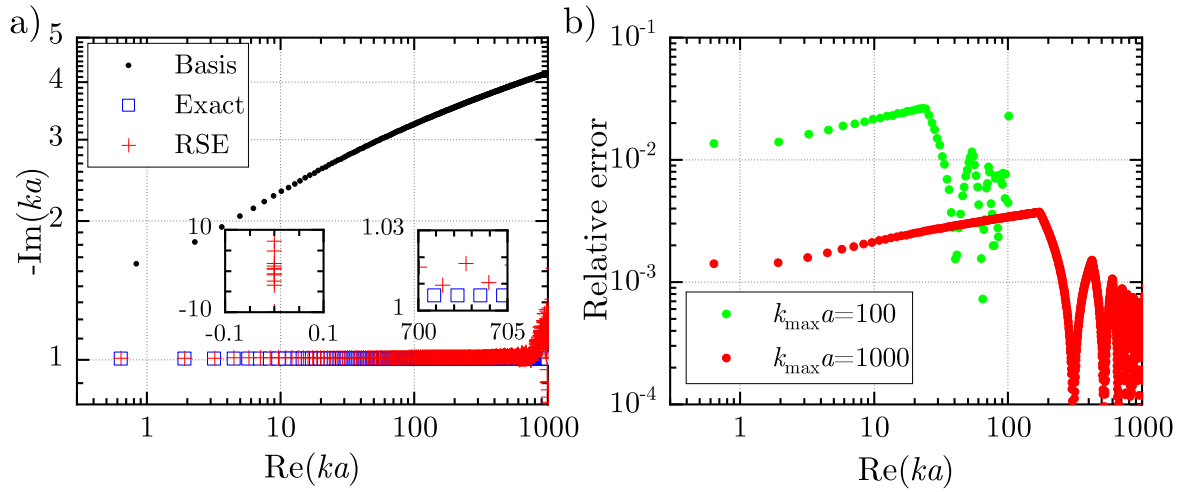

Fig. 2.4.2: Perturbing a slab with a linear permittivity profile (as in Fig. 2.3.4) into a homogeneous slab (as in Fig. 2.3.1). a) RSs wavenumbers in the complex ka plane. The left inset shows the artificial modes along the imaginary axis that are generated by the RSE; the right inset illustrates the absolute error at high frequency. b) Relative error of the perturbed eigenvalues.

The modes and the error are shown on Fig. 2.4.2. Compared to the previous case, when a homogeneous slab was perturbed to a linear profile, here the error converges significantly slower, with a factor of $1/k_{\max}$. This is expected as the ML sum itself, which the RSE relies on, was converging slower in case of a linear slab without a step-like boundary, as it was shown in Sec. 2.3.2. It is also notable that the change of the relative error along ka for a fixed $k_{\max}$ is much slower (a factor of $\sim \sqrt{ka}$) than it was for a homogeneous slab (a factor of $\sim (ka)^2$). Furthermore the error saturates much quicker, at $k \sim 0.2k_{\max}$ here, versus $k \sim k_{\max}$ before. Note that, as shown on the inset, this perturbation also generates artificial modes, this time along the imaginary axis, with negligible real part. These modes do not disappear as we increase the basis size. Nevertheless, the results reproduce and converge to the exact solution, and this provides a further verification of the completeness of the modes of a system without a step-like boundary.

2.5 Convergence of the ML sum in a perturbed system

The convergence of the perturbed field $\tilde{E}_n(x)$ and the perturbed GF was investigated in Ref. [101] for a case when the permittivity was increased in a layer of the slab. It was found that the average error of the perturbed field converges as $1/N$ (or $1/k_{\max}$). This puts a limitation on the convergence rate of the GF itself, at least for G_{er}, as it relies on the accuracy of $\tilde{E}_n(x)$. It was found that the transmission, which is calculated from the GF with

coordinates taken at opposite boundaries, and it is given by the equation [101]

$$T(k) = |2kG(-a, a; k)|^2 \ , \tag{2.31}$$

converges with approximately $1/N$, whereas, from the results in Sec. 2.3.1 we know that with the exact field the convergence could be better, $1/N^2$.

Instead of looking at just the general convergence rate of the perturbed GF, here we also look at this property in conjunction with the completeness of the modes. As mentioned in the introduction of this chapter, Sec. 2.3.1, as well as in Appendix A.1.3, for certain combinations of spacial coordinates the ML sum converges to the exact GF even when one coordinate is taken outside of the system. However, it is not possible to expand the GF into eigenmodes with both spacial points outside of the system. The eigenmodes are not complete under this condition, and the analytic GF does not vanish for large k (see Appendix A.1.3). Despite this, we will show, that when the perturbed modes are generated with the RSE we obtain a set of modes that will allow the GF to be constructed as a ML sum in all regions of the original, unperturbed system.

Lets consider a size perturbation of a homogeneous slab with vacuum as background. We change the width of the slab from $2a \to a$. Therefore, the basis permittivity is

$$\varepsilon(x) = \begin{cases} \varepsilon_{\mathrm{l}} = 1 & x < -a \\ \varepsilon_{\mathrm{s}} = 2 & -a \leq x \leq a \\ \varepsilon_{\mathrm{r}} = 1 & a < x \end{cases} \ , \tag{2.32}$$

and the perturbed is

$$\varepsilon_{\mathrm{p}}(x) = \begin{cases} \varepsilon_{\mathrm{l}} = 1 & x < -\frac{a}{2} \\ \varepsilon_{\mathrm{s}} = 2 & -\frac{a}{2} \leq x \leq \frac{a}{2} \\ \varepsilon_{\mathrm{r}} = 1 & \frac{a}{2} < x \end{cases} \ . \tag{2.33}$$

The perturbed eigenvalues are shown on Fig. 2.5.1a. We can see that while all the analytic eigenmodes are found in a certain spectral range, there are a number of additional modes, with significantly larger imaginary parts (i.e. $\mathrm{Im}\,(ka) < -2$), that are not actual eigenmodes of the slab. As we increase the basis size these additional artificial modes move away from the origin, while the true modes converge to the exact solution. Therefore, we can refer to the true modes as convergent modes, while we can refer to the artificial modes as divergent modes.

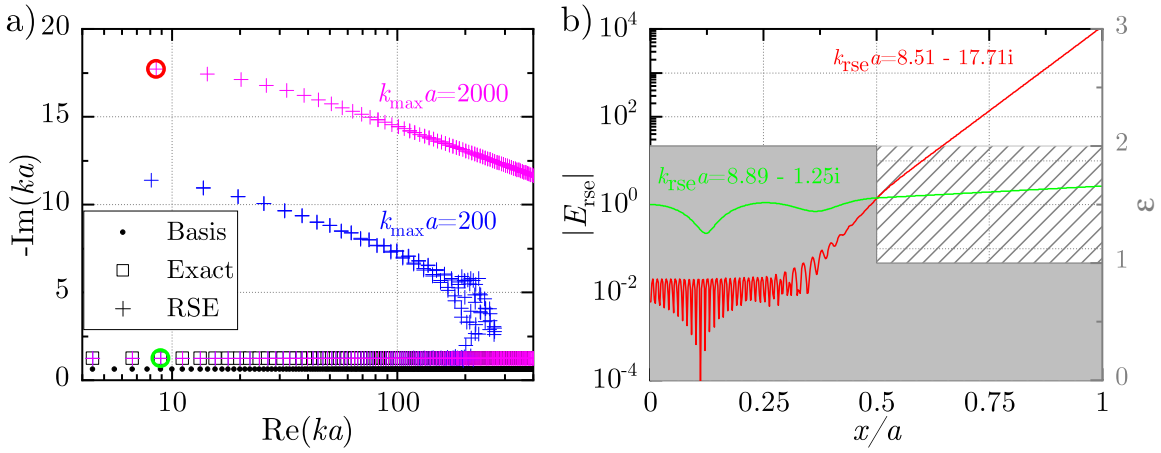

Fig. 2.5.1: Perturbation of a slab into a smaller slab. a) eigenvalues in the complext ka plane. b): absolute value of two modes that are calculated with the RSE. The green is a 'true' eigenmode, the red is an artifical mode due to the RSE. These modes are highlighted with a circle in a). The full gray shading indicates the final permittivity, the striped gray region indicates the perturbation.

To understand the origin and role of these modes, let us consider the following. The expansion of perturbed modes $\tilde{E}_\nu(x) = \sum_n c_{\nu n} E_n(x)$ can be considered simply as a linear transformation, like a rotation, with matrix c applied to the vector of basis modes $E(x)$, which rotates the basis. The linear transformation preserves completeness, therefore the perturbed modes that are obtained as the results of the rotation must be complete under the same spectral and spacial region as the unperturbed modes. This generates additional modes compared to the approximately exact perturbed eigenmodes, as these alone would not be complete under the original system volume which is larger than the perturbed system volume. On Fig. 2.5.1b the field of one of the artificial modes is plotted. As these modes have significantly larger imaginary parts than the true modes their fields grow faster and are mainly located outside of the perturbed slab, which can be seen by comparing the field amplitudes. As opposed to the true eigenmodes, these do not satisfy Maxwell's equations with the outgoing boundary conditions. They correspond to solutions that have waves propagating backwards and forwards in the perturbed region, as if waves are reflected from the position of the original boundary.

To numerically verify the completeness of the perturbed RSE modes outside of the perturbed slab volume we expand the GF into the ML series across the total space of the unperturbed slab. The series will contain both the convergent and the divergent modes. We compare this with a ML expansion of the GF which contains only the exact analytic modes of the perturbed system, and also with the exact analytic GF.

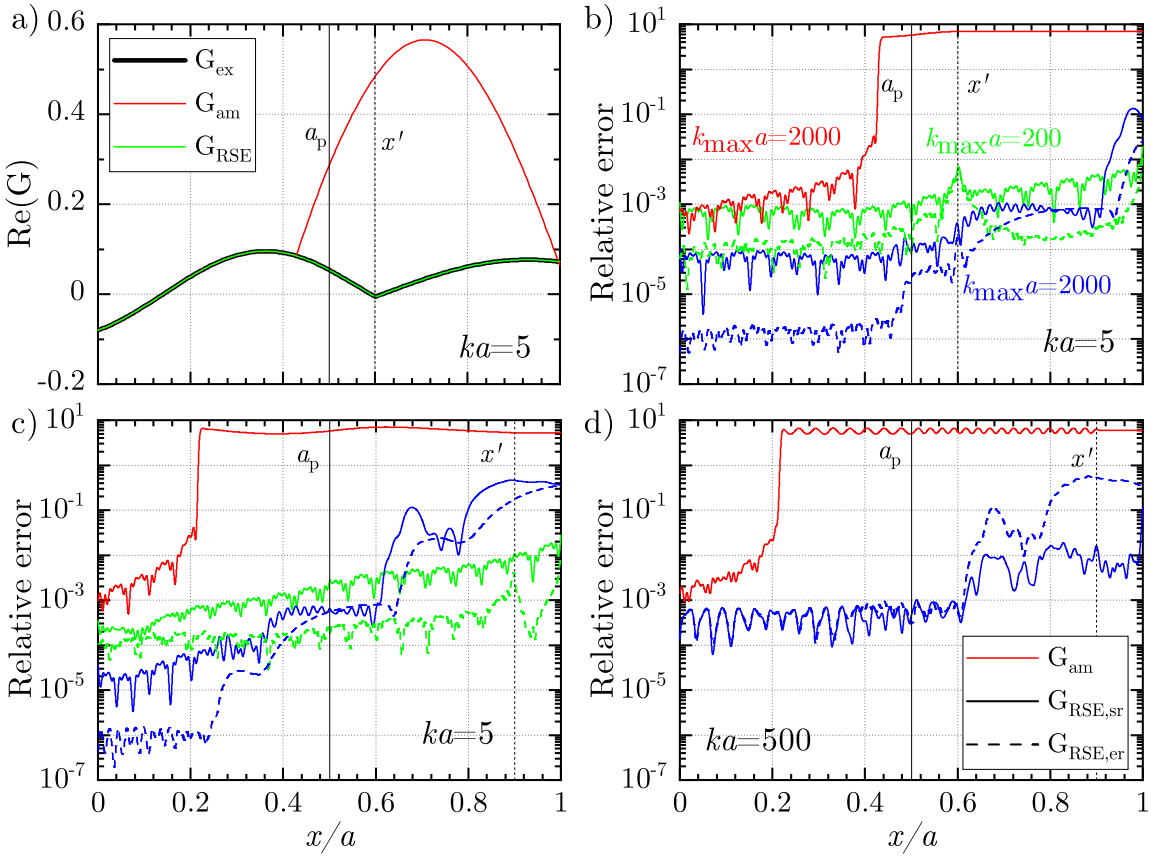

Fig. 2.5.2: a) GF of a slab, with boundary at a_p, and source placed at x'. Exact solution (black), ML expansion into analytic modes using $k_{\max}a = 2000$ (red) , ML expansion into modes generate via the RSE using $k_{\max}a = 200$ (green). b) Error in the ML expansion. Solid line is for $G_{\rm sr}$, dashed is for $G_{\rm er}$, red line shows the use of analytic modes, other colours are with RSE modes, using $k_{\max}a = 200$ (green) and $k_{\max}a = 2000$ (blue). c) as b) but x' placed further away. d) as c) but ka increased. Beyond the initial system boundary at a none of the ML expansions ($G_{\rm am}$, $G_{\rm RSE}$ converge to the correct solution ($G_{\rm ex}$), therefore this is not shown on the plot.

The GFs are shown in Fig. 2.5.2a, as a function of x, with the source placed at $x' = 0.6$, which is outside of the perturbed slab boundary $a_{\rm p} = 0.5a$, and the wavenumber $ka = 5$ is used. We can see that when using only the exact analytical modes in the ML sum, which is labelled $G_{\rm am}$ (red line), the expression deviates from exact solution at $x/a \approx 0.43$. This is expected from the condition $\sqrt{\varepsilon_{\rm s}}x_< < a(1+\sqrt{\varepsilon_{\rm s}})-x_>$. We apply it with x being inside, which gives the boundary for convergence at $x/a = 0.429$. When using all the perturbed modes that are generated by the RSE in the ML series, including convergent and divergent ones, there is a good agreement between sum, labelled $G_{\rm RSE}$ (green line), and the exact solution across the whole unperturbed slab region.

In Fig. 2.5.2b we look at how the results converge to the exact value when $k_{\max}$ is varied.

We can see that for small $k_{\max}$ the RSE ML expansion reproduces the GF well across all space inside the unperturbed slab. There is no qualitative difference between which form of the GF is used, G_{sr} or G_{er}, though the latter shows an order of magnitude lower error. As we increase the basis size, the error deep inside the perturbed slab decreases as expected. However outside the slab, away from the perturbed boundary a_p, the error starts to increase with increasing basis size. This is further highlighted in Fig. 2.5.2c, where the source x' is placed further away from a_p. The error of G_{RSE} starts to resemble that of the G_{am}. This can be understood from the perspective that for large $k_{\max}$ the divergent modes are moved further away from the origin, and within a certain spectral limit k_{lim} only the convergent modes remain. This leads to loosing the completeness property inside k_{lim} that is provided by the divergent modes. Interestingly, as we move to a larger ka while keeping the basis size $k_{\max}$ fixed, the error for G_{sr} reduces outside of the slab, as shown in Fig. 2.5.2d. This could be due to the divergent modes still being relatively close to the real axis in this region, with smaller detuning $k - k_{\text{rse}}$ from the real wavenumber k. In Appendix A.2.2 we investigate in more detail the dependence of the error outside of the perturbed slab on the combination of k and $k_{\max}$ parameters. We find that for fixed k initially the error decreases with increasing $k_{\max}$, however after a certain $k_{\max}$ the error increases again, in line with the observation in Fig. 2.5.2b and Fig. 2.5.2c.

We note that when using modes generated by the RSE for a system with linear continuous permittivity profile, as in Sec. 2.3.2, G_{er} will converge even when $x = x' = a$. This is due to the divergent modes generated, see Fig. 2.4.1a, and it is consistent with the results in this section.

2.6 Conclusion

We studied the convergence of the ML expansion of the GF to the exact values, for a slab at normal incidence. This revealed that when both spacial coordinates are taken at the same boundary, the ML expansion does not necessarily converge to the correct solution. In case of a slab with a step like boundary this is caused by the use of the sum rule, which is not satisfied when both spacial coordinates are taken at the same boundary. The sum rule for a 1D planar system (Eq. (2.12)) is also a special case of the general 3D sum rule (Eq. (1.30)), as the former gives the residue of the single static pole, while the latter gives zero. There are no separate static modes in planar 1D systems due to the vanishing normalisation coefficient. In case of a slab without a step-like boundary the convergence rate of the ML series is slower

than with a step-like boundary, and it does not converge to the correct value when both spacial coordinates are on the same boundary, regardless of the use of the sum rule. We looked at the convergence rate of the RSE results when the basis system has no step-like boundary, and found that these also converge slower, which is due to the slower convergence of the ML series. These examples verify the results of Ref. [31, 66], where it was shown that the eigenmodes form a complete set as long as there is a discontinuity in the permittivity, or in one of its derivatives. By applying a size perturbation to a slab, and expanding the GF outside of the perturbed system into the RSE modes, we have shown that the modes generated by the RSE form a complete set inside the original system volume. This is due to artificial, or divergent, modes generated by the RSE, which can be though of as an analogue to the PML modes, in the sense that they provide completeness inside the original volume, but outside the perturbed volume. These results, in particular, the completeness outside of the size-perturbed system and the limitations on when the sum rule is valid, will be particularly important when we consider scattering calculations later on in Chap. 6, which will depend on these properties.

3

Spherically symmetric, radially inhomogeneous systems

The contents of this chapter are presented in the publication Ref. [104].

3.1 Introduction

Modeling inhomogeneous optical resonators is challenging as generally a simple analytic solution is not available. A special case are spherically symmetric systems, having an inhomogeneity, for example in the permittivity, only dependent on the radius. Examples can be found in core-shell systems which allow highly directional scattering [105], when modeling surface contamination on a sphere due to diffusion [106] or high pressure [107], or when modelling biological cells [108]. Graded index profiles can be used to engineer the cancellation of electric and magnetic dipole excitation which reduces the visibility of small particles at certain wavelengths [109]. With an inhomogeneous and anisotropic sphere one can even achieve perfect cloaking of a cavity over a range of frequencies [110]. On a larger scale, one may use inhomogeneous profiles to model emission from stellar atmospheres [111].

The scattering properties of systems with graded permittivity have been studied in the literature using various approximate methods. In the multilayer approach (also referred to as stratified medium method), the graded index profile is approximated by a piecewise constant function, describing the system by homogeneous regions comprising a core covered by a sequence of shells [112,113]. In the short wavelength limit, a Debye series expansion for the scattered field was used [114], and in the long wavelength limit a Born approximation [115] or a dipole limit [109] were applied to dispersive systems with complex permittivity. Furthermore, the dipole moment of dielectric spherical particles with power law radial profiles of the permittivity was calculated in the electrostatic limit [116]. A generalized scattered field

formulation developed in [106] requires solving scalar Schrödinger-like equations, similar to the scalar wave equations solved in this work. To study the electromagnetic (EM) modes, first and second-order perturbation methods were developed [21] and applied to deformations of a homogeneous sphere [76]. Whispering gallery (WG) modes in both TE and TM polarizations were studied in [107] for small inhomogeneous perturbations of the surface layer of a sphere. In that approach, the modes were found in the complex frequency plane based on the expansion coefficients of the generalized scattered field, and the secular equations were solved numerically using a Runge-Kutta method. The effect of a linearly changing permittivity profile was investigated in [117] for high-frequency TE modes in large spheres, using Airy functions as an approximate solution to the corresponding scalar problem. Finally, in [118], a resonant mode of a sphere was treated in the electrostatic limit, for a negative and frequency dependent permittivity, described by an undamped (i.e. non-absorbing) Drude model, with radial dependencies of the permittivity and the electric field approximated by polynomials.

Here we will use the RSE to study the modes of graded index spherical resonators. For a general perturbation, one needs to include static modes [32, 63] alongside the RSs in the ML representation of the dyadic Green's function. Note that the latter is at the heart of the RSE approach. Recently, the RSE has been reformulated [85], in order to eliminate static modes, and the illustrations provided for perturbations of the size and refractive index of a homogeneous sphere show a significantly improved convergence compared to the original version of the RSE [32]. The approach [85] has also proposed, though without providing illustrations, another quickly convergent version of the RSE, the one which keeps static modes in the basis.

In this chapter we consider both versions of the reformulated RSE, with and without static modes, demonstrating a similar efficiency of both. Using the RSE, we then investigate spherically symmetric inhomogeneous systems, with graded permittivity profiles. The RSs in such systems are still split into TE and TM polarizations, and are characterized by the azimuthal (m) and angular (l) quantum numbers. Importantly, while some graded profiles are approximately solvable analytically [111,119], the RSE can treat arbitrary perturbations and finds all the RSs of the system within the spectral coverage of the basis used, thus generating a full spectrum. This allows us to identify some prominent features in spectra, such as the quasi-degeneracy of modes and the Brewster angle phenomenon, and ultimately to engineer the shape of the spectrum via changing the permittivity profile.

This chapter is organized as follows. In Sec. 3.2 we study the TE and TM RSs of a homogeneous sphere, using the qualitative ray picture of light propagation as well as a more

rigorous phase analysis of the secular equations describing the light eigenmodes, both approaches introducing several useful approximations. In Sec. 3.3 we briefly describe the RSE method and its optimizations used here for calculating the RSs of a graded index sphere. We then recap the analogy between wave optics and quantum mechanics, by introducing a radial Schrödinger-like wave equation containing an effective potential. The RSs of a sphere with linear and quadratic radial permittivity profiles eliminating the discontinuity at the sphere surface are then discussed, and an approximate analytical solution using Morse's potential is presented. In Sec. 3.4 we investigate the TE-TM RS splitting and its reduction for graded index profiles.

3.2 Homogeneous sphere

The secular equation determining the RS eigen wavenumber k_n of a non-magnetic homogeneous sphere of radius R with vacuum outside is given by [85]

$$\frac{J'(n_r k_n R)}{J(n_r k_n R)} = \frac{1}{\beta}\frac{H'(k_n R)}{H(k_n R)}, \tag{3.1}$$

where $\beta = n_r$ ($\beta = n_r^{-1}$) for TE (TM) polarization. Here $J(x) = x j_l(x)$ and $H(x) = x h_l^{(1)}(x)$, with j_l and $h_l^{(1)}$ being, respectively, the spherical Bessel function and Hankel function of first kind, and primes denote the first derivatives of functions with respect to their arguments. Figure 3.2.1 shows the spectrum of the RSs of a homogeneous dielectric sphere in vacuum in the complex wavenumber plane, for a refractive index of the sphere of $n_r = 2$ and an angular momentum quantum number of $l = 20$. For the example given, the combination of parameters n_r and l are chosen such that the spectrum contains a few WG modes. Here, $k = 2\pi/\lambda_0/c$ is the wavenumber in vacuum, λ_0 is the wavelength of light in vacuum. Only $\mathrm{Re}\, k \geq 0$ is shown, noting that RSs come in pairs with both signs of the real part of their wavenumber. The spectrum consist of TE and TM modes which appear in alternating order, with one exception related to the Brewster's angle phenomenon, as discussed later. The RSs of a sphere can be divided into three groups: leaky (L) modes, WG modes, and Fabry-Pérot (FP) modes. Physically, all of them are formed as a results of interference of electromagnetic (EM) waves interacting with the sphere surface.

L modes typically have quality factors (Q factors) which are very low and their EM fields are located mainly outside the sphere. The number of L modes is exactly l in TE and $l-1$ in TM polarization, although the Brewster mode discussed later can be regarded as a hybrid L-FP mode, so that one could say that the number of L modes is effectively the same in both polarization. For comparison, the case of $l = 5$, with the same refractive index n_r, can

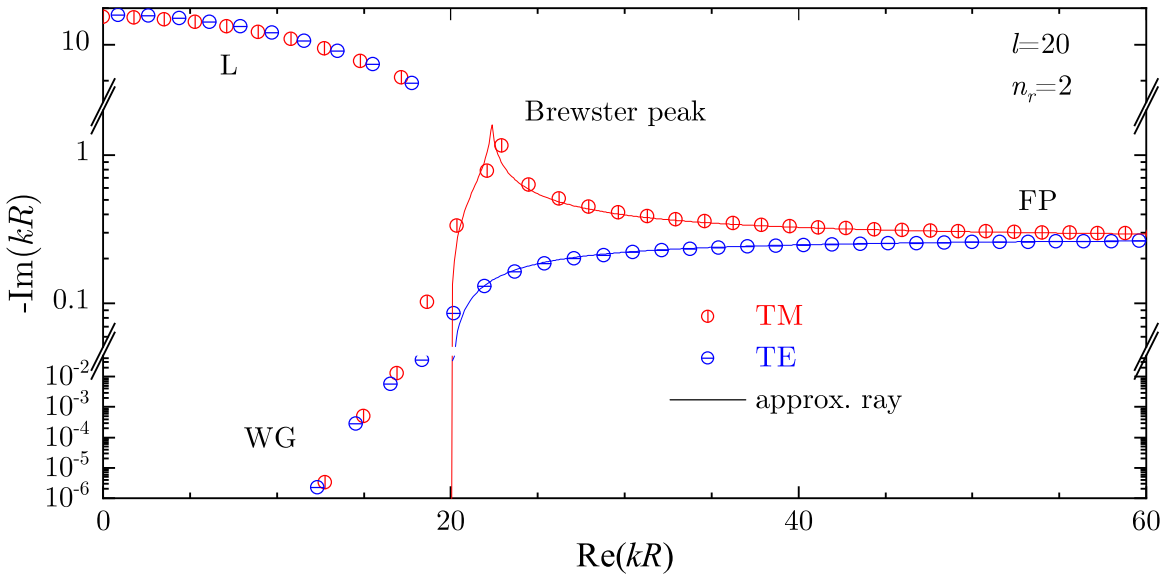

Fig. 3.2.1: Wavenumbers of the TE and TM RSs of a homogeneous sphere in vacuum, with a refractive index of $n_r = 2$ and an angular momentum quantum number of $l = 20$. The regions of leaky modes (L), whispering gallery modes (WG), and Fabry-Perot modes (FP) are indicated. Solid line is the approximation to the imaginary part of the wavenumbers, given by Eq. (3.3). Note the double y-axis break.

be seen in Ref. [63]. L modes arrange around the origin in the complex wavenumber plane, forming a roughly semicircular arc.

WG modes are formed due to the total internal reflection and therefore have wavenumbers with $|\mathrm{Re}\, k| < l/R$, as discussed below. The number of WG modes is increasing with n_r and l. The Q factor of the fundamental WG mode is increasing exponentially with l, and values of up to 10^{10}, only limited by material properties, have been demonstrated experimentally [120]. The EM field of the WG modes is concentrated inside the sphere close to the surface.

FP modes of a sphere have moderate Q factors and are named for their similarity to the original FP modes [121] of a double-mirror planar resonator. In fact, at large frequency, the FP modes of a sphere approach the limit of an equidistant spectrum of a dielectric slab, with all the eigenfrequencies having the same imaginary part [14]. The number of FP modes is countable infinite. Their EM fields are distributed within the sphere, avoiding the centre due to the non-zero angular momentum ($l > 0$). The FP modes are spectrally separated from the WG modes by the critical angle of the total internal reflection, as discussed in more depth below.

The arrangement of the RSs in Fig. 3.2.1 is overall similar in the TE and TM polarizations. The imaginary part of their wavenumbers approaches the same high frequency asymptote, albeit from opposite sides. Additionally, there is a peak in the imaginary part of the TM

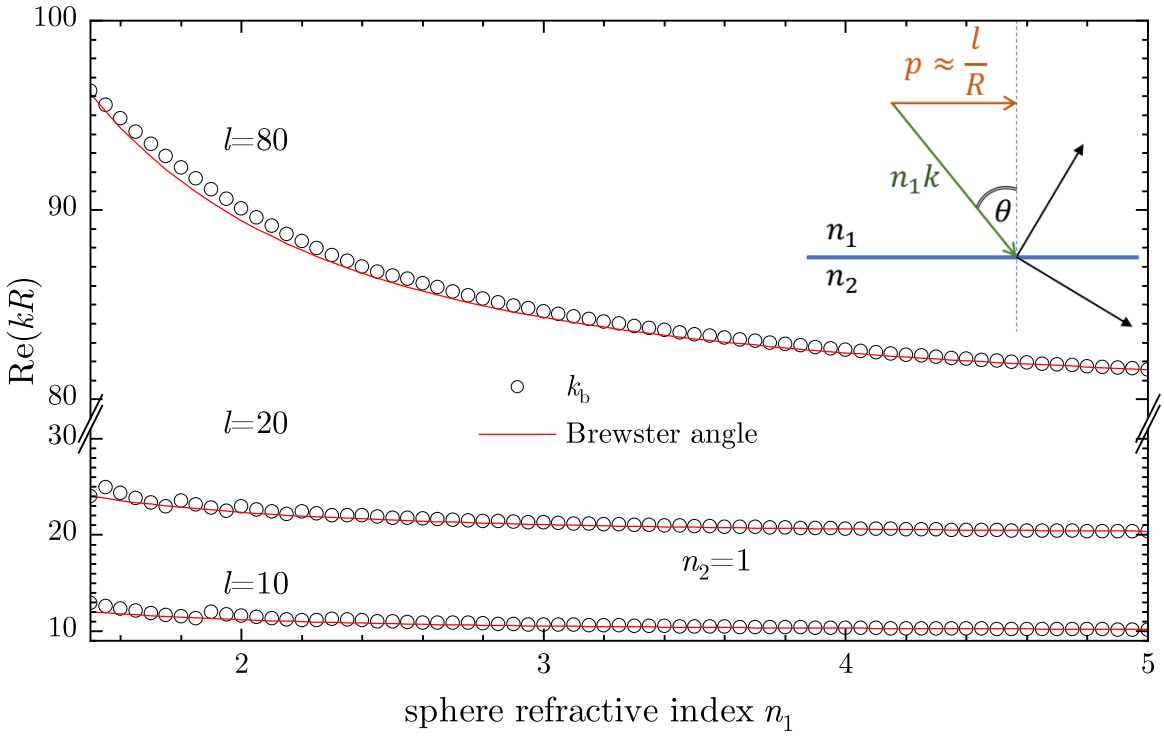

Fig. 3.2.2: Real part of the wavenumber of the TM RS at the Brewster peak (circles) as a function of the sphere refractive index $n_1 = n_r$, for $l = 10$, $l = 20$ and $l = 80$, compared with the ray optics approximation Eq. (3.2) (lines). Inset: sketch of the ray geometry at the boundary.

RS wavenumbers near the transition region from WG to FP modes, which occurs around the Brewster angle in the ray picture of light propagation, and we therefore refer to it as a Brewster peak. At this peak, an additional TM mode is formed, breaking the otherwise alternating order of TE and TM RSs.

Let us know discuss and analyze the spectrum of the RSs of a sphere in more detail, using the ray picture approach. This provides an approximations for the mode positions and linewidths of non-WG modes and offer an intuitive understanding of the origin and properties of the RSs of a sphere.

3.2.1 Ray picture: Brewster's phenomenon and total internal reflection

To understand the observation of the Brewster peak in the spectrum of the RSs, we recall that increasing the angle of light incidence θ at a planar interface between two media, the Fresnel reflection coefficient for TM (aka p) polarized light passes through zero, changing its sign at the Brewster angle [122]. The same occurs at the surface of a sphere in the ray picture, which is valid in the limit of wavelengths much smaller than the surface curvature. This local geometry is illustrated in the inset of Fig. 3.2.2. The magnitude of the incident

wave vector is $n_1 k$, where n_1 is the refractive index of the corresponding medium, i.e. that the sphere, $n_1 = n_r$. Since the angular momentum l gives the number of wave periods along one circumference $2\pi R$, the wave vector component p parallel to the surface is determined by $2\pi l = 2\pi R p$, so that $p = l/R$. With simple trigonometry we can see that $\sin\theta = p/(n_1 k)$. The Brewster angle θ_b is determined by $\tan\theta_b = n_2/n_1$, so that for a sphere in vacuum ($n_2 = 1$) the wavenumber corresponding to the Brewster angle is given by

$$k_b = \frac{l}{R}\sqrt{\frac{1}{n_1^2} + 1}\,. \tag{3.2}$$

At this angle, the reflectivity vanishes. This would correspond to a divergence of the imaginary part of the RS wavenumber for an ideal planar geometry. Here instead it is kept finite due to the finite curvature of the surface and the RS discretization, resulting in the Brewster peak.

In Fig. 3.2.2 we compare Eq. (3.2) with the real part of the wavenumber of the Brewster mode (the TM mode at the Brewster peak in the spectrum), for $l = 10$, $l = 20$ and $l = 80$, all showing good agreement. We find that the relative error for small n_1 increases with decreasing l. For smaller l the peak position shifts to longer wavelength, and the ratio of internal wavelength to the radius increases, therefore the validity of the ray picture reduces. With increasing n_1 the RSs are packed more densely in the complex k plane, so that the discretization does not result in significant deviations. At the same time, the light wavelength within the sphere $2\pi/(n_1 k)$ decreases with n_1, thus improving the accuracy of the ray picture.

The Brewster mode can also be associated with the leaky branch. In fact, as n_1 increases, the Brewster peak in the spectrum is getting sharper, so that the Brewster mode is taking a significantly larger imaginary part of the wavenumber compared to the neighboring FP modes and is thus getting more isolated from them, at the same time approaching the edge of the leaky branch. Indications of this can be seen in Fig. 3.3.2. We also note that for high l, the Brewster peak can be shifted further into the FP spectral region. This happens because the Brewster angle θ_b is always smaller than the critical angle θ_c of the total internal reflection. The latter determines the point in the spectrum separating WG from FP modes and can be evaluated in a similar way, leading to $k_c = l/R$. Comparing it with Eq. (3.2), we see that as l increases or n_1 decreases, the difference $k_b - k_c$ is getting larger, so that the corresponding region in the spectrum, between the critical and the Brewster angles, can accommodate more RSs.

The ray picture is also useful for understanding the imaginary part of the FP mode wavenumbers. Assuming the reflectivity amplitude r_P at the sphere surface in polarization

P is given by the corresponding Fresnel coefficient, we equate it to the ratio of the field amplitude before and after each reflection. This ratio is in turn given by the temporal decay of the field, $|r_P| = \exp(-t/\tau)$, where t is the time between consecutive reflections and τ is the mode decay time which is given by the imaginary part of its eigenfrequency, $1/\tau = -\mathrm{Im}\,(kc)$. At the same time, the optical path length across the sphere between two reflections is given by $L = 2Rn_r \cos\theta$. Finally, using the fact that $t = L/c$ and taking the logarithm of the reflectivity results in

$$\mathrm{Im}\,(k) = \frac{\ln|r_P|}{2Rn_r\cos\theta}, \tag{3.3}$$

where the Fresnel coefficient r_P depends on the angle of incidence θ and the refractive index of the sphere n_r. The expression is valid up to the critical angle θ_c of total internal reflection, at which $\ln|r_P| = 0$. The values obtained according to Eq. (3.3) are shown in Fig. 3.2.1 as solid lines. We can see a good agreement for both polarizations, including the Brewster peak and the asymptotic value for FP modes, evaluated to $-0.27465/R$ for $n_r = 2$ and $\theta = 0$, which again validates the ray optics interpretation of the RS properties. The WG modes are located in the total internal reflection region of the spectrum where Eq. (3.3) is not applicable – their non-vanishing imaginary parts are the result of the finite curvature of the sphere making the reflection imperfect. Such refinement is taken into account in Ref. [123], but with specific focus on WG modes only. In Sec. B.1 of Appendix B we also evaluate the approximation in case of a homogeneous slab at non-normal incidence, and show that it is more accurate in that case due to the planar boundary. At non-normal incidence, the TE and TM FP modes of a slab asymptotically converge to each other in pairs, as shown in Fig. B.1.1 in Sec. B.1. The planar system gives rise to both even and odd modes (using the parity of the electric or magnetic field), with odd TE modes converging to even TM modes at large frequencies, and vise versa. In the sphere, however, there are no even modes, as required by the finiteness of the EM field at the origin (as in any other point in space). Considering only the even modes of the slab spectra, we obtain the FP modes of the sphere, which are alternating between TE and TM RSs with increasing $\mathrm{Re}\,(k)$.

As an alternative approach to the ray picture, if $|\sqrt{\varepsilon_r}k_nR)| >> l$ one can obtain an approximate secular equation that is only a function of $\mathrm{Re}\,(k)$, as in Ref. [104]. From this it is possible to extract an approximation for the imaginary part of the modes. This method also gives the correct asymptotic behaviour for the FP modes, and while it is less accurate in the transition region than the ray picture, it provides an approximation even for WGMs.

3.3 Graded index spheres

In this section we study, using the RSE, the RSs in spherically symmetric non-magnetic systems with graded permittivity profiles. A particularly interesting situation is reached by removing discontinuities of the permittivity. Here we study cases where the discontinuity is removed either only in the permittivity (linear case) or both in the permittivity and its derivative (quadratic case), and compare both cases with each other and with the constant permittivity profile studied in Sec. 3.2. We note that removing discontinuities of the refractive index yields broadband anti-reflecting coatings in planar dielectric layers [124]. For the WG modes, we introduce a radial Schrödinger-like wave equation containing an effective potential, compare potentials and mode properties in all three cases, and provide an analytical approximation based on the Morse potential.

3.3.1 Calculating the resonances

Resonant-state expansion

Here we briefly discuss the methodology based on the RSE [32, 63, 85] which is used for the numerical calculations. The RSE is well suited for calculating the RSs of a graded index sphere. The difference in the permittivity between the target system (a graded index sphere) and the basis system (a constant index sphere) is treated as a perturbation, and the RSs of the constant index sphere serve as a basis for the RSE. The EM fields of the RSs of the target system are expanded into the basis RSs, and the expansion coefficients and the RS wavenumbers of the target system are found by solving a linear eigenvalue problem, see Eq. (3.4). This eigenvalue problem of the RSE contains as input the RS wavenumbers of the basis system and the matrix elements of the perturbation. For spherically symmetric systems, TE and TM polarizations, or RSs with different l and magnetic quantum number m, do not mix and can be treated separately in RSE. However, the matrix elements used in the RSE for the TE and TM RSs are different, see [85] for details, and as discussed below. In particular, for TM polarization, one needs to include in the basis additional functions which are required for completeness and physically describe the part of the EM field in a graded index sphere which is not divergence free. More rigorously, these functions are required to properly describe a longitudinal part of the dyadic GF related to its static pole in the ML expansion. Without these additional functions the mode wavenumbers calculated by the RSE carry a systematic error [32].

The RSE eigenvalue problem leads to an infinite matrix. For computational evaluation,

this matrix is truncated to a finite size $N \times N$, where N is the number of RSs of the basis system used in the calculation. The specific RSs used are the basis RSs having complex wavenumbers with an absolute value below $k_{\max}$.

Previously, the static pole of the GF in the ML expansion has been treated within the RSE by introducing a complete set of static modes [32]. However, even though the treatment of static modes is numerically less complex, a slow convergence versus the basis size N observed in [32] remained an issue. To develop quickly converging versions of the RSE, the full ML representation of the dyadic GF of a spherically symmetric system has been studied in [85], focusing in particular on the static pole of the GF containing a δ-like singularity. A quick convergence of the RSE has been achieved and demonstrated in [85] by an explicit isolation of the singularity that has allowed to avoid its direct expansion into static modes. Two ML forms of the GF have been introduced in [85], called there ML3 and ML4, which led to slightly different versions of the RSE, both quickly convergent to the exact solution.

The quick convergence of the RSE based on ML4, with static mode elimination and suited only for a basis system in a form of a homogeneous sphere, was demonstrated in [85] on examples of both size and material (strength) perturbations of a sphere. However, the version of the RSE based on ML3, which is using explicitly a static mode set and an arbitrary spherically symmetric basis system, has not been studied so far numerically. Such a study is given later in this section, including a comparison with ML4, demonstrating a similar level of convergence. We show here in particular that the RSE based on ML3 and ML4 have both a quick $1/N^3$ convergence to the exact solution, where N is the basis size of the RSE. Furthermore, taking three different static mode sets introduced earlier in [32, 85], we show that the results of the RSE based on ML3 are similar for all the different static mode sets previously suggested.

Let us finally note that for perturbations without discontinuities, the above mentioned optimization of the RSE might be not needed, as demonstrated in a similar approach based on eigen-permittivity modes [88]. However, as we are going to consider a transformation of an optical system from a homogeneous sphere, having a discontinuity, to a sphere with a continuous permittivity profile, the perturbation describing this transformation and used in RSE contains a discontinuity, both in linear and quadratic cases, and therefore the above optimization is in fact needed.

Resonant-state expansion for spherically symmetric systems

According to Ref. [85], the matrix equation of the RSE for non-dispersive systems has the following general form:

$$(k-k_n)a_n = -k\sum_{n'}\tilde{V}_{nn'}a_{n'}\,, \tag{3.4}$$

where a_n are the expansion coefficients of a perturbed RS into the basis RSs labeled by index n. For spherically symmetric systems, all n refer to the same spherical quantum numbers l and m, but the matrix elements $\tilde{V}_{nn'}$ of the perturbation are quite different in TE and TM polarizations.

For a radially-dependent permittivity perturbation $\Delta\varepsilon(r)$ of a nonmagnetic system, the matrix elements in TE polarization are given by

$$\tilde{V}^{\rm TE}_{nn'} = \int_0^R \mathcal{E}_n(r)\Delta\varepsilon(r)\mathcal{E}_{n'}(r)\mathrm{d}r\,, \tag{3.5}$$

where $\mathcal{E}_n(r)$ is the electric field of the basis RS n, satisfying Eq. (3.23), in which $k=k_n$ is the RS wavenumber and $\varepsilon(r)$ is the permittivity profile of the basis system. The fields $\mathcal{E}_n(r)$ are normalized according to [14, 85]

$$2\int_0^R \varepsilon\mathcal{E}_n^2\mathrm{d}r + \frac{1}{k_n}\left[\left(\mathcal{E}_n r\mathcal{E}_n'\right)' - 2r(\mathcal{E}_n')^2\right]_{r=R} = 1\,. \tag{3.6}$$

For TM polarization, the matrix elements have a more complex form:

$$\tilde{V}^{\rm TM}_{nn'} = V_{nn'} - \sum_{jj'} V_{nj}W_{jj'}V_{j'n'} \tag{3.7}$$

where $W_{jj'}$ is the inverse of matrix $\delta_{jj'}+V_{jj'}$, index n labels the basis TM RSs, and index j labels additional functions required for completeness. They are used in the expansion of the perturbed EM vector fields and the dyadic GF, and are responsible for the static pole representation of the latter [85]. It is convenient to introduce a combined index ν which labels together the RSs (n) and the additional basis functions (j). It is also useful to separate each basis electric vector field into the radial $\mathcal{E}^r_\nu(r)$ and tangent $\mathcal{E}^t_\nu(r)$ components. The matrix elements contributing to Eq. (3.7) then take the form [85]:

$$V_{\nu\nu'} = \int_0^R \left[\mathcal{E}^t_\nu\Delta\varepsilon(r)\mathcal{E}^t_{\nu'} + \mathcal{E}^r_\nu\frac{\varepsilon(r)\Delta\varepsilon(r)}{\varepsilon(r)+\Delta\varepsilon(r)}\mathcal{E}^r_{\nu'}\right]\mathrm{d}r \tag{3.8}$$

with $\mathcal{E}^t_\nu(r)$ and $\mathcal{E}^r_\nu(r)$ defined below.

For the basis TM RSs, the fields are given by

$$\begin{pmatrix}\mathcal{E}^t_n(r)\\ \mathcal{E}^r_n(r)\end{pmatrix} = -\frac{1}{k_n\varepsilon(r)}\begin{pmatrix}\frac{\mathrm{d}}{\mathrm{d}r}\\ \frac{\alpha}{r}\end{pmatrix}\mathcal{H}_n(r) \equiv \begin{pmatrix}\mathcal{K}_n(r)\\ \mathcal{N}_n(r)\end{pmatrix}\,, \tag{3.9}$$

where $\mathcal{H}_n(r)$ is the magnetic field of the basis TM RS n, satisfying Eq. (3.25), in which $k = k_n$ is the RS wavenumber and $\varepsilon(r)$ is the permittivity profile of the basis system. The fields $\mathcal{H}_n(r)$ are normalized according to [14, 85]

$$2\int_0^R \mathcal{H}_n^2 \mathrm{d}r + \frac{1}{k_n}\left[\left(\mathcal{H}_n \frac{r}{\varepsilon(r)}\mathcal{H}_n'\right)' - \frac{2r}{\varepsilon(r)}(\mathcal{H}_n')^2\right]_{r=R_+} = 1 \tag{3.10}$$

with $R_+ = R + 0_+$, where 0_+ is a positive infinitesimal.

All other basis states can be expressed in terms of functions $\mathcal{K}_n(r)$ and $\mathcal{N}_n(r)$ introduced in Eq. (3.9) and static modes $\psi_\lambda(r)$ introduced in [32] and also discussed in [85]. Let us note at this point that the two slightly different versions of the efficient (i.e. quickly convergent) RSE developed in Ref. [85] are based on two different Mittag-Leffler representations of the full dyadic GF of a spherically symmetric system, called in [85] ML3 and ML4. Essentially, they differ in the basis functions describing the static pole of the GF. Also, ML4 is introduced for a homogeneous sphere only, while ML3 is valid for any spherically symmetric basis system.

In the ML3 version of the RSE, all the additional basis states can be divided into three groups. In the first two groups, indices j_{I} and j_{II} take the same values as the TM RS index n, and the fields are given by

$$\begin{pmatrix} \mathcal{E}^t_{j_{\mathrm{I}}} \\ \mathcal{E}^r_{j_{\mathrm{I}}} \end{pmatrix} = \begin{pmatrix} i\mathcal{K}_n \\ i\mathcal{N}_n \end{pmatrix} \text{ and } \begin{pmatrix} \mathcal{E}^t_{j_{\mathrm{II}}} \\ \mathcal{E}^r_{j_{\mathrm{II}}} \end{pmatrix} = \begin{pmatrix} \mathcal{K}_n \\ 0 \end{pmatrix}. \tag{3.11}$$

In the third group,

$$\begin{pmatrix} \mathcal{E}^t_{j_{\mathrm{III}}} \\ \mathcal{E}^r_{j_{\mathrm{III}}} \end{pmatrix} = \begin{pmatrix} \alpha\psi_\lambda \\ 0 \end{pmatrix}, \tag{3.12}$$

and the index j_{III} coincides with λ labeling static modes defined in terms of the radial part of their potential function $\psi_\lambda(r)$. Static modes are the solutions of a generalized Sturm-Liouville problem [32, 85] and are normalized according to

$$\lambda^2 \int_0^R \varepsilon(r)\psi_\lambda^2(r) r^2 \mathrm{d}r = 1\,. \tag{3.13}$$

For a basis system in the form of a non-magnetic homogeneous sphere in vacuum, described by the permittivity profile given by

$$\varepsilon(r) = (\epsilon - 1)\theta(R - r) + 1\,, \tag{3.14}$$

the static mode potentials take the explicit form

$$\psi_\lambda(r) = A_\lambda j_l(\lambda r) \tag{3.15}$$

within the sphere ($r \leqslant R$), where $j_l(x)$ is the spherical Bessel function of order l, λ is the mode eigenvalue (here also used to label the modes), and A_λ is a normalization constant determined according to Eq. (3.13). The eigenvalues λ are found from the boundary condition of the Sturm-Liouville problem [32], which leaves a large range of possible sets. Following [85], we consider here three sets of static modes for ML3 version of the RSE: (i) the volume-charge set (VC), with the eigenvalues generated by the secular equation

$$\lambda\epsilon R j_l'(\lambda R) + (l+1) j_l(\lambda R) = 0\,, \tag{3.16}$$

(ii) the volume-surface-charge set (VSC), with a simpler secular equation

$$j_l(\lambda R) = 0\,, \tag{3.17}$$

and (iii) a modified-volume-surface-charge set (MVSC), determined by the following secular equation

$$\lambda R j_l'(\lambda R) + (\epsilon l + 1) j_l(\lambda R) = 0. \tag{3.18}$$

Note that apart from the modes generated by the secular equations, both VSC and MVSC sets include one additional mode, that corresponds to $\lambda = 0$. Also note that the VSC and VC sets were used in [32] for a slowly convergent version of the RSE.

In the ML4 version of the RSE, developed in [85] for the basis system in a form of a homogeneous sphere in vacuum, all basis states responsible for the static pole of the GF can be divided into four groups. The first two groups are the same as in ML3 and are given by Eq. (3.11). The third and fourth groups of basis functions provide an alternative to the static mode sets described above. The third group is given by

$$\begin{pmatrix} \mathcal{E}^t_{j_{\rm III}}(r) \\ \mathcal{E}^r_{j_{\rm III}}(r) \end{pmatrix} = \begin{pmatrix} \mathcal{N}_n(r) \\ 0 \end{pmatrix}\,, \tag{3.19}$$

where index $j_{\rm III}$ again takes the same values as the TM RS index n, in the same way as in the first two groups, and the fourth group consists of the single element

$$\begin{pmatrix} \mathcal{E}^t_{j_{\rm IV}}(r) \\ \mathcal{E}^r_{j_{\rm IV}}(r) \end{pmatrix} = \begin{pmatrix} \mathcal{M}_0(r) \\ 0 \end{pmatrix}\,, \tag{3.20}$$

where

$$\mathcal{M}_0(r) = \sqrt{\frac{l(l+1)}{\epsilon R}\frac{\epsilon-1}{\epsilon l + l + 1}}\left(\frac{r}{R}\right)^l\,, \tag{3.21}$$

which can also be found as

$$\begin{aligned} \mathcal{M}_0(r) &= (\epsilon-1)\sqrt{\frac{l}{\epsilon}}\lim_{k_n\to 0}\mathcal{K}_n(r) \\ &= (\epsilon-1)\sqrt{\frac{l+1}{\epsilon}}\lim_{k_n\to 0}\mathcal{N}_n(r) \end{aligned} \tag{3.22}$$

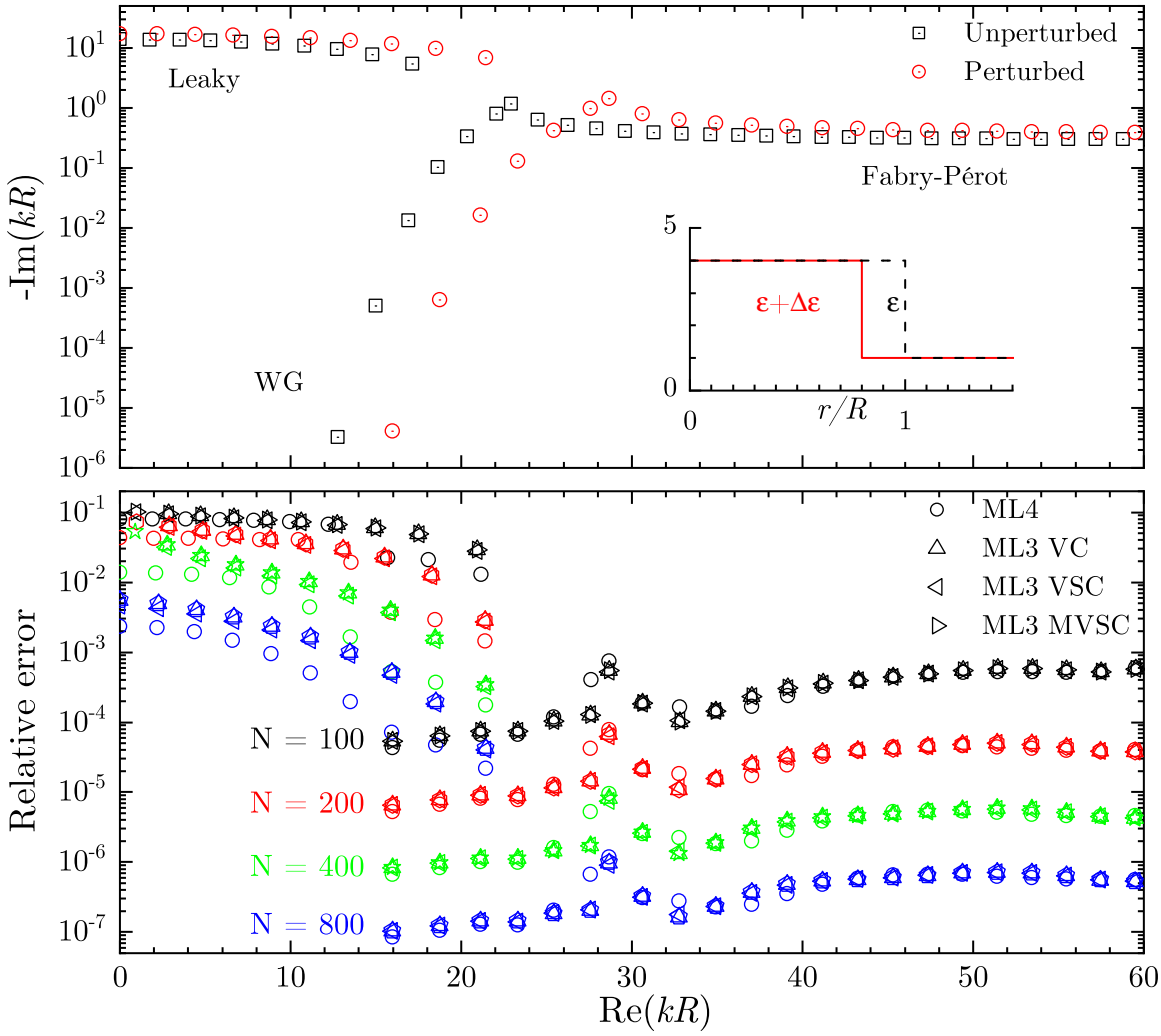

Fig. 3.3.1: RSE applied for size perturbation. TM RSs of a dielectric sphere with permittivity $\epsilon = 4$ and permeability $\mu = 1$, for angular momentum number $l = 20$. Top: Wavenumbers in the complex k plane. Basis RSs for size R, target RSs for size $0.8R$. Bottom: Relative error of the RSs calculated by RSE with method of elimination of static modes (ML4) and with efficient inclusion of static modes (ML3) for various static mode sets and basis sizes N as given. Inset: unperturbed and perturbed permittivity profiles.

by treating both $\mathcal{K}_n(r)$ and $\mathcal{N}_n(r)$ as analytic functions of k_n and taking the limit $k_n \to 0$.

To test the convergence of the RSE based on ML3 for the different static mode sets, we apply the RSE to a size perturbation of a homogeneous sphere. We choose as unperturbed system a homogeneous sphere in vacuum, having radius R, permittivity $\epsilon = 4$, and permeability $\mu = 1$. We focus here on the TM RSs with angular momentum $l = 20$, also noting that in spherically symmetric systems, all states are degenerate in m. The target system is a sphere of the same material and radius $0.8R$, so that the perturbation is given by $\Delta\varepsilon = 1 - \epsilon$ in the outer $0.2R$ thick shell of the basis sphere. Figure 3.3.1 shows the resulting perturbed and unperturbed eigenvalues k, and their error, for various basis sizes N, which include RSs

with $|k_n|R \lesssim 0.77N$ and static modes with $|k_\lambda|R \lesssim 3.31N$. For a homogeneous sphere, in the absence of dispersion the RS wavenumbers k_n and R are inversely proportional, which can be seen as a scaling of the target RSs compared to the basis RSs in the complex plane.

The relative error for ML3 scales as $1/N^3$ (the same as in ML4), independent of which static mode set is used. In the original version of the RSE [32], with a slow $(1/N)$ convergence for static mode inclusion, there was a more significant difference between the VC and VSC sets, as they were used for the expansion of the complete residue of the static pole of the GF, including the δ-function term. We find that ML4 provides smaller errors for the leaky branch. This can be understood by noting that ML4 uses instead of static modes basis functions proportional to the RSs, including L RSs, and thus can be expected to be better suited for expanding the L RSs of the target system. A slow initial convergence of L RSs is testament to their unusual spatial shape, not well described by the basis RSs, but the $1/N^3$ convergence is eventually recovered above $N = 400$.

The results for strength perturbation, that is, changing the permittivity of the sphere homogeneously, are shown in Fig. 3.3.2, displaying a similar behavior. Here, using the same basis sizes as in Fig. 3.3.1, we apply the RSE for a homogeneous increase of the permittivity of the sphere by $\Delta\varepsilon = 5$, giving a target sphere permittivity $\epsilon + \Delta\varepsilon = 9$. The higher refractive index leads to a denser array of RSs, increased number of WG modes and smaller imaginary part for the FP modes. We can see that the error converges with the basis size N as $1/N^3$ for ML3, independent of the static mode set used. For the WG modes, the ML3 representation has some advantage over ML4, having up to five times smaller errors. The static modes thus seem better suited to describe these WG modes, likely because they are bound to the sphere, similar to the WG modes.

We thus conclude that for all three static mode sets, ML3 has a convergence similar to ML4. In all calculations of the RSs of the graded index spheres done later in this chapter, we use the RSE based on ML4, as it has a fixed number of additional basis functions in TM polarization, which is three times the number of the TM RSs included in the basis. We use a basis size of $N = 800$ (reached at $k_{\max}R \approx 600$) in both cases of linear and quadratic profiles, which provides a relative accuracy better than 10^{-6}, as exemplified in Fig. 3.3.2 and Fig. 3.3.1.

3.3.2 Quantum mechanical analogy - the effective potential

To intuitively understand the properties of the RSs in graded-index optical systems, it is useful to consider the analogy between Maxwell's and Schrödinger's wave equations and to introduce

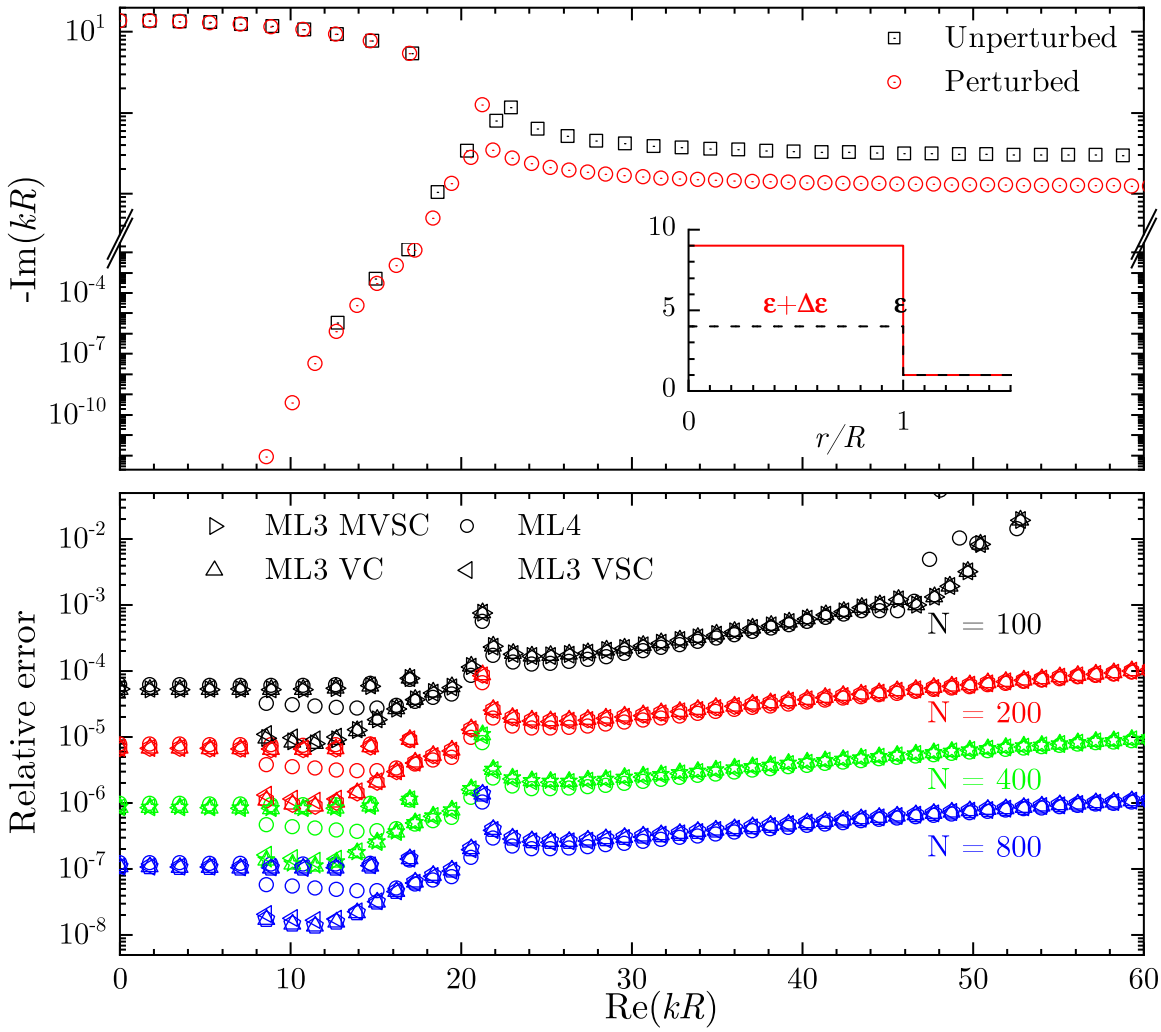

Fig. 3.3.2: As Fig. 3.3.1, but for a homogeneous perturbation. Basis system $\epsilon = 4$, target system $\epsilon + \Delta\varepsilon = 9$.

an effective optical potential [125]. In spherically symmetric systems, all the components of the electric and magnetic fields can be expressed in terms of a radially dependent scalar field [85]. For TE (TM) polarization, this is the magnitude of the electric (magnetic) field, which has only a tangential component $E(r) = \mathcal{E}(r)/r$ ($H(r) = -i\mathcal{H}(r)/r$). For non-magnetic systems, with the radial permittivity profile $\varepsilon(r)$ and permeability $\mu(r) = 1$, the scalar field $\mathcal{E}(r)$ satisfies the Schrödinger-like equation [85]

$$\left(\frac{\mathrm{d}^2}{\mathrm{d}r^2} - \frac{\alpha^2}{r^2} + k^2\varepsilon(r)\right)\mathcal{E}(r) = 0\,, \tag{3.23}$$

where $\alpha = \sqrt{l(l+1)}$. In fact, assuming a particle mass $M = \hbar^2/2$, Eq. (3.23) can be interpreted as a quantum-mechanical analogue (QMA). An obvious limitation of this QMA is that k^2, playing the role of the complex eigenvalue for the RSs, contributes to Eq. (3.23) not in the same way as the energy in Schrödinger's equation. Associating k^2 with the particle

energy, and using the fact that $\varepsilon(r) = 1$ (or a constant) outside the system, Johnson [125] introduced an energy-dependent effective potential, which makes the analogy with quantum mechanics no so straightforward. Here instead, we interpret Eq. (3.23) as an equation for the *zero-energy* state of a particle in a one-dimensional potential

$$V^{\mathrm{TE}}(r) = -k^2\varepsilon(r) + \frac{\alpha^2}{r^2}\,, \tag{3.24}$$

in which k plays the role of a complex parameter of the potential. In this QMA, every RS of the optical system, described by the wave function $\mathcal{E}(r)$, has zero quantum-mechanical energy and a potential Eq. (3.24) valid for this RS only, given by the corresponding value of k.

Likewise, for TM polarization, the scalar field $\mathcal{H}(r)$ satisfies an equation [85]

$$\left(-\frac{1}{\varepsilon(r)}\frac{\mathrm{d}\varepsilon}{\mathrm{d}r}\frac{\mathrm{d}}{\mathrm{d}r} + \frac{\mathrm{d}^2}{\mathrm{d}r^2} - \frac{\alpha^2}{r^2} + k^2\varepsilon(r)\right)\mathcal{H}(r) = 0\,, \tag{3.25}$$

again, valid for a non-magnetic system described by the permittivity $\varepsilon(r)$. Compared to Eq. (3.23), there is an additional term proportional to the logarithmic derivative of the permittivity, which can be included in the potential, yielding

$$V^{\mathrm{TM}}(r) = V^{\mathrm{TE}}(r) + \frac{\varepsilon'(r)}{\varepsilon(r)}\frac{\mathcal{H}'(r)}{\mathcal{H}(r)}\,, \tag{3.26}$$

where the prime indicates the spatial derivative. The second term in Eq. (3.26) is analyzed and discussed in more depth in Sec. 3.4.1, which helps understanding the TE-TM mode splitting. Here, we only note that this term, in its above form depending on the wave function, is inconsistent with the standard definition of the potential. However, introducing a re-scaled wave function $\widetilde{\mathcal{H}}(r) = \sqrt{\varepsilon(r)}\mathcal{H}(r)$ brings the effective potential to the form

$$\widetilde{V}^{\mathrm{TM}}(r) = V^{\mathrm{TE}}(r) + \frac{3}{4}\left[\frac{\varepsilon'(r)}{\varepsilon(r)}\right]^2 - \frac{1}{2}\frac{\varepsilon''(r)}{\varepsilon(r)}\,, \tag{3.27}$$

which is now independent of the wave function, thus providing a valid QMA also for TM polarization, as detailed in Appendix B.2.

Note that the radial equations (3.23) and (3.25) are aligned with the standard Maxwell boundary conditions requiring that $\mathcal{E}$ and $\mathcal{E}'$ are continuous in TE polarization, and $\mathcal{H}$ and $\mathcal{H}'/\varepsilon$ are continuous in TM polarization. Clearly, any discontinuity of ε results in $\mathcal{H}'$ being also discontinuous in TM polarization, which is in particular the case of a homogeneous dielectric sphere in vacuum. We note that one can find the eigenmodes of graded index spheres by solving the radial equations directly with an appropriate numerical method. However this approach does not guarantee that all modes in a region of interest in the complex plane are found. In this paper we therefore use the effective potential picture in the following only for qualitative discussions, and developing an approximation based on the Morse potential.

3.3.3 Graded index permittivity profiles

Constant permittivity

The TE and TM modes of a homogeneous sphere in vacuum, used as basis system in the RSE and described by a constant permittivity

$$\varepsilon(r) = 1 + A\theta(R - r)\,, \tag{3.28}$$

where $\theta(x)$ is the Heaviside function and $A = n_r^2 - 1$, are shown in Fig. 3.3.3a for $n_r = 2$ (note they are the same as in Fig. 3.2.1). The fields, $\mathcal{E}(r)$ and $\mathcal{H}(r)$, and the corresponding effective potentials, given by Eq. (3.24) and Eq. (3.26), are illustrated in Fig. 3.3.3b for the fundamental WG mode for TE and TM polarizations, respectively. Both potentials decrease with radius due to the centrifugal term α^2/r^2 and have similar step-like barriers at the sphere surface ($r = R$) due to the step in the permittivity. In the TM potential, there is additionally a δ function at the sphere surface due to the derivative of the permittivity, see Eq. (3.26). The fields are effectively confined near the sphere surface, on one side by the centrifugal term increasing towards the center of the sphere and on the other side by the refractive index step at the sphere surface. The fields have evanescent tails extending outside of the sphere, which convert at larger distances into propagating waves once the potentials become negative, and then grow exponentially due to the imaginary part of the potentials created by the complex k.

The optical transmission through the barrier determines the losses of the WG modes and hence the imaginary part of their wavenumbers. The height of the barrier depends on the size of the permittivity step and the angular quantum number l, and the transmission reduces about exponentially with l, thus allowing for very low mode losses [49]. Note that in a purely quantum-mechanical problem, having a real potential, the eigenenergy of such a state would necessarily have a finite imaginary part [12] – our potentials are however complex due to the finite imaginary part of the RS wavenumbers, though the latter is small for WG modes. Interestingly, it is the complex potential which allows the state energy in the QMA to have zero imaginary part, even though there is a finite probability for the particle to tunnel through the barrier and to escape from the system.

Linear permittivity

We choose here a linear profile in the form

$$\varepsilon(r) = 1 + B\theta(R - r)(1 - r/R)\,, \tag{3.29}$$

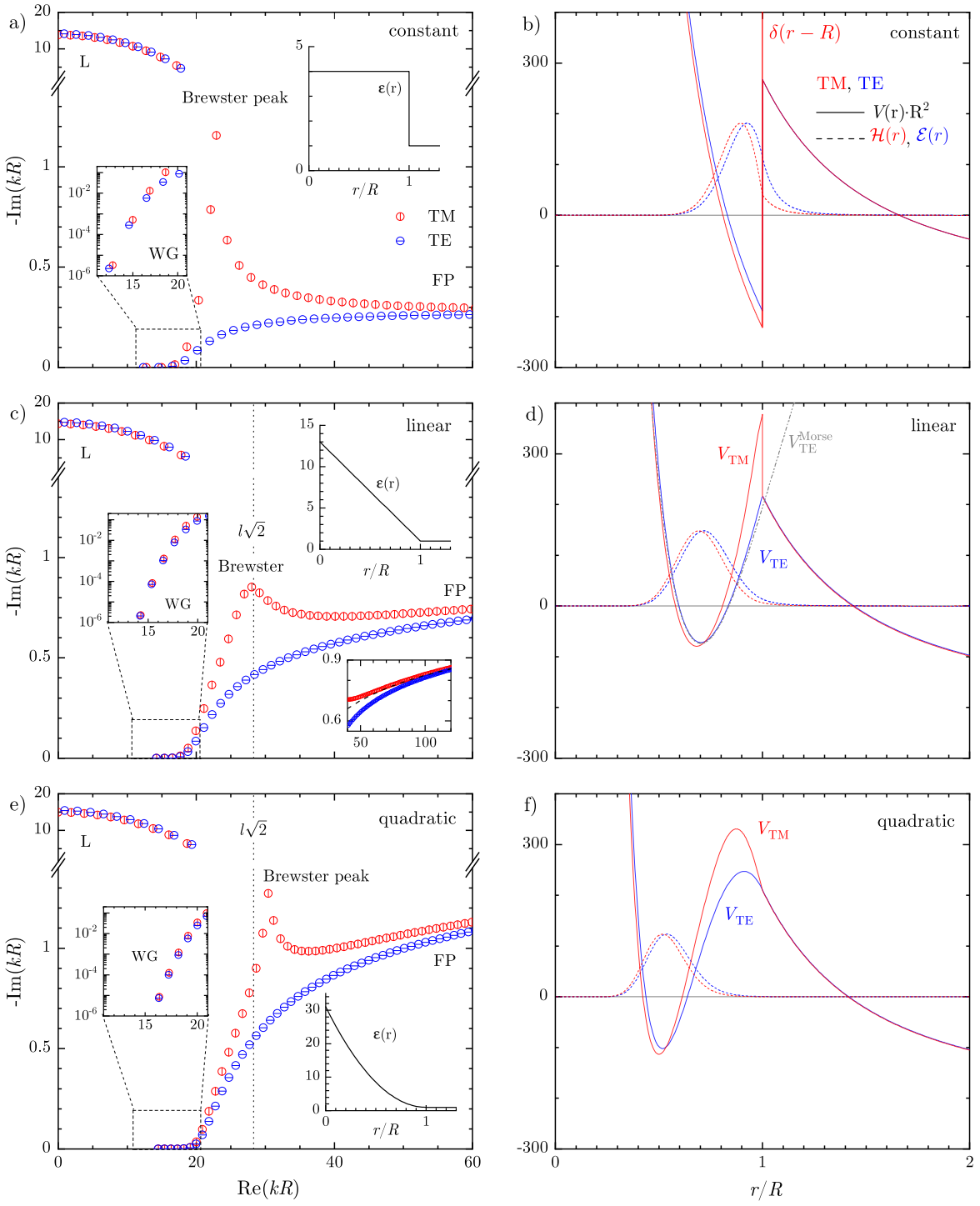

Fig. 3.3.3: RSs for $l = 20$, and constant (a,b), linear (c,d), and quadratic (e,f) permittivity profiles as shown in the insets. Left: RSs in the complex k plane. Right: Real part of the potential and the field of the first WG mode. The TE and TM fields are normalized to the same maximum value. The unitless effective potentials $V^{TE}R^2$ and $V^{TM}R^2$ are given, respectively, by Eqs. (3.24) and (3.26).

so that $\varepsilon(r)$ is a continuous function. The parameter B is chosen such that the volume integral of the permittivity $\int \varepsilon(r)\mathrm{d}V$ within the sphere of radius R is equal to that of the homogeneous sphere with refractive index n_r, yielding $B = 4(n_r^2 - 1)$. Since the basis system used in the RSE has $n_r = 2$, we take here $B = 12$.

The resulting RS wavenumbers calculated via the RSE are shown in Fig. 3.3.3c. Their distribution in the complex k-plane is qualitatively similar to that of the homogeneous sphere. The L RSs are nearly unaffected. The WG RSs have a smaller TE-TM splitting and a quicker growth of the imaginary part of k with the real part. The Brewster peak is less pronounced, broader, and is shifted towards larger values of the real part of k. At the sphere boundary the refractive index is approaching 1, so that using Eq. (3.2) one would expect the Brewster peak to appear at around $k_b R \approx l\sqrt{2}$, which is indeed observed in the spectrum, see a dotted line in Fig. 3.3.3c.

The FP RS wavenumbers show a significantly larger imaginary part compared the homogeneous case. Also, it is increasing with the real part, which is qualitatively different from the homogeneous sphere, where the imaginary part of k for the FP RSs is converging to a finite value with increasing the real part of k. This can be understood again considering the reflection at the sphere surface. For graded index boundaries, the reflectivity is wavelength dependent. It is proportional to the index change over one wavelength, thus proportional to $1/\mathrm{Re}\,(k)$ for short wavelength. An example of this can be found in [103] for a segment having an exponential permittivity profile. Using Eq. (3.3) we therefore expect $\mathrm{Im}\,(k) \propto \ln(\mathrm{Re}\,(k))$, which is shown as a dashed line in the lower inset of Fig. 3.3.3c, in good agreement with the high frequency asymptote of TE and TM wavenumbers.

To understand the behavior of the WG RSs, we consider the QMA, with potentials shown in Fig. 3.3.3d. The potential well is shifted towards the centre of the sphere, and while it is not as deep as in case of the constant case, the barrier itself is wider, providing a good containment for the modes. This is in agreement with observing high quality WGs despite the lack refractive index contrast at R.

Approximation based on the Morse potential

The shape of the potentials suggests that they can be approximated with the anharmonic Morse potential [126], for which analytical solutions are known. The Morse potential is a non-parabolic potential with known analytical solutions for energy levels and corresponding wave functions, often used to describe the binding of diatomic molecules [127]. We take the

Morse potential in the form

$$V_{\mathrm{M}}(r) = D_e \left\{1 - \exp[-a(r - r_e)]\right\}^2 \tag{3.30}$$

where D_e is the dissociation energy, r_e is the position of the potential minimum, and a is an inverse well width. The potential is zero at $r = r_e$ and approaches D_e asymptotically with increasing r. The bound energy levels of a quantum particle with a mass $M = \hbar^2/2$ in this potential are $E_n = -a^2(\lambda - n - 1/2)^2 + D_e$, where $\lambda = \sqrt{D_e}/a$ and $n = 0, 1, ...$ with $n < \lambda - 1/2$.

We apply this potential here to find approximate solutions for WG modes in the QMA, given by Eq. (3.23) for TE and Eq. (3.25) for TM polarization. To do so, we match the coefficients of the Taylor expansion of the Morse potential $V_{\mathrm{M}}(r)$ and the corresponding QMA potential $V(r)$ at their minimum r_e up to third order. Matching the value at the minimum is achieved by adding the value $V(r_e)$ to the Morse potential and its eigenenergies:

$$E_n = -a^2(\lambda - n - 1/2)^2 + D_e + V(r_e)\,. \tag{3.31}$$

The first derivative of both potentials is zero at the minimum and thus is matched by construction. We then determine D_e and a by matching the second and third derivatives, yielding

$$V''(r_e) = 2a^2 D_e \quad \text{and} \quad V'''(r_e) = -6a^3 D_e\,, \tag{3.32}$$

where the prime denotes the derivative with respect to r. As $V(r)$ depends on k, each WG mode has its own Morse potential parameters.

Now, since the solution corresponding to the WG mode has zero energy in the QMA, we can find an explicit equation determining the approximate value of the WG mode wavenumber k_{M}. Eliminating D_e and a from Eqs. (3.31) and (3.32), and requiring that $E_n = 0$ yields

$$\left[\frac{V'''}{3V''}\left(n + \frac{1}{2}\right)\right]^2 = V + \sqrt{2V''}\left(n + \frac{1}{2}\right)\,, \tag{3.33}$$

which is evaluated at $r = r_e$, where r_e is determined by

$$V'(r_e) = 0 \qquad \text{with} \qquad V''(r_e) > 0\,, \tag{3.34}$$

to select a minimum. Generally, Eqs. (3.33) and (3.34) provide a nonlinear set of equations for k_{M}^2, which can be solved numerically. Notably, for the case of a linear permittivity profile $\varepsilon(r)$ and TE polarization, the second and third derivatives of the potential are independent of k. They are given by $V''(r) = 6\alpha^2 R^2/r^4$ and $V'''(r) = -24\alpha^2 R^2/r^5$, so that the minimum

n	$k_{\mathrm{RSE}}R$	$k_{\mathrm{M}}R$	Relative error	r_e/R	$1/aR$	D_eR^2
0	54.11860	54.12054	0.00004	0.71708	0.53781	21266
1	55.26400	55.27396	0.00018	0.70707	0.53030	21872
2	56.40250	56.42867	0.00046	0.69739	0.52304	22484
3	57.53360	57.58464	0.00089	0.68802	0.51602	23100
4	58.65710	58.74180	0.00144	0.67896	0.50922	23721
5	59.77250	59.90012	0.00214	0.67018	0.50263	24347
6	60.87960	61.05955	0.00296	0.66167	0.49625	24977
7	61.97800	62.22004	0.00391	0.65341	0.49006	25612
8	63.06740	63.38155	0.00498	0.64541	0.48405	26251
9	64.14750	64.54401	0.00618	0.63763	0.47822	26895
10	65.21800	65.70736	0.00750	0.63008	0.47256	27544
11	66.27870	66.87152	0.00894	0.62275	0.46706	28196

Tab. 3.1: Comparison of TE WG mode wavenumbers calculated by the RSE (real part) and the Morse approximation Eq. (3.35), along with the Morse parameters for each fit. The relative error is calculated with respect to the RSE. Results are shown for the linear permittivity profile as in Sec. 3.3.3 and $l = 80$.

position is determined by $r_e^3 = -2R\alpha^2/(k^2\varepsilon')$. Inserting these into Eq. (3.33) provides the explicit algebraic expression for the approximate wavenumbers of the WG modes:

$$k_n^{\mathrm{TE}} \approx \frac{\alpha B}{2R(1+B)^{\frac{3}{2}}}\left(3+\sqrt{3}\frac{2n+1}{\alpha}-4\left(\frac{2n+1}{3\alpha}\right)^2\right)^{\frac{3}{2}} \tag{3.35}$$

with the level number $n = 0, 1, ...$ In this expression n has the physical meaning of number of nodes of the field inside the resonator. The accuracy of this expression relies on a high potential barrier, providing a small tunneling (and thus small imaginary part of k) which is typical for WG modes. Therefore the approximation Eq. (3.35) has a higher accuracy for the lowest WG modes at higher l and lower n. For $l = 80$, Eq. (3.35) gives k_n values with the a relative error to the RSE values of only 10^{-5} for the first WG mode ($n = 0$) to 10^{-2} for the 12th WG modes ($n = 11$), as illustrated by Table 3.1. Furthermore, Eq. (3.35) creates, for $n \ll \alpha$, equidistant levels of spacing $9B/(2R\sqrt{(1+B)^3})$, resembling a harmonic oscillator.

A fit of the effective potential $V(r)$ for the first WG mode ($n = 0$) in TE polarization with a Morse potential $V_{\mathrm{M}}(r)$ is illustrated in Fig. 3.3.3d, showing an excellent visual agreement between the two.

Finally, Table 3.2 shows the six lowest states in each of the Morse potentials corresponding to the first five WG modes in TE polarization. The state describing the WG mode has zero

	WG 1	WG 2	WG 3	WG 4	WG 5
$k_\mathrm{M}R$	54.12	55.26	56.40	57.53	58.66
n	$E_n(k_\mathrm{M})R^2$				
0	0	-551	-1124	-1720	-2338
1	535	0	-558	-1139	-1742
2	1064	543	0	-566	-1154
3	1585	1080	551	0	-573
4	2100	1609	1095	558	0
5	2608	2131	1631	1109	565

Tab. 3.2: Energy levels in the five different Morse potentials corresponding to the first five WG modes for TE polarization, $l = 80$, and a linear permittivity profile as in Sec. 3.3.3.

energy, and is changing from the first ($n = 0$) to the fifth state ($n = 4$) in the Morse potential. Importantly, the other states at non-zero energy are not describing WG modes, different from what could be implied by the QMA.

The Morse approximation of the TM potential Eq. (3.27) for linear permittivity, and of both TE and TM potentials for other spatial dependencies of the permittivity, result in non-linear simultaneous equations for k_n^2. Solving these numerically is still a lower cost compared to using the RSE or solving the radial equations (3.23) and (3.25) directly. The Morse approximation also provides analytical wave functions, which can be used for applying perturbation approaches like the one presented in Sec. 3.4.1 later.

Quadratic permittivity

In addition to the continuity of the permittivity we can require also that its first derivative is continuous, which can be achieved by using a quadratic profile

$$\varepsilon(r) = 1 + C\theta(R - r)(1 - r/R)^2\,, \tag{3.36}$$

where we again choose to conserve $\int \varepsilon(r)\mathrm{d}V$ relative to the basis system, yielding $C = 10(n_r^2 - 1)$, so that $C = 30$ for $n_r = 2$. The resulting RS wavenumbers are shown in Fig. 3.3.3e. The RSs change further along the same trends as seen when going from constant to linear profile. Notably, the Brewster peak is shifted further to higher wavenumbers compared to constant and linear case. The contrast with the surrounding is lower compared to the linear profile, creating an increased uncertainty in the position of the plane of reflection. It can also be seen from the permittivity profile that the effective radius of the sphere is reduced

compared to the constant and linear cases, which results in a larger k_b, in accordance with Eq. (3.2).

The imaginary part of the FP RSs is increased compared to the linear case as the reflection is further reduced at the surface due to the smooth permittivity. There are still high quality WG modes, with a decreased splitting between TE and TM RSs. Looking at the potential Fig. 3.3.3f, we find the well further inside the sphere with a wide barrier extended towards the outside, which provides good containment for the RSs. Higher-order TM WG modes along with the corresponding TM effective potentials are shown in Fig. B.2.1 of Appendix B.2.

3.4 TE-TM splitting

We found in the previous section that for the linear and quadratic permittivity, the splitting between TE and TM RSs is reduced compared to the constant permittivity, and this effect is further investigated in this section. The degeneracy of TE and TM modes might be of particular interest for chirality sensing, as that can convert second order perturbation effects due to a chiral material in the surrounding into the first order, similar to the effect of Faraday rotation by a circular magnetic field [128, 129]. To understand the cause of the reduced splitting we first develop in Sec. 3.4.1 a perturbative approach. Then, we revisit the optical systems discussed in Sec. 3.3.3 and quantify the splitting, followed by considering in Sec. 3.4.3 a new system featuring a wide effective potential well to reduce the splitting of the fundamental WG mode.

3.4.1 Perturbation treatment

The RSs form, together with static modes or their equivalents, a complete set inside the system and therefore provide a suitable basis for expanding any vector field within the system. This is the core principle of the RSE. In fact, an expansion into known basis modes is used in this paper to find the modes of the graded index profiles. In this subsection, we apply the same principle, however, in a simpler situation. Namely, we solve the scalar wave equation (3.25) with the TM potential by expanding its solution into the complete set of eigenstates of the corresponding wave equation (3.23) for TE polarization. In the simplest case, we reduce our basis to a single TE mode and thus solve Eq. (3.25) in the so-called diagonal approximation which can further be reduced to and interpreted as a first-order perturbation theory result.

The scalar equation (3.23) for the TE RSs can be written as

$$\hat{L}(k_n, r)\mathcal{E}_n(r) = 0\,, \tag{3.37}$$

where

$$\hat{L}(k, r) = \frac{\mathrm{d}^2}{\mathrm{d}r^2} - \frac{\alpha^2}{r^2} + k^2\varepsilon(r)\,. \tag{3.38}$$

The corresponding scalar Green's function satisfies

$$\hat{L}(k, r)G_k(r, r') = k\delta(r - r') \tag{3.39}$$

and can be expanded as

$$G_k(r, r') = \sum_n \frac{\mathcal{E}_n(r)\mathcal{E}_n(r')}{k - k_n} = k\sum_n \frac{\mathcal{E}_n(r)\mathcal{E}_n(r')}{k_n(k - k_n)}\,, \tag{3.40}$$

where $\mathcal{E}_n$ is normalized according to Eq. (3.6), the same way as in Ref. [85]. Accordingly, Eq. (3.25) for TM polarization takes the form

$$\hat{L}(k, r)\mathcal{H}(r) = \Delta\hat{L}(r)\mathcal{H}(r)\,, \tag{3.41}$$

where

$$\Delta\hat{L}(r) = \frac{\varepsilon'(r)}{\varepsilon(r)}\frac{\mathrm{d}}{\mathrm{d}r}\,, \tag{3.42}$$

and can be further written as a Lippman-Schwinger equation, in terms the Green's function of the operator $\hat{L}(k, r)$:

$$\mathcal{H}(r) = \frac{1}{k}\int_0^R G_k(r, r')\Delta\hat{L}(r')\mathcal{H}(r')\mathrm{d}r'\,. \tag{3.43}$$

Now, using the completeness of the basis states $\mathcal{E}_n(r)$,

$$\mathcal{H}(r) = \sum_n c_n\mathcal{E}_n(r)\,, \tag{3.44}$$

and the Green's function expansion Eq. (3.40), we convert Eq. (3.43) into the following matrix equation

$$k_n(k - k_n)c_n = \sum_{n'}\Delta_{nn'}c_{n'}\,, \tag{3.45}$$

where

$$\Delta_{nn'} = \int_0^R \mathcal{E}_n(r)\frac{\varepsilon'}{\varepsilon}\mathcal{E}'_{n'}(r)\mathrm{d}r \tag{3.46}$$

and the primes in ε and $\mathcal{E}$ mean derivatives with respect to r. Finally, using a single state only ($n' = n$), this reduces to the diagonal approximation:

$$k \approx k_n + \frac{\Delta_{nn}}{k_n}\,, \tag{3.47}$$

which is clearly equivalent to the first-order result in terms of the perturbation matrix $\Delta_{nn'}$. We call the above method re-expansion as the basis functions $\mathcal{E}_n(r)$ used in the expansion Eq. (3.44) are in turn expanded into the RSs of the homogeneous sphere.

A less rigorous and perhaps simpler approach is to treat the extra term in the TM potential, added to the TE equation, in a single mode approximation, in a manner it is usually applied to closed systems. Assuming $\mathcal{H}(r) \approx \mathcal{E}(r)$ and taking the difference between Eqs. (3.23) and (3.25), we find

$$\left[-\frac{\varepsilon'(r)}{\varepsilon(r)}\frac{\mathrm{d}}{\mathrm{d}r} + (k_{\mathrm{TM}}^2 - k_{\mathrm{TE}}^2)\varepsilon(r)\right]\mathcal{E}(r) \approx 0\,, \tag{3.48}$$

where k_{TE} (k_{TM}) is the TE (TM) RS wavenumber. Multiplying Eq. (3.48) with $\mathcal{E}(r)$ and integrating over the system volume yields

$$k_{\mathrm{TM}}^2 - k_{\mathrm{TE}}^2 \approx \frac{\int_0^R \mathcal{E}(r)\frac{\varepsilon'(r)}{\varepsilon(r)}\mathcal{E}'(r)\mathrm{d}r}{\int_0^R \mathcal{E}(r)\varepsilon(r)\mathcal{E}(r)\mathrm{d}r} \equiv 2\Delta\,. \tag{3.49}$$

The first-order correction to the wavenumber, determining the TE-TM splitting is then given by

$$k_{\mathrm{TM}} \approx k_{\mathrm{TE}} + \frac{\Delta}{k_{\mathrm{TE}}}\,. \tag{3.50}$$

For high-quality WG modes, the field $\mathcal{E}(r)$ is small at the surface, so that the integral in the denominator of Eq. (3.49) is getting close to the exact normalization, $2\int_0^R \varepsilon(r)\mathcal{E}^2(r)\mathrm{d}r \approx 1$, and the two results, Eqs. (3.47) and (3.50), become identical.

3.4.2 Constant, linear and quadratic profiles

The exact splitting of TE and TM RSs is quantified in Fig. 3.4.1, showing the distance from each TE RS to its nearest TM RS, both in the complex plane (Fig. 3.4.1a) and for the real part only (Fig. 3.4.1b). Considering first the constant permittivity (black circles), we find that the TE-TM splitting of WG modes is smaller than that of FP modes, and the real part of the splitting changes its sign at the Brewster peak, due to the additional TM mode as discussed in Sec. 3.2.1. At this peak there is a maximum of the absolute difference, due to the much larger imaginary part of the TM mode.

Moving to the linear profile (blue diamonds), the splitting decreases by a factor of about 5 for the WG modes, but only by about 30% for FP modes. Consistent with the weaker Brewster peak in the spectrum (see Fig. 3.3.3c), the splitting also does not show a pronounced peak. Finally, for the quadratic profile (red squares), the splitting is further reduced by a factor of about two for the WG modes and by about 10% for the FP modes. Due to the larger imaginary part (see Fig. 3.3.3e), also the absolute difference shows a Brewster peak.

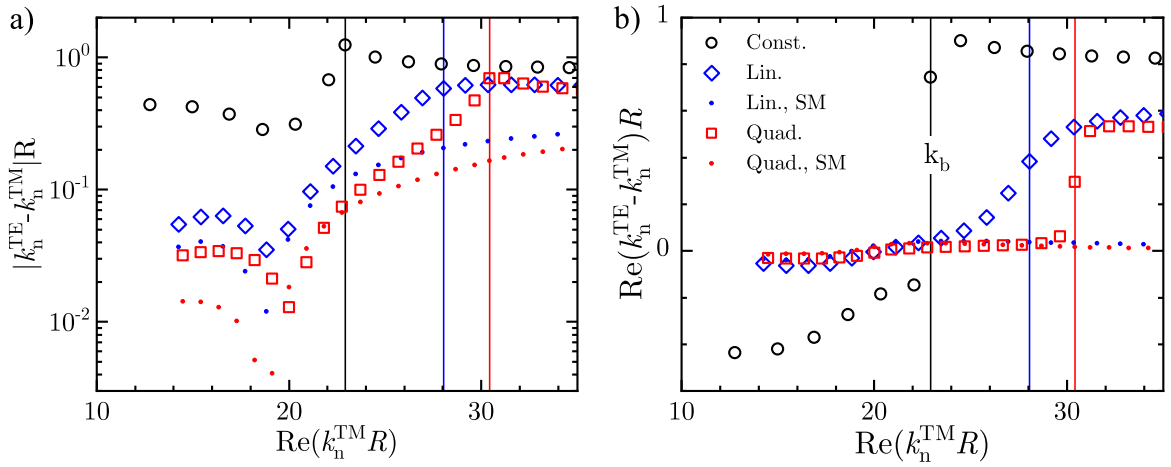

Fig. 3.4.1: Absolute value (a) and the real part (b) of the splitting between a TE (k_{TE}) and the nearest TM (k_{TM}) RS, for the considered permittivity profiles and $l = 20$. The vertical lines are the positions of the Brewster peak (k_b) in each TM spectra. The single-mode (SM) values are based on the re-expansion Eq. (3.47).

For all three cases, the smallest absolute distance between RSs is found for the WG modes near the critical wavenumber $k_c = l/R$ of the total internal reflection.

A similar behavior is observable for higher l, as shown in Appendix B.3. In this case, it is also easer to see that the graded permittivity profile reduces the dispersion of the WG modes, creating an approximately equidistant spectrum as shown in Appendix B.4. This has been also discussed in literature [117] and is consistent with results from the Morse potential approximation given by Eq. (3.35).

The RS splitting can be understood more mathematically by looking at the additional term of the TM potential in Eq. (3.26), which is the product of the logarithmic derivatives of the permittivity and the field. An obvious way to reduce the influence of this term is to spatially separate the maxima of the logarithmic derivative of the permittivity and the field amplitude. For the constant permittivity, the derivative creates a δ function at the boundary which overlaps much with the field thus creating a rather large splitting. Moving to the linear profile, the field maximum is shifted to smaller radii but the derivative of the permittivity is constant everywhere within the sphere. Still its influence is more spatially distributed compared to the δ function, and this reduces the splitting. Finally, for the quadratic profile, the maxima of both functions are spatially separated, and this reduces the splitting even further.

We also evaluated the TE-TM mode splitting using the diagonal approximation Eq. (3.47) for the linear (blue dots) and quadratic (red dots) profiles and compare it with the accurate

RSE result in Fig. 3.4.1. The obtained values from the single mode approximation are in qualitative but not quantitative agreement with the RSE result, and for the WG modes about a factor of two smaller. So interestingly, while the TE-TM splitting is small, suggesting that a single mode approximation would be suitable, the TE and TM field distributions are actually significantly different. This is due to a rather large perturbation of the potential (see Fig. 3.3.3), showing both positive and negative regions, and thus mixing with other modes while having a small single-mode perturbation integral.

A qualitative discussion of the TE-TM splitting of the fundamental WG mode is provided in Ref. [104], in terms of the radial and polar confinement of light in an effective waveguide with an asymmetric cross-section.

3.4.3 Reduction of splitting in a wide potential well

We expect the TE-TM degeneracy may be reduced for a wider potential well, as this can decrease the overlap of the RS field with the gradients of the permittivity, thus reducing the perturbation of the potential treated in Sec. 3.4.1. To create such a well in the effective potential V^{TE}, given by Eq. (3.24), the centrifugal radial term α^2/r^2 has to be compensated by a permittivity with the same functional dependence, $\varepsilon(r) \propto 1/r^2$. In this case the refractive index $n(r)$ scales as $1/r$, so that the circular round-trip phase, $2\pi krn(r)$, which is equal to $2\pi l$ in the ray picture, is independent of r. In other words, this graded index creates equal optical ray path lengths at all radii.

Since a permittivity diverging towards the sphere centre is not realistic, we introduce a cut-off radius $r_0 \ll R$ at which the permittivity saturates, using the expression

$$\varepsilon_{\mathrm{w}}(r) = \epsilon_{\mathrm{w}} \frac{R^2 + r_0^2}{r^2 + r_0^2} \,. \tag{3.51}$$

Here ϵ_{w} is the permittivity at the sphere surface $r = R$. In order to create a smooth potential with no discontinuities up to the first derivative across the sphere surface, we further introduce a transition region of width r_0 by defining the permittivity as

$$\varepsilon(r) = \begin{cases} 1 & r > R \,, \\ \varepsilon_{\mathrm{w}}(r) & r < R - r_0 \,, \\ 1 + [\varepsilon_{\mathrm{w}}(r) - 1] \sin^2\!\left(\pi \frac{r-R}{2r_0}\right) & \text{otherwise} \,. \end{cases} \tag{3.52}$$

The resulting permittivity profile and RSs for $\epsilon_{\mathrm{w}} = 2$ and $r_0 = 0.1R$ are shown in Fig. 3.4.2a, calculated by the RSE with $N = 1600$ ($k_{\max}R \approx 1200$). The number of basis modes was increased to retain the accuracy at the higher perturbation strength used. The Brewster peak

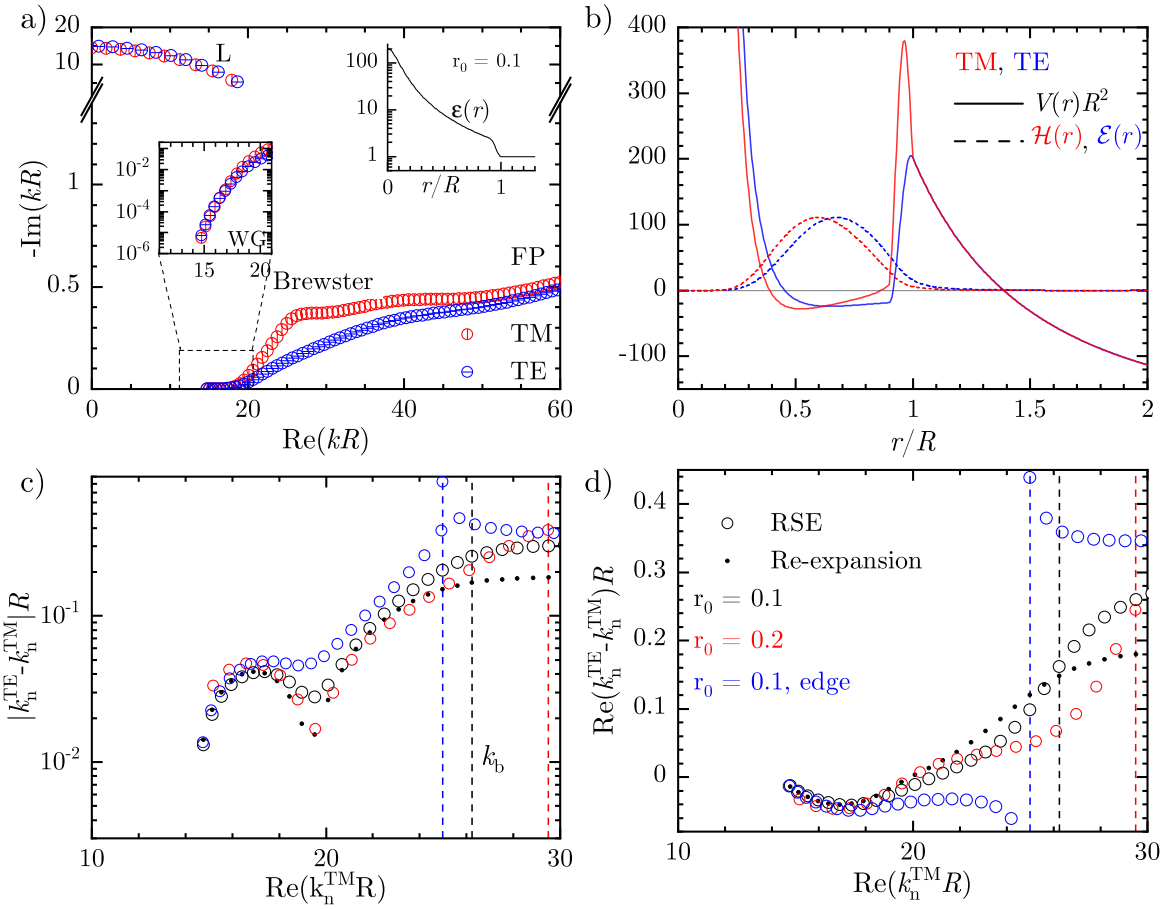

Fig. 3.4.2: RSs in a graded index profile Eq. (3.52) creating a wide potential well. a) as Fig. 3.3.3 left column. b) as Fig. 3.3.3 right column. c) and d) as Fig. 3.4.1 but using Eq. (3.45) with $N = 100$ basis modes, in comparison with the full RSE. As the imaginary part of k_n is monotonously increasing from WG to FP modes, the Brewster peak value k_b is chosen at the mode that has the largest difference of $\mathrm{Im}\,(k)$ between the closest TE and TM modes.

is blended in with the rest of the TM RSs, which have a monotonously increasing imaginary part; however we can still identify the peak in the difference of the imaginary part compared to the TE RSs. The potential for the first WG mode (Fig. 3.4.2b) shows a wide and flat well, as designed. The splitting between TE and TM RSs (see black on Fig. 3.4.2c) has reduced overall compared to the other profiles considered, and now the smallest absolute distance is observed for the first WG mode, being about twice smaller than for the quadratic profile (see Fig. 3.4.1). Increasing r_0 reduces the well width leading to larger splitting (see red on Fig. 3.4.2c,d). When using a sharp boundary at the edge, i.e. without the $\sin^2$ term in Eq. (3.52), the splitting of the first mode is not significantly changed, as it has a small field at the boundary. Higher order modes instead acquire a larger splitting, and furthermore a sharper Brewster's peak is found (see blue on Fig. 3.4.2c,d).

We also calculated the splitting using the perturbation method introduced in Sec. 3.4.1. While the degeneracy in k is decreased, the TE and TM fields are still spatially separated, so that instead of using a single mode we evaluate the full matrix equation Eq. (3.45) for $N = 100$ RSs. On Fig. 3.4.2 we can see that this leads to a much better agreement with the results compared to the single mode approximation used for the linear and quadratic case before. For increasing k the error in the results increases. This is due to a combination of factors, including the truncation of the matrix, the slow convergence of the expansion Eq. (3.40) as discussed in Ref. [85], and the error in the unperturbed fields $\mathcal{E}_n$.

3.5 Conclusion

We have studied, for different static-mode sets, an optimized version of the resonant-state expansion (RSE) and demonstrated the same quick ($1/N^3$, where N is the basis size of the RSE) convergence to the exact solution for different static-mode sets. We have also compared it with a similar version of the RSE, studied earlier in [85], in which static modes are eliminated from the basis, and demonstrated the same convergence for both versions. We have then applied the RSE to spheres with graded permittivity profiles and showed that the RSE is a reliable and simple method to determine all the resonant states (RSs) up to a maximum wavenumber controlled by the basis choice. Looking at the full spectrum provided by the RSE, instead of just distinct RSs, allows us to identify physical phenomena reliably and rapidly, as shown by the results presented. We have further discussed the results using the ray picture with surface reflections, the phase analysis based on the secular equation, and the concept of an effective potential, treating the radial wave equation as a quantum-mechanical analogue. Importantly, we provide a MATLAB program to calculate modes of a spherically symmetric system with a polynomial permittivity profile [130]. Once the basis modes are calculated across the whole system volume, applying the perturbation and finding the new modes takes only a few seconds on a modern computer, therefore the RSE is particularly suited to explore large parameter spaces. From the eigenmodes of graded index spheres one can calculate their scattering cross section [38]. The results shown here are thus relevant for applications such as atmospheric aerosol detection by light detection and ranging (LIDAR) [131], the modeling of the human head in medical imaging [132, 133], and the propagation of EM waves around Earth [134].

For a homogeneous sphere, we have provided a detailed analysis of the spectrum of the RSs in the complex wavenumber plane, consisting of leaky, Fabry-Pérot (FP), and whispering-

gallery (WG) modes. This analysis includes development of a number of approximations. For the transverse-magnetic (TM) polarization, we have explained the peak in the RS linewidth and an additional mode with respect to the transverse-electric (TE) polarization in terms of the Brewster phenomena. Using the ray picture further, we have evaluated the RS linewidth from Fresnel's coefficients of reflection which provides a good agreement with the exact solution for FP modes. We have shown that the wavenumber $k_c = l/R$ evaluated at the critical angle of the total internal reflection plays the role of a boundary in the spectrum separating the WG from FP modes.

We have then investigated graded index spheres with linear or quadratic permittivity profiles eliminating the discontinuity at the sphere surface. We have found that the imaginary part of FP modes is increasing logarithmically with their wavenumber, with a larger slope for quadratic profiles. We have used the concept of the effective potential for the radial electro-magnetic wave equation and suggested an interpretation of this quantum-mechanical analogy by associating all the physical solutions with zero-energy states, emphasizing that the effective potentials are complex. This provides a clear qualitative picture explaining the existence and properties of WG modes. We have further approximated the obtained effective potentials around their minimum with the analytically solvable Morse potential, which for TE polarization yields a simple explicit algebraic expression of high accuracy for the WG mode wavenumbers. For large angular quantum numbers l, this solution predicts a nearly equidistant spectrum of WG modes, similar to that of a harmonic oscillator.

We have studied the TE-TM splitting and demonstrated its reduction for WG modes when going from constant to linear and then to quadratic permittivity profile. We have shown that the splitting is further reduced in a wide flat potential well designed via the radial permittivity. To understand the TE-TM splitting, we have developed a re-expansion method, which perturbatively treats the difference between the effective potentials of TE and TM polarizations. The results are in good agreement with the exact solution. We have also provided a diagonal approximation, which turns out to be insufficient for the investigated cases despite the small splitting – a consequence of the underlying strong perturbation. Using this understanding, we have designed a graded index profile providing a wide effective potential well leading to a reduced TE-TM splitting, which in turn enhances the sensitivity of optical systems to chiral materials.

4

First order perturbation theory of resonant states

The contents of this chapter are submitted as an article to Physical Review Letters, which is under review at the time of writing, and it is also available on arXiv [50].

4.1 Introduction

Eigenmodes, which are solutions to a differential equation of Sturm-Liouville type with a set of boundary conditions, are used to describe physical phenomena across physics, including gravitational astronomy [20], acoustics [135], seismology [136], quantum mechanics (QM) [19], and electromagnetism (EM) [137]. The eigenmodes of open systems are also referred to as resonant states [14], or quasi-normal modes [51]. They determine the optical properties of a resonator, such as its scattering cross-section or Purcell enhancement [60]. For simple electromagnetic systems, such as a slab or a sphere, the RSs can be found analytically [70]. For more complicated shapes they can be found numerically [51, 138] or via perturbative approaches [51, 60]. The resonant-state expansion is a method that treats perturbations in all perturbation orders by transforming the problem of solving Maxwell's equation into a matrix eigenvalue problem [14]. Its accuracy is controlled by the selection of eigenmodes in the basis.

For small changes of the system, it is sufficient to take only a few suited RSs in the basis, or even a single one in a non-degenerate case. The latter corresponds to the diagonal approximation in terms of the matrix equation, and in certain cases this can also be equivalent to the first-order approximation, though not necessarily, as we will show in this paper. Following the terminology of Ref. [139], we distinguish two different kinds of perturbations: *volume* perturbation (VP) and *boundary* perturbation (BP). A VP is a small change of the

medium properties over a finite volume, for example, in QM a small change in the potential over the width of a quantum well, or in acoustics a small change of the density of the medium. A BP instead moves the spatial position of a medium interface with a discontinuity in medium properties, such as changing the width of a quantum well in QM. In EM, VPs could be a small change of a resonator's permittivity $\Delta\varepsilon$, for which first- and second-order results are well know [63, 76], or a small change of the background medium surrounding the resonator [46, 48, 140]. The VP examples in EM correspond to the diagonal approximation in the RSE matrix equation, and they include an overlap integral of the eigenmode field with the perturbation (e.g., $\Delta\varepsilon$), in complete analogy with conventional QM [71]. For BPs, this approach is not suited, because the local change of the medium property is not small. Instead, the deformation depth $h(\mathbf{r})$, which is the shift of the surface at position $\mathbf{r}$, plays the role of a small perturbation parameter, and an interesting consequence arises from the boundary conditions. For an open system, these are *outgoing waves* [141] which cannot be expressed as a combination of Neumann and Dirichlet boundary conditions, which makes the approach of Ref. [139] inapplicable. The underlying cause for the different treatment required in EM is the discontinuity of the normal component of the electric field at a material boundary [142, 143]. We note that similar effects can also occur in condensed matter physics when the effective mass in Schrödinger's equation is discontinuous, or in acoustics at the boundary between two media with different densities. In EM, the first-order correction to the RS frequency for a BP was treated for closed isotropic dielectric systems by using the electric displacement field normal to the surface [144]. In case of isotropic open dispersive systems, it was also recognized that the VP diagonal matrix element does not give the correct first-order results, and an alternative treatment was found based on distinguishing the electric fields inside and outside the resonator, and Taylor expanding them [51]. The case of a thin contamination layer surrounding the resonator has also been treated similarly to BP cases, with a local field correction [145]. The two approaches [51, 144] are equivalent apart from the frequency-dependent permittivity and the different field normalization for open systems [51]. It is also known that generally zero-frequency [32] or zero-permittivity [88] longitudinal modes need to be included in the basis alongside the RSs, however the contribution of these additional modes to the first-order results have not been considered in detail. Notably, the above BP methods [51, 144] do not treat VPs, and the mentioned VP methods do not treat BPs.

The purpose of this chapter is twofold. Firstly, we show that when treating a BP by applying the standard perturbation theory valid for VP, all orders of the perturbation series can contribute linearly in h. Using EM for illustration, we demonstrate this surprising finding

in terms of static (zero-frequency) modes of a non-dispersive open optical system.

Secondly, we derive a unified treatment of small BP and VP, describing correctly the first-order RS wave number change, linear in h and $\Delta\varepsilon$, respectively. This treatment is generalized to include frequency dispersion, arbitrary media (including magnetic and chiral), and arbitrary shape. Illustrations for both spherical and non-spherical dispersive systems are provided.

4.2 Perturbations of a dielectric sphere

For clarity of presentation, we start by considering an unperturbed dielectric system described by a non-dispersive permittivity tensor $\hat{\boldsymbol{\varepsilon}}(\mathbf{r})$ with known RSs having wave numbers k_n and electric fields $\mathbf{E}_n(\mathbf{r})$. This system is perturbed by a change of the permittivity $\Delta\hat{\boldsymbol{\varepsilon}}(\mathbf{r})$, where $\Delta\hat{\boldsymbol{\varepsilon}}(\mathbf{r})$ is inside the original system volume. In the RSE approach [14, 63], the electric field $\mathbf{E}(\mathbf{r})$ of a perturbed RS is expanded as

$$\mathbf{E}(\mathbf{r}) = \sum_{\nu} c_\nu \mathbf{E}_\nu(\mathbf{r})\,, \tag{4.1}$$

leading to a matrix eigenvalue problem

$$(k - k_\nu)c_\nu = -k \sum_{\nu'} V_{\nu\nu'} c_{\nu'}\,, \tag{4.2}$$

which determines the exact values of the perturbed RS wave numbers k and the expansion coefficients c_ν in the limit of all unperturbed modes included in the summation. Here, index ν labels both the RSs ($\nu = n$, with $k_n \neq 0$) and static modes ($\nu = \lambda$, with all $k_\lambda = 0$ [32]), and the matrix elements of the perturbation have the form

$$V_{\nu\nu'} = \int \mathbf{E}_\nu(\mathbf{r}) \cdot \Delta\hat{\boldsymbol{\varepsilon}}(\mathbf{r}) \mathbf{E}_{\nu'}(\mathbf{r}) d\mathbf{r}\,, \tag{4.3}$$

where all fields $\mathbf{E}_\nu$ are properly normalized [14, 68]. From the exact RSE equation (4.2) one can extract, in the spirit of a standard perturbation theory [71], corrections to the eigenvalue k_n in all orders, in a form of an infinite series [63] (for details see Appendix C.1)

$$k = k_n - k_n V_{nn} + k_n V_{nn}^2 + k_n^2 \sum_{\nu \neq n} \frac{V_{n\nu} V_{\nu n}}{k_n - k_\nu} + \dots\,, \tag{4.4}$$

which suggests that

$$k^{(1)} = -k_n V_{nn} \tag{4.5}$$

is the first-order correction to the wave number k_n. In fact, each matrix element Eq. (4.3) is linear both in the permittivity perturbation $\Delta\hat{\boldsymbol{\varepsilon}}$ and in the deformation depth h in lowest order.

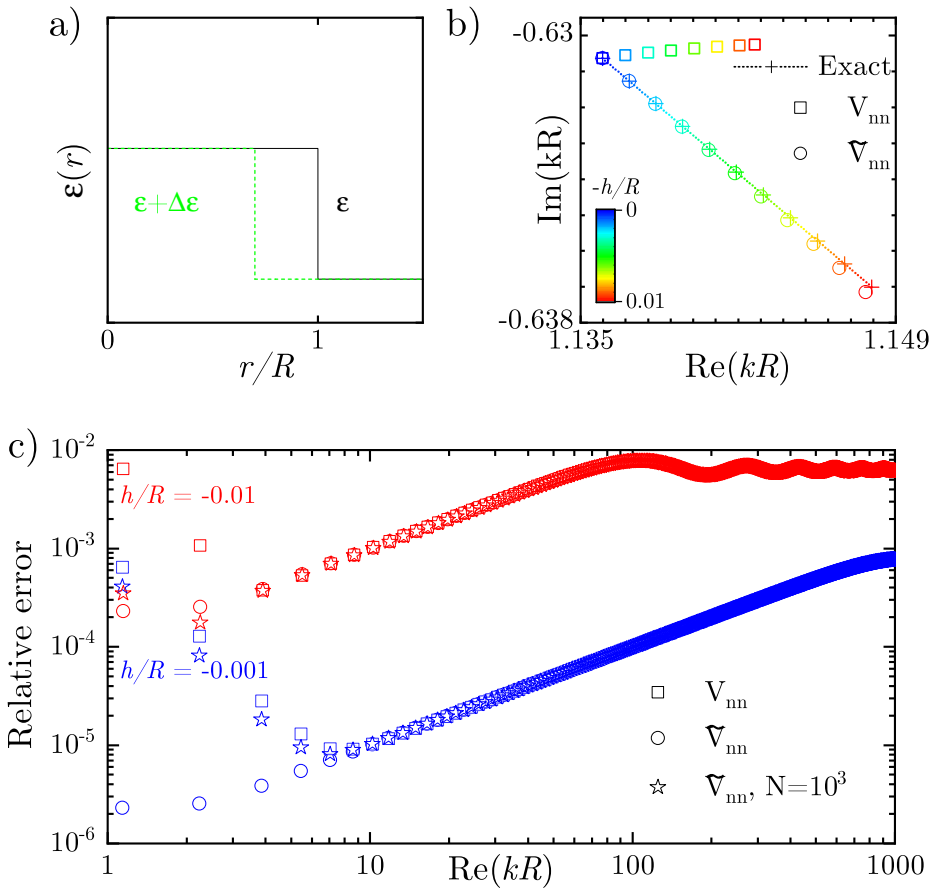

Fig. 4.2.1: (a) Schematic illustration of a BP as a permittivity perturbation of the sphere, with its radius R changing by h. (b) Effect of the BP on the wave number k of first RS with orbital number $l = 1$ in a sphere of permittivity $\varepsilon = 4$ surrounded by vacuum. (c) Relative error of RS wave numbers calculated without static modes (squares), with all static modes (circles), and with 1000 static modes included (stars), for two different BPs as given.

The above first-order correction $k^{(1)}$ is illustrated in Fig. 4.2.1 for TM modes of a dielectric sphere of radius R in vacuum, with angular momentum $l = 1$, for a BP changing the radius of the sphere by h. Clearly, for the fundamental mode, Eq. (4.5) (squares) does not describe correctly the first-order changes of the RS wave number k, as a deviation linear in h is observed implying that first-order contributions to k are missing.

The origin of this mismatch lies in the role of static modes, which surprisingly can contribute linearly in h via the second-order sum, $k_n \sum_\lambda V_{n\lambda} V_{\lambda n}$, and also via all higher-order terms of the perturbation series Eq. (4.4). Using the closure relation for the modes this is indicated for the second order term only in Appendix C.1.2. To take the cumulative effect of static modes into account, let us write the RSE equation (4.2) in terms of the RSs only, by

using the $k_\lambda = 0$ degeneracy of static modes [85]:

$$(k - k_n)c_n = -k \sum_{n'} \tilde{V}_{nn'} c_{n'} \,, \tag{4.6}$$

where

$$\tilde{V}_{nn'} = V_{nn'} - \sum_{\lambda\lambda'} V_{n\lambda} W_{\lambda\lambda'} V_{\lambda' n} \tag{4.7}$$

and the matrix $W_{\lambda\lambda'}$ is the inverse of $\delta_{\lambda\lambda'} + V_{\lambda\lambda'}$ with $\delta_{\lambda\lambda'}$ being the Kronecker delta. The full linear correction to the RS wave number is then given by

$$\tilde{k}^{(1)} = -k_n \tilde{V}_{nn}. \tag{4.8}$$

To evaluate the sum in Eq. (4.7), we use a Neumann series expansion $W = (I + V)^{-1} = I - V + V^2 - V^3 + \ldots$, where W (V) is a matrix with elements $W_{\lambda\lambda'}$ $(V_{\lambda\lambda'})$ and I is the identity matrix. Substituting it into Eq. (4.7) results in an infinite series

$$\tilde{V}_{nn'} = V_{nn'} - \sum_{\lambda} V_{n\lambda} V_{\lambda n'} + \sum_{\lambda\lambda'} V_{n\lambda} V_{\lambda\lambda'} V_{\lambda' n'} - \ldots, \tag{4.9}$$

which we evaluate below to first order in h, using the static pole residue of the dyadic Green's function (here, its electric part only, which is sufficient for permittivity perturbation). For a spherically symmetric dielectric systems with permittivity $\varepsilon(r)$, the residue can be written explicitly as (see Sec. C.1.3 in Appendix C)

$$\sum_{\lambda} \mathbf{E}_\lambda(\mathbf{r}) \otimes \mathbf{E}_\lambda(\mathbf{r}') = \frac{\hat{\mathbf{r}} \otimes \hat{\mathbf{r}}}{\varepsilon(r)} \delta(\mathbf{r} - \mathbf{r}') + \hat{\mathbf{R}}(\mathbf{r}, \mathbf{r}') \,, \tag{4.10}$$

where the tensor $\hat{\mathbf{R}}(\mathbf{r}, \mathbf{r}')$ is a regular part of the residue, $\hat{\mathbf{r}}$ is the unit vector in the radial direction and $\otimes$ denotes the dyadic product. Using Eq. (4.10) for each sum over static modes in Eq. (4.9), one can see that the δ function in Eq. (4.10) eliminates one volume integration, reducing each term in Eq. (4.9) to a single volume integral, proportional to h. Furthermore, the contribution of the regular part can be neglected in linear order in h, as it comes with an additional volume integral, and hence is of higher order. Summing over all orders, we arrive, after some algebra, at

$$\begin{aligned} \frac{\tilde{k}^{(1)}}{k_n} &= -\int \mathbf{E}_n \cdot \left[\hat{\mathbf{1}} + \frac{\Delta\hat{\boldsymbol{\varepsilon}}(\mathbf{r})}{\varepsilon(r)} \hat{\mathbf{r}} \otimes \hat{\mathbf{r}} \right]^{-1} \Delta\hat{\boldsymbol{\varepsilon}}(\mathbf{r}) \mathbf{E}_n d\mathbf{r} \\ &= -\int \left[\mathbf{E}_n^{\parallel} \cdot \Delta\varepsilon(\mathbf{r}) \mathbf{E}_n^{\parallel} + \mathbf{E}_n^{\perp} \cdot \frac{\varepsilon(r)\Delta\varepsilon(\mathbf{r})}{\varepsilon(r) + \Delta\varepsilon(\mathbf{r})} \mathbf{E}_n^{\perp} \right] d\mathbf{r} \,, \end{aligned} \tag{4.11}$$

where $\hat{\mathbf{1}}$ is the identity tensor, and the perturbation $\Delta\varepsilon(\mathbf{r})$ in the second line is assumed isotropic but not necessarily spherically symmetric. The superscript $\parallel$ $(\perp)$ labels the vector

component parallel (normal) to the interface of the basis system. More details of the derivation of the above equations and their extension to magnetic and chiral materials are provided in Appendix C.1.4.

Figure 4.2.1 demonstrates that Eq. (4.11) (circles) correctly describes the effect of the size perturbation in first-order. In fact, comparing $h/R = -0.01$ and -0.001, one can see that the residual error scales quadratically, i.e. is of second order in h, as expected. We also show in Fig. 4.2.1 the error for the RS wave numbers calculated with an explicit use of $N = 10^3$ static modes [104] in $\tilde{V}_{nn}$ via Eq. (4.7) (stars). This demonstrates that as h gets smaller, even a large number of static modes is not sufficient to represent the δ function in Eq. (4.10) well, resulting in errors for the eigenmodes close to zero wave number that are similar with and without the static modes. More details about the static mode contribution can be found in Appendix C.2.2, while in Appendix C.2.1 we consider a homogeneous perturbation of a dielectric sphere where the static modes do not contribute to the first order results. For higher l, the static modes can still contribute to the RSs in first-order, thought the effect is less pronounced due to the higher frequencies of the RSs (see Fig. C.2.3 in Appendix C). Note that, while the total number of static modes is countable infinite, the freedom of choosing such a set, granted by their wave number degeneracy, allows one to concentrate the effect of the boundary shift in a single-mode contribution [146], which is sufficient to describe the full first-order correction.

As it is clear from Fig. 4.2.1 and the above derivation, the first-order term of the standard perturbation series Eq. (4.4) does not contain all first-order effects of the BP. Instead, additional first-order terms can be found in all orders of the perturbation theory. An alternative derivation of the first order results based on scalar equations can be found in Appendix C.3. We emphasize that this occurs in any area of physics describing wave phenomena, and we give in Appendix C.4, examples from condensed matter and acoustics illustrating this effect.

4.3 Perturbations of an arbitrary resonator

The first-order result Eq. (4.11) was for clarity obtained for a spherically symmetric non-dispersive system. We now generalize Eq. (4.11) to optical systems with (i) any geometry, (ii) magnetic and chiral materials, and (iii) arbitrary frequency dispersion. To do this, we write Maxwell's equations for the unperturbed system in the compact form [68]

$$\left[k_n \hat{\mathbb{P}}_0(k_n, \mathbf{r}) - \hat{\mathbb{D}}(\mathbf{r})\right] \vec{\mathbb{F}}_n(\mathbf{r}) = 0\,, \tag{4.12}$$

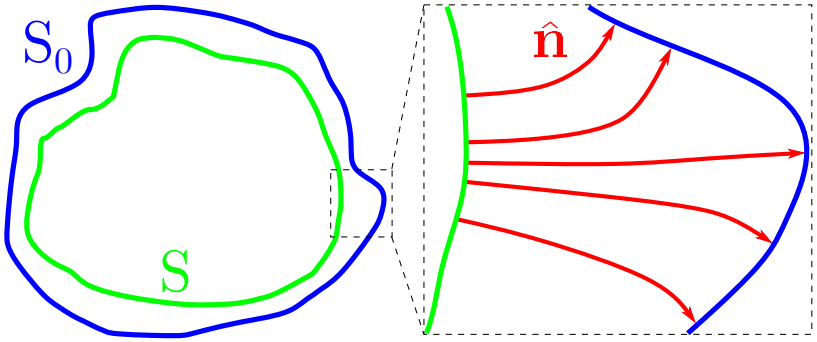

Fig. 4.3.1: Sketch of the unperturbed and perturbed systems occupying the volumes V_0 and V and having surfaces S_0 and S, respectively. The vector field $\hat{\mathbf{n}}(\mathbf{r})$ is normal to both S_0 and S.

where

$$\hat{\mathbb{P}}_0 = \begin{pmatrix} \hat{\varepsilon} & -i\hat{\boldsymbol{\xi}} \\ i\hat{\boldsymbol{\zeta}} & \hat{\boldsymbol{\mu}} \end{pmatrix}, \quad \hat{\mathbb{D}} = \begin{pmatrix} \hat{\mathbf{0}} & \nabla\times \\ \nabla\times & \hat{\mathbf{0}} \end{pmatrix}, \quad \vec{\mathbb{F}}_n = \begin{pmatrix} \mathbf{E}_n \\ i\mathbf{H}_n, \end{pmatrix} \tag{4.13}$$

and $\hat{\mathbf{0}}$ is the 3×3 zero matrix. $\hat{\mathbb{P}}_0(k,\mathbf{r})$ is a 6×6 tensor describing the system which consists of frequency-dispersive tensors of permittivity $\hat{\boldsymbol{\varepsilon}}(k,\mathbf{r})$, permeability $\hat{\boldsymbol{\mu}}(k,\mathbf{r})$, and bi-anisotropy $\hat{\boldsymbol{\xi}}(k,\mathbf{r})$ and $\hat{\boldsymbol{\zeta}}(k,\mathbf{r})$. $\vec{\mathbb{F}}_n(\mathbf{r})$ is a 6×1 vector comprising $\mathbf{E}_n(\mathbf{r})$ and $\mathbf{H}_n(\mathbf{r})$, the electric and magnetic fields of the RS with the wave number k_n. Applying a perturbation $\Delta\hat{\mathbb{P}}(k,\mathbf{r})$ of the generalized permittivity, the electromagnetic field and the wave number of this RS change, respectively, to $\vec{\mathbb{F}}(\mathbf{r})$ and k, which in turn satisfy perturbed Maxwell's equations

$$\left[k\hat{\mathbb{P}}(k,\mathbf{r}) - \hat{\mathbb{D}}(\mathbf{r})\right]\vec{\mathbb{F}}(\mathbf{r}) = 0 \tag{4.14}$$

with $\hat{\mathbb{P}}(k,\mathbf{r}) = \hat{\mathbb{P}}_0(k,\mathbf{r}) + \Delta\hat{\mathbb{P}}(k,\mathbf{r})$ of the perturbed system. For clarity of presentation, we assume below isotropic and reciprocal materials; and a further generalization to anisotropic [147] or non-reciprocal materials is possible [69]. Multiplying Eq. (C.48) with $\vec{\mathbb{F}}$ and Eq. (C.50) with $\vec{\mathbb{F}}_n$, integrating both equations over the unperturbed system volume V_0 (which contains the perturbation $\Delta\hat{\mathbb{P}}$, see Fig. 4.3.1), taking the difference between the results, and applying the divergence theorem to the terms with $\hat{\mathbb{D}}$-operators [68], we obtain

$$\begin{aligned} &\int_{V_0} \vec{\mathbb{F}}_n(\mathbf{r}) \cdot \left[k_n\hat{\mathbb{P}}_0(k_n,\mathbf{r}) - k\hat{\mathbb{P}}(k,\mathbf{r})\right]\vec{\mathbb{F}}(\mathbf{r})d\mathbf{r} \\ &= i\oint_{S_0} \left[\mathbf{E}_n(\mathbf{r})\times\mathbf{H}(\mathbf{r}) - \mathbf{E}(\mathbf{r})\times\mathbf{H}_n(\mathbf{r})\right]\cdot d\mathbf{S}\,, \end{aligned} \tag{4.15}$$

where S_0 is the boundary of V_0.

To extract from Eq. (C.52) the first-order correction $\tilde{k}^{(1)}$ to the wave number, we introduce a real vector field $\hat{\mathbf{n}}(\mathbf{r})$ which is normal to both surfaces S_0 and S (of the unperturbed and perturbed systems) and is normalized at each point as $|\hat{\mathbf{n}}(\mathbf{r})| = 1$ (if there are other surfaces

with material discontinuities, $\hat{\mathbf{n}}$ should be chosen normal also to them). Then we introduce a perturbed field component

$$\vec{\mathbb{F}}^{\perp}(\mathbf{r}) = \begin{pmatrix} \mathbf{E}^{\perp}(\mathbf{r}) \\ i\mathbf{H}^{\perp}(\mathbf{r}) \end{pmatrix} = \begin{pmatrix} \hat{\mathbf{n}}(\mathbf{r})[\hat{\mathbf{n}}(\mathbf{r}) \cdot \mathbf{E}(\mathbf{r})] \\ \hat{\mathbf{n}}(\mathbf{r})[\hat{\mathbf{n}}(\mathbf{r}) \cdot i\mathbf{H}(\mathbf{r})] \end{pmatrix}, \tag{4.16}$$

which is normal to both S_0 and S. The tangential component is then given by $\vec{\mathbb{F}}^{\parallel} = \vec{\mathbb{F}} - \vec{\mathbb{F}}^{\perp}$. Now, according to Maxwell's boundary conditions, fields $\vec{\mathbb{F}}^{\parallel}(\mathbf{r})$ and $\hat{\mathbb{P}}(k, \mathbf{r})\vec{\mathbb{F}}^{\perp}(\mathbf{r})$ are continuous everywhere. Similarly, the unperturbed fields $\vec{\mathbb{F}}_n^{\parallel}(\mathbf{r})$ and $\hat{\mathbb{P}}_0(k_n, \mathbf{r})\vec{\mathbb{F}}_n^{\perp}(\mathbf{r})$, introduced in the same manner, are also continuous. Then, approximating $\vec{\mathbb{F}}^{\parallel}(\mathbf{r}) \approx \vec{\mathbb{F}}_n^{\parallel}(\mathbf{r})$ and $\hat{\mathbb{P}}(k, \mathbf{r})\vec{\mathbb{F}}^{\perp}(\mathbf{r}) \approx \hat{\mathbb{P}}_0(k_n, \mathbf{r})\vec{\mathbb{F}}_n^{\perp}(\mathbf{r})$, which is sufficient for determining the wave number k to first order, we use in Eq. (C.52)

$$\vec{\mathbb{F}}(\mathbf{r}) = \vec{\mathbb{F}}_n^{\parallel}(\mathbf{r}) + \hat{\mathbb{P}}^{-1}(k, \mathbf{r})\hat{\mathbb{P}}_0(k_n, \mathbf{r})\vec{\mathbb{F}}_n^{\perp}(\mathbf{r}), \tag{4.17}$$

where $\hat{\mathbb{P}}^{-1}$ is the inverse of $\hat{\mathbb{P}}$. Finally, applying a Taylor expansion $k\hat{\mathbb{P}}(k, \mathbf{r}) = k_n\hat{\mathbb{P}}(k_n, \mathbf{r}) + [k\hat{\mathbb{P}}(k, \mathbf{r})]'(k - k_n) + \dots$ and $\vec{\mathbb{F}}(\mathbf{r}) = \vec{\mathbb{F}}_n(\mathbf{r}) + \vec{\mathbb{F}}_n'(\mathbf{r})(k - k_n) + \dots$ for the field outside the systems and keeping only terms linear in $k - k_n$, we arrive, after some algebra at (see Appendix C.5 for more details)

$$\frac{\tilde{k}^{(1)}}{k_n} = \frac{-\int_{V_0}\left[\vec{\mathbb{F}}_n^{\parallel} \cdot \Delta\hat{\mathbb{P}}\vec{\mathbb{F}}_n^{\parallel} + \vec{\mathbb{F}}_n^{\perp} \cdot \hat{\mathbb{P}}_0\hat{\mathbb{P}}^{-1}\Delta\hat{\mathbb{P}}\vec{\mathbb{F}}_n^{\perp}\right]d\mathbf{r}}{\int_{V_0}\vec{\mathbb{F}}_n \cdot \left[k\hat{\mathbb{P}}_0\right]'\vec{\mathbb{F}}_n d\mathbf{r} + i\oint_{S_0}(\mathbf{E}_n \times \mathbf{H}_n' - \mathbf{E}_n' \times \mathbf{H}_n) \cdot d\mathbf{S}}, \tag{4.18}$$

where the prime indicates the derivative with respect to k and all quantities are taken at $k = k_n$. Equation (4.18) is a generalization of Eq. (4.11), which is valid also for small perturbations outside the basis system, including deformation outwards. Note that we have not assumed so far any specific normalization of $\vec{\mathbb{F}}_n(\mathbf{r})$. The analytic normalization introduced in [14, 68] ensures that the denominator in Eq. (4.18) is equal to 1.

It is important to note that Eqs (4.11) and (4.18) contain the exact first-order correction both in terms of the permittivity change ($\Delta\hat{\boldsymbol{\varepsilon}}$ or $\Delta\hat{\mathbb{P}}$) and in the deformation depth h. They also include higher order corrections which are not exact. For simplicity we assumed non-degenerate modes in the above derivation. To find the first order correction to degenerate modes, a matrix equation similar to Eq. (4.6), including only degenerate states, will need to be diagonalized.

The above derivation provides a clue for understanding the demonstrated phenomenon that the standard perturbation series Eq. (4.4) can have contributions to the RS wave number which are linear in h in all perturbation orders. The zeroth-order approximation of the field Eq. (C.57), which is the key point of the derivation, is different from the standard expansion Eq. (4.1) used for a single mode. The failure to extract the correct first order from a series

like Eq. (4.4) technically arises from approximating discontinuous functions with continuous ones. Further illustrations of this fact and a link to the completeness of the basis functions are provided in Sec. C.3 of Appendix C.

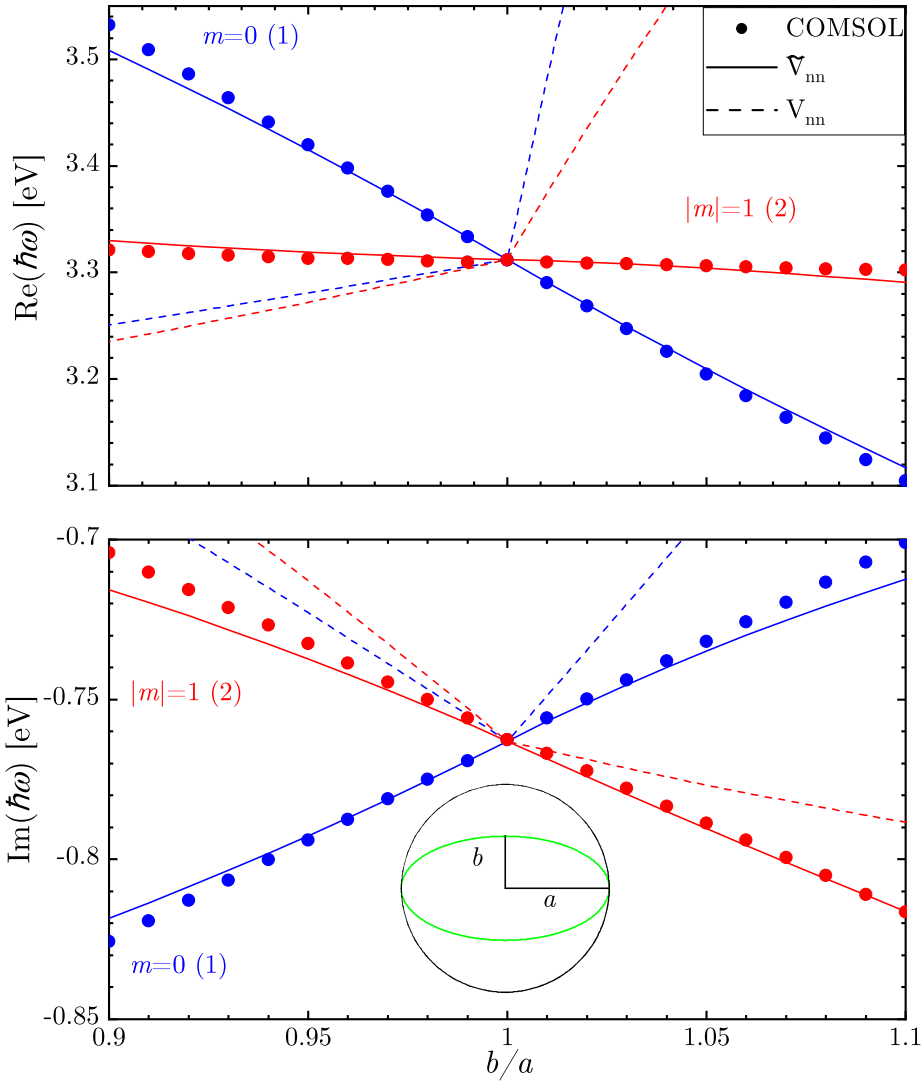

Fig. 4.3.2: (a) Real and (b) imaginary part of the wave number of the dipolar surface plasmon mode of a silver sphere perturbed to an ellipsoid, which is sketched in the inset of (b). The mode degeneracy is shown in brackets, and m is its magnetic quantum number. The COMSOL data is taken from [51].

We now demonstrate the first-order formula Eq. (4.18) on a non-spherical system with frequency dispersion. Figures 4.3.2(a) and (b) show, respectively, the real and imaginary part of k for the dipolar surface plasmon mode of a silver sphere being distorted in to an ellipsoid. The permittivity of silver is given by the Drude model: $\epsilon(\omega) = 1 - \omega_p^2/(\omega^2 + i\omega\gamma)$ with $\hbar\omega_p = 9\,\mathrm{eV}$ and $\hbar\gamma = 0.021\,\mathrm{eV}$, as used in [51]. The perturbation theory Eq. (4.18) (solid lines) agrees in first order of h with numerically calculated values (circles), for both inwards

($a < R$) and outwards ($a > R$) perturbations of the silver sphere. The results using $k^{(1)}$ are also shown for comparison (dashed lines), and are clearly incorrect. This example was chosen identical to the one used in [51], where the first-order RSE was taken as $k^{(1)}$ given by Eq. (4.5), even though earlier works [32, 85] indicate that static modes could contribute in first order. Thus the statement in Ref. [51] that the RSE is providing an incorrect first-order result was premature.

4.4 Conclusion

In conclusion, we have shown that a first-order perturbation theory of the eigenfrequencies in open systems requires separate considerations for volume perturbations and interface shifts. While volume perturbations lead to first-order diagonal matrix elements capturing the complete first-order effect, moving interfaces which host discontinuities of the underlying medium properties leads to additional first-order contributions arising from higher-order terms. In case of electromagnetism, this is due to the coupling to the countable infinite number of degenerate static modes. The underlying mechanism is clarified by explicitly treating the static pole of the Green's dyadic, as well as the discontinuity of the electric field, and a first-order perturbation theory expression valid for both medium changes and interface shifts is provided.

5

Three dimensional systems with rotational symmetry

5.1 Introduction

While the spherically symmetric approximation might be sufficient to describe certain physical system [131–134], for many applications one needs to consider systems of lower symmetry, such as when describing nanorods [148, 149], dimers [36], or cubes [150]. When describing such systems, where the polar, azimuthal, or both symmetries are broken the RSE formalism remains valid but the eigenmodes of different polarisations (TE, TM), and different angular momentum (l) and magnetic quantum number (m) can be mixed by the perturbation [63]. Previously, when treating such systems with the RSE it was observed that while the results converge to the correct solution, which is calculated by another numerical method, such as COMSOL, the convergence is usually only $1/k_{\max}$, similar to when the TM modes of the sphere are perturbed to that of a smaller sphere [32]. As discussed in Sec. 1.2.3 and Sec. 3.3.1, it was shown in Ref. [85] that the slow convergence of TM modes in case of the size perturbation of a spherically symmetric resonators was due to a δ function in the GD being expanded into a set of static modes. The expansion is a poor, slowly converging representation of the δ function, which then impacts the performance of the RSE. Extracting the delta function from the static pole residue, and expanding only the remainder of the residue into static-like modes resulted in significant improvement in performance and a $1/k_{\max}^3$ convergence rate. In this chapter we will test if the new formalism improves the performance of the RSE when the perturbation is not spherically symmetric anymore, and the modes of different l, m, and polarisations are mixed.

For the purpose of testing we will limit the perturbed system to be axially symmetric. This has the benefit that, by assuming a rotational symmetry along the polar axis, the vol-

ume integral in $V_{\nu\nu'}$ (Eq. (1.46)) can be reduced to a 2D surface integral, as the integral along the azimuthal angle can be calculated analytically. Furthermore, modes with different m are not all mixed together, allowing the factorisation of the problem into smaller matricies [63]. Rotationally symmetric systems can describe cylindrical resonators [17,34,56,151] or rods [148,149], but also ellipsoids [51], spherical dimers [152], cylindrical or rod dimers if they are aligned at the rotational-symmetry axis [40]. These systems can give rise to interesting physical phenomena, such as dielectric cylinders supporting supercavity modes [153], which are analogues to bound-states in the continuum [154]. Such modes have recently been experimentally observed in a high permittivity dielectric cylinder [155]. The utilisation of supercavity modes can lead to efficient second-harmonic generation [55], and semiconductor lasers with very small size-to-wavelength ratios [156].

It is important to note that, as previously discussed in Sec. 1.1.5, one can use fully numerical methods to calculate the eigenmodes, but the existing perturbation methods only treat first and second order corrections to the wavenumber, except for the RSE, which can treat perturbations of arbitrary strength.

In Sec. 5.2 we calculate the RSE matrix elements in case of an arbitrary shape perturbation. In Sec. 5.3 we apply the RSE to a perturbation that deforms a spherical resonator to a cylindrical one, and investigate the convergence of the modes.

5.2 Matrix elements of the RSE

In Ref. [85], and in Sec. 3.3.1 of Chap. 3, the matrix elements $\tilde{V}_{\nu\nu'}$ were given in case of a spherically symmetric perturbation. Here we give the matrix elements under an arbitrary perturbation. For simplicity we consider only permittivity perturbations. This allows us to use only the electric part $\mathbf{G}^{\mathrm{EE}}$ of the 6×6 GD (Eq. (1.21)). Using Eq. (1.22) and Eq. (1.50), in spherical coordinates we can write $\mathbf{G}^{\mathrm{EE}}$ of the unperturbed spherically symmetric basis system as

$$\mathbf{G}(\mathbf{r},\mathbf{r}') = \sum_n \frac{\mathbf{E}_n(\mathbf{r})\otimes\mathbf{E}_n(\mathbf{r}')}{k-k_n} + \frac{\delta(\mathbf{r}-\mathbf{r}')}{k\varepsilon(r)}\hat{\boldsymbol{r}}\otimes\hat{\boldsymbol{r}} + \sum_j \frac{\mathbf{E}_j(\mathbf{r})\otimes\mathbf{E}_j(\mathbf{r}')}{k}\,. \tag{5.1}$$

Then, as described in Ref. [85], we introduce an isotropic perturbation $\Delta\varepsilon(\mathbf{r})$ to the basis system, integrate out the delta function, collect terms, expand the perturbed eigenmodes into the unperturbed eigenmodes, which then leads to the matrix elements

$$V_{\nu\nu'} = \int \mathbf{E}_\nu(\mathbf{r})\cdot\Delta\mathbf{P}(\mathbf{r})\mathbf{E}_{\nu'}(\mathbf{r})\mathrm{d}V\,, \tag{5.2}$$

where

$$\Delta\mathbf{P}(\mathbf{r}) = \begin{pmatrix} \Delta\varepsilon(\mathbf{r}) & 0 & 0 \\ 0 & \Delta\varepsilon(\mathbf{r}) & 0 \\ 0 & 0 & \frac{\varepsilon(r)\Delta\varepsilon(\mathbf{r})}{\varepsilon(r)+\Delta\varepsilon(\mathbf{r})} \end{pmatrix}. \tag{5.3}$$

Here $\varepsilon(r)\Delta\varepsilon(\mathbf{r})/(\varepsilon(r)+\Delta\varepsilon(\mathbf{r}))$ is at the position of the $\hat{\boldsymbol{r}}\otimes\hat{\boldsymbol{r}}$ dyad, and $\varepsilon(r)$ is the permittivity of the spherically symmetric basis system. In spherical coordinates we can write this as

$$V_{\nu\nu'} = \int \left[E_{\nu}^{\hat{\boldsymbol{\phi}}}(\mathbf{r})\Delta\varepsilon(\mathbf{r})E_{\nu'}^{\hat{\boldsymbol{\phi}}}(\mathbf{r}) + E_{\nu}^{\hat{\boldsymbol{\theta}}}(\mathbf{r})\Delta\varepsilon(\mathbf{r})E_{\nu'}^{\hat{\boldsymbol{\theta}}}(\mathbf{r}) + E_{\nu}^{\hat{\mathbf{r}}}(\mathbf{r})\frac{\varepsilon(r)\Delta\varepsilon(\mathbf{r})}{\varepsilon(r)+\Delta\varepsilon(\mathbf{r})}E_{\nu'}^{\hat{\mathbf{r}}} \right] \mathrm{d}V \tag{5.4}$$

where the superscript denote respective component of the field, see Ref. [63] for representation of the eigenmodes in spherical coordinates. In vector spherical harmonic (VSH) basis we can write this as

$$\begin{aligned} V_{\nu\nu'} = &\int E_{1lm\nu}(r)E_{1l'm'\nu'}(r)\Delta\varepsilon(\mathbf{r})\hat{\boldsymbol{Y}}_{1lm}(\Omega)\cdot\hat{\boldsymbol{Y}}_{1l'm'}(\Omega)\mathrm{d}V \\ &+ \int E_{2lm\nu}(r)E_{2l'm'\nu'}(r)\Delta\varepsilon(\mathbf{r})\hat{\boldsymbol{Y}}_{2lm}(\Omega)\cdot\hat{\boldsymbol{Y}}_{2l'm'}(\Omega)\mathrm{d}V \\ &+ \int E_{3lm\nu}(r)E_{3l'm'\nu'}\frac{\varepsilon(r)\Delta\varepsilon(\mathbf{r})}{\Delta\varepsilon(\mathbf{r})+\varepsilon(r)}\hat{\boldsymbol{Y}}_{3lm}(\Omega)\cdot\hat{\boldsymbol{Y}}_{3l'm'}(\Omega)\mathrm{d}V\,. \\ &+ \int E_{1lm\nu}(r)E_{2l'm'\nu'}(r)\Delta\varepsilon(\mathbf{r})\hat{\boldsymbol{Y}}_{1lm}(\Omega)\cdot\hat{\boldsymbol{Y}}_{2l'm'}(\Omega)\mathrm{d}V \\ &+ \int E_{2lm\nu}(r)E_{1l'm'\nu'}(r)\Delta\varepsilon(\mathbf{r})\hat{\boldsymbol{Y}}_{2lm}(\Omega)\cdot\hat{\boldsymbol{Y}}_{1l'm'}(\Omega)\mathrm{d}V \end{aligned} \tag{5.5}$$

Here $E_{ilm\nu}(r)$ is the radial component of the basis field, and in terms of the notation in Sec. 3.3.1 of Chap. 3 TE modes are $E_{1lm\nu}(r) = \mathcal{E}_{\nu}(r)/r$, and TM modes are $E_{2lm\nu}(r) = \mathcal{E}^{t}_{\nu}(r)/r$, $E_{3lm\nu} = \mathcal{E}^{r}_{\nu}(r)/r$. Under a non-spherically symmetric perturbation the modes with different l and m can mix, therefore in this section we keep these subscripts alongside ν, as opposed to the spherically symmetric systems in Chap. 3 where they were dropped. The VSH basis vectors $\hat{\boldsymbol{Y}}$ are defined in Appendix D.1, and note that $\hat{\boldsymbol{Y}}_{1lm}(\Omega)\cdot\hat{\boldsymbol{Y}}_{3l'm'} = 0$ and $\hat{\boldsymbol{Y}}_{2lm}(\Omega)\cdot\hat{\boldsymbol{Y}}_{3l'm'} = 0$, therefore such terms do not appear above. The last two terms in Eq. (5.5) make it possible for TE and TM modes to mix, as the former polarisation only has E_1 non-zero, while the latter has E_2 and E_3 as non-zero. So far, the matrix elements are valid for arbitrary isotropic perturbations without any symmetry. Generally the volume integrals need to be evaluated numerically, which can be computationally expensive. If the permittivity can be factorised as $\Delta\varepsilon(\mathbf{r}) = f(r)g(\phi)h(\theta)$, then we can separate the integrals along each variable, significantly reducing the computational time needed. When the perturbation is spherically symmetric due to the orthogonality of the VSH basis vectors under integration (see Eq. (D.12) in Appendix D.1) the modes of different l and m do not mix anymore and $V_{\nu\nu'}$ reduces to a line integral, as in Ref. [85] or Sec. 3.3.1 of Chap. 3.

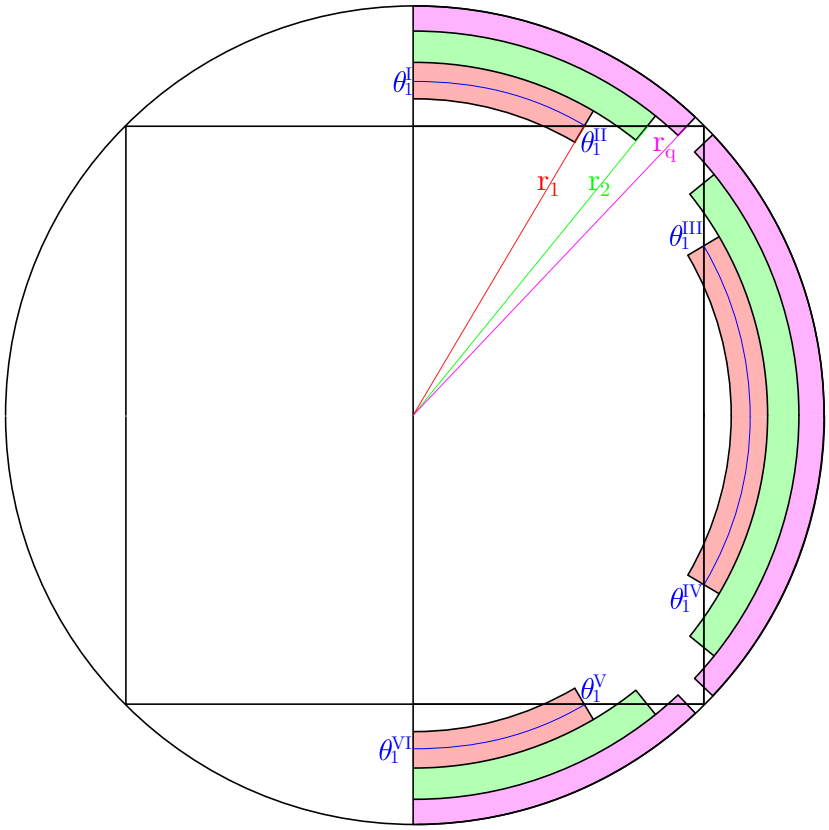

Fig. 5.2.1: Illustration of the discretisation and factorisation of the 2D integral along the radial and angular direction. For example, for radius r_1 we obtain limits for the intervals of the integral as: from θ_1^I to θ_1^{II}, from $\theta_1^I II$ to θ_1^{IV}, and from θ_1^V to θ_1^{VI}.

Let us restrict our attention to rotational symmetry along the azimuthal angle, so $\Delta\varepsilon(\mathbf{r}) = \Delta\varepsilon(r,\theta)$. As shown in Appendix D.2, this will provide selection rules for the polarisation and m. Specifically, TE modes with magnetic quantum number m will only mix with other TE modes of the same m, and with TM modes of $-m$. Similarly, TM modes with m mix with TM modes of m and TE modes with $-m$. In practice this means that we can solve the RSE equation for each magnetic quantum number $|m|$ and polarisation pair separately. Furthermore, solving the azimuthal integral analytically reduces the volume integral to a surface integral, which is much faster to calculate numerically. Modes with different l will generally mix, though symmetry along the polar angle can provide further selection rules for l (see Appendix D.2.1 for an example), simplifying the calculation.

Computationally we can further optimise the calculation by considering the integral along the polar angle, and performing a shell integrations, as in Ref. [32]. If the limits of the integral depend on r, such as would be the case for perturbing a sphere to a cylinder, then $\Delta\varepsilon(r,\theta)$ can not be factorised further into $f(r)g(\theta)$ form. However, at a certain radius $r = r_q$, where q

labels a set of radial points inside the resonator, we have a number s of fixed θ_q^s integral limits and we can evaluate the polar integral. This is illustrated on Fig. 5.2.1 for a case when a sphere is perturbed into a cylinder, which will be the example taken in the next section. The more slices along r we take, the more accurately the shape of the object will be reproduced. By evaluating the polar integral at several radial points r_q, we in practice sample at discrete points in r space the function

$$[\Delta P(r)]_{ilm}^{i'l'm'} = \int \hat{\boldsymbol{Y}}_{ilm}(\Omega) \cdot \Delta\mathbf{P}(\mathbf{r})\hat{\boldsymbol{Y}}_{i'l'm'}(\Omega)\mathrm{d}\Omega\,. \tag{5.6}$$

For further details on how to evaluate the integral see Appendix D.2. For a spherically symmetric $\Delta\mathbf{P}(\mathbf{r})$ the above expression can be evaluated analytically and it simplifies to the orthogonality of the VSHs, see Eq. (D.12) in Appendix D.1. Using Eq. (5.6) in Eq. (5.2) simply means doing the angular integrals first, for each radial distance r_q, leaving only the line integral

$$V_{\nu\nu'} = \int_0^R \sum_{i,i'} E_{ilm\nu}(r)[\Delta P(r)]_{ilm}^{i'l'm'} E_{i'l'm'\nu'}(r) r^2 \mathrm{d}r \tag{5.7}$$

to be evaluate, which is even quicker computationally than the surface integral mentioned in the previous paragraph.

In this section we use the ML4 version of the RSE (see Sec. 3.3.1 of Chap. 3 for the details of this version).

5.3 Sphere to cylinder perturbations

We perturb a sphere to a cylinder. We take the same cylinder as in Ref. [32,43], with permittivity $\varepsilon_\mathrm{r} = 9$, height $2h$ and diameter $2a$, both equal to $a = h = 2R/\sqrt{2}$. In the 2D projection onto the polar axis the cylinder will be a square, see Fig. 5.2.1, and the equation defining the boundary of the square $r_s(\theta)$ in polar coordinates is $r_s = a/\left(|\cos(\theta) - \sin(\theta)| + |\cos(\theta) + \sin(\theta)|\right)$.

For a cylindrically symmetric perturbations the number of modes in the basis are no longer $N \propto k_\mathrm{max}$, instead they are $N \propto k_\mathrm{max}^2$. This is due to the modes of different l coupling to each other by the perturbation.

On Fig. 5.3.1 we show how the eigenvalues evolve in the complex k plane under a permittivity perturbation. $\Delta\varepsilon = 0$ corresponds to a homogeneous sphere of $\varepsilon_r = 9$, $\Delta\varepsilon = -8$ corresponds to a cylinder. For $\Delta\varepsilon$ values in between these the structure is a cylinder of permittivity $\varepsilon_r = 9$, and a shell of permittivity $\varepsilon_\mathrm{shell} = 9 + \Delta\varepsilon$ extending up to the surface of the basis sphere. Generally, breaking the spherically symmetry, and lowering the permittivity

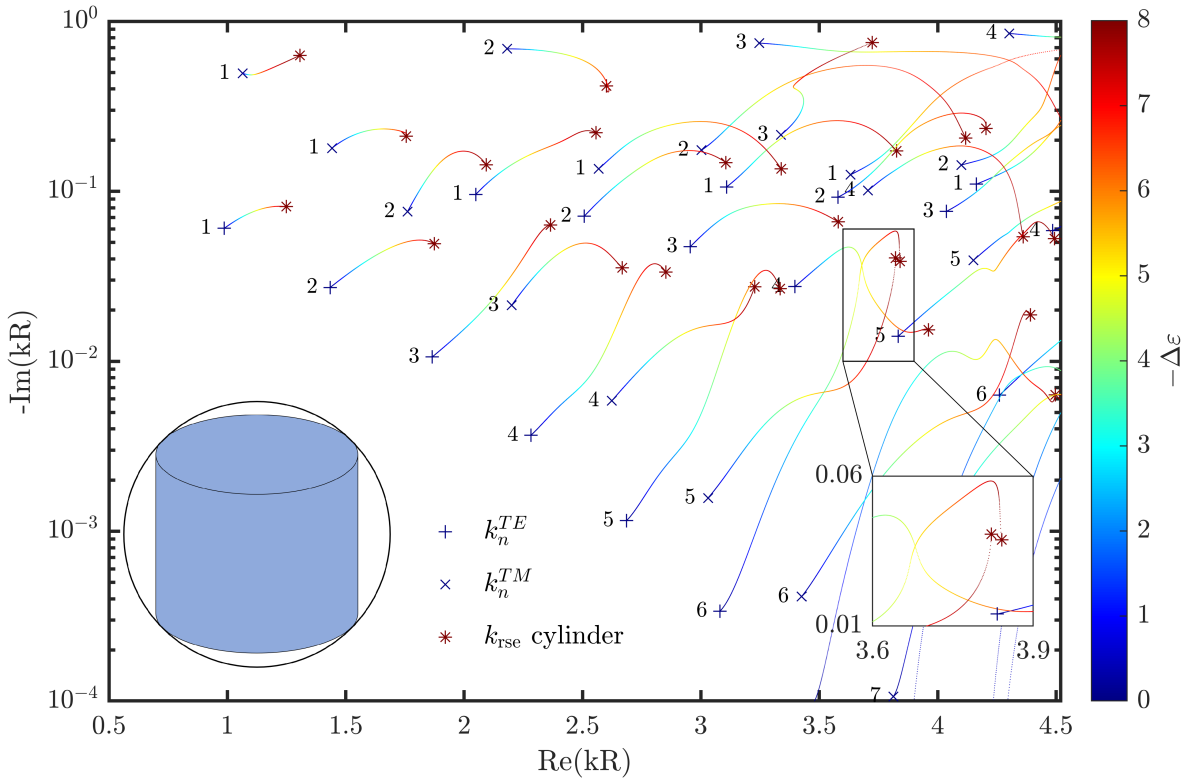

Fig. 5.3.1: Evolution of RS when a sphere is perturbed to a cylinder, for $m_{\text{TE}} = 1$, $m_{\text{TM}} = -m_{\text{TE}}$. The numbers show l of the unperturbed modes, marked with + and x. After perturbation each RS is a combination of different l, polarisation and corresponding m. Modes of a cylinder in vacuum are marked with $*$. Leaky modes, which have $\text{Im}\,(k_n a) < -1$ are outside of the displayed range. Results of the RSE using $k_{\max} R = 10$.

of the outside shell reduces the quality of the modes, and causes a shift to higher frequencies. Qualitatively this is consistent with observation of how the size and permittivity change modifies the modes of a sphere (see Fig. 3.3.1 and Fig. 3.3.2 in Chap. 3), namely, reduction of the size of the resonator, or reduction of its permittivity both reduce the quality of the modes and shift them to higher frequency. One could consider the perturbation acting as a scatterer, which also changes the modes of a spherical resonator in a similar fashion. Note the tightly packed modes around $kR = 3.84 - 0.04i$, which maybe candidates for supercavity modes [153] or exceptional points [157] if further perturbation of the cylinder is performed, such as changing its hight to diamater ratio, or its permittivity. It is important to re-iterate that after perturbation, each of the modes is a combination of different basis polarisations, ls, and m_{TE} and m_{TM}.

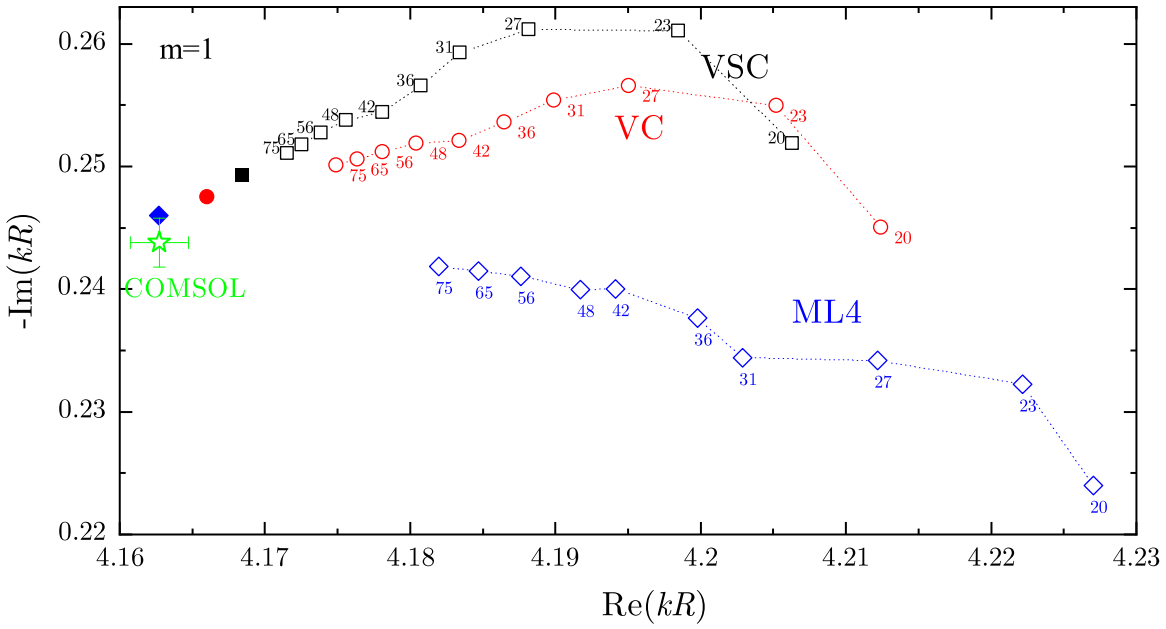

Fig. 5.3.2: Convergence of one selected RSE mode for various $k_{\max}$ values, when a sphere is perturbed into a cylinder. The label shows $\sqrt{\varepsilon_s}k_{\max}R$, with $\sqrt{\varepsilon_s}=3$. The COMSOL mode, which includes approximate error bars, and the VC and VSC RSE modes are from [32]. Solid markers are extrapolated values.

5.3.1 Convergence rate of modes

To test the convergence rate of the ML4 version of the RSE under a cylindrical perturbation we take a range of $k_{\max}$ values and we investigate how the results converge to the eigenvalue that was calculated with COMSOL in Ref. [43]. The results are shown on Figure 5.3.2. When compared against the COMSOL result the RSE wavenumbers converge only at a rate of $1/k_{\max}$. For reference, we plotted the results from Ref. [32], which are labelled VSC and VC, which are two different static mode sets, and are based on the slowly converging expansion of the static pole residue (Eq. (1.22)). These shows a similar rate of convergence as ML4, albite the error is approximately a factor of 2 smaller. This may be due to that the integral $V_{\nu\nu'}$ was calculated using a different numerical method, or due to the difference in the static modes sets. Interestingly however, when using the extrapolation, which provides an estimate for the final convergence point of the mode based on at least three RSE calculation with different basis sizes [101], the final error in the mode is smaller for ML4.

5.3.2 Influence of static modes

Previously in Ref. [32] the slow convergence of TM modes of a sphere under size perturbation was due to the influence of the static modes, and the expansion of the δ function into a

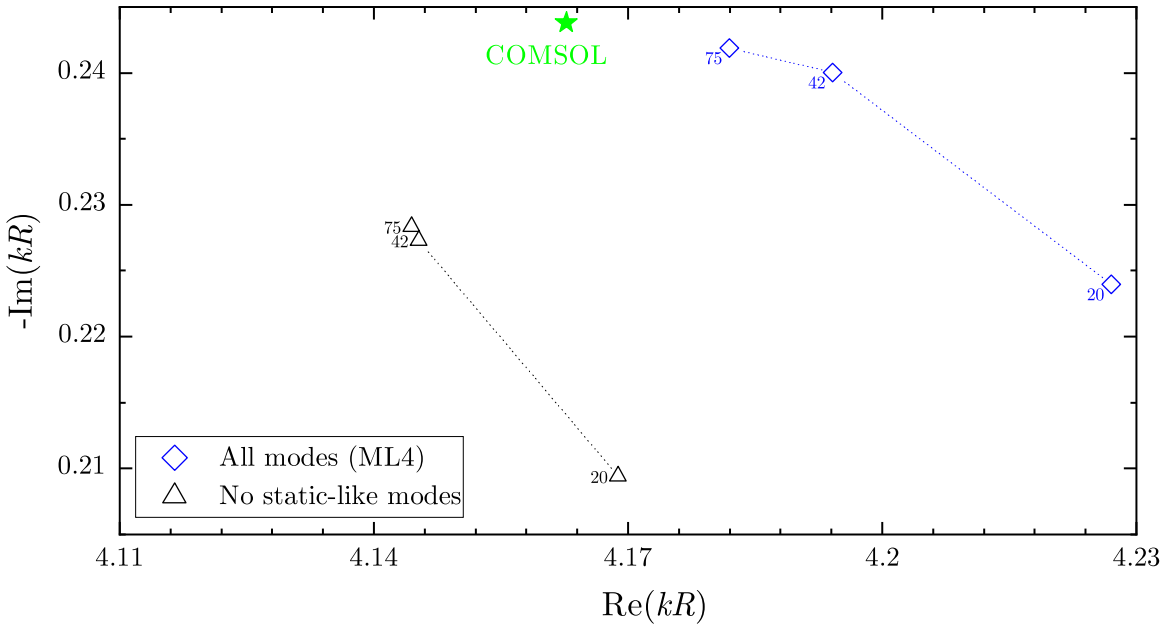

Fig. 5.3.3: As Fig. 5.3.2, but not including static-like modes in the RSE basis.

summation form [85]. To rule a possible problem coming from the representation of the static pole we evaluate the RSE for a cylindrical perturbation using the ML4 formalism, but using RSs only ($k_\nu \neq 0$), i.e. not including the static-like modes. That is, we take $\overline{V}_{nn'} = V_{nn'}$ in Eq. (1.48). The results are shown on Fig. 5.3.3. From the decrease of the step size between the different $k_{\max}$ we can see the convergence rate is improving significantly to approximately $1/k_{\max}^3$. However, the results converge to the wrong values. This confirms that the representation of the static pole, its expansion into the static-like modes is responsible for the slow convergence in Fig. 5.3.2.

To better understand the reason for this we consider now the exact form of the static pole residue of $\mathbf{G}^{\mathrm{EE}}$. For simplicity, we will focus on the $\hat{\boldsymbol{Y}}_{3lm} \otimes \hat{\boldsymbol{Y}}_{3lm} = Y_{lm} Y_{lm} \hat{\boldsymbol{r}} \otimes \hat{\boldsymbol{r}}$ dyad. In VSH representation, for a homogeneous sphere as a basis, it has the form [85]

$$R_{33} = R_{33}^R + R_{33}^S \,, \tag{5.8}$$

where

$$R_{33}^S = \frac{1}{\varepsilon(r)} \delta(r - r') \,, \tag{5.9}$$

$$R_{33}^R = -\alpha^2 \frac{l}{l+1} c_1 \xi(r) \xi(r') + \alpha^2 c_2 \xi(r_<) \eta(r_>) \,, \tag{5.10}$$

and

$$c_1 = -\frac{1}{2l+1}\frac{1}{\varepsilon(r)R}\frac{(\mu-1)(l+1)}{\varepsilon(r)l+l+1}\,, \tag{5.11}$$

$$c_2 = -\frac{1}{2l+1}\frac{1}{\varepsilon(r)R}\,, \tag{5.12}$$

$$\xi(r) = \left(\frac{r}{R}\right)^l\,, \tag{5.13}$$

$$\eta = \left(\frac{R}{r}\right)^{(l+1)}\,. \tag{5.14}$$

The term R_{33}^S has the delta-like singularity, and R_{33}^R is a regular term. Keeping R_{33}^S as it is, and expanding R_{33}^R into static-like modes (Eq. (1.50)) led to the improved performance of the RSE in Ref. [85] for spherically symmetric perturbations. Let us write the regular part as

$$R_{33}^R = A + B\,, \tag{5.15}$$

where

$$\begin{aligned} A &= \left(l(l+1)\frac{l}{l+1}\right)\left(\frac{1}{2l+1}\frac{1}{\varepsilon(r)R}\frac{(\varepsilon(r)-1)(l+1)}{\varepsilon(r)l+l+1}\right)\left(\frac{rr'}{R^2}\right)^l \\ &= \frac{(\varepsilon(r)-1)(l^3+l^2)}{\varepsilon(r)R(2l^2(\varepsilon(r)+1)+(\varepsilon(r)+3)l+1)}\left(\frac{rr'}{R^2}\right)^l\,, \end{aligned} \tag{5.16}$$

$$\begin{aligned} B &= -l(l+1)\frac{1}{2l+1}\frac{1}{\varepsilon(r)R}\left(\frac{r_<}{R}\right)\left(\frac{R}{r_>}\right)^{l+1} \\ &= -\frac{l(l+1)}{(2l+1)\varepsilon(r)}\left(\frac{r_<}{r_>}\right)^l\frac{1}{r_>}\,. \end{aligned} \tag{5.17}$$

We note that for a homogeneous sphere A is already in the symmetric form $f(r)\otimes f(r')$ which would be convenient to used in the eigenfunction expansion of the GF, however B can not be factorised in such way, and therefore needs to be represented by a summation of a large number of modes, which can impact the performance of the RSE. For large l Eq. (5.16) and Eq. (5.17) are $A_l \propto l(rr'/R^2)^l$ and $B_l \propto l(r_</r_>)^l$. To further simplify the calculation we take $\theta = \theta' = 0$, which means that the Associated Legendre polynomials P in the spherical harmonics (see Eq. (D.2) of Appendix D.1) will be zero unless $m = 0$, in which case $P = 1$. For $m = 0$ the azimuthal function is $\chi_0(\phi) = 1/\sqrt{2\pi}$, the normalisation of the VSH is $\sqrt{l}$, therefore the total (summed over l and m) regular part of the GD of a spherically symmetric system is

$$\sum_{lm} R_{33}^R Y_{lm} Y_{lm} = \sum_l lA_l + lB_l\,, \tag{5.18}$$

$$\tag{5.19}$$

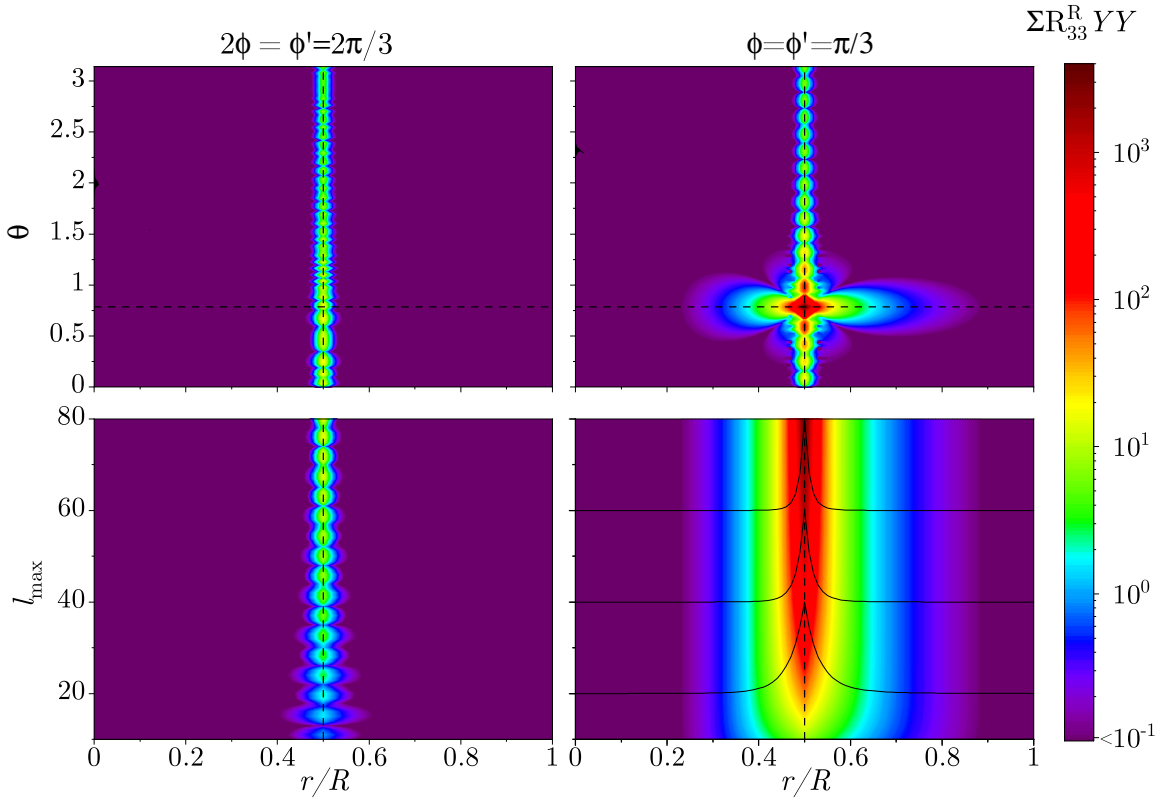

Fig. 5.3.4: Divergence of the static pole $\sum_{lm}^{l_{\max}} R^R_{33} Y_{lm} Y_{lm}$ with $l_{\max}$. Horizontal (vertical) dashed line shows the value of θ' (r'). Top row: $l_{\max} = 40$. Bottom: $\theta = \theta' = \pi/4$. Solid lines on the bottom right show the normalised values at $l_{\max} = 20, 40, 60$.

and in the large l limit

$$\sum_l l A_l \sim \sum_l l^2 \left(\frac{r r'}{R^2}\right)^l , \tag{5.20}$$

$$\sum_l l B_l \sim \sum_l l^2 \left(\frac{r_<}{r_>}\right)^l . \tag{5.21}$$

From the convergence test, which states that the series u with k-th element u_k converges, if $\lim_{k\to\infty} |u_k|^{1/k} = q$ and $q < 1$ [158], we can see that $\sum_l l A_l$ diverges if $r = r' = R$, and $\sum_l l B_l$ diverges if $r = r'$. However, these terms are not $\delta(r - r')$-like divergences, as for $r \neq r'$ the sums do not go to zero.

On Fig. 5.3.4 we plot the value of $\sum_{lm}^{l_{\max}} R^R_{33} Y_{lm} Y_{lm}$ for a combination of different spacial coordinates and $l_{\max}$ to illustrate the divergence of the summation more generally and accurately. On the top left, for $l_{\max} = 40$ and $\phi \neq \phi'$, we can see that the value diverges in case $r = r'$. There is an oscillation along the polar angle which is expected due to the angular distribution. In the region of $\theta \approx \theta'$ the divergence is stronger. On the top right, for $l_{\max} = 40$ and $\phi = \phi'$ we can see the same behaviour, but the diver-

gence now is much stronger. The features resemble the spherical harmonics closure relation $\sum_{l=0}^{\infty}\sum_{m=-l}^{l} Y_{lm}(\theta,\phi)Y_{lm}(\theta',\phi') = \delta(\cos\theta - \cos\theta')\delta(\phi-\phi')$, but the δ singularity is now spread out over a region, not only because of the finite sum, but also because of the additional coefficient R_{33}^{R} in the sum. On the bottom of the figure we show how the term diverges when we increase the limit of the summation l_{max}, while $\theta = \theta'$. On the bottom left, for $\phi \neq \phi'$, the term diverges as we increase $l_{\max}$, but retains an oscillatory behaviour now with respect to $l_{\max}$. On the bottom right, for $\phi = \phi'$, the divergence is much quicker and seemingly without oscillation. It also shows that for $r \neq r'$ the sum tends to a finite non-zero value. The lines show the normalised value of the sum for a fixed $l_{\max}$. As we increase $l_{\max}$ the lines get sharper, which also illustrates the divergent nature.

To verify that this additional divergence, with respect to l_{max}, and its expansion into static modes has an impact on the convergence, we evaluate the RSE for a cylindrical perturbation using the ML4 formalism, but limit the maximum l for which modes (static and RS) are included in the basis. The results are shown on Fig. 5.3.5 for $l_{max} = 5$. From the decrease of the step size between the different $k_{\max}$ we can again see the convergence rate is improving. However the results once again converge to the wrong value, which is also expected as not all theoretically contributing modes are taken into account in practice. Interestingly, while static modes are included, for the particular mode (at $k = 4.16 - 0.24i$) limiting $l_{max} = 5$ creates a larger error for the maximum basis size used, compared to when there was no limit on l, but static modes were not included. This can be understood from the first-order results which showed that static mode influence is decreasing with increasing k, while the influence of neighbouring modes, with $k_n \neq 0$ and $l > 5$ could be more important. These results provide further confirmation that the summation representation of the divergence of the static pole, with increasing $l_{\max}$, is responsible for the slow convergence of the ML4 version of the RSE under non-spherically symmetric perturbation.

5.4 Conclusion

We calculated the modes of a cylinder structure by perturbing the permittivity of a homogeneous sphere. As the permittivity of the sphere is changed inhomogeneously, generally, the modes shift to higher frequency and their Q-factor reduces.

We tested the ML4 representation of the GD in the RSE in case of a cylindrically symmetric perturbation. We found that it produces a similar slow, $1/k_{\max}$ convergence rate as the full expansion of the static pole in ML1 (Eq. (1.22)). This is despite that for spherically

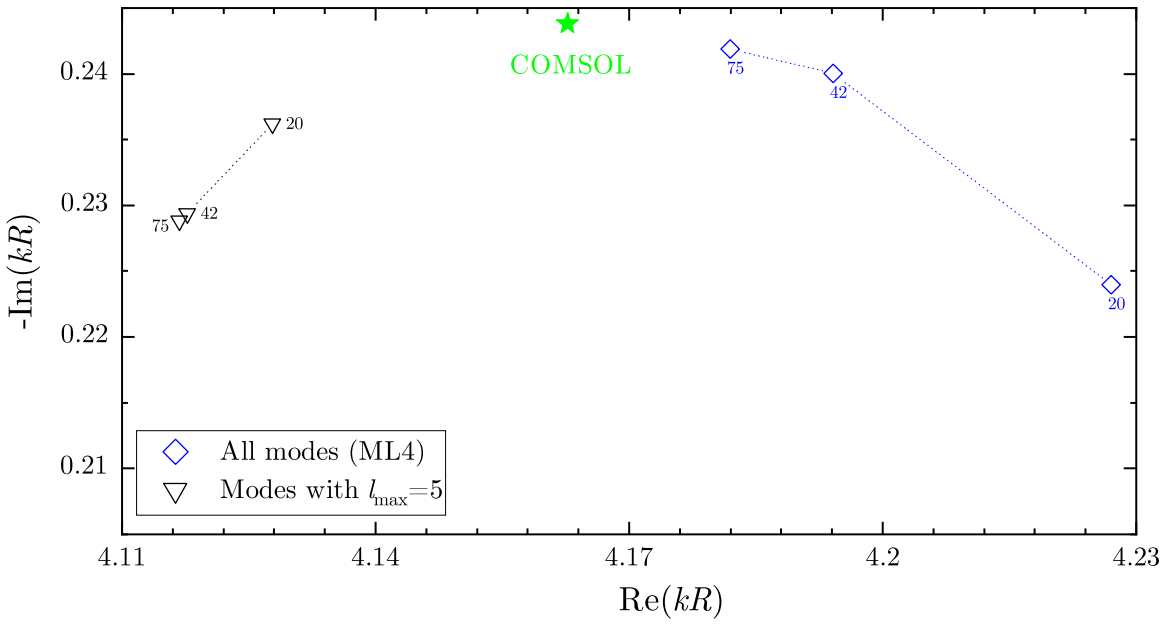

Fig. 5.3.5: As Fig. 5.3.2, but also for a calculation with only $l_{\max} = 5$ modes in the basis. For blue diamond all modes within $k_{\max}$ are taken, regardless of their angular momentum number.

symmetric perturbation ML4 was showing a $1/k_{\max}^3$ convergence rate. By considering the exact static pole residue we showed that there can be additional divergent terms alongside the δ function in ML4, which appear when the full GD is used, that is, when modes of different l and m are coupled. As previously seen for the δ function, this additional divergent term can also cause slow convergence of the error, as it is poorly represented in terms of the continuous and smooth (except at the basis surface) static modes.

To avoid the poor representation of the divergence one can consider an optimised set of static modes, where one static modes has surface charges on the perturbed and one on the unperturbed surface, similarly to the method in [159]. Alternatively, for an isotropic perturbation, one could directly fit R_{33}^R with a function of the form $f(r)f(r')$. Other required dyadic components of the static pole residue can be found from R_{33}^R [85]. This would in practice reduce the number of static modes needed to two per l. One could also consider continuously perturbing the sphere along the vector field $\hat{\boldsymbol{n}}$, which was introduced for the first-order results in Chap. 4 and it is normal to both the unpertrubed and the perturbed surface. This would mean treating the parallel and tangental component of the electric field separately in the RSE. Beyond first-order however all RSs will contribute to the perturbation.

Important to note that the observed divergence only happens when the different ls are no longer independent. So while it affects general shape perturbations of arbitrary perturbation order, it does not affect the first-order perturbation results or spherically symmetric results.

6

Scattering

6.1 Introduction

Cross-section measurements in conjunction with simulations are an important sensing and characterisation method in optics. The optical cross-section spectrum of an object is determined by its morphology, its material, and the surrounding medium [24]. If three of the four quantities are know, the fourth can be inferred. For example, if one knows the shape and material of a resonator, and measures the cross-section, one can infer properties of the surrounding medium, which is of particular interest in biosensing, providing a label free detection method capable of sensing single molecules based on the spectral shift [49]. Alternatively, if the medium and the resonator material are know, the shape of the resonator can be found, thereby providing a cheap and non-invasive alternative method to electron tomography measurements [149]. If the shape and the medium is know, the material of the particle can be measured optically, which, for example, provides a simple method to measure permittivity [160]. These methods rely on measuring the cross-section experimentally, and then comparing it with simulated data covering a large parameter range, and finding a fit. By conducting such a study we recently detected optically a tarnish layer, which was only a few atomic layer thick, on silver nanocubes [150] and nanodecahedra [161]. In these studies I conducted scattering and absorption cross-section simulations using COMSOL, a commercially available numerical solver using FEM [162].

The correct determination of the aforementioned properties require knowing the quantitative cross-section spectrum with exact amplitudes, as opposed to qualitative spectrum which only give the position and lineshape of the resonance. The former can be particularly expensive computationally when a range of illumination and detection angles need to be taken into account [148], while the latter can be quicker as often only a specific coherent illumination, such as a normal incidence incoming wave, is considered [163]. The cross-section

of homogeneous spheres can be analytically calculated, and this is often referred to as Mie scattering [164]. For some other shapes, or certain illumination cases, approximate solutions are available, such as scattering from small particles (compared to the wavelength) [165]. Generally however, for arbitrary shapes and excitations, numerical methods are used for calculation, such as DDA [166], FEM [150], FDTD [167]. These rely on calculating the field in the entire simulation domain which usually consists of the particle, the surrounding medium, and a PML layer. While these are well established and reliable methods, computationally they can be slow, especially if high resolution spectra are needed. An alternative approach that emerged in the last decade is based on the eigenmodes of a resonator, as detailed in the next section. The benefit of this approach is that once the eigenmodes are know, usually it is fast to calculate the response of the system under excitation, particularly if the response is dominated by very few modes, which is often the case in plasmonics.

This chapter is organised as follows. In Sec. 6.2 we review various methods in literature that use RSs to calculate cross-section, and in Sec. 6.3 we review in more detail the formalism of Ref. [38] which we will use for the scattering cross-section calculation in this chapter. In relation to this, in Appendix E.2 we also investigate the validity of sum rules in a spherical system, just as we did for a planar system in Chap. 2. In Sec. 6.4 we consider a case of size perturbation of a sphere and illustrate that the modes generates via the RSE are complete on the surface of the unperturbed sphere, similarly to what we saw in case of a slab in Chap. 2. Finally in Sec. 6.5 we apply the method to a scattering calculation of a non-spherical case, specifically to the cylinder studied in Chap. 5.

6.2 Review of resonance based methods

We review some of the main scattering (and absorption) calculation methods in recent literature that are based on RSs, QNMs, or similar approaches. We will progress in approximately chronological order of publication dates, as some of the papers build on each other and are cross referenced.

Ref. [168] develops a temporal coupled-mode theory based scattering calculation, which expresses the scattering matrix as a sum of a background, or non-resonant term, and a single resonant term, thus using a single mode limit. The method is applied to a 2D scatterer that is not cylindrically symmetric, with the assumption that it is small compared to the incoming wavelength, so that for the background term an identity matrix can be used, further simplifying the calculation. The material permittivity is given by the Drude model, and

calculations are made with and without damping. The results show approximate agreement with FEM calculations. Ref. [169] uses the Lippman-Schwinger integral equation and the background GF (GF of infinite homogeneous media) to find a matrix equation, similarly to the methods used to find the RSE equation in Sec. 1.2.3, but here the matrix equation is solved directly for the scattered field coefficients, which is expanded into spherical wave functions in each scatterer. The authors of Ref. [169] do not use an eigenmode expansion into RSs, therefore we can assume there is no contribution from static modes to the scattering. Results, which are obtained for spherical dimer scatterers, are compared to a dipole approximation of the individual scatterers. The authors note that the approximation has only limited accuracy. Ref. [40] develops a formula for the decay rate of an emitter, with a similar matrix method to Ref. [169], except the expansion of the emitted field is using QNMs, but the non-resonant background term is again assumed to be negligible. The method is tested on a gold nanorod, with permittivity given by the Drude model, in the single mode limit, assuming a dipole-like emission. The decay rate shows good agreement with results from FMM. It is also tested on a pair of nanorods using two modes, showing good agreement with FMM. However the contribution of the two modes to the decay rate are seemingly taken individually, so in terms of the full 2×2 matrix equation only the diagonal elements are kept. Ref. [17] extends on the work of Ref. [40], deriving a full expression for the cross-section in terms of QNMs. The background term and the static modes, the non-resonant contributions, are again neglected. The method is tested on a gold nanorod in the single mode limit, with both scattering and absorption showing a good agreement with FEM calculations from COMSOL. The expansion coefficients of the scattered field include an integral of the incoming field at the excitation frequency. Ref. [34] provides an improvement of the formulas in Ref. [17] by replacing the normalisation integral of the QNMs, which includes the PML region, with one that can be evaluated only inside the resonator. Ref. [151] develops a scattering calculation method for an open dispersive resonator, by the pole expansion of the impedance matrix. The paper avoids using RSs or QNMs, however it still requires a numerical method to find the poles of the impedance matrix. The peak positions are accurate due to the accurate pole positions, however the scattering amplitude shows a slow convergence with respect to the number of poles in the basis. Ref. [170] develops a QNM expansion of the scattering matrix. The non-resonant terms are found by minimizing a so-called objective function that is related to the QNMs. The method is tested on various photonic crystals where the non-resonant background term is assumed to be an identity matrix. It is unclear how difficult it is to find the non-resonant term in a non-trivial case, or when many QNMs contribute to the objective

function. The method is also tested on a core-shell metal-dielectric sphere. Ref. [36] is an extension of Ref. [17] (and thus Ref. [40]), with slightly different expansion coefficients of the scattered field, which now take into account non-resonant contribution of static and zero permittivity modes. The method is tested on a silver bowtie antenna in homogeneous background, with permittivity given by the Drude model. The authors distinguish between resonant and non-resonant contribution to the cross-section, where presumably the non-resonant contribution is due to zero-permittivity modes, as the PML mode contribution is discussed separately. Another system, a silver bullet on a slab, so a resonator in a non-homogeneous background, is also investigated. It is found that in this case the PML modes are particularly important, as without taking them into account in the calculation the cross-section amplitude is incorrect, though the peak position is determined correctly. This can be understood from that the resonant scattering response is dominated by the modes of the bullet, and knowing those give the correct peak position, but the modes of the bullet alone are not complete over the total system, which includes the slab, therefore, additional modes, the PML modes are required to have the correct expansion of the scattered field. Ref. [171] uses a pole expansion of the scattering matrix in terms of QNMs, and highlights the importance of non-resonant terms when calculating the scattering efficiency of a dielectric resonator. The method relies on finding the residues of the scattering matrix separately, for which a method is not outlined, and hence only an analytically treatable spherical problem is solved. The authors express the outgoing waves in the far-field (FF) in terms of the diverging QNMs, and the divergence of the mode fields outside is treated by considering causality and time dependence [172]. In Ref. [35] the scattering matrix was split into a resonant contribution and a background term. A rigorous form for the background term is not provided. It is suggested that it can be found via the method of [170], or alternatively by fitting, though it is unclear what to fit exactly, it could be the long wavelength limit of the response. The residues of the scattering matrix are clearly defined in terms of overlap integrals of the incoming field and the eigenmodes. Interestingly, in contrast to Ref. [17], here the incoming field is evaluated at eigenmode frequency k_n, and the overlap integral is a surface integral not a volume integral. The method is tested with the use of 300 RSs on a slab at normal incidence, for which the background term can be found analytically. It is also tested with 4 RSs in case of a dielectric grating with the incident field propagating at non-normal incidence, with the background term found by fitting. A test with plasmonic antennas and circularly polarised incident waves is also carried out with the use of 2 RSs and fitting the background. All tests show good agreement with results from FMM. Ref. [38]

gives an explicit formalism which links the GD to the scattering matrix. Non-resonant terms are included in the GD via the static mode contribution and an explicit identity matrix as background term. The method relies on expressing all fields in VSH, and a GD expansion that is complete on a spherical surface including the resonator. This allows a computationally simple treatment of the scattering problem, which could be significantly faster to calculate than the methods which rely on volume overlap integrals between the RSs and the incoming field. Treatment of z (in Cartesian coordinates) propagating excitations waves is presented, but for waves propagating in other direction the formalism needs to be extended. This is the method that we will use in this chapter for scattering calculation and it will be reviewed in more detail in Sec. 6.3. Ref. [44] developed a method based Riesz-projection to calculate the electric field of a resonator excited with a dipole emitter. The total field is expanded into a sum of integrals of the electric field around contours in the complex eigenfrequency plane. Resonant contribution is given by clockwise contour integrals enclosing a RS eigenfrequency, whereas explicit expression for the non-resonant term is given by the anti-clockwise contour integral around the chosen eigenfrequencies and the real excitation frequency of interest. The eigenfrequencies are calculated using a PML to enforce the outgoing waves boundary conditions, which results in the generation of PML modes. However it is possible that their contribution can be neglected as the non-resonant integral term expresses all contributions from non-physical eigenmodes. Ref. [173] considers highly dispersive media, where material properties, such as the permittivity, are given by general non-Hermitian invertible matrices. They expand the scattered field into eigenmodes, obtaining a similar expression to Ref. [17]. The background term is assumed to be zero. The method is tested on a 2D system over a large range of frequency with many modes used in a calcuation, showing a generally good agreement with calculations from another numerical method. The paper itself considers only a closed system, with testing on open systems left for future work. Ref. [95] does a comparative study of the different scattered field expansions from Refs. [36], [173], and [58], the latter one reviewing results from Ref. [17] and Ref. [36] and introducing an additional form of expansion coefficients. The paper also shows how the various forms are linked to each other. The convergence rate of the error, with respect to the number of modes used for expansion of the scattered field, is studied in case of a 2D cylinder and a 3D metallic sphere, showing that all three expansions converge at identical rates. The paper demonstrates the importance of PML modes for the convergence rate even in case of a homogeneous background. Ref. [174] also compares formulas from Refs. [173] and [40], and similarly to Ref. [95] derives a general formalism from which the previous two individual forms can be extracted. They investigate

the accuracy of the scattered field, and find that issues can occur at frequencies close to the plasmonic branch $\varepsilon(\omega) = -1$, or at the poles of the permittivity, as both of these result in an accumulation of large number of modes in a small area in the complex frequency plane. In addition, at high frequencies accuracy can be limited due to the instability of PML modes. Ref. [99] discusses the differences between expansions for the scattered field based on the GD and its direct ML expansion, showing that when the overlap integrals in the resonant term are independent of the incoming frequency, as in Ref. [35], the formalism leads to a more complicated background term, as opposed to cases when the overlap integral is dependent on the incoming frequency, as in Ref. [17]. The drawback of the latter, frequency dependent form however is that for each frequency the overlap integrals have to be calculated separately, which can be computationally expensive. Ref. [37] investigates the role of static modes in the background term in the scattering formalism of Ref. [17]. It was found that for a homogeneous lossless sphere the static modes do not contribute to the scattering cross-section directly, however static modes are needed for an absorbing sphere. It is noted that in both cases the static modes contribute to the calculation of the total field, which includes the near field where static modes are important, or when a perturbation is done to the system modes, such as in case of the RSE. Ref. [47] rectifies the missing element of Ref. [35] and provides a method to calculate the background term in the pole expansion of the scattering matrix. The role of static modes is not discussed however. The method is tested on chiral systems with up to three modes in the expansion. The authors remark in the conclusion that when a large number of modes are needed the approach might not be efficient. This could be due to the frequency dependent volume integral expressing the residue, which is also remarked as a potential drawback in Ref. [99].

6.3 Formalism

In this chapter we will use the method from Ref. [38], which is based on the RSE, to calculate the cross-section of resonators. We do not replicate the entire formalism of the paper here, but summarise the key elements. The overall steps of the method is as follows: the incoming field, such as a plane wave excitation with wavenumber k, is represented in VSHs, with distinct angular momentum number l', orbital magnetic number m', and polarisation p', which is either TE or TM. Each incoming field component is projected onto a spherical surface enveloping the scatterer, creating a source term for the excitation of the system. The response of the system to the excitation is calculated via the radially dependent part of the

electric GD ($\mathbf{G}^{\mathrm{EE}}$), expressed in VSH for the decoupled equation as (see Appendix E.1)

$$G(r,r';k)^{l'm'p'}_{lmp} = \sum_{\tilde{n}} \frac{\left[\mathbf{E}^{lm}_{\tilde{n}}(\mathbf{r})\right]_p \left[\mathbf{E}^{l'm'}_{\tilde{n}}(\mathbf{r}')\right]_{p'}}{\tilde{k}_{\tilde{n}}(k-\tilde{k}_{\tilde{n}})} + \sum_{\tilde{\lambda}} \frac{\left[\mathbf{E}^{lm}_{\tilde{\lambda}}(\mathbf{r})\right]_p \left[\mathbf{E}^{l'm'}_{\tilde{\lambda}}(\mathbf{r}')\right]_{p'}}{k^2}\,, \tag{6.1}$$

which is evaluated with both spacial coordinates at the surface, so $G^{l'm'p'}_{lmp}(R,R;k)$ is used. We denote with tilde ($\sim$) the modes of the system of interest, which may be expanded into the RSs (with index n) and static modes (with index λ) of a basis system. Note that compared to [85] this GF is divided by k, and the sum rule (Eq. (1.30)) of the eigenmodes was used. The super and subscript of G denote the source (or incoming) channel $l'm'p'$ and the response (or outgoing) channel lmp, respectively, for the excitation wavenumber k, and $\mathbf{E}^{lm}_{\tilde{n}}$ is the lm component in VSH of the eigenmode $\mathbf{E}_{\tilde{n}}$. The outgoing (or scattered) field amplitudes, which are also expressed in VSHs, are found from the scattering matrix, which is expressed in terms of the GF as

$$S^{l'm'p'}_{lmp} = G^{l'm'p'}_{lmp}(R,R;k)\sigma_{l',p'}(k) - \delta_{pp'}\delta_{ll'}\delta_{mm'}\,, \tag{6.2}$$

where δ is the Kronekker delta, and $\sigma_{l',p'}(k)$ is the effective source term evaluated at the frequency of the incoming field, defined as

$$\sigma_{l,\mathrm{TE}}(k) = R\left[\gamma^{-1}_{l,\mathrm{out}}(k) - \gamma^{-1}_{l,\mathrm{in}}(k)\right]\,, \tag{6.3}$$

$$\sigma_{l,\mathrm{TM}}(k) = k^2R^3\left[\gamma_{l,\mathrm{in}}(k) - \gamma_{l,\mathrm{out}}(k)\right]\,. \tag{6.4}$$

Here $\gamma_{l,d}(k) = h_{l,d}(kR)/\xi'_{l,d}(kR)$, where $h_{l,d}(x)$ is the spherical-Hankel function with $d = \mathrm{out}$ denoting the first-kind and $d = \mathrm{in}$ denoting the second-kind, $\xi_{l,d}(x) = xh_{l,d}(x)$, and the prime denotes the derivative with respect to the argument.

From Eq. (6.2) we can identify the Kronekker delta term, and the static pole of the GD as the so called off-resonant contribution to the S-matrix. When the electric GD is represented in VSHs, the polarisation TE (TM) corresponds to $p = 1$ ($p = 2$), and $\mathbf{G}^{\mathrm{EE}}_{pp'}$ denotes the pth row and p' column of the GD. Therefore, the component $\mathbf{G}^{\mathrm{EE}}_{11}$ is a coupling between TE and TE, $\mathbf{G}^{\mathrm{EE}}_{12}$ is a coupling between TE and TM, and $\mathbf{G}^{\mathrm{EE}}_{22}$ is a coupling between TM and TM fields. Importantly, in VSH representation the static modes contribute to $\mathbf{G}^{\mathrm{EE}}_{22}$ [85], therefore, in this formalism they directly contribute to the S-matrix, and later on to the cross-section. This is in contrast with, for example, Ref. [37], where seemingly the static modes did not contribute to the cross-section of a spherically symmetric homogeneous dielectric resonator, though they still contribute in the expansion of the total electric field.

Note that $G^{l'm'p'}_{lmp}(R,R;k)$ is evaluated with both coordinates at the surface of the sphere. Therefore care needs to be taken which ML representation one uses for the resonant part,

the one with (Eq. (1.31)) or the one without (Eq. (1.28)) the application of the sum rule (Eq. (1.30)), as the latter may not necessarily converge to the correct value with both coordinates taken at the surface, as we have seen in 1D in Chap. 2. This is discussed in more detail Appendix E.2, and it is found that only the form $\sum_n \mathbf{E}_n(\mathbf{r}) \otimes \mathbf{E}_n(\mathbf{r}')/(k_n(k-k_n))$ gives the correct resonant part of the GD when both radial coordinates are taken at the surface. The expression $\sum_n \mathbf{E}_n(\mathbf{r}) \otimes \mathbf{E}_n(\mathbf{r}')/(k(k-k_n))$ however does not give the correct value as it uses the sum rule, which is not valid when both radial coordinates are on the surface.

An advantage of this approach is that it directly links the GD, constructed from the eigenmodes of the system, to the scattering matrix. Also, in contrast to other approaches which use an overlap volume integral of the incoming field with the eigenmodes in order to find the residues of the scattering matrix, as is done in Ref. [17] or Ref. [47], such integrals are not present here. Therefore this method is potentially computationally efficient even when large number of modes are needed. We note that it may be possible to reduce the overlap surface integrals in Ref. [35] to a single point evaluation by using a VSH basis and the orthogonality relations of the VSH, therefore improving the computational efficiency of that approach as well.

From the S-matrix we find the plane-wave scattering amplitudes into an outgoing channel lmp by summing over all incoming channels $l'm'p'$ as

$$A^{\text{sca}}_{lmp} = \sum_{l'm'p'} S^{l'm'p'}_{lmp} B^{\text{in}}_{l'm'p'} - B^{\text{out}}_{lmp}\,, \tag{6.5}$$

where $B_{l'm'p'}$ is the expansion coefficient of the electric field, with 'in' and 'out' denoting the incoming and outgoing amplitudes, respectively. From the scattered field amplitude of the outgoing channel l and m one can find the partial cross-section for that channel by summing over the polarisations as $\sigma^{\text{sca}}_{lm} = \sum_p \Gamma_{lmp} \left|A^{\text{sca}}_{lmp}\right|^2$, where Γ_{lmp} is a weight function defined as $\Gamma_{lm,\text{TE}} = |kh_{l,\text{in}}(kR)|^{-2}$ and $\Gamma_{lm,\text{TM}} = k^2R^2|\gamma_{l,\text{out}}|^2\Gamma_{lm,\text{TE}}$. From the partial cross-section we can find the total cross-section σ^{sca} by summing up over all outgoing channels

$$\sigma_{\text{sca}} = \sum_{lmp} \Gamma_{lmp} \left|A^{\text{sca}}_{lmp}\right|^2 . \tag{6.6}$$

What makes most of the calculation analytically treatable, that is, without volume overlap integrals of the incoming and the eigenmode field, are two key elements of the derivation in Ref. [38]: firstly expressing the incoming wave in VSH, and secondly the use of a GD, also expressed in VSH, that is know on a spherical surface around the resonator.

The first requirement gives a simple expression for B for an incoming plane wave propagating along the polar (z) axis, as it described in Ref. [38], and this propagation direction

will be used in this chapter as well. For other propagation direction a modified expression for B needs to be found. Note that when the system is cylindrically symmetric along the polar (z) axis, as all examples will be in this chapter, for a z propagating incoming plane wave it is enough to calculate only the $m = \pm 1$ modes of the resonator. This is because the incoming plane wave contains terms of $m = \pm 1$ modes only, and the GD of the cylindrically symmetric system with this orientation only mixes modes with the same magnitude of $|m|$. Specifically, x (y) polarised incoming light only couples to $m_{\mathrm{TE}} = -1$ and $m_{\mathrm{TM}} = 1$ ($m_{\mathrm{TE}} = 1$ and $m_{\mathrm{TM}} = -1$), so only that set of modes is needed.

The second requirement, for the GD expression, is clearly true if the resonator itself is spherical, as the RSs are complete on the surface. However, it is not necessarily true if the resonator is not spherically symmetric. Generally it is assumed that eigenmodes are complete in the minimal convex volume including the resonator [68]. For example, in case of a cylinder, the true eigenmodes are only complete on the surface of the cylinder, and not on the surface of the smallest sphere fully enveloping it. However, this is not a limitation in practice. As we have demonstrated in Chap. 2 the RSE generates modes that are complete on the original, unperturbed surface, which in case of a 3D system is usually a sphere. Therefore, when the modes are generated with the RSE the formalism outlined above remains valid. Note, that when eigenmodes are calculated via other numerical methods and with the use of PML, if PML modes are present they could be sufficient to obtain a correct expansion of the GD on the surface of a spherical volume around the resonator, making this approach potentially viable even without the use of the RSE, as long as the electric field and the GD is expressed in VSH. The importance of PML modes in other scattering calculation methods have been demonstrated [36, 95], so in comparison to those, the second requirement is not a drawback. Alternatively, one might be able to find the GD on the spherical surface from true eigenmodes only via causality-related regularisation [172], or via an approximate ML expansion where the divergence in terms of k is partially compensated based on the methods outlined in Ref. [99] for the expansion of the scattered field, or via a simple Taylor expansion of the GD at the resonator surface.

The method has already been tested on a homogeneous sphere [38]. It was found that the amplitude of the cross-section converges at a rate of $1/k_{\mathrm{max}}$, which is due to the $1/k_{\mathrm{max}}$ convergence rate of $\mathbf{G}_{11}^{\mathrm{EE}}$ and $\mathbf{G}_{22}^{\mathrm{EE}}$ [85]. While it is not stated explicitly in Ref. [38], presumably in the ML1 (Eq. (1.22)) expansion of the GD, which was used in the paper, the single $\lambda = 0$ mode of the VSC static mode set was used alongside the RSs. This mode alone is sufficient to represent all the static mode contribution to $\mathbf{G}_{22}^{\mathrm{EE}}$ at the surface, as all other static modes

in the VSC set have zero tangential field at the surface [32, 85]. In this chapter we will use the ML4 version of the RSE, and to generate the static modes of the perturbed system we simply use the RSE equation Eq. (1.45), which includes static modes in the main RSE matrix, they are not subtracted as in Eq. (1.47). This results in a larger matrix eigenvalue problem to solve as the ML4 expansion contains many static modes, but it is a simple and straight forward method to find the static modes of the perturbed system.

6.4 Size-perturbed sphere

To illustrate the completeness of the modes generated by the RSE outside of the perturbed resonator, but inside the original system volume, we calculate the scattering cross-section of a sphere of reduced radius $0.7R$ on its exact perturbed surface and on the surface of the unperturbed sphere, which has radius R. The cross-section is calculated with and without using the diverging modes (modes that tend to infinite k, rather than to the true eigenmodes, as we increase the basis size $k_{\max}$). The results are demonstrated in Fig. 6.4.1, with the modes shown on the inset. When the cross-section is calculated on the surface of the perturbed sphere the results with and without diverging modes are nearly identical. In this case there is no significant benefit or drawback from using the artificial modes in the calculation for the given parameters. When the cross-section is calculated on the original, unperturbed surface, which now lies outside the perturbed resonator, the impact of the artificial, diverging modes are significant. If only the true, converging modes are used in the calculation the resulting spectrum is an order of magnitude larger than the exact solution. This is expected as the true eigenmode field amplitudes diverge outside the perturbed system, and they are not suitable for a ML expansion of the GD in that region, as discussed in Chap. 2, with the convergence of the 1D GF outside the system studied in Sec. 2.5. Including the diverging RSE modes in the calculation restores the convergence of the ML expansion, and the results show good agreement with the exact solution.

We can conclude that the use of artificial modes is required in the expansion of the GD on the surface of the unperturbed system. This implies that the scattering formalism developed in Ref. [38] is suitable in case of non-spherical perturbation as well. This will be shown in the next section.

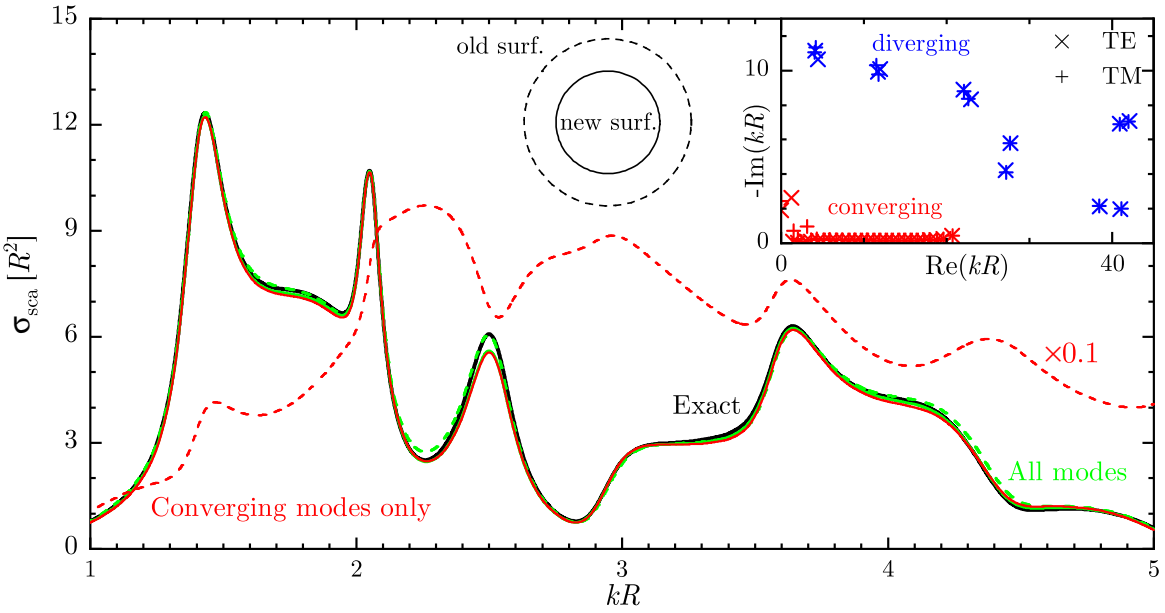

Fig. 6.4.1: Scattering cross-section calculated on the perturbed (solid line) and unperturbed sphere surface (dashed line). Inset shows the modes in the complex plane, with red ones representing the true RSs, and blue ones the artificial modes. Exact solution, using the analytic GD is shown with black line. Only angular momentum $l = 1, 2$ taken into account in all calculations. The number of modes is $N = 40$ per polarisation per angular momentum (total of 160 RSs). The permittivity of the sphere is $\varepsilon_s = 9$, the unperturbed sphere has radius R, the perturbed sphere has radius $0.7R$. The red dashed curved is scaled down by a factor of 10.

6.5 Cylinder perturbation

We apply the scattering calculation method to the cylinder from Chap. 5. To summarise the procedure: first the eigenmodes of a sphere of radius R are calculated, then we introduce a perturbation and calculate the modes of a cylinder via the RSE, and based on the modes of the cylinder we calculate the scattering cross-section, using Eq. (6.1)-Eq. (6.6).

The results are shown on Fig. 6.5.1, and they are compared to a simulation with COMSOL. The estimated accuracy of the COMSOL result is within 1% of the exact value, based on the convergence of the amplitude of the scattering cross-section at the dipole peak, at $k_d R = 1.25$, with respect to refining the size of mesh elements in the domain. We can see that the dipole peak is reproduced within the error, already when $k_{\max} R = 6.5 \approx 5 k_d R$. Higher order mode positions show a slight blueshift compared to COMSOL, and usually an increase in amplitude. Both of these deviations decrease approximately linearly with the increasing basis size $k_{\max} R$. The linear convergence of the peak position corresponds to the slow convergence of the eigenfrequencies, as discussed in Chap. 5. The linear convergence of the scattering

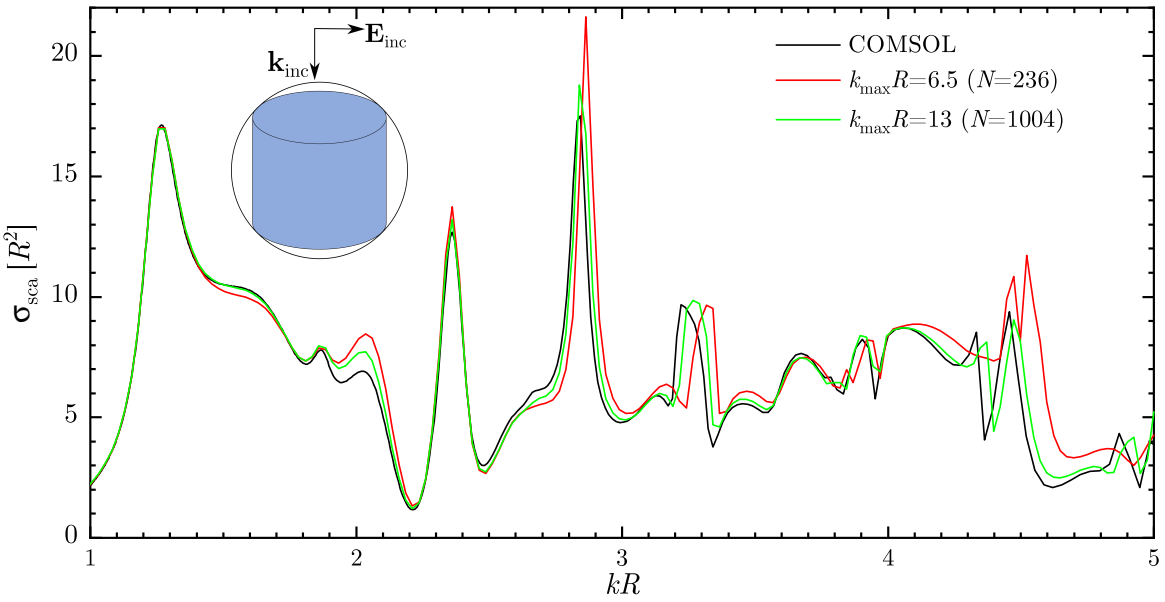

Fig. 6.5.1: cross-section calculated for a cylinder of permittivity $\varepsilon = 9$, height $2h = 4R/\sqrt{2}$, and radius $a = h$, with incident light propagating along the axis of symmetry of the cylinder. Inset shows the schematic view of the perturbation incident wave propagation. The cross-section is calculated based on the value of the GD on the surface of the basis sphere (black line on inset) enveloping the cylinder (blue).

amplitude is due to the $1/k_{\text{max}}$ convergence of $\mathbf{G}_{11}^{\text{EE}}$ and $\mathbf{G}_{22}^{\text{EE}}$ (see Appendix E.2 or Ref. [85]), and it is consistent with the observations in Ref. [38].

Considering the computational efficiency of the method, once the perturbed modes are known, the $k_{\text{max}}R = 13$ curve on Fig. 6.5.1 was calculated in 15s using 200 spectral points (on a i5-8500 CPU). In comparison, obtaining a conventional full wave solution with COMSOL takes at least a couple seconds per spectral point, even with the axial symmety of the system taken into account, which results in approximately 15min total simulation time for 200 spectral points. This is significantly slower then method described in this section. If we consider that generating the perturbed modes for the same curve takes about 3-4min with the RSE, this method is still potentially 3-5 times faster than COMSOL or other similar approaches.

6.6 Conclusion

By considering a size perturbation of a spherical resonator we have shown numerically that the RSE generates a set of modes, which include true (convergent) RSs and artificial (divergent) modes, that are complete inside the unperturbed system volume. This allows the ML expansion of the GD on the original, unperturbed surface. Following from this, we implemented the formalism of Ref. [38] to calculate the cross-section of a cylindrical resonator. The

results show a good agreement with calculations from COMSOL. The accuracy of the peak position and the amplitude scales as $1/k_{\max}$. Instead of just increasing the basis size, the former can be improved by the extrapolation method detailed in Ref. [101], while the latter can be improved with the first-order approximation of high frequency terms, as described in Ref. [38]. While the results in Sec. 2.5 of Chap. 2 imply that the smallest spherical surface should be chosen around the target resonator to evaluate the GD, it should be investigated if using a larger basis sphere in the RSE is beneficial for the accuracy.

Apart from the method [38] used in this chapter, in the literature reviewed only a handful of other methods consider carefully the non-resonant contribution to the scattered quantities rigorously, and formulate explicit expression for these in terms of eigenmodes. Namely, these are Refs. [36] and [37], which are both extensions of Ref. [17], and they explicitly acknowledge the contribution of static modes. Ref. [47] gives a general expression for the scattering matrix in terms of eigenmodes, which could potentially include static modes, but this is not explicitly stated. Ref. [44] formulates the background term as a contour integral instead of an eigenmode expansion. Most of other methods neglect the background term completely, or use various assumptions or fitting methods to find it. The convergence of the average error of the cross-section versus the basis size is studied only in [36], showing an approximately $1/N$ convergence rate for non-spherical systems, and in [37] a remarkable $1/N^3$ rate for a homogeneous sphere, while [38] has a $1/k_{\max} = 1/\sqrt{N}$ convergence rate. However in the former two, the modes were sorted with respect to their contribution to the scattering, which maybe results in a different convergence rate compared to [38] where the modes taken with increasing distance from the origin $kR = 0$. A thorough comparison of all the methods mentioned in this paragraph would be appropriate, particularly, because apart from the convergence rate with respect to the number of modes used, the computational cost itself should also be investigate. While based on the initial results it may seem that Ref. [38] has a slower convergence rate than Ref. [36, 37], as opposed to other methods [36, 37, 47] it does not rely on the overlap integral of the incoming field with the eigenmodes, which could result in significantly better computation times.

7

Conclusion

7.1 Summary

In this thesis we have rigorously tested the ML expansion of the GD and applied the RSE for a variety of dielectric systems.

On a planar 1D example we numerically verified that eigenmodes form a complete set even when the permittivity of the system does not have a step like boundary. In this case the imaginary part of the eigenmodes can grow unbounded due to the decreasing reflection coefficient at high frequencies, and the ML expansion of the GF converges slower than for a homogeneous slab with a step like boundary.

Using a recently formulated, quickly convergent version of the RSE, we investigated the modes of 3D spherically symmetric systems, including ones with inhomogeneities. We provided physically insightful approximations explaining the formation of the Fabry-Pérot modes, and related the peak in the TM spectra to the Brewster phenomenon. We found that removing the discontinuity of the permittivity at the boundary, for example with a linear permittivity profile, can reduce the splitting of the TE and TM spectral mode positions. We provided an approximation based on the Morse potential to find the eigenmodes of certain inhomogeneous systems, which in case of a linear profile and TE polarisation reduces to a simple closed form expression. We analysed the modes based on a quantum mechanical analogy, the effective potential picture. Based on this we designed a permittivity profile that gives rise to an extended flat potential well, which can further reduce the splitting of the fundamental TE and TM WGMs.

We derived a first-order perturbation theory based on the RSE matrix equation for the eigenmodes of an optical resonator. We found that due to the divergence in the static pole residue, all orders of the perturbation series can contribute linearly in the small parameter describing the deformation of the resonator boundary. Correctly taking all of these terms into

account we presented a unified perturbation theory, that can treat both material and shape changes of the resonator in first-order, using the same formalism and a single RS only. The results have implication beyond optics as similar effects in the perturbation series could occur for interface shifts in system where the wavefunction is not smooth across the boundary.

We applied the quickly converging version of the RSE, to non-spherically symmetric perturbations, and discovered that in this case the convergence is much slower. We found that additional, previously unaccounted divergences of the static pole residue are adversely affecting the convergence rate when modes of different l couple to each other under the perturbation.

We have shown numerically that modes generated by the RSE form a complete set inside the unperturbed system volume, which can be larger than the perturbed system, as opposed to the exact eigenmodes of the perturbed system, which are complete only within the perturbed system volume.

We examined the validity of the eigenmode sum rules, and discovered that they are not valid when both spacial coordinates are on the surface of a spherical resonator. In this case, only one of the two forms of the ML expansion of the resonant part of the GD is valid.

Building on the latter two results, we successfully applied a novel method to calculate the scattering cross-section of a cylinder based on its eigenmodes, which were obtained from perturbing the shape of a spherical resonator and calculated via the RSE. The method uses the value of the radial part of the GD in VSH representation, and potentially can be computationally much faster than other existing techniques which rely on the volume integral of the excitation field and the eigenmodes.

7.2 Future work

Regarding the development of the RSE, it is important to improve the convergence rate of the eigenmodes in case of non-spherical perturbations. One way address this issue could be using an optimised set of static modes, where only a limited number of them couple to the RSs. Alternatively, once could attempt to find the vector field describing the change of the surface elements from the unperturbed surface to the perturbed one. This would allow the separation of tangential and normal component of the field, treating the discontinuity of the latter explicitly. For size perturbation of spherical resonators, both of these methods can be applied analytically, but for arbitrary geometries numerical methods based on FEM type meshing would be needed.

For generality, the above method also has to be extended to dispersive resonators as well. The dispersive RSE has only been implemented for spherically symmetric homogeneous resonators so far. In addition, while zero-frequency modes have a vanishing amplitude in systems which have a permittivity pole at zero frequency, dispersive systems have additional modes at zero-permittivity, which are presently not taken into account in the dispersive RSE formulation.

To generalise the scattering calculation method further, the VSH expansion of plane waves propagating in arbitrary directions needs to be found. One could also investigate the validity of the eigenmode sum rule on the surface of non-spherical dielectric resonators, or the sum rules of dispersive systems.

So far the RSE has only been implemented for systems with homogeneous background. While this can be a reasonable approximation for many real physical scenarios, an important class of systems can not be treated, namely a resonator on a mirror. While one could start from a basis systems that is rotationally symmetric, it would not have translational symmetry, and no convenient unperturbed system can be chosen which has known analytic solutions for the eigenmodes.

Another interesting problem that arises often, is finding the modes of two (or more) coupled resonators. Naturally, we could defined the perturbation in the RSE so that the final structure is made up of multiple individual resonators, and find all the modes the usual way. However this may be computationally expensive if a large perturbation is needed to express the target system. An alternative approach to address this issue could be the coupled mode theory, that is, expressing the modes of the total system by the modes of two (or more) individual resonators. While attempts have been made to find such theory for RSs, no methods can presently treat perturbations up to arbitrary order. This is due to the lack of completeness and the divergence of the modes outside of the individual resonators.

In terms of device applications, the approximation of the eigenmodes based on the Morse potential in spherically symmetric systems, combined with the efficiency of the RSE in this case, allows a rapid exploration of large parameter spaces, and custom design of resonators. Particularly, one can engineer an optical resonators that has a double well structure, with a smooth, continuously changing permittivity barrier between the wells, which in practical applications can reduce scattering effects due to fabrication imperfections, allowing an efficient and reliable storage of optical modes.

APPENDIX

A

One dimensional systems

A.1 RS mode normalisation and the GF in 1D

A.1.1 Normalisation

Here we derive the ML expansion of a GF of a dielectric slab, with arbitrary permittivity profile, and with a background that is piecewise homogeneous to the left and right of the slab, but the left and right media are not necessarily identical. The slab is extended from $-a$ to a, the halfspace left of the slab ($x < -a$) has refractive index $\sqrt{\varepsilon_{\rm l}}$, the slab has refractive index $\sqrt{\varepsilon_{\rm s}(x)}$, and the halfspace right of the slab ($a < x$) has refractive index $\sqrt{\varepsilon_{\rm r}}$. The GF can be written as [175]

$$G(x,x';k) = \frac{E_L(x_<)E_R(x_>)}{W}\,, \tag{A.1}$$

where $x_< = \min(x,x')$, $x_> = \max(x,x')$ and W is the Wronskian

$$W(k) = E_L(x)\frac{\mathrm{d}E_R(x)}{\mathrm{d}x} - \frac{\mathrm{d}E_L(x)}{\mathrm{d}x}E_R(x)\,, \tag{A.2}$$

$E_L(x)$ is the left solution, satisfying the left boundary condition (which is that waves propagating away from the slab on the left hand side)

$$E_L(x) = \begin{cases} e^{-ik\sqrt{\varepsilon_{\rm l}}x} & x < -a \\ \psi(x) & -a < x < a \\ B_L e^{-ik\sqrt{\varepsilon_{\rm r}}x} + A_L e^{ik\sqrt{\varepsilon_{\rm r}}x} & a < x \end{cases}, \tag{A.3}$$

and $E_R(x)$ is the right solution, satisfying the right boundary condition (which is that waves propagating away from the slab on the right hand side)

$$E_R(x) = \begin{cases} B_R e^{-ik\sqrt{\varepsilon_{\rm l}}x} + A_R e^{ik\sqrt{\varepsilon_{\rm l}}x} & x < -a \\ \phi(x) & -a < x < a \\ e^{ik\sqrt{\varepsilon_{\rm r}}x} & a < x \end{cases}, \tag{A.4}$$

The field is continuous and smooth at all points in line with Maxwell's boundary conditions. The coefficients A, B are dependent on k, while the Wronskian is independent of x. The latter can be seen by considering that for the equation $y'' + py' + qy = 0$ we can write $W = Ce^{-\int^x p(u)\mathrm{d}u}$ [175], and in the wave equation $p(u) = 0$. When $W(k) = 0$ the GF has a pole, and we obtain the eigenmodes. At $W(k) = 0$ the left and right solutions agree up to a factor f, which can be seen by rearranging the equation to $E_L \frac{\mathrm{d}E_R}{\mathrm{d}x} = \frac{\mathrm{d}E_L}{\mathrm{d}x} E_R$, dividing both sides by $E_L E_R$, then integrating $\int \frac{\mathrm{d}E_R}{\mathrm{d}x}/E_R \, \mathrm{d}x = \int \frac{\mathrm{d}E_L}{\mathrm{d}x}/E_L \, \mathrm{d}x$, which gives $\ln E_R = \ln E_L + C$, so we can write $E_L = fE_R$.

Before we find the residues of the GF we show how to obtain the orthogonality and normalisation conditions. First lets take the wave equation

$$\frac{\mathrm{d}^2 E_L(x)}{\mathrm{d}x^2} + \varepsilon(x) k_L^2 E_L(x) = 0\,. \tag{A.5}$$

Now dropping the dependence on x for brevity, multiplying with E_R and integrating over the slab width, we obtain

$$\int_{-a}^{a} E_R \frac{\mathrm{d}^2 E_L}{\mathrm{d}x^2} \mathrm{d}x + \int_{-a}^{a} \varepsilon E_R k_L^2 E_L \mathrm{d}x = 0\,. \tag{A.6}$$

Taking the interchange expression $L \leftrightarrow R$ and subtracting it from the above equation we get

$$\int_{-a}^{a} E_R \frac{\mathrm{d}^2 E_L}{\mathrm{d}x^2} \mathrm{d}x - \int_{-a}^{a} E_L \frac{\mathrm{d}^2 E_R}{\mathrm{d}x^2} \mathrm{d}x + (k_L^2 - k_R^2) \int_{-a}^{a} \varepsilon E_R E_L \mathrm{d}x = 0\,. \tag{A.7}$$

Integration by parts of the first two terms give

$$\left[E_R \frac{\mathrm{d}E_L}{\mathrm{d}x} \right]_{-a}^{a} - \left[E_L \frac{\mathrm{d}E_R}{\mathrm{d}x} \right]_{-a}^{a} + (k_L^2 - k_R^2) \int_{-a}^{a} \varepsilon E_R E_L \mathrm{d}x = 0\,. \tag{A.8}$$

The left and right solution is satisfied for any wavenumber. Therefore, taking a wavenumbers at the eigenmodes $k_L = k_m$ and $k_R = k_n$, with n, m labeling different eigenmodes, we obtain

$$\left[E_n \frac{\mathrm{d}E_m}{\mathrm{d}x} \right]_{-a}^{a} - \left[E_m \frac{\mathrm{d}E_n}{\mathrm{d}x} \right]_{-a}^{a} + (k_m^2 - k_n^2) \int_{-a}^{a} \varepsilon E_n E_m \mathrm{d}x = 0\,. \tag{A.9}$$

As the eigenmodes E are known outside and at the boundary, and we have

$$E_n(a) = e^{ik_n \sqrt{\varepsilon_\mathrm{r}} a}\,, \tag{A.10}$$

$$\frac{\mathrm{d}E_n(a)}{\mathrm{d}x} = ik_n \sqrt{\varepsilon_\mathrm{r}} E_n(a)\,, \tag{A.11}$$

$$E_n(-a) = e^{ik_n \sqrt{\varepsilon_\mathrm{l}} a}\,, \tag{A.12}$$

$$\frac{\mathrm{d}E_n(-a)}{\mathrm{d}x} = -ik_n \sqrt{\varepsilon_\mathrm{l}} E_n(-a)\,. \tag{A.13}$$

Putting these into Eq. (A.9), and after rearranging the terms and dividing the equation with $k_m - k_n$ we get

$$i\left(\sqrt{\varepsilon_\mathrm{r}}E_n(a)E_m(a) + \sqrt{\varepsilon_\mathrm{l}}E_n(-a)E_m(-a)\right) + (k_m + k_n)\int_{-a}^{a}\varepsilon E_n E_m \mathrm{d}x = 0\,. \tag{A.14}$$

Requiring that for $n = m$ the above equation is one half, which we can do due to the $k_m - k_n$ term that was factorised out, we obtain the orthonormality condition

$$\int_{-a}^{a}\varepsilon E_n E_m \mathrm{d}x - \frac{\sqrt{\varepsilon_\mathrm{r}}E_n(a)E_m(a) + \sqrt{\varepsilon_\mathrm{l}}E_n(-a)E_m(-a)}{i(k_n + k_m)} = \frac{\delta_{nm}}{2}\,. \tag{A.15}$$

Compared to Ref. [14] the surface terms on the left hand side are multiplied with the refractive index outside (in Ref. [14] $\sqrt{\varepsilon_\mathrm{l}} = \sqrt{\varepsilon_\mathrm{r}} = 1$ was taken), and the right hand side is scaled by a factor of 1/2.

A.1.2 GF residue

To find the residue of the GF at the poles we take the Taylor-expansion of the Wronskian around a pole, up to first order, as

$$W(k) = W(k_n) + w_n(k - k_n)\,. \tag{A.16}$$

where $W(k_n) = 0$, and

$$w_n = \left.\frac{\mathrm{d}W}{\mathrm{d}k}\right|_{k=k_n} = \left[\frac{\mathrm{d}E_L}{\mathrm{d}k}\frac{\mathrm{d}E_R}{\mathrm{d}x} + E_L\frac{\mathrm{d}^2E_R}{\mathrm{d}k\mathrm{d}x} - \frac{\mathrm{d}^2E_L}{\mathrm{d}k\mathrm{d}x}E_R - \frac{\mathrm{d}E_L}{\mathrm{d}x}\frac{\mathrm{d}E_R}{\mathrm{d}k}\right]_{k=k_n}\,, \tag{A.17}$$

where all terms are evaluated at $k = k_n$. Inserting these into Eq. (A.1) gives the GF G_n near the pole n as

$$G_n = \frac{fE_n(x)E_n(x')}{w_n(k - k_n)}\,, \tag{A.18}$$

where f is the ratio of the left and right solution at a pole, as defined in the previous section, and we used $E_R = E_n$ and $E_L = fE_R = fE_n$. Taking the derivative of Eq. (A.8) with respect to k_R, we obtain

$$\left[\frac{\mathrm{d}E_R}{\mathrm{d}k_R}\frac{\mathrm{d}E_L}{\mathrm{d}x}\right]_{-a}^{a} - \left[E_L\frac{\mathrm{d}^2E_R}{\mathrm{d}k_R\mathrm{d}x}\right]_{-a}^{a} - I = 0\,, \tag{A.19}$$

$$\tag{A.20}$$

with

$$I = 2k_R\int_{-a}^{a}\varepsilon E_R E_L \mathrm{d}x - (k_L^2 - k_R^2)\int_{-a}^{a}\varepsilon\frac{\mathrm{d}E_R}{\mathrm{d}k_R}E_L\mathrm{d}x\,. \tag{A.21}$$

This can be written as

$$\left[-\frac{\mathrm{d}E_R}{\mathrm{d}k_R}\frac{\mathrm{d}E_L}{\mathrm{d}x}+E_L\frac{\mathrm{d}^2E_R}{\mathrm{d}k_R\mathrm{d}x}\right]_{x=-a}=\left[E_L\frac{\mathrm{d}^2E_R}{\mathrm{d}k_R\mathrm{d}x}-\frac{\mathrm{d}E_R}{\mathrm{d}k_R}\frac{\mathrm{d}E_L}{\mathrm{d}x}\right]_{x=a}+I\,. \tag{A.22}$$

Taking $w_n(-a)$, and using the above expression we get

$$w(-a)=\left\{\left[\frac{\mathrm{d}E_L}{\mathrm{d}k}\frac{\mathrm{d}E_R}{\mathrm{d}x}-\frac{\mathrm{d}^2E_L}{\mathrm{d}k\mathrm{d}x}E_R\right]_{x=-a}+\left[E_L\frac{\mathrm{d}^2E_R}{\mathrm{d}k_R\mathrm{d}x}-\frac{\mathrm{d}E_R}{\mathrm{d}k_R}\frac{\mathrm{d}E_L}{\mathrm{d}x}\right]_{x=a}+I\right\}_{k=k_n} \tag{A.23}$$

where all wavenumbers are evaluated at k_n. The fields just outside the surface at $x=-a$ are

$$E_L(-a)=e^{ik_L\sqrt{\varepsilon_\mathrm{l}}a}\,, \tag{A.24}$$

$$\frac{\mathrm{d}E_L(-a)}{\mathrm{d}x}=-ik_L\sqrt{\varepsilon_\mathrm{l}}E_L(-a)\,, \tag{A.25}$$

$$\frac{\mathrm{d}E_L(-a)}{\mathrm{d}k}=ia\sqrt{\varepsilon_\mathrm{l}}E_L(-a)\,, \tag{A.26}$$

$$\frac{\mathrm{d}^2E_L(-a)}{\mathrm{d}k\mathrm{d}x}=-i\sqrt{\varepsilon_\mathrm{l}}E_L(-a)+k\sqrt{\varepsilon_\mathrm{l}}^2aE_L(-a)\,, \tag{A.27}$$

while at $x=a$

$$E_R(a)=e^{ik_R\sqrt{\varepsilon_\mathrm{r}}a}\,, \tag{A.28}$$

$$\frac{\mathrm{d}E_R(a)}{\mathrm{d}x}=ik_R\sqrt{\varepsilon_\mathrm{r}}E_R(a)\,, \tag{A.29}$$

$$\frac{\mathrm{d}E_R(a)}{\mathrm{d}k}=ia\sqrt{\varepsilon_\mathrm{r}}E_R(a)\,, \tag{A.30}$$

$$\frac{\mathrm{d}^2E_R(a)}{\mathrm{d}k\mathrm{d}x}=i\sqrt{\varepsilon_\mathrm{r}}E_R(a)+k\sqrt{\varepsilon_\mathrm{r}}^2aE_R(a)\,. \tag{A.31}$$

For evaluating the term at $x=-a$ we replace E_R with E_L/f, which we can do as the expression is evaluated at the eigenwavenumber, and the derivative with respect to x is continuous

$$\left[\frac{\mathrm{d}E_L}{\mathrm{d}k}\frac{\mathrm{d}E_R}{\mathrm{d}x}-\frac{\mathrm{d}^2E_L}{\mathrm{d}k\mathrm{d}x}E_R\right]_{x=-a}\Bigg|_{k=k_n}=\frac{1}{f}e^{2ik_n\sqrt{\varepsilon_\mathrm{l}}a}\left[\sqrt{\varepsilon_\mathrm{l}}^2ak_n+i\sqrt{\varepsilon_\mathrm{l}}-k_n\sqrt{\varepsilon_\mathrm{l}}^2a\right] \tag{A.32}$$

$$=\frac{1}{f}E_L^2(-a)i\sqrt{\varepsilon_\mathrm{l}} \tag{A.33}$$

$$=fE_R^2(-a)i\sqrt{\varepsilon_\mathrm{l}}\,. \tag{A.34}$$

For evaluating the term at $x=a$ we replace E_L with fE_R,

$$\left[E_L\frac{\mathrm{d}^2E_R}{\mathrm{d}k_R\mathrm{d}z}-\frac{\mathrm{d}E_R}{\mathrm{d}k_R}\frac{\mathrm{d}E_L}{\mathrm{d}x}\right]_{x=a}\Bigg|_{k=k_n}=fe^{2ik_n\sqrt{\varepsilon_\mathrm{r}}a}\left[i\sqrt{\varepsilon_\mathrm{r}}-\sqrt{\varepsilon_\mathrm{r}}^2k_na+\sqrt{\varepsilon_\mathrm{r}}^2k_na\right] \tag{A.35}$$

$$=fE_R^2(a)i\sqrt{\varepsilon_\mathrm{r}}\,. \tag{A.36}$$

As we approach the limit $k_L=k_R=k_n$ in the integral I we can drop the second term and also make the substitution $E_L=fE_R$, $E_R=E_n$, and from the normalisation condition

(Eq. (A.15)) for the eigenmode n we get

$$w_n = w(-a) = fE_R^2(-a)i\sqrt{\varepsilon_\mathrm{l}} + fE_R^2(a)i\sqrt{\varepsilon_\mathrm{r}} + 2k_n f\int_{-a}^{a}\varepsilon E_R E_R \mathrm{d}x \tag{A.37}$$

$$= fk_n\,. \tag{A.38}$$

Placing this in the pole structure of the GF we get

$$G_n = \frac{E_n(x)E_n(x')}{k_n(k-k_n)}\,. \tag{A.39}$$

In addition to the poles at $k_n \neq 0$ the GF can also have a pole at $k = 0$. We write this term as $G_0 = R_0/k$. Summing over all poles, including the static one, gives Eq. (2.9). We note that a derivation of Eq. (2.9), based on contour integrals in the complex plane, can be found in Ref. [59].

A.1.3 GF

The explicit functional form of the GF can be found from Eq. (A.1)-Eq. (A.4). We list them and briefly describe how they are found for a homogeneous slab. We take the background to be $\sqrt{\varepsilon_\mathrm{l}} = \sqrt{\varepsilon_\mathrm{r}} = 1$ unless noted otherwise.

GF with both points inside the slab

For a homogeneous slab for the left solution (Eq. (A.3)) we can write

$$\psi(x) = A_L^s e^{ik\sqrt{\varepsilon_\mathrm{s}}x} + B_L^s e^{-ik\sqrt{\varepsilon_\mathrm{s}}x}\,, \tag{A.40}$$

where we denote the amplitudes inside the slab with a superscript 's'. Using the condition that the field is continuous and smooth at $x = -a$ we get

$$e^{ika} = A_L^s e^{-ik\sqrt{\varepsilon_\mathrm{s}}a} + B_L^s e^{ik\sqrt{\varepsilon_\mathrm{s}}a}\,, \tag{A.41}$$

$$-ike^{ika} = ik\sqrt{\varepsilon_\mathrm{s}}\left(A_L^s e^{-ik\sqrt{\varepsilon_\mathrm{s}}a} - B_L^s e^{ik\sqrt{\varepsilon_\mathrm{s}}a}\right)\,, \tag{A.42}$$

$$B_L^s = \alpha A_L^s e^{-2ik\sqrt{\varepsilon_\mathrm{s}}a}\,, \tag{A.43}$$

$$\psi(x) = A_L^s e^{ik\sqrt{\varepsilon_\mathrm{s}}x} + \alpha A_L^s e^{-2ik\sqrt{\varepsilon_\mathrm{s}}a}e^{-ik\sqrt{\varepsilon_\mathrm{s}}x}\,. \tag{A.44}$$

Similarly, the right solution (Eq. (A.4)) is

$$\phi(x) = B_R^s e^{-ik\sqrt{\varepsilon_\mathrm{s}}x} + A_R^s e^{ik\sqrt{\varepsilon_\mathrm{s}}x}\,, \tag{A.45}$$

and based on the continuity and smoothness of the field at $x = a$ we get

$$e^{ika} = A_R^s e^{ik\sqrt{\varepsilon_s}a} + B_R^s e^{-ik\sqrt{\varepsilon_s}a}\,, \tag{A.46}$$

$$ike^{ika} = ik\sqrt{\varepsilon_s}\left(A_R^s e^{ik\sqrt{\varepsilon_s}a} - B_R^s e^{-ik\sqrt{\varepsilon_s}a}\right)\,, \tag{A.47}$$

$$B_R^s = \frac{A_R^s e^{2ik\sqrt{\varepsilon_s}a}}{\alpha}\,, \tag{A.48}$$

$$\phi(x) = \frac{A_R^s e^{2ik\sqrt{\varepsilon_s}a}}{\alpha} e^{-ik\sqrt{\varepsilon_s}x} + A_R^s e^{ik\sqrt{\varepsilon_s}x}\,. \tag{A.49}$$

Taking the derivative of these and inserting them into the Wronskian gives

$$W = 2ik\sqrt{\varepsilon_s}\frac{1}{\alpha}A_L^s A_R^s\left(\alpha e^{-ik\sqrt{\varepsilon_s}a} - e^{ik\sqrt{\varepsilon_s}a}\right)\left(\alpha e^{-ik\sqrt{\varepsilon_s}a} + e^{ik\sqrt{\varepsilon_s}a}\right)\,, \tag{A.50}$$

giving the GF as in Ref. [14]

$$G(x,x';k) = \frac{1}{2i\sqrt{\varepsilon_s}k}\frac{e^{i\sqrt{\varepsilon_s}k(a-x_>)} + \alpha e^{-i\sqrt{\varepsilon_s}k(a-x_>)}}{e^{i\sqrt{\varepsilon_s}ka} + \alpha e^{-i\sqrt{\varepsilon_s}ka}}\frac{e^{i\sqrt{\varepsilon_s}k(a+x_<)} + \alpha e^{-i\sqrt{\varepsilon_s}k(a+x_<)}}{-e^{i\sqrt{\varepsilon_s}ka} + \alpha e^{-i\sqrt{\varepsilon_s}ka}}\,. \tag{A.51}$$

Taking the limit of $\mathrm{Im}\,(k) \to \pm\infty$ will show that the GF is vanishes in both the upper and the lower half of the complex plane, therefore it is possible to expand it into a ML series.

GF with one point inside and one outside the slab

We take one point inside the slab, and one point outside, for example to the right of the slab. Following from Eq. (A.1) the left solution will be taken inside the slab and it is given by Eq. (A.44). The form of the right solution, from Eq. (A.4), is e^{ikx}. While the Wronskian (Eq. (A.2)) does not depend on the position, for convenience we re-evaluate it here to a different form (which will later allow us to simplify with the field amplitudes A), and write it as

$$W = ike^{ikx(1-\sqrt{\varepsilon_s})}A_L^s\left(\sqrt{\varepsilon_s}-1\right)\left(\alpha e^{-ik\sqrt{\varepsilon_s}a} - e^{ik\sqrt{\varepsilon_s}x}\right)\left(\alpha e^{-ik\sqrt{\varepsilon_s}a} + e^{ik\sqrt{\varepsilon_s}x}\right)\,. \tag{A.52}$$

Evaluating it at $x = a$ for simplicity, and inserting it into Eq. (A.1) gives the GF

$$G(x,x';k) = \frac{1}{ik(\sqrt{\varepsilon_s}-1)}\frac{\left(e^{ik\sqrt{\varepsilon_s}(x_<+a)} + \alpha e^{-ik\sqrt{\varepsilon_s}(x_<+a)}\right)e^{ik(x_>-a)}}{\left(e^{ik\sqrt{\varepsilon_s}a} + \alpha e^{-ik\sqrt{\varepsilon_s}a}\right)\left(\alpha e^{-ik\sqrt{\varepsilon_s}a} - e^{ik\sqrt{\varepsilon_s}a}\right)}\,. \tag{A.53}$$

This expression is the same as if we were to evaluate the 'inside' GF with one point at the right boundary, and then multiply it with $e^{ikx_>}$ to account for wave propagation on the right. This expression vanishes when $\mathrm{Im}\,(k) \to \infty$ for any combination of $x_<, x_>$. However in the lower half of the complex plane, when $\mathrm{Im}\,(k) \to -\infty$, it only vanishes when the condition

$$\sqrt{\varepsilon_s}x_< < a(1+\sqrt{\varepsilon_s}) - x_>\,, \tag{A.54}$$

is satisfied. This can be seen by approaching $\mathrm{Im}\,(k) \to -\infty$, then dropping the exponential terms that ave $-i$ in the above expression, as these tend to zero. This is consistent with the results from Ref. [59], where they found that the ML expansion of the GF work up to this cut-off condition.

GF with both points outside the slab

For this example we take the region right from the slab $a < x, x'$, where

$$E_L(x) = B_L e^{-ikx} + r B_L e^{ikx}\,, \tag{A.55}$$

$$E_R(x) = e^{ikx}\,. \tag{A.56}$$

Here r is the reflection coefficient from the slab. This can be found, for example by using an Airy summation approach, such as in Ref. [103]. We note that using the Airy sum approach Ref. [176] has an error in their transmission coefficient. Here we just used the boundary conditions of continuity and smoothness at both edges of the slab to find

$$r = e^{-2ika}\alpha\frac{e^{2ik\sqrt{\varepsilon_\mathrm{s}}a} - e^{-2ik\sqrt{\varepsilon_\mathrm{s}}a}}{\alpha^2 e^{-2ik\sqrt{\varepsilon_\mathrm{s}}a} - e^{2ik\sqrt{\varepsilon_\mathrm{s}}a}} = e^{-2ika}\alpha\frac{\left(e^{ik\sqrt{\varepsilon_\mathrm{s}}a} - e^{-ik\sqrt{\varepsilon_\mathrm{s}}a}\right)\left(e^{ik\sqrt{\varepsilon_\mathrm{s}}a} + e^{-ik\sqrt{\varepsilon_\mathrm{s}}a}\right)}{\left(\alpha e^{-ik\sqrt{\varepsilon_\mathrm{s}}a} - e^{ik\sqrt{\varepsilon_\mathrm{s}}a}\right)\left(\alpha e^{-ik\sqrt{\varepsilon_\mathrm{s}}a} + e^{ik\sqrt{\varepsilon_\mathrm{s}}a}\right)}\,. \tag{A.57}$$

The Wronskian is just going to be

$$W = 2ikB_L\,, \tag{A.58}$$

and the GF is

$$G(x, x'; k) = \frac{e^{-ikx_<}e^{ikx_>}}{2ik} + \frac{r e^{ikx_<}e^{ikx_>}}{2ik}\,. \tag{A.59}$$

The first term is just the GF of the vacuum background, and the second term is the scattered part of the GF, which could be thought of as an interference term due to the reflection of the wave from the slab. In the above expression in the first term $x_> - x_<$ is always larger than zero, in the second term $x_> + x_<$ is also always larger than zero, therefore when $\mathrm{Im}\,(k) \to \pm\infty$ the GF tends to infinity exponentially, thus it can not be expressed in a ML expansion.

GF of the background

To find the background GF of system consisting of two half-spaces, the left ranging from $x < a$ and the right from $a < x$, with refractive indices $\sqrt{\varepsilon_\mathrm{l}}$ and $\sqrt{\varepsilon_\mathrm{r}}$, respectively, we construct the GF from left and right solutions as before. The left solution is

$$E_L(x) = \begin{cases} e^{-ik\sqrt{\varepsilon_\mathrm{l}}x} & x < a \\ B_L e^{-ik\sqrt{\varepsilon_\mathrm{r}}x} + A_L e^{ik\sqrt{\varepsilon_\mathrm{r}}x} & a \le x \end{cases}\,. \tag{A.60}$$

Using the condition that the field is smooth and continuous at $x = a$ we obtain

$$A_L = e^{-ika(\sqrt{\varepsilon_\mathrm{r}}+\sqrt{\varepsilon_\mathrm{l}})}\frac{\sqrt{\varepsilon_\mathrm{r}}-\sqrt{\varepsilon_\mathrm{l}}}{2\sqrt{\varepsilon_\mathrm{r}}}\,, \tag{A.61}$$

$$B_L = e^{ika(\sqrt{\varepsilon_\mathrm{r}}-\sqrt{\varepsilon_\mathrm{l}})}\frac{\sqrt{\varepsilon_\mathrm{r}}+\sqrt{\varepsilon_\mathrm{l}}}{2\sqrt{\varepsilon_\mathrm{r}}}\,. \tag{A.62}$$

The right solution, satisfying the right boundary condition

$$E_R(x) = \begin{cases} B_R e^{-ik\sqrt{\varepsilon_\mathrm{l}}x} + A_R e^{ik\sqrt{\varepsilon_\mathrm{l}}x} & x < a \\ e^{ik\sqrt{\varepsilon_\mathrm{r}}x} & a \le x \end{cases}\,. \tag{A.63}$$

Using the condition that the field is smooth and continuous at $x = a$ we get

$$A_R = e^{ika(\sqrt{\varepsilon_\mathrm{r}}-\sqrt{\varepsilon_\mathrm{l}})}\frac{\sqrt{\varepsilon_\mathrm{r}}+\sqrt{\varepsilon_\mathrm{l}}}{2\sqrt{\varepsilon_\mathrm{l}}}\,, \tag{A.64}$$

$$B_R = e^{ika(\sqrt{\varepsilon_\mathrm{r}}+\sqrt{\varepsilon_\mathrm{l}})}\frac{\sqrt{\varepsilon_\mathrm{l}}+\sqrt{\varepsilon_\mathrm{r}}}{2\sqrt{\varepsilon_\mathrm{l}}}\,. \tag{A.65}$$

To find the static pole residue of the GF we take both points to be in the left half space $x, x' < a$, giving the GF to be

$$G(x,x';k) = \frac{e^{-ik\sqrt{\varepsilon_\mathrm{l}}x_<}\left(e^{ik\sqrt{\varepsilon_\mathrm{l}}x_>} + \frac{\sqrt{\varepsilon_\mathrm{l}}-\sqrt{\varepsilon_\mathrm{r}}}{\sqrt{\varepsilon_\mathrm{l}}+\sqrt{\varepsilon_\mathrm{r}}}e^{2ik\sqrt{\varepsilon_\mathrm{l}}a}e^{-ik\sqrt{\varepsilon_\mathrm{l}}x_>}\right)}{2ik\sqrt{\varepsilon_\mathrm{l}}}\,. \tag{A.66}$$

Which has the residue at the static pole

$$\lim_{k\to 0} kG(x,x';k) = \frac{1}{i(\sqrt{\varepsilon_\mathrm{r}}+\sqrt{\varepsilon_\mathrm{l}})}\,. \tag{A.67}$$

We note that when $\sqrt{\varepsilon_\mathrm{b}} = \sqrt{\varepsilon_\mathrm{r}} = \sqrt{\varepsilon_\mathrm{l}}$, Eq. (A.66) will take the form as in Ref. [59]

$$G(x,x';k) = \frac{e^{-ik\sqrt{\varepsilon_\mathrm{b}}x_<}e^{ik\sqrt{\varepsilon_\mathrm{b}}x_>}}{2ik\sqrt{\varepsilon_\mathrm{b}}}\,, \tag{A.68}$$

and has the static pole residue of $1/(2i\sqrt{\varepsilon_\mathrm{b}})$.

A.2 ML sum convergence

A.2.1 Sum rule with both points on the same boundary

Here we show how to obtain Eq. (2.19), which is a special case of the expression $\sum_{-\infty}^{\infty} E_n(x)E_n(x')/ik_n$ (Eq. (2.18)) when $x = x' = a$. We take the exact form of the eigenmodes [14]

$$E_n = A_n\left(e^{ik_n\sqrt{\varepsilon_\mathrm{s}}x} + (-1)^n e^{-ik_n\sqrt{\varepsilon_\mathrm{s}}z}\right)\,, \tag{A.69}$$

$$A_n = \frac{(-i)^n}{2\sqrt{a}\sqrt{\varepsilon_\mathrm{s}}}\,. \tag{A.70}$$

Multiplying out the terms in the numerator and using the values for k_n (Eq. (2.16)) gives

$$E_n(a)E_n(a) = \frac{(-1)^n}{4a\varepsilon_s}\left(e^{2i\sqrt{\varepsilon_s}k_n a} + e^{-2i\sqrt{\varepsilon_s}k_n a} + (-1)^n\right) = \frac{1}{a(\varepsilon_s - 1)}\,. \tag{A.71}$$

The $n = 0$ term is

$$\frac{E_0(a)E_0(a)}{ik_0} = \frac{2\sqrt{\varepsilon_s}}{(\varepsilon_s - 1)\ln\alpha}\,. \tag{A.72}$$

For convenience we can add the $n \neq 0$ terms in pairs as

$$E_n(a)E_n(a) + E_{-n}(a)E_{-n}(a) = \frac{1}{a(\varepsilon_s - 1)}\left(\frac{1}{k_n} + \frac{1}{k_{-n}}\right)\,, \tag{A.73}$$

$$= \frac{1}{a(\varepsilon_s - 1)}\left(\frac{2a\sqrt{\varepsilon_s}}{\pi n - i\ln\alpha} - \frac{2a\sqrt{\varepsilon_s}}{\pi n + i\ln\alpha}\right)\,, \tag{A.74}$$

$$= \frac{4\sqrt{\varepsilon_s}\ln\alpha}{(\varepsilon_s - 1)\pi^2} \times \frac{1}{n^2 + b^2}\,, \tag{A.75}$$

$$\tag{A.76}$$

with

$$b = \frac{\ln\alpha}{\pi}\,. \tag{A.77}$$

Therefore, we can write the total sum, including the $n = 0$ term, as

$$\sum_{-\infty}^{\infty}\frac{E_n(a)E_n(a)}{ik_n} = \frac{2\sqrt{\varepsilon_s}}{(\varepsilon_s - 1)\ln\alpha} + \frac{4\sqrt{\varepsilon_s}\ln\alpha}{(\varepsilon_s - 1)\pi^2}\sum_{1}^{\infty}\frac{1}{n^2 + b^2}\,. \tag{A.78}$$

Noting that [158]

$$\sum_{0}^{\infty}\frac{1}{n^2 + b^2} = \frac{1}{2}\left(\frac{1}{b^2} + \frac{\pi\coth(b\pi)}{b}\right)\,, \tag{A.79}$$

so

$$\sum_{1}^{\infty}\frac{1}{n^2 + b^2} = \frac{1}{2}\left(-\frac{1}{b^2} + \frac{\pi\coth(b\pi)}{b}\right)\,, \tag{A.80}$$

we can arrive at the result

$$\sum_{-\infty}^{\infty}\frac{E_n(a)E_n(a)}{ik_n} = \frac{2\sqrt{\varepsilon_s}}{(\varepsilon_s - 1)\ln\alpha} + \frac{4\sqrt{\varepsilon_s}\ln\alpha}{(\varepsilon_s - 1)\pi^2}\frac{\pi}{\ln\alpha}\left(-\frac{\pi}{2\ln\alpha} + \frac{\pi\coth(\ln\alpha)}{2}\right)\,, \tag{A.81}$$

$$= \frac{2\sqrt{\varepsilon_s}}{\varepsilon_s - 1}\coth(\ln\alpha)\,. \tag{A.82}$$

A.2.2 Error outside

We take a brief look at the error of the ML expansion of the GF in the region outside of the perturbed slab. We take $a_p = 0.5a$, $x' = 0.6a$, $\varepsilon_s = 2$. We evaluate the relative error of the GF in the region outside of the perturbed slab, then integrate the results over the spacial region to obtain a single error value. We take a range of k and $k_{\max}$ combinations,

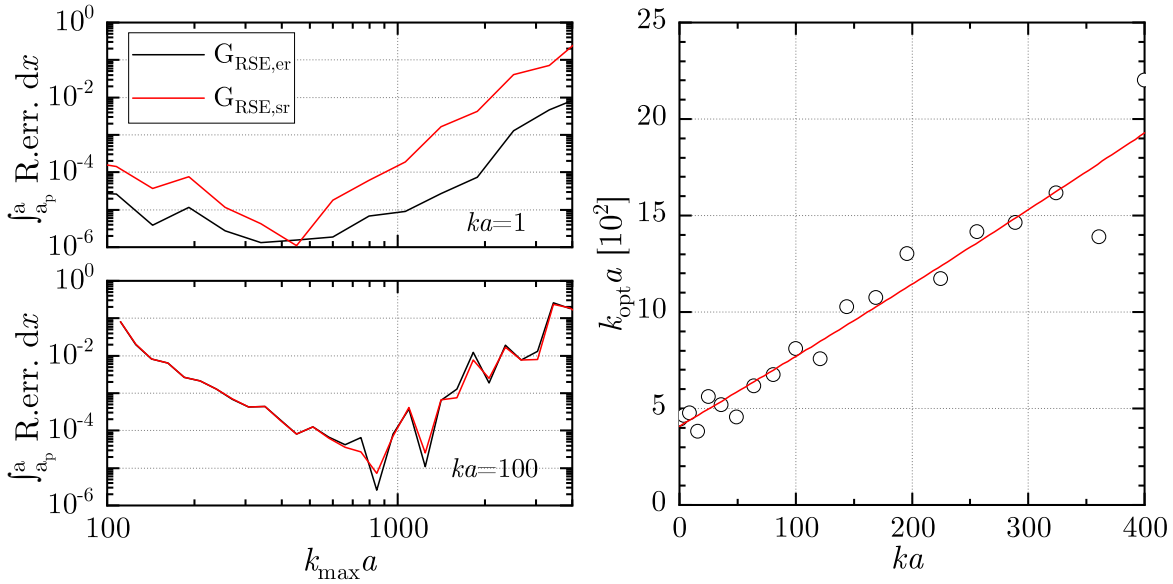

Fig. A.2.1: Relative error of the ML expansion of the GF for size perturbed slab, with error calculated outside of the perturbed slab, but inside the original system volume. On the left, the integral of the relative error shown, as it scales with the choice of $k_{\max}$. On the right optimal $k_{\max}$ value is shown for different ks, where the optimum is found from minimizing the relative error.

and we find the optimal $k_{\max}$ value, which we label k_{opt}, where the integral of the relative error (R.err.) is minimised. The results are shown on Fig. A.2.1. For $ka = 1$ the error decreases to approximately $k_{\max}a \approx 400$, after which it increases. For $ka = 100$ the error decreases up to $k_{\max}a \approx 800$, after which it increases. Looking at the trend for a different ka values, the optimal cut-off point in $k_{\max}$ to minimise the error outside is approximately linear $k_{opt}a = Ska + O$. On the specific example here the scaling factor is $S \approx 4$ and the offset is $O \approx 400$. We can expect that the specific values of S and O will depend on the parameters a_p, x', and ε_s, but the overall trend will likely be similar.

B

Spherically symmetric, radially inhomogeneous systems

B.1 Eigenmodes of a homogeneous slab

By approximating the surface of the sphere with a flat boundary, we compare the modes of a sphere with those of a homogeneous slab, in which EM waves propagate at a non-normal incidence to the boundary. We also compare here the modes of the slab with an approximation similar to Eq. (3.3) which is provided by the ray picture.

The secular equation determining the TE modes of a homogeneous slab of thickness $2a$, permittivity ϵ, and permeability μ is given by [9]

$$e^{2iq_n a} = (-1)^n \frac{q_n + \mu k_n}{q_n - \mu k_n}\,, \tag{B.1}$$

where $q = \sqrt{\epsilon\mu\omega^2 - p^2}$ and $k = \sqrt{\omega^2 - p^2}$ are the normal components of vector inside the slab and in vacuum, respectively, ω is the wave vector in vacuum here, and p is its in-plane component, which is conserved. Note that p was also introduced to discuss the Brewster peak, see Fig. 3.2.2. The factor $(-1)^n$ gives the mode parity and can be used to label the modes. The corresponding equation for TM modes is provided by just swapping ϵ and μ in Eq. (B.1).

One can find an approximate imaginary part of the mode wavenumbers in the same way as described in Sec. 3.2.1. The angle of incidence inside the slab is given by $\theta = \mathrm{atan}(p/q)$, and the optical path length is $L = 2an_r/\cos\theta$ where a is the slab half width. The imaginary part of the RS wavenumbers is then given by

$$\mathrm{Im}\,(k) = \frac{\ln|r_P|}{2an_r}\cos\theta\,, \tag{B.2}$$

where again r_P is the polarization dependent Fresnel coefficient taken at real wavenumbers – compare Eqs. (B.2) and (3.3).

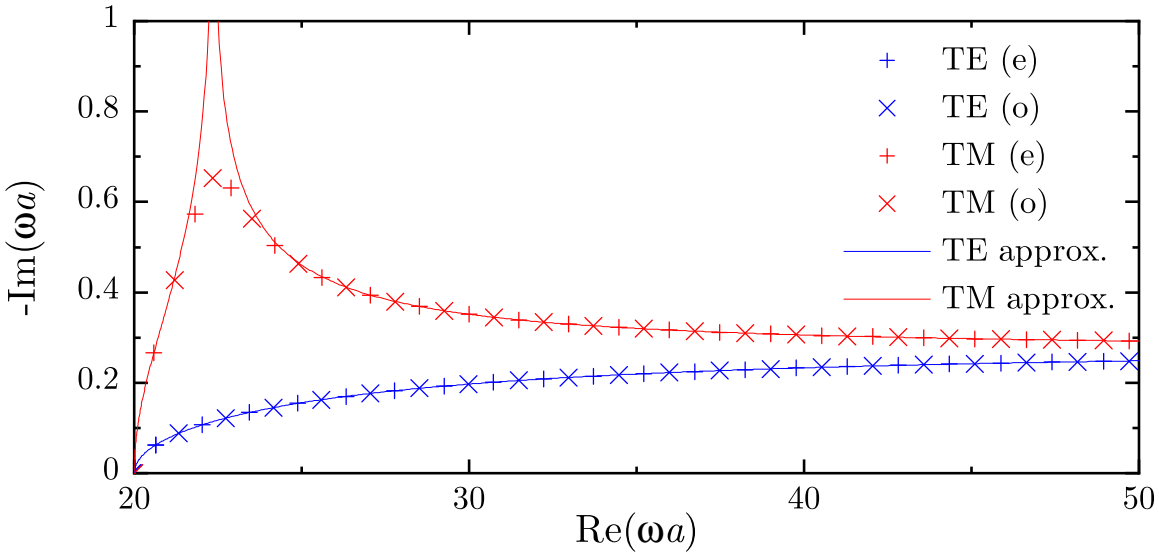

Fig. B.1.1: Eigenmodes of a homogeneous slab with $\epsilon = 4$, $\mu = 1$, and $p = 20$, along with approximate solutions for the imaginary part obtained from Eq. (B.2). The '(e)' and '(o)' label the even and odd modes, respectively. Here ω is the wavenumber in vacuum.

We show in Fig. B.1.1 the TE and TM modes of a slab with permittivity $\epsilon = 4$, permeability $\mu = 1$, and in-plane wavenumber $p = 20/a$, so that the system parameters are matching those used for the sphere in Sec. 3.2.1. In the TM spectrum, there is a peak again, which is aligned with the position of the Brewster angle. Overall, for these parameters the approximation works better for the slab than for the sphere, as the boundary is strictly flat. The observed small deviation of the modes from the approximation at the Brewster peak stems from the neglecting the imaginary part of the wavenumber in r_P, which can be significant around the peak. We can see that for both polarizations, there are even and odd modes alternating with increasing $\mathrm{Re}(\omega a)$. We can also see that at high frequencies, both TE and TM FP modes converge to the same asymptote, which is the same behavior as for the sphere. As in the spherical case, the TE and TM modes of the same parity appear in alternating order. In fact, even TE modes align with the odd TM modes, and vice versa. However, in case of a sphere even modes do not exist. Finally, instead of the WG modes of a sphere, in case of a slab there are waveguide modes with purely real eigenfrequencies, formed as a consequence of total internal reflection at the planar boundary, and instead of the L modes of a sphere, there are anti-waveguide modes in case of a slab [80]. Both waveguide and anti-waveguide modes have $\omega < p$ and are not shown in Fig. B.1.1.

B.2 Effective potential for TM modes

Here we show that the wave equation (3.25) for the scalar magnetic field $\mathcal{H}(r)$ in TM polarization can be brought to a Schrödinger-like equation with an effective potential independent of the wave function. Following [114], we introduce a substitution $\mathcal{H}(r) = \sqrt{\varepsilon(r)}\widetilde{\mathcal{H}}(r)$, from which we find

$$\frac{\mathrm{d}\mathcal{H}}{\mathrm{d}r} = \frac{1}{2}\frac{\varepsilon'}{\sqrt{\varepsilon}}\widetilde{\mathcal{H}} + \sqrt{\varepsilon}\widetilde{\mathcal{H}}' \tag{B.3}$$

$$\frac{\mathrm{d}^2\mathcal{H}}{\mathrm{d}r^2} = \left(-\frac{1}{4}\frac{(\varepsilon')^2}{\varepsilon^{\frac{3}{2}}} + \frac{1}{2}\frac{\varepsilon''}{\sqrt{\varepsilon}}\right)\widetilde{\mathcal{H}} + \frac{\varepsilon'}{\sqrt{\varepsilon}}\widetilde{\mathcal{H}}' + \sqrt{\varepsilon}\widetilde{\mathcal{H}}'', \tag{B.4}$$

where the prime indicates the derivative with respect to r and where we omit the dependencies on r for brevity. Using these expressions the wave equation takes the form

$$\left(\frac{\mathrm{d}^2}{\mathrm{d}r^2} - \frac{\alpha^2}{r^2} + k^2\varepsilon - \frac{3}{4}\left(\frac{\varepsilon'}{\varepsilon}\right)^2 + \frac{1}{2}\frac{\varepsilon''}{\varepsilon}\right)\widetilde{\mathcal{H}} = 0\,, \tag{B.5}$$

in which the first derivative of the wave function present in Eq. (3.25) has cancelled out, so that the corresponding effective potential $\widetilde{V}^{\mathrm{TM}}$ given by Eq. (3.27) is independent of the wave function $\widetilde{\mathcal{H}}$. This comes at the cost of adding a term containing the second derivative of the permittivity to $\widetilde{V}^{\mathrm{TM}}$. We show $\widetilde{V}^{\mathrm{TM}}$ in Fig. B.2.1 for the lowest four WG modes, for the quadratic permittivity profile described in Sec. 3.3.3. Overall, the potential has a shape similar to V^{TE} shown in Fig. 3.3.3(f), apart from the step at the sphere surface due to the contribution from the second derivative of the permittivity which has a discontinuity. As in the TE polarization, the potential is getting deeper with the mode number, and its minimum is slightly shifting towards the center, as it is clear from Fig. B.2.1.

B.3 TE-TM splitting for $l = 80$

In Fig. B.3.1 the difference between the TE and nearest TM RSs for $l = 80$ is shown, for the constant, linear, and quadratic permittivity profiles, using a basis size of $N = 800$. The qualitative behaviour is similar to $l = 20$ shown in Fig. 3.4.1, but the RSs are shifted to higher wavenumbers, and more WG RSs are present. For the linear and quadratic profile the minimum splitting is reduced by approximately a factor of four. This is consistent with the modes being more tightly packed which can be seen by comparing Fig. 3.3.3 and Fig. B.3.1.

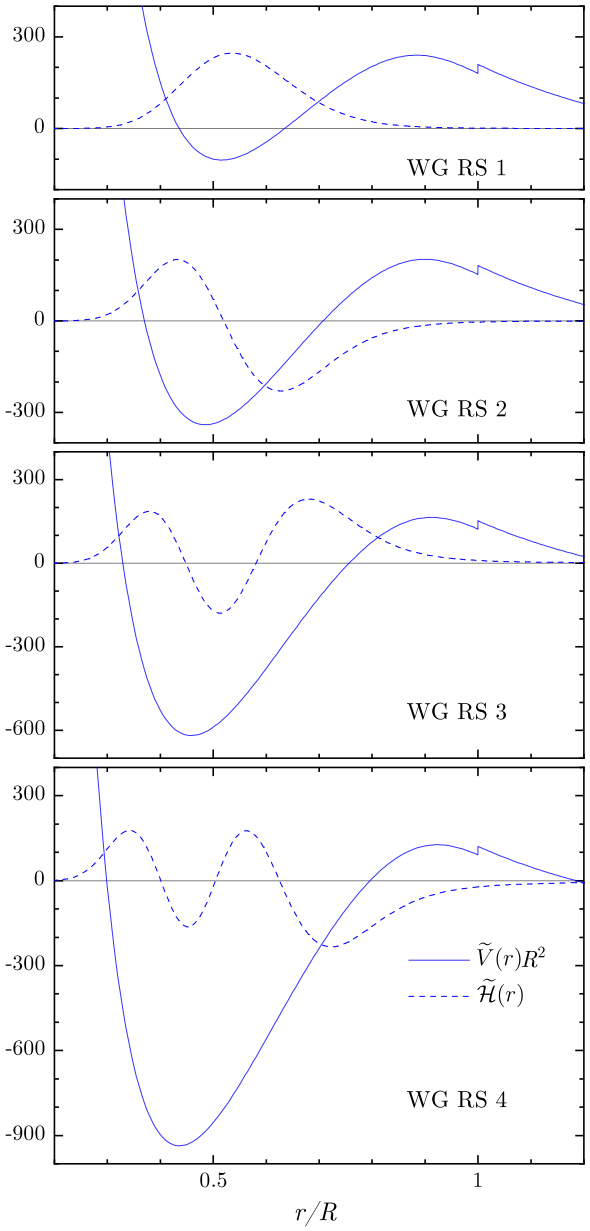

Fig. B.2.1: Real part of the unitless effective potential $\widetilde{V}^{\mathrm{TM}}R^2$ and the normalized field $\widetilde{\mathcal{H}}$ for the first four TM WG RSs, for the quadratic permittivity profile and $l = 20$ as in Fig. 3.3.3. WG RS 1 $kR = 14.4 - 6.74 \times 10^{-9}i$, WG RS 2 $kR = 15.4 - 3.51 \times 10^{-7}i$, WG RS 3 $kR = 16.3 - 8.47 \times 10^{-6}i$, WG RS 4 $kR = 17.2 - 1.22 \times 10^{-4}i$.

B.4 RS separation

It is interesting to investigate the RS separation of each polarization for the different permittivity profiles. This is shown in Fig. B.4.1. Let us consider in the ray picture a nearly normal incidence, corresponding to RS wavenumbers much larger than the critical wavenumber, $k_c = l/R$. In this case, the mode separation Δk can be evaluated from the optical path

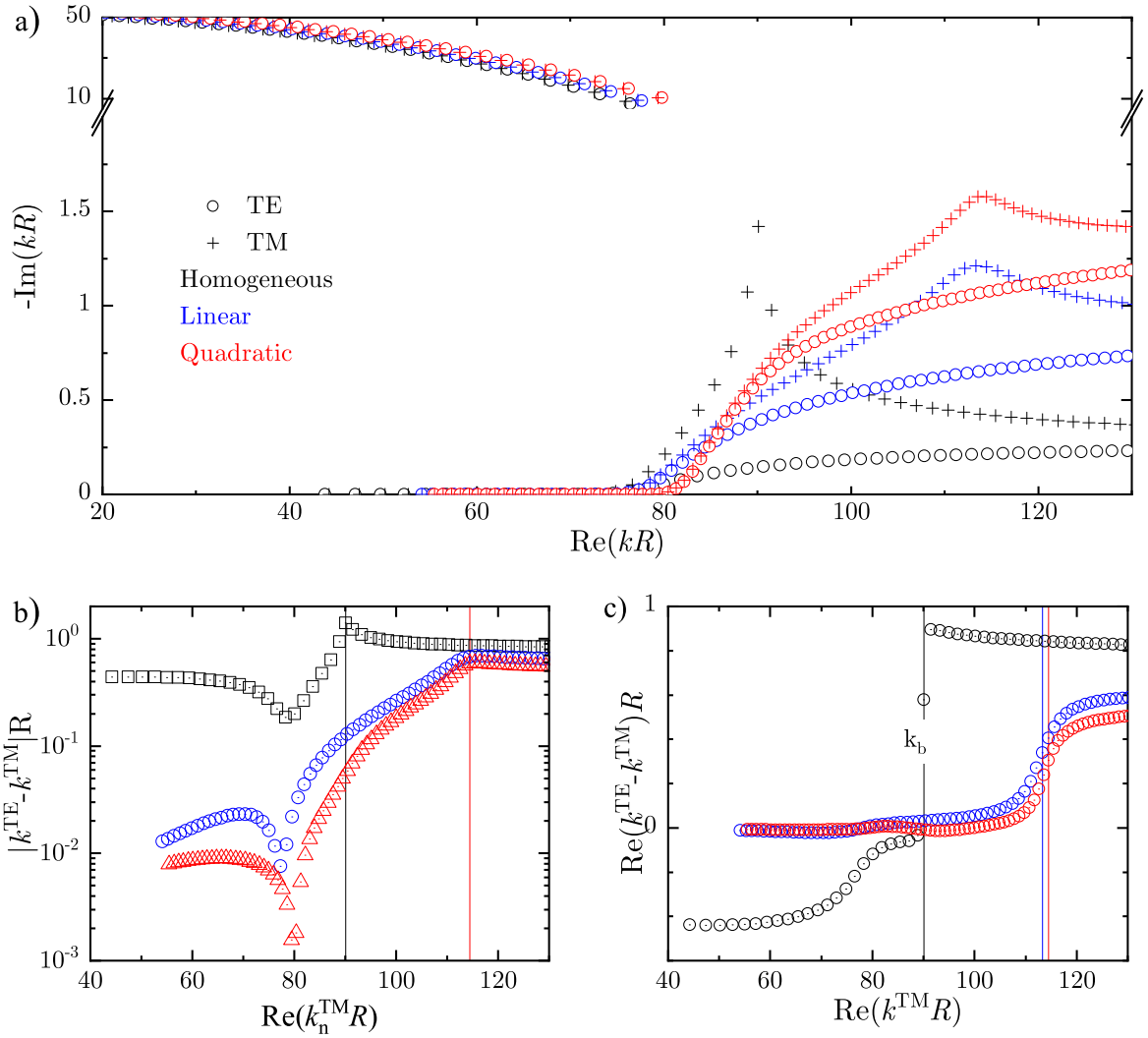

Fig. B.3.1: As Fig. 3.4.1, but for $l = 80$.

length between successive reflections, $L = 2\int_0^R \sqrt{\varepsilon(r)}\mathrm{d}r$. L/R takes the values of 4.0, 5.1, and 6.0, for the employed constant, linear, and quadratic permittivity profiles, respectively. Using the resonator condition of constructive interference of waves, $2L = n\lambda_n$, where n is a natural number, and the missing even states, we find $\Delta k = 2\pi/\lambda_{n+1} - 2\pi/\lambda_n = 2\pi/L$. Therefore, Δk in units of $2\pi/L$ tends towards unity for large k, which can be observed in Fig. B.4.1.

Overall, for the constant profile, the spacing reduces with $\mathrm{Re}\, k$, while for the linear and quadratic profiles, the spacing is nearly constant, increasing only slightly. There are two regions of deviation from the monotonous behaviour, indicated by vertical arrows in Fig. B.4.1. Firstly, at the Brewster peak k_b, where the spacings of TM RSs, which otherwise are nearly identical to the TE RSs, are reduced in order to accommodate the additional Brewster RS, as discussed in Sec. 3.2.1. Secondly, at the wavenumber for the critical angle of total internal

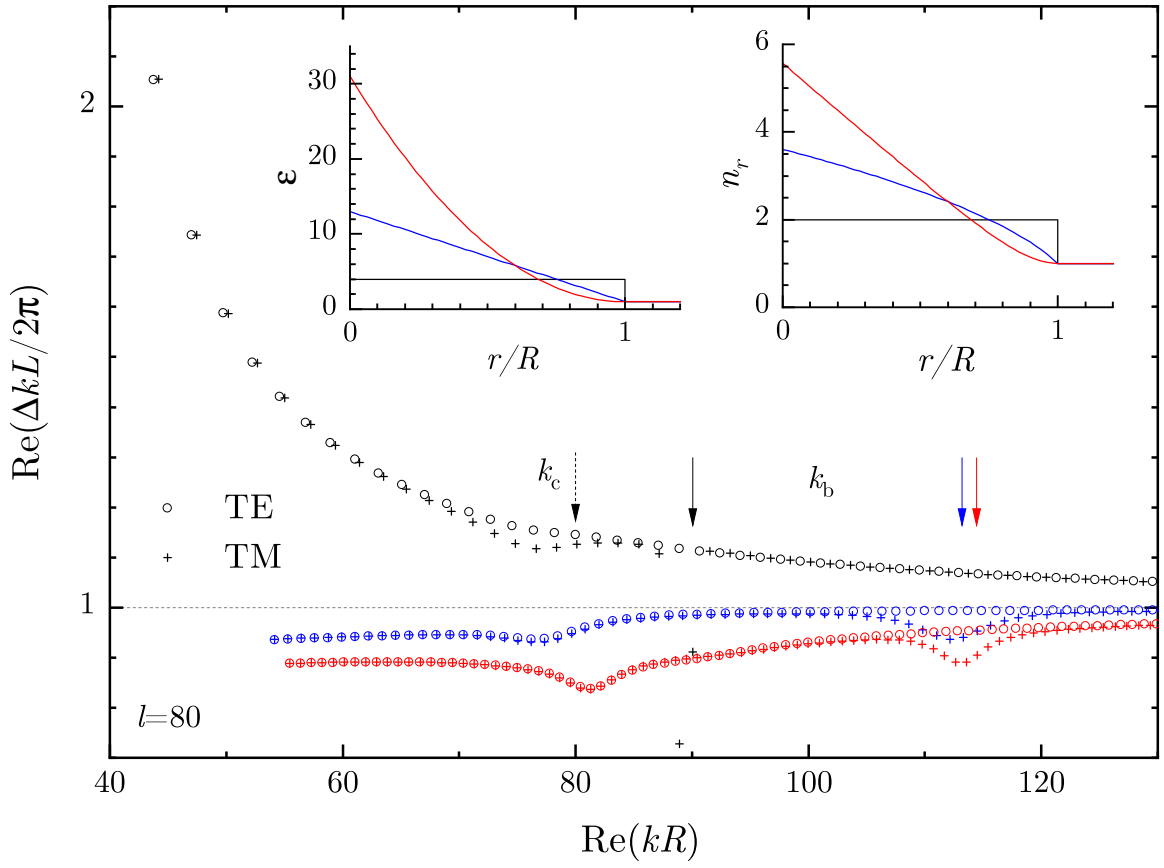

Fig. B.4.1: RS separation for $l = 80$, for constant (black), linear (blue), and quadratic (red) permittivity profiles shown in the left inset. The right inset shows the corresponding refractive index profiles. The separation Δk is taken between a RS at k and the following RS of the same polarization. The vertical arrows indicate positions k_b of the Brewster peak mode and the wavenumber k_c at the critical angle of total internal reflection.

reflection at the surface, $k_c = l/R$, which is the transition region between WG and FP modes, where both TE and TM RSs show a slightly reduced splitting, somewhat more pronounced for the TM RSs, specifically for the constant permittivity.

C

First order perturbation theory of resonant states

C.1 First-order approximations based on the RSE

In this section we provide, based on the RSE, a more general and detailed derivation of the correct first-order change of the RS wave number due to a small perturbation. Based on the closure relation of the modes, we discuss qualitatively how the second-order term can lead to a linear contribution in the deformation depth $h(\mathbf{r})$. We then show explicitly, for spherically-symmetric basis systems, the exact conversion from second to first order based on the residue of the Green's function at the static pole. Finally, we extract the exact first-order correction from all higher orders.

C.1.1 Perturbation series up to second order

Instead of solving the complete matrix equation in Eq. (4.2), one can extract a perturbation series for $\varkappa$ in terms of powers of the matrix elements $V_{\nu\nu'}$ of the perturbation. This is done below by applying a standard procedure, namely, by taking a perturbed solution in the form

$$\varkappa = \varkappa^{(0)} + \varkappa^{(1)} + \varkappa^{(2)} + \dots\,, \qquad \vec{\mathbb{F}} = \sum_{\nu} c_\nu \vec{\mathbb{F}}_\nu\,, \qquad c_\nu = c_\nu^{(0)} + c_\nu^{(1)} + c_\nu^{(2)} + \dots \tag{C.1}$$

where the superscript indicates the related power of the matrix elements. Here we consider terms only up to second order, simply for the purpose of illustrating how can a second-order term be turned into a first-order correction. Later we extract first-order corrections from all higher-order terms.

Substituting the above expansions into Eq. (4.2), we find the first-order corrections to the wave number and the wave function of state n,

$$\varkappa^{(1)} = -k_n V_{nn}\,, \qquad c_{\nu\neq n}^{(1)} = -\frac{k_n V_{\nu n}}{(k_n - k_\nu)}\,. \tag{C.2}$$

Using these one can find the second order correction to the wave number,

$$\varkappa^{(2)} = k_n V_{nn}^2 + k_n^2 \sum_{\nu \neq n} \frac{V_{n\nu} V_{\nu n}}{k_n - k_\nu}\,, \tag{C.3}$$

giving the perturbed wave number up to second order as

$$\varkappa = k_n - k_n V_{nn} + k_n V_{nn}^2 + k_n^2 \sum_{\nu \neq n} \frac{V_{n\nu} V_{\nu n}}{k_n - k_\nu} + \dots\,, \tag{C.4}$$

where the sum in the last term includes all other RSs ($k_\nu \neq 0$) and all static modes ($k_\nu = 0$). The first three terms in Eq. (C.4) can also be understood as a diagonal (i.e., $\nu = n$) approximation to the matrix equation (4.2), expanded to second order in V_{nn}:

$$\varkappa \approx \frac{k_n}{1 + V_{nn}} = k_n - k_n V_{nn} + k_n V_{nn}^2 + \dots \tag{C.5}$$

However, the diagonal approximation Eq. (C.5) does not contain the full first-order information. In fact, the last term in Eq. (C.4) can contain implicit first-order corrections arising from the static-modes as we will show in the following subsection.

C.1.2 Converting second-order terms to first order based on closure relation

Let us consider only the static-mode contribution to the sum in Eq. (C.4), setting $\nu = \lambda$, and $k_\nu = 0$. The last term then reduces to

$$\sum_\lambda V_{n\lambda} V_{\lambda n} = \sum_\lambda \iint \vec{\mathbb{F}}_n(\mathbf{r}) \cdot \Delta\mathbb{P}(\mathbf{r}) \vec{\mathbb{F}}_\lambda(\mathbf{r}) \otimes \vec{\mathbb{F}}_\lambda(\mathbf{r}') \Delta\mathbb{P}(\mathbf{r}') \vec{\mathbb{F}}_n(\mathbf{r}') d\mathbf{r} d\mathbf{r}'\,, \tag{C.6}$$

leaving out the factor k_n^2. Using the closure relation [85]

$$\mathbb{P}(\mathbf{r}) \sum_\nu \vec{\mathbb{F}}_\nu(\mathbf{r}) \otimes \vec{\mathbb{F}}_\nu(\mathbf{r}') = \mathbb{I}\delta(\mathbf{r} - \mathbf{r}')\,, \tag{C.7}$$

where $\mathbb{I}$ is the 6×6 identity matrix, one can express the sum in the middle of Eq. (C.6) as

$$\sum_\lambda \vec{\mathbb{F}}_\lambda(\mathbf{r}) \otimes \vec{\mathbb{F}}_\lambda(\mathbf{r}') = \mathbb{P}^{-1}(\mathbf{r}) \mathbb{I}\delta(\mathbf{r} - \mathbf{r}') - \sum_n \vec{\mathbb{F}}_n(\mathbf{r}) \otimes \vec{\mathbb{F}}_n(\mathbf{r}'). \tag{C.8}$$

Inserting this into Eq. (C.6) and integrating out the delta function gives

$$\begin{aligned} \sum_\lambda V_{n\lambda} V_{\lambda n} = &\int \vec{\mathbb{F}}_n(\mathbf{r}) \cdot \Delta\mathbb{P}(\mathbf{r}) \mathbb{P}^{-1}(\mathbf{r}) \Delta\mathbb{P}(\mathbf{r}) \vec{\mathbb{F}}_n(\mathbf{r}) d\mathbf{r} \\ &- \sum_n \iint \vec{\mathbb{F}}_n(\mathbf{r}) \cdot \Delta\mathbb{P}(\mathbf{r}) \vec{\mathbb{F}}_n(\mathbf{r}) \otimes \vec{\mathbb{F}}_n(\mathbf{r}') \Delta\mathbb{P}(\mathbf{r}') \vec{\mathbb{F}}_n(\mathbf{r}') d\mathbf{r} d\mathbf{r}'. \end{aligned} \tag{C.9}$$

The first term is clearly second order in $\Delta\mathbb{P}(\mathbf{r})$. However, $\Delta\mathbb{P}(\mathbf{r})$ may not be small, and if we consider a perturbation that is a thin layer of thickness $h(\mathbf{r})$ and approximate the volume

integral with a surface integral multiplied with $h(\mathbf{r})$ (this is equivalent to taking the zeroth order Taylor expansion of the field $\vec{\mathbb{F}}_n(\mathbf{r})$ normal to the surface), then it is clear that the term is first order in the layer thickness h.

The elimination of the static mode contribution via the closure relation has been already explored in [85], in the context of the full matrix equation Eq. (4.2) – this is referred to as ML2 in [85] and corresponds to one of the Mittag-Leffler representations of the dyadic Green's function (GF). However, as shown in [85] this leads to a slow convergence of the RSE, as it turns out that the term $\sum_n \vec{\mathbb{F}}_n(\mathbf{r}) \otimes \vec{\mathbb{F}}_n(\mathbf{r}')$ can also contain a singularity. In the next subsection we will see how the result changes if the full singularity of the static-pole residue of the dyadic GF is taken into account.

C.1.3 Converting second-order term to first order based on the static pole of the Green's dyadic

So far we have not used any symmetry of the basis system. Let us now consider a spherically-symmetric basis system, with isotropic radially dependent permittivity $\hat{\boldsymbol{\varepsilon}}(\mathbf{r}) = \hat{\mathbf{1}}\varepsilon(r)$ and permeability $\hat{\boldsymbol{\mu}}(\mathbf{r}) = \hat{\mathbf{1}}\mu(r)$, where $\hat{\mathbf{1}}$ is the 3×3 identity matrix. As derived in [85], the static pole residue of the dyadic GF of such a system has a δ-like singularity. Following [85], one can write the full dyadic GF in the basis of vector spherical harmonics (VSHs) as

$$\mathbb{G}(\mathbf{r},\mathbf{r}') = \sum_{ij}\sum_{lm}\left[\hat{G}_{ij}(r,r')\right]_{l,m}\mathbf{Y}_{ilm}(\Omega)\otimes\mathbf{Y}_{jlm}(\Omega)\,, \tag{C.10}$$

where $\mathbf{Y}_{ilm}(\Omega)$ are the VSHs with $i = 1,\ 2,\ 3$, and l and m being, respectively, the orbital and magnetic quantum numbers. Here, $\hat{G}_{ij}$ are 2×2 matrices, each consisting of four elements: G_{ij}^{EE}, G_{ij}^{EH}, G_{ij}^{HE}, and G_{ij}^{HH} [compare with Eq. (1.21)], the first and the last element being, respectively, the electric and magnetic part of the Green's dyadic. These two were shown [85] to have δ-like singularities, and their singular parts are given by

$$G_{33}^{EE}(r,r') = \frac{\delta(r-r')}{r^2 k\varepsilon(r)}\,,\quad G_{33}^{HH}(r,r') = \frac{\delta(r-r')}{r^2 k\mu(r)}\,. \tag{C.11}$$

Using the definition $\mathbf{Y}_{3lm}(\Omega) = \hat{\mathbf{r}}Y_{lm}(\Omega)$, where $Y_{lm}(\Omega)$ is a spherical harmonic and $\hat{\mathbf{r}}$ is a unit vector in the radial direction, the closure relation for spherical harmonics

$$\sum_{lm} Y_{lm}(\Omega)Y_{lm}(\Omega') = \frac{1}{\sin\theta}\delta(\theta-\theta')\delta(\phi-\phi')\,, \tag{C.12}$$

and the spherical-coordinate representation of $\delta(\mathbf{r}-\mathbf{r}')$, the static-pole singularity of the Green's dyadic of a spherically-symmetric system takes the form

$$\mathbb{G}_{\text{sing}}(\mathbf{r},\mathbf{r}') = \begin{pmatrix} \hat{\mathbb{G}}_{\text{sing}}^{EE}(\mathbf{r},\mathbf{r}') & 0 \\ 0 & \hat{\mathbb{G}}_{\text{sing}}^{HH}(\mathbf{r},\mathbf{r}') \end{pmatrix} = \frac{\delta(\mathbf{r}-\mathbf{r}')}{k}\mathbb{I}_{\hat{\mathbf{r}}\otimes\hat{\mathbf{r}}}\mathbb{P}^{-1}(\mathbf{r})\,, \tag{C.13}$$

where

$$\mathbb{I}_{\hat{\mathbf{r}}\otimes\hat{\mathbf{r}}} = \begin{pmatrix} \hat{\mathbf{r}}\otimes\hat{\mathbf{r}} & 0 \\ 0 & \hat{\mathbf{r}}\otimes\hat{\mathbf{r}} \end{pmatrix} \quad \text{and} \quad \mathbb{P}(\mathbf{r}) = \begin{pmatrix} \hat{\boldsymbol{\varepsilon}}(\mathbf{r}) & 0 \\ 0 & \hat{\boldsymbol{\mu}}(\mathbf{r}) \end{pmatrix} \tag{C.14}$$

are 6×6 diagonal tensors.

Equation (C.13) allows us to write the static-pole residue of the dyadic GF [see Eq. (1.22)] in the form

$$\sum_{\lambda} \vec{\mathbb{F}}_{\lambda}(\mathbf{r}) \otimes \vec{\mathbb{F}}_{\lambda}(\mathbf{r}') = \mathbb{I}_{\hat{\mathbf{r}}\otimes\hat{\mathbf{r}}}\mathbb{P}^{-1}(\mathbf{r})\delta(\mathbf{r}-\mathbf{r}') + \mathbb{R}(\mathbf{r},\mathbf{r}')\,, \tag{C.15}$$

where $\mathbb{R}(\mathbf{r},\mathbf{r}')$ is a regular part of the Green's dyadic. Using Eq. (C.15) in Eq. (C.6) and integrating the term containing the δ function leads to

$$\begin{aligned} \sum_{\lambda} V_{n\lambda}V_{\lambda n} = &\int \vec{\mathbb{F}}_n(\mathbf{r})\cdot\Delta\mathbb{P}(\mathbf{r})\mathbb{I}_{\hat{\mathbf{r}}\otimes\hat{\mathbf{r}}}\mathbb{P}^{-1}(\mathbf{r})\Delta\mathbb{P}(\mathbf{r})\vec{\mathbb{F}}_n(\mathbf{r})d\mathbf{r} \\ &- \sum_{n}\iint \vec{\mathbb{F}}_n(\mathbf{r})\cdot\Delta\mathbb{P}(\mathbf{r})\mathbb{R}(\mathbf{r},\mathbf{r}')\Delta\mathbb{P}(\mathbf{r}')\vec{\mathbb{F}}_n(\mathbf{r}')d\mathbf{r}d\mathbf{r}'. \end{aligned} \tag{C.16}$$

The first term on the right-hand side of Eq. (C.16) is a single-volume integral and is thus of first order in h, which needs to be included in the first-order perturbation theory result. The second term in Eq. (C.16) contains a double-volume integral, not reducible to a single-volume integral, and is thus of second order, both in $\Delta\mathbb{P}$ and h. We note that $\mathbb{R}(\mathbf{r},\mathbf{r}')$ may also show a singularity when the summation over all quantum numbers l and m is taken, similar to Eq. (C.12); however, this does not influence the first-order results as modes with different l do not mix in first order.

C.1.4 Extracting the first-order correction from all higher-order terms

Based on the results for second order we can expect that even higher-order terms can have a linear in h contribution. Instead of attempting to derive corrections in the infinite perturbation series Eq. (C.4) to arbitrary order and then extracting first-order corrections from them, we take the RSE matrix equation (4.2) in a form which does not explicitly depend on static modes [32, 38, 85]:

$$(\varkappa - k_n)c_n = -\varkappa\sum_{n'}\tilde{V}_{nn'}c_{n'}\,, \tag{C.17}$$

where

$$\tilde{V}_{nn'} = V_{nn'} - S_{nn'} \tag{C.18}$$

and

$$S_{nn'} = \sum_{\lambda\lambda'} V_{n\lambda}W_{\lambda\lambda'}V_{\lambda' n'}, \tag{C.19}$$

with W being the inverse of the matrix $\delta_{\lambda\lambda'} + V_{\lambda\lambda'}$. Note that in what concerns the RSs, Eq. (C.17) is equivalent to Eq. (4.2). We can express the matrix W as a Neumann series [177],

$$W = (I + V)^{-1} = I - V + V^2 - V^3 + V^4 \dots , \tag{C.20}$$

where I is the identity matrix and V has matrix elements $V_{\lambda\lambda'}$, which are overlap integrals between static modes only. Inserting the expansion Eq. (C.20) into Eq. (C.19), we obtain a series (for $n' = n$)

$$S_{nn} = \sum_{\lambda} V_{n\lambda} V_{\lambda n} - \sum_{\lambda\lambda_1} V_{n\lambda} V_{\lambda\lambda_1} V_{\lambda_1 n} + \sum_{\lambda\lambda_1\lambda_2} V_{n\lambda} V_{\lambda\lambda_1} V_{\lambda_1\lambda_2} V_{\lambda_2 n} - \dots , \tag{C.21}$$

which can also be understood as part of the full perturbation series Eq. (C.4) relevant to the first-order correction we are looking for.

Now, using Eq. (C.15) and neglecting any terms containing the regular part of the static-pole residue, we find approximately

$$S_{nn} \approx \int \vec{\mathbb{F}}_n \cdot \left[\Delta\mathbb{P}\mathbb{I}_{\hat{\mathbf{r}}\otimes\hat{\mathbf{r}}}\mathbb{P}^{-1} - \left(\Delta\mathbb{P}\mathbb{I}_{\hat{\mathbf{r}}\otimes\hat{\mathbf{r}}}\mathbb{P}^{-1}\right)^2 + \left(\Delta\mathbb{P}\mathbb{I}_{\hat{\mathbf{r}}\otimes\hat{\mathbf{r}}}\mathbb{P}^{-1}\right)^3 - \dots \right] \Delta\mathbb{P}\vec{\mathbb{F}}_n d\mathbf{r} \,. \tag{C.22}$$

The above infinite series in the square brackets can be summed up, again using the Neumann series Eq. (C.20), which results in

$$S_{nn} \approx \int \vec{\mathbb{F}}_n \cdot \left[\mathbb{I} - \left(\mathbb{I} + \Delta\mathbb{P}\mathbb{I}_{\hat{\mathbf{r}}\otimes\hat{\mathbf{r}}}\mathbb{P}^{-1}\right)^{-1} \right] \Delta\mathbb{P}\vec{\mathbb{F}}_n d\mathbf{r}, \tag{C.23}$$

so that finally

$$\tilde{V}_{nn} = V_{nn} - S_{nn} \approx \int \vec{\mathbb{F}}_n \cdot \left(\mathbb{I} + \Delta\mathbb{P}\mathbb{I}_{\hat{\mathbf{r}}\otimes\hat{\mathbf{r}}}\mathbb{P}^{-1}\right)^{-1} \Delta\mathbb{P}\vec{\mathbb{F}}_n d\mathbf{r}. \tag{C.24}$$

Equation (C.24) is a generalization of Eq. (9) of the main text, and is one of the main results of this work. It provides the exact first-order correction to the wave number via

$$\varkappa = k_n - k_n \tilde{V}_{nn} \,. \tag{C.25}$$

The above result is valid for spherically-symmetric systems described by the generalized permittivity $\mathbb{P}(r)$, which are subject to an arbitrary perturbation $\Delta\mathbb{P}(\mathbf{r})$ without assumptions regarding its symmetry. Equation (C.25) can also be seen as a first-order approximation to the diagonal version of Eq. (C.17), similar to Eq. (C.5) but using the modified matrix elements Eq. (C.18). When $\Delta\mathbb{P}$ is small, for example in case of a small homogeneous perturbation across the whole sphere, the term $\Delta\mathbb{P}\mathbb{I}_{\hat{\mathbf{r}}\otimes\hat{\mathbf{r}}}\mathbb{P}^{-1}$ in Eq. (C.24) provides a second-order contribution due to the static modes, and the original first-order approximation Eq. (C.2) to the matrix equation Eq. (4.2) is recovered. However, when $\Delta\mathbb{P}$ is not small, as in the case of a shape

deformation of an interface hosting a discontinuity of $\mathbb{P}$, the term $\Delta\mathbb{P}\mathbb{I}_{\hat{\mathbf{r}}\otimes\hat{\mathbf{r}}}\mathbb{P}^{-1}$ provides a first-order contribution coming from the static modes, in this way modifying the first-order perturbation theory result.

In order to bring the above result to a more familiar form, let us consider unperturbed and perturbed non-magnetic systems with isotropic permittivity. Equation (C.24) then simplifies to

$$\tilde{V}_{nn} \approx \int \mathbf{E}_n(\mathbf{r}) \cdot \Delta\hat{P}(\mathbf{r})\mathbf{E}_n(\mathbf{r}) d\mathbf{r}\,, \tag{C.26}$$

where

$$\Delta\hat{P}(\mathbf{r}) = \begin{pmatrix} \Delta\varepsilon(\mathbf{r}) & 0 & 0 \\ 0 & \Delta\varepsilon(\mathbf{r}) & 0 \\ 0 & 0 & \frac{\varepsilon(r)\Delta\varepsilon(\mathbf{r})}{\varepsilon(r)+\Delta\varepsilon(\mathbf{r})} \end{pmatrix}, \tag{C.27}$$

with the bottom-right corner representing the $\hat{\mathbf{r}}\otimes\hat{\mathbf{r}}$ component of the tensor. In terms of the electric field components parallel and normal to the surface of the basis system, Eq. (C.26) can be written as

$$\tilde{V}_{nn} \approx \int \left[\mathbf{E}_n^{\parallel}(\mathbf{r}) \cdot \Delta\varepsilon(\mathbf{r})\mathbf{E}_n^{\parallel}(\mathbf{r}) + \mathbf{E}_n^{\perp}(\mathbf{r}) \cdot \frac{\varepsilon(r)\Delta\varepsilon(\mathbf{r})}{\varepsilon(r)+\Delta\varepsilon(\mathbf{r})}\mathbf{E}_n^{\perp}(\mathbf{r})\right] d\mathbf{r}\,. \tag{C.28}$$

This is consistent with the results in [85], where the same perturbation matrix was obtained for the general RSE from a modified spectral representation of the Green's dyadic, in which the singular part of the static pole was kept as a δ-like term, not expanded as a series. This has led, in particular, to a significantly faster convergence of the RSE. Interestingly, in [21], the same perturbation matrix as in Eq. (C.27) was obtained, specifically for a shape perturbation. It was derived by using both the inside and outside fields in the overlap integral, and by taking the zeroth order of the Taylor expansion of the field, i.e. its value at the surface. A similar method was used later on in [51], again for shape perturbations. The approach of [21, 51], however, masks the contribution of the static modes to the first-order correction and is limited to shape deformations only. Here we reproduce their results by fully considering the static pole of the Green's dyadic. In [77], which builds on the results of [76], the perturbation term $\frac{\varepsilon\Delta\varepsilon}{\varepsilon+\Delta\varepsilon}$ was also used, but for both components of the TM field. For small $\Delta\varepsilon$ this gives the correct results as it was shown in the paper, however we expect that this fails for larger $\Delta\varepsilon$, which is the case of a shape perturbation. In [102], TM polarization was considered for a photonic-crystal slab at non-normal incidence. While the permittivity change was large, the volume of the change was small, and seemingly accurate results could be obtained without using static modes for RSs of $ka \approx 0.2$, where $a = 100\,\text{nm}$ was the characteristic length of the structure (of the order of the thickness of the grating and its period). To the best of

our knowledge, the role of static modes has not been yet investigated in photonic-crystal structures.

C.2 Example: Dielectric sphere in vacuum

In this section, we provide a few illustrations of the first-order results derived in Sec. C.1 and their comparison with the exact solutions for a dielectric sphere in vacuum, perturbing either its refractive index (volume perturbation) or its size (boundary perturbation). The general formula correctly describing the wave number of a perturbed RS to first order is given by Eq. (C.25),

$$\varkappa = k_n - k_n \tilde{V}_{nn} = k_n - k_n (V_{nn} - S_{nn}) \,, \tag{C.29}$$

here written also in terms of V_{nn} and S_{nn}, given by Eqs. (4.3) and (C.23), respectively. This highlights the importance of the static-mode contribution S_{nn}, which will be evaluated for the examples treated below, along with the diagonal matrix element V_{nn}. As basis system we choose in all examples a dielectric sphere of radius R and permittivity $\varepsilon = 4$, surrounded by vacuum.

C.2.1 Material perturbation

We apply the first-order formula Eq. (C.29) to the homogeneous dielectric sphere in vacuum, perturbed uniformly, so that the permittivity of the sphere changes by $\Delta\varepsilon$. A particular change of the permittivity profile is illustrated in Fig. C.2.1b. Here we focus on perturbation of the transverse-magnetic (TM) RSs with $l = 1$. For this value of the angular momentum, the spectrum of the basis system in the complex k plane, shown in Fig. C.2.1a, consists of only Fabry-Pérot modes, which for large $|k|$ are spaced with a period of $\pi/2\sqrt{\varepsilon}R$ in $\mathrm{Re}(k)$, and have the imaginary part converging to $\mathrm{Im}(k) = -\ln((\sqrt{\varepsilon}-1)/(\sqrt{\varepsilon}+1))/(2\sqrt{\varepsilon}R)$, similar to the modes of a homogeneous slab at normal incidence [14, 104].

Applying a perturbation to the fundamental mode, shown in Fig. C.2.1(c) up to $\Delta\varepsilon = 0.04$, reveals excellent agreement between the first-order result Eq. (C.29) and the exact solution. For all the RSs shown in Fig. C.2.1a, we provide in d) and e) more details for $\Delta\varepsilon = 0.004$ and $\Delta\varepsilon = 0.04$, corresponding to, respectively, 0.1% and 1% change of the permittivity. V_{nn} and S_{nn} are given in Fig. C.2.1d. For the applied perturbations, $\Delta\varepsilon \ll 1$. Therefore, V_{nn} which is of first order in $\Delta\varepsilon$ dominates, whereas S_{nn} which is of second order in $\Delta\varepsilon$ is negligible. Accordingly, V_{nn} scales linearly and S_{nn} scales quadratically with $\Delta\varepsilon$. This is consistent with examples in the literature, where for small $\Delta\varepsilon$ static mode contributions were not included

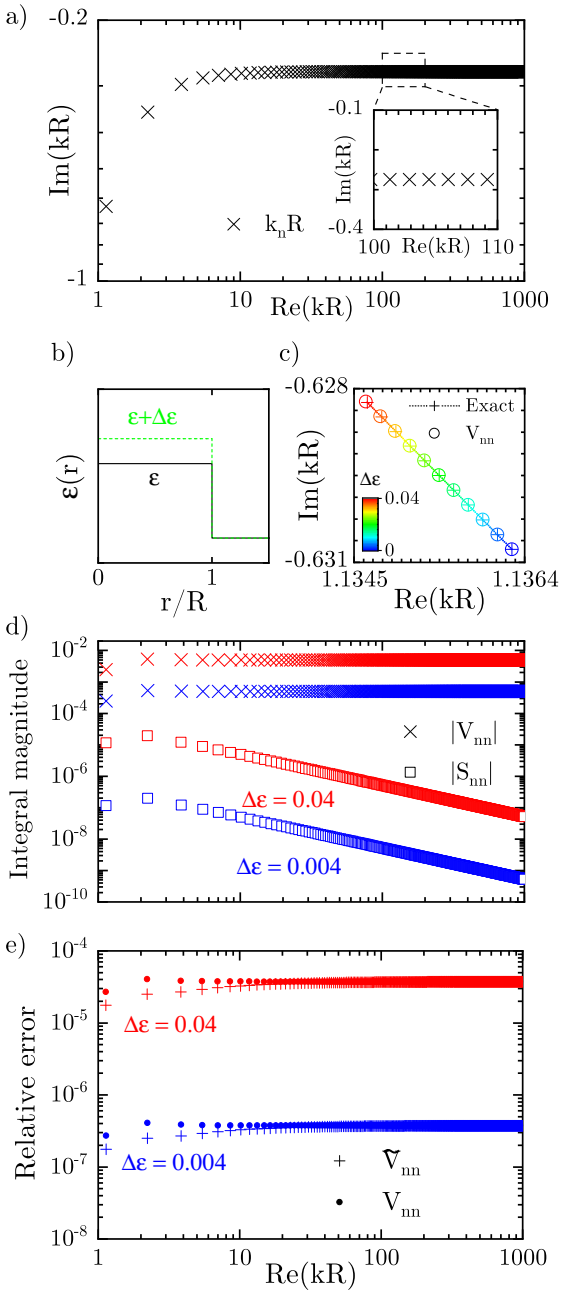

Fig. C.2.1: a) Wave numbers of TM modes with angular momentum $l = 1$ of a dielectric sphere with permittivity $\varepsilon = 4$ and radius R, surrounded by vacuum; b) illustration of the homogeneous permittivity perturbation across the sphere; c) perturbed wave number of the fundamental RS with the permittivity change given by the color code; d) magnitude of the matrix elements $|V_{nn}|$ and $|S_{nn}|$ of the perturbation; e) relative error of the perturbed RS wave numbers calculated with (crosses) and without (dots) inclusion of static modes.

in the RSE [178]. The magnitude of S_{nn} is reducing with increasing $|k|$. This is intuitively expected as we move away from the influence of the $k = 0$ pole in the k-plane. Figure C.2.1e shows the relative error with respect to the exact solution of the first-order Eq. (C.29), with

or without the static-mode contribution, which is given by S_{nn}. One can see that the error scales quadratically in $\Delta\varepsilon$ for both, confirming that first-order correction to k is accurate for all the RSs. The relative errors calculated with or without static modes are very similar, confirming that the static pole of the Green's dyadic has a weak contribution when $\Delta\varepsilon$ is small.

C.2.2 Size perturbation

We now apply to the same homogeneous dielectric sphere as in the previous section a perturbation that changes its size by h. This corresponds to a perturbation $\Delta\varepsilon = 1 - \varepsilon$, applied to a layer of thickness $|h|$ on the inner side of the surface of sphere. The permittivity change is illustrated in Fig. C.2.2a, which corresponds to the shift of an interface hosting a discontinuity of ε. We apply a perturbation of $h/R = -0.01$ and $h/R = -0.001$, corresponding to, respectively, 1% and 0.1% change of the initial size, with the minus sign noting a decrease of the sphere radius. One can see from Fig. C.2.2b that in the complex k plane, the first-order result for the fundamental mode, calculated via Eq. (C.29), is in good agreement with the exact solution.

Figure C.2.2c shows the values of V_{nn} and S_{nn} for a large number of the RSs. For small k both V_{nn} and S_{nn} contribute with a similar magnitude, and for all k both change linearly with h. This confirms that both terms contribute in first order under size perturbation. The magnitude of S_{nn} decreases for large k as discussed above. We can see that in this region $\tilde{V}_{nn} = V_{nn} - S_{nn}$ fluctuates with k, which we would not expect if the first order approximation was correct. To understand this, we recall that the secular equation determining the modes use the dimensionless quantity kR, so that k and R are inversely proportional to each other for a given mode under size perturbation. Therefore, the perturbed wave number should be $\varkappa = k_n R/(R+h) \approx k_n/(1+\tilde{V}_{nn})$, or alternatively, $\varkappa \approx k_n(1-\tilde{V}_{nn}) \approx k_n(1-h/R)$, implying that V_{nn} should be constant with respect to k_n in first order.

One can see from Fig. C.2.2d that the error for RSs of low $|k|$ can increase by several orders of magnitude when the static modes are not included, exemplifying their importance. The relative error scales quadratically with h for $|kh| \ll 1$. The error increases with k, and at $|kh| = 1$ we can observe that the error only reduces proportionally to h. This is further exemplified in Fig. C.2.2e by showing the absolute error (expected to scale quadratically) relative to the change of the wave number scaling linearly when $|kh| < 1$. This suggests that the first-order approximation requires $|kh| \ll 1$. This, together with the oscillations in the magnitude of the matrix elements, also suggests that for size perturbations, contributions

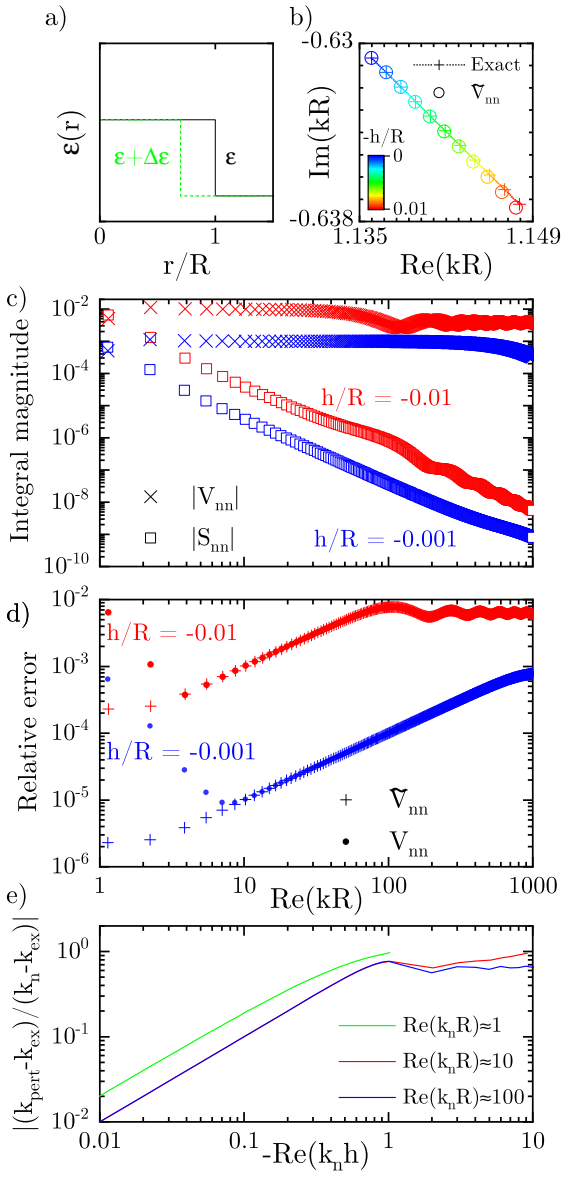

Fig. C.2.2: a) Illustration of the permittivity perturbation corresponding to a radius reduction of the sphere by $-h$; b) perturbed wave number of the fundamental RS with the sphere radius change given by the color code; c) magnitude of the matrix elements $|V_{nn}|$ and $|S_{nn}|$ of the perturbation; d) relative error of the perturbed RS wave numbers calculated with (crosses) and without (dots) inclusion of static modes; e) absolute error of the perturbed RS wave numbers relative to the wave number change due to the perturbation, as functions of $-h$, for three selected modes.

from other neighbouring RSs are important for Fabry-Pérot modes when $|kh| \gtrsim 1$, meaning that higher-order corrections need to be taken into account in the perturbation series representation Eq. (C.4), or alternatively, in the context of the full matrix equation Eq. (4.2), the off-diagonal elements cannot be neglected.

Moving to an angular momentum number $l = 50$, the results of the size perturbation

are shown in Fig. C.2.3. For larger values of l, high-quality whispering-gallery modes form in spectra, and the fundamental mode position shifts to higher k. Also, a sharper peak associated with the Brewster angle is formed in the spectrum of the RSs [104].

We find that for this high l the role of the static pole is lessened, but still relevant, reducing the error by up to an order of magnitude for the whispering-gallery modes. The contribution from both matrix elements scales about the same way as for the $l = 1$ case, i.e. linearly in h, but here the magnitude of the static-mode contribution is significantly smaller than the RS contribution. This is related to the large detuning $1 \ll |kR|$ from the static pole. Considering the field contribution to the overlap integrals, for low values of the angular momentum the tangential and radial component of the field are similar in magnitude, whereas for high l the radial part, which contributes to the static-pole integral, is much weaker.

Considering the relative error, we observe the same features as for $l = 1$, namely, small error for the initial modes, which then grows up to the point $|kh| \approx 1$. If we compare relative errors with and without the static pole included, we can see that with their correct inclusion we still gain an order of magnitude accuracy for the $h/R = -0.001$ case, and about a factor of 2 for $h/R = -0.01$. In Fig. C.2.3d we can see that for larger perturbations, the fundamental whispering-gallery mode produces higher errors relative to the change of the wave number when compared to Fabry-Pérot modes. This could be due to the strong localization of the whispering-gallery mode close to the surface of the sphere.

C.3 Alternative derivation for spherically-symmetric systems

In this section, we focus on non-dispersive dielectric spherically-symmetric systems, in order to provide explicit and easy-to-follow derivations of the first-order correction to the RS wave numbers. We start with the RSs in transverse-electric (TE) polarization where the correct first-order result is identically to the diagonal approximation within the standard RSE approach. We then focus on TM polarization where we will illustrate the difference between the standard first-order term (diagonal approximation) and our modified first-order term (which includes static mode), and discuss the source of their inconsistency in relation to the smoothness of the field. For simplicity we use a closed system approximation, therefore the integrals have a finite limit, but identical results based on more rigorous approaches, either with the regularisation of the field, as in Ref. [48], or with use of the expansion formulas for the field, can be found in the the supplement of [50].

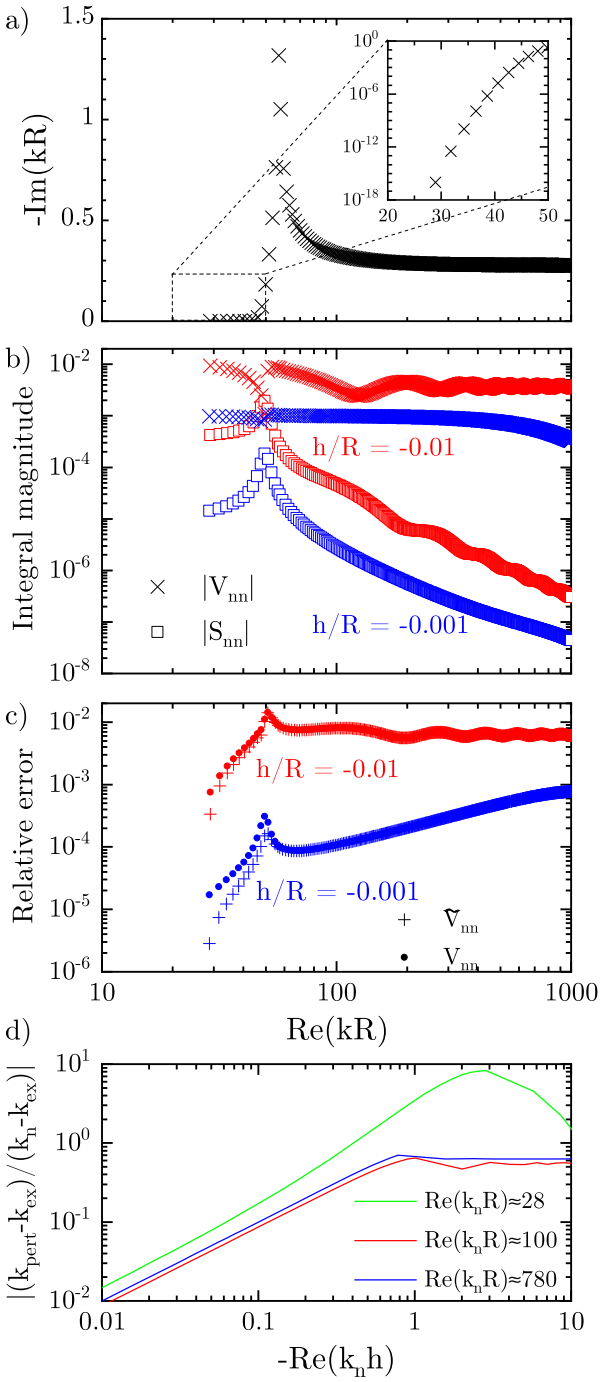

Fig. C.2.3: a) Wave numbers of TM modes with angular momentum $l = 50$ of a dielectric sphere with radius R and permittivity $\varepsilon = 4$, surrounded by vacuum. Inset shows a zoom of the high-quality whispering-gallery modes in a logarithmic scale; b) magnitude of the matrix elements $|V_{nn}|$ and $|S_{nn}|$ of the perturbation; c) relative error of the perturbed RS wave numbers calculated with (crosses) and without (dots) inclusion of static modes; d) absolute error of the perturbed RS wave numbers relative to the wave number change due to the perturbation, as functions of $-h$, for three selected modes. Green line is the fundamental whispering-gallery mode.

C.3.1 TE polarization

In TE polarization, Maxwell's wave equation for the RSs is reduced to a scalar wave equation for the electric field [85, 104],

$$\left[\frac{d^2}{dr^2} - \frac{\alpha^2}{r^2} + \varepsilon(r)k_n^2\right] E_n(r) = 0\,, \tag{C.30}$$

where r is the radial coordinate, $\varepsilon(r)$ is the permittivity of the unperturbed spherically-symmetric system, $\alpha^2 = l(l+1)$, l is the orbital quantum number, k_n is the RS wave number, and $E_n(r)/r$ is the radially-dependent part of the RS electric field.

A perturbed RS in TE polarization, with the wave number k and electric field $E(r)$, satisfies the perturbed wave equation

$$\left[\frac{d^2}{dr^2} - \frac{\alpha^2}{r^2} + \varepsilon(r)k^2 + \Delta\varepsilon(r)k^2\right] E(r) = 0\,, \tag{C.31}$$

where $\Delta\varepsilon(r)$ is a perturbation of the permittivity.

Multiplying Eq. (C.30) with $E(r)$, and Eq. (C.31) with $E_n(r)$, then integrating over the system volume up to just outside the boundary, then taking the difference between the two equations, approximating the *continuous* and *smooth* functions as $E(r) \approx E_n(r)$ we obtain

$$\int_0^R \left(\varepsilon k_n^2 - \varepsilon k^2 - \Delta\varepsilon k^2\right) E_n E_n dr = 0\,, \tag{C.32}$$

Then, using the approximate normalisation for high quality modes $2\int_0^R \varepsilon(r)E^2(r)\mathrm{d}r \approx 1$, keeping only the first order terms we get

$$k - k_n \approx -k_n \int_0^R \Delta\varepsilon(r)E_n^2(r)dr\,, \tag{C.33}$$

The same equation can be derived more rigorously for any mode, regardless of the quality, and this is done more generally in Appendix C.5.

C.3.2 TM polarization

Now we apply the approach to the RSs in TM polarization. In this polarization, Maxwell's wave equation is also reducible to a scalar wave equation, but for the magnetic field [85, 104]:

$$\left[\frac{d}{dr}\frac{1}{\varepsilon(r)}\frac{d}{dr} - \frac{\alpha^2}{r^2\varepsilon(r)} + k_n^2\right] H_n(r) = 0\,, \tag{C.34}$$

where $-iH_n(r)/r$ is the radially-dependent part of the RS magnetic field. The wave equation for a perturbed RS with the wave number k and magnetic field $H(r)$ is given by

$$\left[\frac{d}{dr}\frac{1}{\varepsilon_\mathrm{p}(r)}\frac{d}{dr} - \frac{\alpha^2}{r^2\varepsilon_\mathrm{p}(r)} + k^2\right] H(r) = 0\,, \tag{C.35}$$

where

$$\varepsilon_{\mathrm{p}}(r) = \varepsilon(r) + \Delta\varepsilon(r) \tag{C.36}$$

and $\Delta\varepsilon(r)$ is a perturbation of the permittivity, as before. Again, multiplying Eq. (C.34) with $H(r)$ and Eq. (C.35) with $H_n(r)$, taking their difference and integrating the result over they system we find

$$\int_0^R \left(H \frac{d}{dr}\frac{1}{\varepsilon} H_n' - H_n \frac{d}{dr}\frac{1}{\varepsilon_{\mathrm{p}}} H' \right) dr + \int_0^R \frac{\alpha^2}{r^2} \left(\frac{1}{\varepsilon_{\mathrm{p}}} - \frac{1}{\varepsilon} \right) H H_n dr + (k_n^2 - k^2) \int_0^R H H_n dr = 0\,. \tag{C.37}$$

Integrating by parts, and approximating the perturbed *continuous* functions with continuous unperturbed functions in zeroth order as

$$H(r) \approx H_n(r)\,, \qquad \frac{H'(r)}{\varepsilon_{\mathrm{p}}(r)} \approx \frac{H_n'(r)}{\varepsilon(r)}\,, \tag{C.38}$$

we obtain

$$-\int_0^R \left[\frac{\Delta\varepsilon}{\varepsilon^2} \left(H_n'\right)^2 + \frac{\alpha^2}{r^2} \frac{\Delta\varepsilon_{\mathrm{p}}}{\varepsilon_{\mathrm{p}}\varepsilon} H_n^2 - (k^2 - k_n^2) H_n^2 \right] dr \approx 0\,, \tag{C.39}$$

from where we find the first-order correction to the wave number:

$$k - k_n \approx \frac{1}{k_n} \frac{-\int_0^R \Delta\varepsilon \left[\left(\frac{H_n'}{\varepsilon} \right)^2 + \frac{\alpha^2}{r^2} \frac{H_n^2}{\varepsilon_{\mathrm{p}}\varepsilon} \right] dr}{2\int_0^R H_n^2 dr}\,. \tag{C.40}$$

Now, using the electric field component definitions from Ref. [85] or Chap. 3, and the approximate normalisation for high quality modes $2\int_0^R H_n^2 dr \approx 1$ we end up with the correct first-order formula

$$k - k_n \approx -k_n \int_0^R \Delta\varepsilon \left[{E_n^{\parallel}}^2 + \frac{\varepsilon}{\varepsilon_{\mathrm{p}}} {E_n^{\perp}}^2 \right] dr\,, \tag{C.41}$$

Using only the 'naive' zeroth order approximation $H(r) \approx H_n(r)$ and then differentiating it in the expression leads to incorrect results in case of boundary shift. This is due to the discontinuity of the field derivative shifting with the boundary.

In terms of standard expansion formulas for the field, as the eigenmdoes are complete, we can write $H(r) = \sum_n c_n H_n(r)$, which results in the derivative $H'(r) = \sum_n c_n H_n'(r)$. The latter follows from the completeness of the modes, but it is a slowly converging expansion due to the discontinuity. Instead, we can chose the expansion $H'(r)/\varepsilon_{\mathrm{p}}(r) = \sum_n c_n H_n'(r)/\varepsilon(r) + \sum_\lambda c_\lambda f_\lambda(r)$, where we need to add the additional functions f_λ, such as static modes, in the form of the second term on the right hand side, as the validity of the expansion without them does not follow from the standard expansion.

C.4 Other fields of physics

In this section, we consider examples from other fields of physics describing wave phenomena and demonstrate that for systems with interfaces, the same effect of higher-order terms of the perturbation series contributing to the first-order correction (in the deformation depth) to the eigenmode wave numbers takes place.

C.4.1 Condensed matter physics: Effective-mass approximation for semiconductor heterostructures

In condensed matter physics, an effective Schrödinger wave equation describing the motion of a carrier (an electron or a hole) has the following form in the effective-mass approximation:

$$\left[-\frac{\hbar^2}{2}\nabla\cdot\hat{\boldsymbol{\mu}}^{-1}(\mathbf{r})\nabla + V(\mathbf{r})\right]\Psi(\mathbf{r}) = E\Psi(\mathbf{r})\,, \tag{C.42}$$

where $\hat{\boldsymbol{\mu}}(\mathbf{r})$ is a spatially-dependent tensor of the effective mass which depends on the material and can change abruptly at material interfaces. While typical semiconductor heterostructures have planar interfaces separating different materials, we concentrate below on spherically-symmetric systems, in order to ease a comparison with TM modes in optical systems considered in detail in Sec. C.3.2.

For a spherically-symmetric isotropic effective mass $\mu(r)$ and spherically-symmetric potential $V(r)$, Eq. (C.42) reduces to:

$$\left[\frac{d}{dr}\frac{1}{\mu(r)}\frac{d}{dr} - \frac{\alpha^2}{r^2} - V(r) + k_n^2\right]\psi_n(r) = 0\,, \tag{C.43}$$

where $\psi_n(r)/r$ is the radial part of the full wave function $\Psi(\mathbf{r})$, $k_n = \sqrt{E_n}$ is a wave number corresponding to the state energy E_n, and index n is used to label quantum RSs. Here units with $\hbar^2 = 2$ are used for brevity of notations.

We consider also a perturbed Schrödinger wave equation

$$\left[\frac{d}{dr}\frac{1}{\mu_p(r)}\frac{d}{dr} - \frac{\alpha^2}{r^2} - V_p(r) + k^2\right]\psi(r) = 0 \tag{C.44}$$

for perturbed wave number k and wave function $\psi(r)$, and

$$\mu_p(r) = \mu(r) + \Delta\mu(r)\,, \quad V_p(r) = V(r) + \Delta V(r)\,, \tag{C.45}$$

where $\Delta\mu(r)$ and $\Delta V(r)$ are perturbations of the effective mass and potential, respectively. There is a clear similarity with the TM optical case Sec. C.3.2, with once again the wavefunction being continuous and non-smooth, and the first-order results would be similarly modified as before.

C.4.2 Acoustics

The acoustic wave equation for the total pressure $P = p + \delta p$ in inhomogeneous quiescent (static) media, with constant ambient pressure p, spatially variable ambient density ρ and speed of sound c, with gravity neglected, can be written, assuming harmonic time dependence, as [179]

$$\rho \boldsymbol{\nabla} \cdot \left(\frac{1}{\rho} \boldsymbol{\nabla} P \right) + k^2 P = 0 \,, \tag{C.46}$$

which, in case of a spherically symmetric inhomogeneity creating an acoustic cavity can be written as

$$\left(\rho(r) \frac{d}{dr} \frac{1}{\rho(r)} \frac{d}{dr} - \frac{\alpha^2}{r^2} \right) P(r) + k^2 P(r) = 0 \,. \tag{C.47}$$

The acoustic boundary conditions at an interface mean that the pressure is continuous, though not necessarily smooth, but the medium velocity normal to the surface is continuous. "The requirement of pressure continuity assumes no mass transport across the interface and neglects surface tension; under such circumstances it is the fluid-dynamic counterpart of Newton's third law" [179]. The requirement for the velocity component approximately means that the normal component of the displacement to the surface element is continuous. The second-order operator in Eq. (C.46) has the form similar to that in Eq. (C.42), with a discontinuous density $\rho(\mathbf{r})$ in the case of a boundary between two media playing the same role as the discontinuous effective mass tensor. Note that here it is assumed that the densities of both media separated by an interface are finite, allowing propagation of waves on either side of the interface. This is different from the boundary perturbation for eigenmodes in cavities where a soft or hard (rigid) boundary is assumed. The former assumption leads to zero pressure at the boundary, whereas the latter to zero propagation velocity along the surface normal. Both cases allow application of the perturbative methods from [139] and have been treated in the literature [180, 181].

C.5 Full derivation of Eq. (4.18)

In this section, we provide a full derivation of Eq. (4.18) of the main text and indicate its validity in first order for perturbations located also outside the optical resonator.

Maxwell's equations for the unperturbed system can be written in the form [68]

$$\left[k_n \hat{\mathbb{P}}_0(k_n, \mathbf{r}) - \hat{\mathbb{D}}(\mathbf{r}) \right] \vec{\mathbb{F}}_n(\mathbf{r}) = 0 \,, \tag{C.48}$$

where

$$\hat{\mathbb{P}}_0(k,\mathbf{r}) = \begin{pmatrix} \hat{\boldsymbol{\varepsilon}}(k,\mathbf{r}) & -i\hat{\boldsymbol{\xi}}(k,\mathbf{r}) \\ i\hat{\boldsymbol{\zeta}}(k,\mathbf{r}) & \hat{\boldsymbol{\mu}}(k,\mathbf{r}) \end{pmatrix}, \quad \hat{\mathbb{D}}(\mathbf{r}) = \begin{pmatrix} \hat{\mathbf{0}} & \nabla\times \\ \nabla\times & \hat{\mathbf{0}} \end{pmatrix}, \quad \vec{\mathbb{F}}_n(\mathbf{r}) = \begin{pmatrix} \mathbf{E}_n(\mathbf{r}) \\ i\mathbf{H}_n(\mathbf{r}) \end{pmatrix}. \tag{C.49}$$

The electromagnetic field $\vec{\mathbb{F}}(\mathbf{r})$ and the wave number k of a perturbed RS are, in turn, solutions of the perturbed Maxwell equations

$$\left[k\hat{\mathbb{P}}(k,\mathbf{r}) - \hat{\mathbb{D}}(\mathbf{r})\right]\vec{\mathbb{F}}(\mathbf{r}) = 0\,, \tag{C.50}$$

where $\hat{\mathbb{P}}(k,\mathbf{r}) = \hat{\mathbb{P}}_0(k,\mathbf{r}) + \Delta\hat{\mathbb{P}}(k,\mathbf{r})$,

$$\vec{\mathbb{F}}(\mathbf{r}) = \begin{pmatrix} \mathbf{E}(\mathbf{r}) \\ i\mathbf{H}(\mathbf{r}) \end{pmatrix}, \quad \text{and} \quad \Delta\hat{\mathbb{P}}(k,\mathbf{r}) = \begin{pmatrix} \Delta\hat{\boldsymbol{\varepsilon}}(k,\mathbf{r}) & -i\Delta\hat{\boldsymbol{\xi}}(k,\mathbf{r}) \\ i\Delta\hat{\boldsymbol{\zeta}}(k,\mathbf{r}) & \Delta\hat{\boldsymbol{\mu}}(k,\mathbf{r}) \end{pmatrix} \tag{C.51}$$

is a perturbation. As in the main text, we assume below isotropic and reciprocal materials. Multiplying Eq. (C.48) with $\vec{\mathbb{F}}$ and Eq. (C.50) with $\vec{\mathbb{F}}_n$, integrating both equations over the unperturbed system volume V_0 containing the perturbation $\Delta\hat{\mathbb{P}}$, and taking the difference between the results, we obtain

$$\begin{aligned} &\int_{V_0}\left[\vec{\mathbb{F}}(\mathbf{r})\cdot k_n\hat{\mathbb{P}}_0(k_n,\mathbf{r})\vec{\mathbb{F}}_n(\mathbf{r}) - \vec{\mathbb{F}}_n(\mathbf{r})\cdot k\hat{\mathbb{P}}(k,\mathbf{r})\vec{\mathbb{F}}(\mathbf{r})\right]d\mathbf{r} \\ &-\int_{V_0}\left[\vec{\mathbb{F}}(\mathbf{r})\cdot\hat{\mathbb{D}}(\mathbf{r})\vec{\mathbb{F}}_n(\mathbf{r}) - \vec{\mathbb{F}}_n(\mathbf{r})\cdot\hat{\mathbb{D}}(\mathbf{r})\vec{\mathbb{F}}(\mathbf{r})\right]d\mathbf{r} = 0\,. \end{aligned} \tag{C.52}$$

The second line in Eq. (C.52) can be transformed, using the divergence theorem, to the surface integral [68]

$$-i\oint_{S_0}\left[\mathbf{E}_n(\mathbf{r})\times\mathbf{H}(\mathbf{r}) - \mathbf{E}(\mathbf{r})\times\mathbf{H}_n(\mathbf{r})\right]\cdot d\mathbf{S}\,, \tag{C.53}$$

where S_0 is the boundary of V_0. To proceed with the first line in Eq. (C.52), we use the real, normalized vector field $\hat{\mathbf{n}}(\mathbf{r})$ introduced in the main text, which is normal to both surfaces S_0 and S of the unperturbed and perturbed systems, respectively. We then define the projections of perturbed and unperturbed RS fields,

$$\begin{aligned} \vec{\mathbb{F}}^{\perp}(\mathbf{r}) &= \begin{pmatrix} \mathbf{E}^{\perp}(\mathbf{r}) \\ i\mathbf{H}^{\perp}(\mathbf{r}) \end{pmatrix} = \begin{pmatrix} \hat{\mathbf{n}}(\mathbf{r})[\hat{\mathbf{n}}(\mathbf{r})\cdot\mathbf{E}(\mathbf{r})] \\ \hat{\mathbf{n}}(\mathbf{r})[\hat{\mathbf{n}}(\mathbf{r})\cdot i\mathbf{H}(\mathbf{r})] \end{pmatrix}, \\ \vec{\mathbb{F}}_n^{\perp}(\mathbf{r}) &= \begin{pmatrix} \mathbf{E}_n^{\perp}(\mathbf{r}) \\ i\mathbf{H}_n^{\perp}(\mathbf{r}) \end{pmatrix} = \begin{pmatrix} \hat{\mathbf{n}}(\mathbf{r})[\hat{\mathbf{n}}(\mathbf{r})\cdot\mathbf{E}_n(\mathbf{r})] \\ \hat{\mathbf{n}}(\mathbf{r})[\hat{\mathbf{n}}(\mathbf{r})\cdot i\mathbf{H}_n(\mathbf{r})] \end{pmatrix}, \end{aligned} \tag{C.54}$$

which are normal to both S_0 and S, and

$$\vec{\mathbb{F}}^{\parallel}(\mathbf{r}) = \vec{\mathbb{F}}(\mathbf{r}) - \vec{\mathbb{F}}^{\perp}(\mathbf{r})\,, \qquad \vec{\mathbb{F}}_n^{\parallel}(\mathbf{r}) = \vec{\mathbb{F}}_n(\mathbf{r}) - \vec{\mathbb{F}}_n^{\perp}(\mathbf{r})\,, \tag{C.55}$$

which are parallel (tangential) to both surfaces. Note that the field is normal or parallel to a surface only when its argument $\mathbf{r}$ describes a point at that surface. Now, according to Maxwell's boundary conditions, fields $\vec{\mathbb{F}}^{\parallel}(\mathbf{r})$ and $\hat{\mathbb{P}}(k,\mathbf{r})\vec{\mathbb{F}}^{\perp}(\mathbf{r})$ are continuous everywhere. Similarly, the unperturbed fields $\vec{\mathbb{F}}_n^{\parallel}(\mathbf{r})$ and $\hat{\mathbb{P}}_0(k_n,\mathbf{r})\vec{\mathbb{F}}_n^{\perp}(\mathbf{r})$, introduced in the same manner, are also continuous. To derive the first-order correction to the wave number, we approximate the perturbed RS field in zeroth order as

$$\vec{\mathbb{F}}^{\parallel}(\mathbf{r}) \approx \vec{\mathbb{F}}_n^{\parallel}(\mathbf{r})\,, \qquad \hat{\mathbb{P}}(k,\mathbf{r})\vec{\mathbb{F}}^{\perp}(\mathbf{r}) \approx \hat{\mathbb{P}}_0(k_n,\mathbf{r})\vec{\mathbb{F}}_n^{\perp}(\mathbf{r})\,, \tag{C.56}$$

in this way respecting Maxwell's boundary conditions on both surfaces. This results in

$$\vec{\mathbb{F}} = \vec{\mathbb{F}}_n^{\parallel} + \hat{\mathbb{P}}^{-1}(k)\hat{\mathbb{P}}_0(k_n)\vec{\mathbb{F}}_n^{\perp} = \vec{\mathbb{F}}_n + \left[\hat{\mathbb{P}}^{-1}(k)\hat{\mathbb{P}}_0(k_n) - 1\right]\vec{\mathbb{F}}_n^{\perp}\,, \tag{C.57}$$

where $\hat{\mathbb{P}}^{-1}(k)$ is the inverse of $\hat{\mathbb{P}}(k)$. Note that here and below, we omit for brevity the spatial arguments but keep the wave number dependence. Now, using Eq. (C.57), the reciprocity of the optical systems, and a Taylor expansion to first order in $k - k_n$ of terms containing the generalized permittivity, such as $\hat{\mathbb{P}}(k,\mathbf{r}) \approx \hat{\mathbb{P}}(k_n,\mathbf{r}) + [\hat{\mathbb{P}}(k,\mathbf{r})]'_{k_n}(k-k_n)$, we find for the integrand of the first line in Eq. (C.52)

$$\begin{aligned}
\left[k_n\hat{\mathbb{P}}_0(k_n) - k\hat{\mathbb{P}}(k)\right]\vec{\mathbb{F}} \;&\approx\; \left[k_n\hat{\mathbb{P}}_0(k_n) - k\hat{\mathbb{P}}_0(k)\right]\vec{\mathbb{F}}_n - k\Delta\hat{\mathbb{P}}(k)\vec{\mathbb{F}}_n \\
&\quad + k_n\hat{\mathbb{P}}_0(k_n)\left[\hat{\mathbb{P}}^{-1}(k)\hat{\mathbb{P}}_0(k_n) - 1\right]\vec{\mathbb{F}}_n^{\perp} - k\left[\hat{\mathbb{P}}_0(k_n) - \hat{\mathbb{P}}(k)\right]\vec{\mathbb{F}}_n^{\perp} \\
&\approx\; -(k-k_n)\left[k\hat{\mathbb{P}}_0(k)\right]'_{k_n}\vec{\mathbb{F}}_n - k\Delta\hat{\mathbb{P}}(k)\vec{\mathbb{F}}_n^{\parallel} \\
&\quad - k_n\hat{\mathbb{P}}_0(k_n)\hat{\mathbb{P}}^{-1}(k)\left[\hat{\mathbb{P}}(k) - \hat{\mathbb{P}}_0(k_n)\right]\vec{\mathbb{F}}_n^{\perp} - k\left[\hat{\mathbb{P}}_0(k_n) - \hat{\mathbb{P}}_0(k)\right]\vec{\mathbb{F}}_n^{\perp} \\
&\approx\; -(k-k_n)\left[k\hat{\mathbb{P}}_0(k)\right]'_{k_n}\vec{\mathbb{F}}_n - k\Delta\hat{\mathbb{P}}(k)\vec{\mathbb{F}}_n^{\parallel} - k_n\hat{\mathbb{P}}_0(k_n)\hat{\mathbb{P}}^{-1}(k)\Delta\hat{\mathbb{P}}(k)\vec{\mathbb{F}}_n^{\perp}\,,
\end{aligned} \tag{C.58}$$

in the last line neglecting higher-order terms, which are

$$k_n(k-k_n)\left[\hat{\mathbb{P}}(k) - \hat{\mathbb{P}}_0(k_n)\right]\hat{\mathbb{P}}^{-1}(k)\left[\hat{\mathbb{P}}_0(k)\right]'_{k_n}\vec{\mathbb{F}}_n^{\perp} + (k-k_n)^2\left[\hat{\mathbb{P}}_0(k)\right]'_{k_n}\vec{\mathbb{F}}_n^{\perp}\,.$$

Finally, using an analytic continuation $\vec{\mathbb{Q}}(k,\mathbf{r})$ of the RS field in the area outside the resonator, such that $\vec{\mathbb{Q}}(k,\mathbf{r}) = \vec{\mathbb{F}}(\mathbf{r})$ and $\vec{\mathbb{Q}}(k_n,\mathbf{r}) = \vec{\mathbb{F}}_n(\mathbf{r})$, and also Taylor expanding it to first order,

$$\vec{\mathbb{Q}}(k,\mathbf{r}) \approx \vec{\mathbb{F}}_n(\mathbf{r}) + (k-k_n)\vec{\mathbb{F}}'_n(\mathbf{r})\,, \tag{C.59}$$

the surface term Eq. (C.53) transforms to

$$-i(k-k_n)\oint_{S_0}\left[\mathbf{E}_n(\mathbf{r})\times\mathbf{H}'_n(\mathbf{r}) - \mathbf{E}'_n(\mathbf{r})\times\mathbf{H}_n(\mathbf{r})\right]\cdot d\mathbf{S}\,. \tag{C.60}$$

Substituting the last line of Eq. (C.58) and the surface integral Eq. (C.60) into Eq. (C.52) and taking the limit $k \to k_n$, we find the first-order correction to the wave number:

$$k - k_n \approx -\frac{k_n \int_{V_0} \left[\vec{\mathbb{F}}_n^{\parallel} \cdot \Delta\hat{\mathbb{P}}\vec{\mathbb{F}}_n^{\parallel} + \vec{\mathbb{F}}_n^{\perp} \cdot \hat{\mathbb{P}}_0\hat{\mathbb{P}}^{-1}\Delta\hat{\mathbb{P}}\vec{\mathbb{F}}_n^{\perp}\right] d\mathbf{r}}{\int_{V_0} \vec{\mathbb{F}}_n \cdot \left[k\hat{\mathbb{P}}_0\right]'_{k_n} \vec{\mathbb{F}}_n d\mathbf{r} + i \oint_{S_0} (\mathbf{E}_n \times \mathbf{H}'_n - \mathbf{E}'_n \times \mathbf{H}_n) \cdot d\mathbf{S}}\,, \tag{C.61}$$

which is identical to Eq. (18) of the main text. Using the analytic normalization [68] of the RSs,

$$\int_{V_0} \vec{\mathbb{F}}_n \cdot \left[k\hat{\mathbb{P}}_0\right]'_{k_n} \vec{\mathbb{F}}_n d\mathbf{r} + i \oint_{S_0} (\mathbf{E}_n \times \mathbf{H}'_n - \mathbf{E}'_n \times \mathbf{H}_n) \cdot d\mathbf{S} = 1\,, \tag{C.62}$$

Eq. (C.61) simplifies to

$$k - k_n \approx -k_n \int_{V_0} \left[\vec{\mathbb{F}}_n^{\parallel} \cdot \Delta\hat{\mathbb{P}}\vec{\mathbb{F}}_n^{\parallel} + \vec{\mathbb{F}}_n^{\perp} \cdot \hat{\mathbb{P}}_0\hat{\mathbb{P}}^{-1}\Delta\hat{\mathbb{P}}\vec{\mathbb{F}}_n^{\perp}\right] d\mathbf{r}\,. \tag{C.63}$$

For perturbations outside of the systems, in the form of a thin layer, the volume integral in Eq. (C.52) will extend over the bass volume V_0 and the shell volume V_s. This will result in the integral in the numerator of Eq. (C.61) being extended over the external layer as well, while in the denominator there will be an additional integral term over only the volume of the thin shell. This additional volume integral is proportional to its thickness, therefore it is of second order. Therefore, Eq. (C.61) is valid for thin layer perturbations, or shape deformations outside of the system, where the RS fields are not diverging significantly. This is also consistent with results in Ref. [45, 51, 182].

C.6 Evaluation of the matrix elements for elliptical perturbations

For TM polarization, the electric field of a non-magnetic sphere is defined in spherical coordinates as

$$\mathbf{E}(\mathbf{r}) = E_\phi(\mathbf{r})\hat{\boldsymbol{\phi}} + E_\theta(\mathbf{r})\hat{\boldsymbol{\theta}} + E_r(\mathbf{r})\hat{\mathbf{r}}, \tag{C.64}$$

or in terms of the notation of Eq. (C.28) the field is given by

$$\mathbf{E}^{\parallel} = E_\phi(\mathbf{r})\hat{\boldsymbol{\phi}} + E_\theta(\mathbf{r})\hat{\boldsymbol{\theta}}, \tag{C.65}$$

$$\mathbf{E}^{\perp} = E_r(\mathbf{r})\hat{\mathbf{r}}. \tag{C.66}$$

The electric-field components of the RS with the wave number k_n take the form [63, 83]

$$E_\phi(\mathbf{r}) = -A\frac{J'(x)}{n_r r}\frac{1}{\alpha}\frac{1}{\sin\theta}\frac{\partial}{\partial\phi}Y_{lm}(\theta,\phi), \tag{C.67}$$

$$E_\theta(\mathbf{r}) = -A\frac{J'(x)}{n_r r}\frac{1}{\alpha}\frac{\partial}{\partial\theta}Y_{lm}(\theta,\phi), \tag{C.68}$$

$$E_r(\mathbf{r}) = -A\frac{j_l(x)}{n_r r}\alpha Y_{lm}(\theta,\phi), \tag{C.69}$$

where $J(x) = xj_l(x)$ is the Ricatti-Bessel function, $j_l(x)$ is the spherical Bessel function, and the prime means the derivative with respect to the argument. In Eqs. (C.67), (C.68), and (C.69) we use $x = n_r k_n r$, where $n_r = \sqrt{\varepsilon(k_n)}$ is the refractive index of the sphere. The normalization constant A is defined as [43, 83]

$$A = \frac{1}{J(x_0)} \frac{1}{\sqrt{R(n_r^2 - 1)D}}, \tag{C.70}$$

$$D = \left(\frac{j_{l-1}(x_0)}{j_l(x_0)} - \frac{l}{x_0} \right)^2 \frac{1}{n_r^2} + \frac{\alpha^2}{x_0^2} + \eta C, \tag{C.71}$$

$$(n_r^2 - 1)C = -\frac{2l}{x_0^2} + \left(\frac{j_{l-1}(x_0)}{j_l(x_0)} \right)^2 - \frac{j_{l-2}(x_0)}{j_l(x_0)}, \tag{C.72}$$

$$\eta = \frac{k}{2\varepsilon(k)} \frac{\partial \varepsilon(k)}{\partial k}\bigg|_{k=k_n}, \tag{C.73}$$

where $x_0 = n_r k_n R$, with R being the radius of the sphere. $Y_{lm}(\theta, \phi)$ are real-valued spherical harmonics in the form

$$Y_{lm}(\theta, \phi) = c_l^{|m|} P_l^{|m|}(\cos\theta) \chi_m(\phi), \tag{C.74}$$

$$c_l^{|m|} = \sqrt{\frac{2l+1}{2} \frac{(l-|m|)!}{(l+|m|)!}}, \tag{C.75}$$

$$\chi_m(\phi) = \begin{cases} \pi^{-1/2} \sin(m\phi) & m < 0 \\ (2\pi)^{-1/2} & m = 0 \\ \pi^{-1/2} \cos(m\phi) & m > 0, \end{cases} \tag{C.76}$$

and $P_l^{|m|}$ are the associated Legendre polynomials.

Generally, the integral in Eq. (C.28) needs to be evaluated in 3D, but in case of a cylindrically-symmetric perturbation the integration along ϕ can be done analytically, and the remaining integrals along θ and r can be done numerically. In case of the sphere deformed to a cylindrically-symmetric ellipsoid, the lower limit of the radial integral is given by the equation of the corresponding ellipse and takes the form

$$r_<(\theta) = \frac{ab}{\sqrt{b\cos^2\theta + a\sin^2\theta}} \tag{C.77}$$

where a and b are, respectively, the semi-minor and semi-major axes of the ellipse. This makes the integrals along θ and r non-separable. As the integral along r cannot be done analytically, we evaluate the double integral numerically in 2D. We note that to align the ellipsoid as in [51], the ellipse given by Eq. (C.77) is rotated by 90° degrees, so θ in Eq. (C.77) is replaced by $\pi/2 - \theta$. This results in the semi-axis a aligned with the polar axis. If we do not make this substitution then the semi-axis a would be aligned normal to the polar axis and

the modes $m = 0$ and $|m| = 1$ would be swapped. Here we consider perturbations changing the length a. Putting all of the above together results in the following form of the diagonal matrix element:

$$\begin{aligned} V_{nn} &= \left[\frac{c_l^{|m|}A}{n_r}\right]^2 \int_0^\pi \sin\theta d\theta \int_{r_<(\theta)}^R dr \Bigg\{ \left[P_l^{|m|}(\cos\theta)\right]^2 \left[\alpha j_l(n_r kr)\right]^2 \frac{\varepsilon\Delta\varepsilon}{\varepsilon+\Delta\varepsilon} \\ &\quad + \frac{1}{\alpha^2}\left(\frac{m^2}{\sin^2\theta}\left[P_l^{|m|}(\cos\theta)\right]^2 + \sin^2\theta\left[\frac{P_l^{|m|}(\cos\theta)}{\cos\theta}\right]^2\right)\left[J'(n_r kr)\right]^2\Delta\varepsilon\Bigg\}, \end{aligned} \tag{C.78}$$

with $\Delta\varepsilon = 1 - \varepsilon(k)$ for the shape or size perturbation. In case of homogeneous size perturbations which are spherically symmetric, the integral along θ can also be done analytically, leaving only the radial integral to be evaluated, which then takes the form

$$V_{nn} = \frac{A^2}{n_r^2}\int_{r_<}^{r_>} dr \left\{\alpha^2 j_l^2(n_r kr)\frac{\varepsilon\Delta\varepsilon}{\varepsilon+\Delta\varepsilon} + \left[J'(n_r kr)\right]^2\Delta\varepsilon\right\}, \tag{C.79}$$

where $r_<$ and $r_>$ denote, respectively, the upper and lower limits of r.

D

Three dimensional systems with rotational symmetry

D.1 Vector spherical harmonics

We defined the real valued VSH as in Ref. [32, 38, 85]

$$\hat{\boldsymbol{Y}}_{1lm} = \frac{\mathbf{r}}{\alpha} \times \boldsymbol{\nabla} Y_{lm}\,, \qquad \hat{\boldsymbol{Y}}_{2lm} = \frac{r}{\alpha}\boldsymbol{\nabla} Y_{lm}\,, \qquad \hat{\boldsymbol{Y}}_{3lm} = \frac{\mathbf{r}}{r} Y_{lm} \qquad \alpha = \sqrt{l(l+1)}\,, \tag{D.1}$$

where

$$Y_{lm}(\Omega) = c_l^{|m|} P_l^{|m|}(\cos\theta)\chi_m(\varphi)\,, \tag{D.2}$$

is the real values spherical harmonics and

$$c^{|m|} = \sqrt{\frac{2l+1}{2}\frac{(l-|m|)!}{(l+|m|)!}}\,. \tag{D.3}$$

Here $P_l^{|m|}$ is the associated Legendre polynomial, and

$$\chi_m(\varphi) = \begin{cases} \pi^{-1/2}\sin(m\varphi) & m < 0 \\ (2\pi)^{-1/2} & m = 0 \\ \pi^{-1/2}\cos(m\varphi) & m > 0 \end{cases}. \tag{D.4}$$

The $\boldsymbol{\nabla}$ operator in spherical coordinates is

$$\boldsymbol{\nabla} = \hat{\boldsymbol{r}}\frac{\partial}{\partial r} + \hat{\boldsymbol{\theta}}\frac{1}{r}\frac{\partial}{\partial\theta} + \hat{\boldsymbol{\varphi}}\frac{1}{r\sin\theta}\frac{\partial}{\partial\varphi}\,, \tag{D.5}$$

and the gradient of spherical harmonics is

$$\boldsymbol{\nabla} Y_{lm} = \hat{\boldsymbol{\theta}}\frac{1}{r}c_l^{|m|}\chi_m(\varphi)\frac{\partial}{\partial\theta}P_l^{|m|}(\cos\theta) + \hat{\boldsymbol{\varphi}}\frac{1}{r\sin\theta}c_l^{|m|}P_l^{|m|}(\cos\theta)\frac{\partial}{\partial\varphi}\chi_m(\varphi)\,, \tag{D.6}$$

giving the VSH as

$$\mathbf{Y}_{1lm} = \frac{c_l^{|m|}}{\alpha}\left[\hat{\boldsymbol{\varphi}}\chi_m(\varphi)\frac{\partial}{\partial\theta}P_l^{|m|}(\cos\theta) - \hat{\boldsymbol{\theta}}\frac{1}{\sin\theta}P_l^{|m|}(\cos\theta)\frac{\partial}{\partial\varphi}\chi_m(\varphi)\right], \tag{D.7}$$

$$\mathbf{Y}_{2lm} = \frac{c_l^{|m|}}{\alpha}\left[\hat{\boldsymbol{\theta}}\chi_m(\varphi)\frac{\partial}{\partial\theta}P_l^{|m|}(\cos\theta) + \hat{\boldsymbol{\varphi}}\frac{1}{\sin\theta}P_l^{|m|}(\cos\theta)\frac{\partial}{\partial\varphi}\chi_m(\varphi)\right], \tag{D.8}$$

$$\mathbf{Y}_{3lm} = \hat{\boldsymbol{r}}c_l^{|m|}P_l^{|m|}(\cos\theta)\chi_m(\varphi) \tag{D.9}$$

where

$$\frac{\partial}{\partial\theta}P_l^{|m|}(\cos\theta) = \frac{\partial}{\partial x}\left(P_l^{|m|}(x)\right)(-\sin\theta), \tag{D.10}$$

with $x = \cos\theta$, and

$$\frac{\mathrm{d}\chi_m}{\mathrm{d}\varphi} = \begin{cases} m\pi^{-1/2}\cos(m\varphi) & m < 0 \\ 0 & m = 0 \\ -m\pi^{-1/2}\sin(m\varphi) & m > 0 \end{cases}. \tag{D.11}$$

The VSH are orthogonal vectors if they have same l and m. They are not necessarily orthogonal vectors for different l and m (so often $\mathbf{Y}_{ilm}\cdot\mathbf{Y}_{il'm'} \neq 0$), but the exception is that $\mathbf{Y}_{3lm}$ is always orthogonal to $\mathbf{Y}_{2l'm'}$ and $\mathbf{Y}_{1l'm'}$. The VSH satisfy the orthogonality relation

$$\int \mathbf{Y}_{jlm}(\Omega)\mathbf{Y}_{j'l'm'}(\Omega)\mathrm{d}\Omega = \delta_{jj'}\delta_{ll'}\delta_{mm'}, \tag{D.12}$$

where $\mathrm{d}\Omega = \sin\theta\mathrm{d}\theta\mathrm{d}\varphi$, and the integral is over a closed spherical surface.

D.2 Evaluation of the integral

Following from Eq. (5.2) the possible combination of VSH products that we need to consider are

$$\mathbf{Y}_{1lm}\cdot\mathbf{Y}_{1l'm'} = \frac{c_l^{|m|}c_{l'}^{|m'|}}{\alpha\alpha'}\left[\frac{1}{\sin^2\theta}P_l^{|m|}P_{l'}^{|m'|}\frac{\partial}{\partial\varphi}(\chi_m)\frac{\partial}{\partial\varphi}(\chi_{m'}) + \frac{\partial}{\partial\theta}P_l^{|m|}\frac{\partial}{\partial\theta}P_{l'}^{|m'|}\chi_m\chi_{m'}\right], \tag{D.13}$$

$$\mathbf{Y}_{2lm}\cdot\mathbf{Y}_{2l'm'} = \mathbf{Y}_{1lm}\cdot\mathbf{Y}_{1l'm'}, \tag{D.14}$$

$$\mathbf{Y}_{1lm}\cdot\mathbf{Y}_{2l'm'} = \frac{c_l^{|m|}c_{l'}^{|m'|}}{\alpha\alpha'}\frac{1}{\sin\theta}\left[P_{l'}^{|m'|}\frac{\partial}{\partial\theta}P_l^{|m|}\frac{\partial}{\partial\varphi}(\chi_{m'})\chi_m - P_l^{|m|}\frac{\partial}{\partial\theta}P_{l'}^{|m'|}\frac{\partial}{\partial\varphi}(\chi_m)\chi_{m'}\right], \tag{D.15}$$

$$\mathbf{Y}_{3lm}\cdot\mathbf{Y}_{3l'm'} = c_l^{|m|}c_{l'}^{|m'|}P_l^{|m|}P_{l'}^{|m'|}\chi_m\chi_{m'}. \tag{D.16}$$

We continue with assuming rotational symmetry around the azimuthal angle. Lets consider the azimuthal integral first. Starting with the coupling between $i \neq i'$, so the product

$\mathbf{Y}_{1lm} \cdot \mathbf{Y}_{2l'm'}$, we have terms

$$\frac{\partial}{\partial\varphi}\left(\chi_m\right)\chi_{m'} = \begin{cases} m\pi^{-1/2}\cos(m\varphi)\pi^{-1/2}\sin(m'\varphi) & m,m'<0 \\ m\pi^{-1/2}\cos(m\varphi)(2\pi)^{-1/2} & m<0=m' \\ m\pi^{-1/2}\cos(m\varphi)\pi^{-1/2}\cos(m'\varphi) & m<0<m' \\ 0 & m=0 \\ -m\pi^{-1/2}\sin(m\varphi)\pi^{-1/2}\sin(m'\varphi) & m'<0<m \\ -m\pi^{-1/2}\sin(m\varphi)(2\pi)^{-1/2} & m'=0<m \\ -m\pi^{-1/2}\sin(m\varphi)\pi^{-1/2}\cos(m'\varphi) & 0<m',m \end{cases} . \tag{D.17}$$

After integrating the above terms from 0 to 2π only the integrals with term $\cos(m\varphi)\cos(m'\varphi)$ and $\sin(m\varphi)\sin(m'\varphi)$ can be non zero, as $\int_0^{2\pi}\cos(m\varphi)\sin(m'\varphi)\mathrm{d}\varphi = 0$, $\int_0^{2\pi}\cos(m\varphi)\mathrm{d}\varphi = 0$, and $\int_0^{2\pi}\sin(m\varphi)\mathrm{d}\varphi = 0$ for all combination of m, m'. The integral $\int_0^{2\pi}\cos(m\varphi)\cos(m'\varphi)\mathrm{d}\varphi$ and $\int_0^{2\pi}\sin(m\varphi)\sin(m'\varphi)\mathrm{d}\varphi$ is non zero only if $m = m'$ or $m = -m'$. The integrals appear above only for the case $m = -m'$. In this case the former integral with cos evaluates to π, and the latter integral with sin evaluates to $(-\pi)$. Collecting all this gives the integral as

$$\int_0^{2\pi}\frac{\partial}{\partial\varphi}\left(\chi_m\right)\chi_{m'}\mathrm{d}\varphi = \begin{cases} 0 & m,m'<0 \\ 0 & m<0=m' \\ m & m<0<m' \\ 0 & m'=0=m \\ m & m'<0<m \\ 0 & m'=0<m \\ 0 & 0<m',m \end{cases} . \tag{D.18}$$

Therefore, we can conclude that for rotationally symmetric permittivity perturbations, when $m = -m'$ the TE modes, which have electric field along $\mathbf{Y}_1$, only couple to TM modes, which have field along $\mathbf{Y}_2$ and $\mathbf{Y}_3$. A similar selection rule applies in case of rotationally symmetric permeability perturbations. Note that for chirality perturbations $m = m'$ mode mixing between polarisation have to be considered as well, even if the perturbations is rotationally symmetric. After the azimuthal integral the product of VSH will be

$$\int_0^{2\pi}\mathbf{Y}_{1lm}\cdot\mathbf{Y}_{2l'm'}\mathrm{d}\varphi = \frac{c_l^{|m|}c_{l'}^{|m'|}}{\alpha\alpha'}\frac{1}{\sin\theta}\left[P_{l'}^{|m'|}\frac{\partial}{\partial\theta}P_l^{|m|}m' - P_l^{|m|}\frac{\partial}{\partial\theta}P_{l'}^{|m'|}m\right], \tag{D.19}$$

$$= -m\frac{c_l^{|m|}c_{l'}^{|m'|}}{\alpha\alpha'}\frac{1}{\sin\theta}\left[P_l^{|m|}\frac{\partial}{\partial\theta}P_{l'}^{|m'|} + P_{l'}^{|m'|}\frac{\partial}{\partial\theta}P_l^{|m|}\right], \tag{D.20}$$

and the result of the integral along the polar angle gives

$$\int_{\theta_1}^{\theta_2}\int_0^{2\pi}\mathbf{Y}_{1lm}\cdot\mathbf{Y}_{2l'm'}\mathrm{d}\varphi\ \sin\theta\mathrm{d}\theta = -m\frac{c_l^{|m|}c_{l'}^{|m'|}}{\alpha\alpha'}\left[P_l^{|m|}P_{l'}^{|m'|}\right]_{\theta_1}^{\theta_2}, \tag{D.21}$$

where we made that assumption that there is no further angular dependence function $g(\theta)$ apart from the one that give the integral limits (e.g. $g(\theta)$ is only a Heaviside function).

Now we will consider the coupling between $i = i'$ states, between $\mathbf{Y}_3\cdot\mathbf{Y}_3$ and $\mathbf{Y}_1\cdot\mathbf{Y}_1$. This has azimuthal terms

$$\chi_m\chi_{m'} = \begin{cases} \pi^{-1/2}\sin(m\varphi)\pi^{-1/2}\sin(m'\varphi) & m<0, m'<0 \\ \pi^{-1/2}\sin(m\varphi)(2\pi)^{-1/2} & m<0, m'=0 \\ \pi^{-1/2}\sin(m\varphi)\pi^{-1/2}\cos(m'\varphi) & m<0, m'>0 \\ (2\pi)^{-1/2}\pi^{-1/2}\sin(m'\varphi) & m=0, m'<0 \\ (2\pi)^{-1/2}(2\pi)^{-1/2} & m=0, m'=0 \\ (2\pi)^{-1/2}\pi^{-1/2}\cos(m'\varphi) & m=0, m'>0 \\ \pi^{-1/2}\cos(m\varphi)\pi^{-1/2}\sin(m'\varphi) & m>0, m'<0 \\ \pi^{-1/2}\cos(m\varphi)(2\pi)^{-1/2} & m>0, m'=0 \\ \pi^{-1/2}\cos(m\varphi)\pi^{-1/2}\cos(m'\varphi) & m>0, m'>0 \end{cases}, \tag{D.22}$$

and

$$\frac{\partial}{\partial\varphi}(\chi_m)\frac{\partial}{\partial\varphi}(\chi_{m'}) = \begin{cases} m\pi^{-1/2}\cos(m\varphi)m'\pi^{-1/2}\cos(m'\varphi) & m<0, m'<0 \\ 0 & m<0, m'=0 \\ m\pi^{-1/2}\cos(m\varphi)(-m')\pi^{-1/2}\sin(m'\varphi) & m<0, m'>0 \\ 0 & m=0 \\ -m\pi^{-1/2}\sin(m\varphi)m'\pi^{-1/2}\cos(m'\varphi) & m>0, m'<0 \\ 0 & m>0, m'=0 \\ -m\pi^{-1/2}\sin(m\varphi)(-m')\pi^{-1/2}\sin(m'\varphi) & m>0, m'>0 \end{cases}. \tag{D.23}$$

As before, only terms with $\sin(m\varphi)\sin(m'\varphi)$ and $\cos(m\varphi)\cos(m'\varphi)$ survive the integration between 0 and 2π, and only for $m = m'$ and $m = -m'$. These integrals only appear in the cases when $m, m' < 0$ and $0 < m, m'$, therefore $m = -m'$ case can be neglected.The integrals of trigonometric functions for $m = m'$ give $+\pi$. In addition the integral of a constant C, which appears for $m = m' = 0$, is also non zero, and over the interval of 2π this gives $2\pi C$.

Combining all this leads to

$$\int_0^{2\pi} \chi_m \chi_{m'} \mathrm{d}\varphi = \begin{cases} 1 & m = m' < 0 \\ 1 & m = m' = 0 \\ 1 & m = m' > 0 \end{cases}, \tag{D.24}$$

and

$$\int_0^{2\pi} \frac{\partial}{\partial\varphi}\chi_m \frac{\partial}{\partial\varphi}\chi_{m'} \mathrm{d}\varphi = \begin{cases} mm' & m = m' < 0 \\ 0 & m = m' = 0 \\ mm' & m = m' > 0 \end{cases}, \tag{D.25}$$

which gives the integrals of the VSH products as

$$\int_0^{2\pi} \mathbf{Y}_{1lm} \cdot \mathbf{Y}_{1l'm'} \mathrm{d}\varphi = \frac{c_l^{|m|} c_{l'}^{|m'|}}{\alpha\alpha'} \left[\frac{1}{\sin^2\theta} P_l^{|m|} P_{l'}^{|m'|} m^2 + \frac{\partial}{\partial\theta} P_l^{|m|} \frac{\partial}{\partial\theta} P_{l'}^{|m'|} \right] \tag{D.26}$$

$$\int_0^{2\pi} \mathbf{Y}_{3lm} \cdot \mathbf{Y}_{3l'm'} \mathrm{d}\varphi = c_l^{|m|} c_{l'}^{|m'|} P_l^{|m|} P_{l'}^{|m'|} . \tag{D.27}$$

These expression are then be integrated along the polar angle.

D.2.1 Mirror symmetry along the equatorial plane

The parity of associated Legendre polynomials is

$$P_l^m(-x) = (-1)^{l+m} P_l^m(x) . \tag{D.28}$$

So they are even when $l + m$ is even, and odd when $l + m$ is odd.

The derivative of an even function is odd, and vice versa. The integrals along θ are

$$\int \mathbf{Y}_{1lm} \cdot \mathbf{Y}_{1l'm'} \sin\theta \mathrm{d}\theta \propto \int \left[\frac{1}{\sin\theta} P_l^{|m|} P_{l'}^{|m'|} m^2 + \sin\theta \frac{\partial}{\partial\theta} P_l^{|m|} \frac{\partial}{\partial\theta} P_{l'}^{|m'|} \right] D(\theta) \mathrm{d}\theta , \tag{D.29}$$

$$\int \mathbf{Y}_{1lm} \cdot \mathbf{Y}_{2l'm'} \sin\theta \mathrm{d}\theta \propto \int \left[P_l^{|m|} \frac{\partial}{\partial\theta} P_{l'}^{|m'|} + P_{l'}^{|m'|} \frac{\partial}{\partial\theta} P_l^{|m|} \right] D(\theta) \mathrm{d}\theta , \tag{D.30}$$

$$\int \mathbf{Y}_{3lm} \cdot \mathbf{Y}_{3l'm'} \sin\theta \mathrm{d}\theta \propto \int \left[P_l^{|m|} P_{l'}^{|m'|} \sin\theta \right] D(\theta) \mathrm{d}\theta , \tag{D.31}$$

where the function $D(\theta)$ gives the polar angle distribution of the perturbation. For example this can be one (or more) Heaviside step function(s) determining the specific region of the perturbation. We can take the limits of the integral from $\theta = 0$ to $\theta = \pi$, resulting in the argument of P (which is $\cos\theta$) running from -1 to 1. If $D(\theta)$ is symmetric in the equatorial plane we can potentially use the even/odd parity of P to simplify the integrals. Between these integral limits of θ the function $\sin\theta$ is even. We limit ourselves to the rotationally

symmetric case, with the selection rules applied from the previous section. If $D(\theta)$ is even, such as would be for a cylinder perturbations, then the TE and TM modes only couple if their angular momentum number l differs by an odd number (due to Eq. (D.30)), while TE to TE and TM to TM coupling only happens if the angular momentum numbers l differ by an even number (due to Eq. (D.29) Eq. (D.31)).

E

Scattering

E.1 GD of an arbitrary system

The electric GD of a general system (including a perturbed one), can be written in VSH as

$$\mathbf{G}(\mathbf{r},\mathbf{r}';k)=\sum_{ii'll'mm'} G(r,r';k)_{ilm}^{i'l'm'}\,\hat{\boldsymbol{Y}}_{ilm}(\theta,\phi)\otimes\hat{\boldsymbol{Y}}_{i'l'm'}(\theta',\phi')\,. \tag{E.1}$$

Based on [38] we need $G(R,R';k)_{ilm}^{i'l'm'}$ of the decoupled wave equation in order to find the scattering matrix. For the perturbed GD, which is a ML sum of the perturbed eigenmodes, the perturbed modes are expanded into the basis modes as $\tilde{\mathbf{E}}_{\tilde{\nu}}=\sum_{\nu}c_{\tilde{\nu}\nu}\mathbf{E}_{\nu}(\mathbf{r})$, where $\mathbf{E}_{\nu}(\mathbf{r})$ are the basis eigenmodes, and $\sim$ denotes the perturbed modes. We can factorise out the sum over the different m and l as

$$\tilde{\mathbf{E}}_{\tilde{\nu}}(\mathbf{r})=\sum_{\nu}c_{\tilde{\nu}\nu}\mathbf{E}_{\nu}(\mathbf{r})=\sum_{lm}\sum_{\nu'}c_{\tilde{\nu}\nu'}^{lm}\mathbf{E}_{\nu'}^{lm}(\mathbf{r})=\sum_{lm}\mathbf{E}_{\tilde{\nu}}^{lm}(\mathbf{r})\,. \tag{E.2}$$

The field in the last sum, $\mathbf{E}_{\tilde{\nu}}^{lm}(\mathbf{r})=\sum_{\nu'}c_{\tilde{\nu}\nu'}^{lm}\mathbf{E}_{\nu'}^{lm}(\mathbf{r})$, is simply the contribution of all basis eigenmodes ν' of a specific l and m, and the sum over l and m takes into account the various multipole contributions. Then, we can write the electric GD of the coupled Maxwell's wave equations as

$$\mathbf{G}_c(\mathbf{r},\mathbf{r}';k)=\sum_{\tilde{\nu}}\frac{\tilde{\mathbf{E}}_{\tilde{\nu}}(\mathbf{r})\otimes\tilde{\mathbf{E}}_{\tilde{\nu}}(\mathbf{r}')}{k-\tilde{k}_{\tilde{\nu}}}\,, \tag{E.3}$$

$$=\sum_{\tilde{\nu}}\frac{\sum_{lm}\mathbf{E}_{\tilde{\nu}}^{lm}(\mathbf{r})\otimes\sum_{l'm'}\mathbf{E}_{\tilde{\nu}}^{l'm'}(\mathbf{r}')}{k-\tilde{k}_{\tilde{\nu}}}\,, \tag{E.4}$$

$$=\sum_{ll'mm'}\sum_{\tilde{\nu}}\frac{\mathbf{E}_{\tilde{\nu}}^{lm}(\mathbf{r})\otimes\mathbf{E}_{\tilde{\nu}}^{l'm'}(\mathbf{r}')}{k-\tilde{k}_{\tilde{\nu}}}\,, \tag{E.5}$$

from which we can identify

$$G_c(r,r';k)_{ilm}^{i'l'm'}=\sum_{\tilde{\nu}}\frac{\left[\mathbf{E}_{\tilde{\nu}}^{lm}(\mathbf{r})\right]_i\left[\mathbf{E}_{\tilde{\nu}}^{l'm'}(\mathbf{r}')\right]_{i'}}{k-\tilde{k}_{\tilde{\nu}}}\,, \tag{E.6}$$

where $[\mathbf{E}]_i$ is the ith component of the field in VSH.

Note on the practical computational implementation: the selection rules for m, m', l, l' in Appendix D allow to reduce the number of modes needed in the RSE matrix. If this is utilized, then one needs to implement these selection rule in the above summation as well.

E.2 Using the sum rule in the GD

The key element of the scattering formalism is a correct GD representation on the surface of the sphere, with both spacial coordinates at $r = r' = R$. This can depend on the form of the ML representation used, which we have shown for the GF in 1D, in Chap. 2, where a difference between the two ML sums due to the application of the sum rule was observed. In 3D spherical system the sum rule is the well know dyadic of the form [66, 82]

$$\sum_n \frac{\mathbf{E}_n(\mathbf{r}) \otimes \mathbf{E}_n(\mathbf{r})}{k_n} = 0\,, \tag{E.7}$$

which is a sum over RS only, and not the static modes. The first form of the GD of the decoupled wave equation can be written as

$$\mathbf{G}(\mathbf{r}, \mathbf{r}'; k) = \sum_n \frac{\mathbf{E}(\mathbf{r}) \otimes \mathbf{E}(\mathbf{r})}{k_n(k - k_n)} + \sum_\lambda \frac{\mathbf{E}_\lambda(\mathbf{r}) \otimes \mathbf{E}_\lambda(\mathbf{r})}{k^2}\,, \tag{E.8}$$

and we can find the second one with the sum rule as

$$\mathbf{G}_{\mathrm{sr}}(\mathbf{r}, \mathbf{r}'; k) = \sum_n \frac{\mathbf{E}(\mathbf{r}) \otimes \mathbf{E}(\mathbf{r})}{k_n(k - k_n)} - \frac{1}{k}\sum_n \frac{\mathbf{E}_n(\mathbf{r}) \otimes \mathbf{E}_n(\mathbf{r})}{k_n} + \sum_\lambda \frac{\mathbf{E}_\lambda(\mathbf{r}) \otimes \mathbf{E}_\lambda(\mathbf{r})}{k^2}\,, \tag{E.9}$$

$$= \sum_n \frac{\mathbf{E}(\mathbf{r}) \otimes \mathbf{E}(\mathbf{r})}{k(k - k_n)} + \sum_\lambda \frac{\mathbf{E}_\lambda(\mathbf{r}) \otimes \mathbf{E}_\lambda(\mathbf{r})}{k^2}\,, \tag{E.10}$$

which is valid only for $k \neq 0$ due to the factor $0/k$ added.

On Fig. E.2.1 we show the convergence of the sum rule Eq. (E.7) for two cases: $r = r' \neq R$ and $r = r' = R$. In VSH representation the $\mathbf{Y}_{1lm} \otimes \mathbf{Y}_{2lm}$ and $\mathbf{Y}_{1lm} \otimes \mathbf{Y}_{3lm}$ terms are zero, as TE modes only have $\mathbf{Y}_{1lm}$ component, and TM only have $\mathbf{Y}_{2lm}$ and $\mathbf{Y}_{3lm}$, while the dyadic Eq. (E.7) is also symmetric, therefore all together we shown only four dyads.

The components $\mathbf{Y}_{1lm} \otimes \mathbf{Y}_{1lm}$ and $\mathbf{Y}_{2lm} \otimes \mathbf{Y}_{2lm}$ converge to zero as $1/k_{\max}$ when $r = r' \neq R$, and similarly to the 1D case, they do not converge when both coordinates are at the same surface coordinate $r = r' = R$. Interestingly, the components $\mathbf{Y}_{2lm} \otimes \mathbf{Y}_{3lm}$ and $\mathbf{Y}_{3lm} \otimes \mathbf{Y}_{3lm}$ converge as $1/k_{\max}^3$ when $r = r' \neq R$, while for $r = r' = R$ the former slows to $1/k_{\max}$ and the latter keeps the rapid convergence rate. The component $\mathbf{Y}_{1lm} \otimes \mathbf{Y}_{1lm}$ and $\mathbf{Y}_{2lm} \otimes \mathbf{Y}_{2lm}$ contribute to the TE to TE, and to the TM to TM scattering, respectively, therefore one needs to use to correct GD form (Eq. (E.8)) for the scattering calculation.

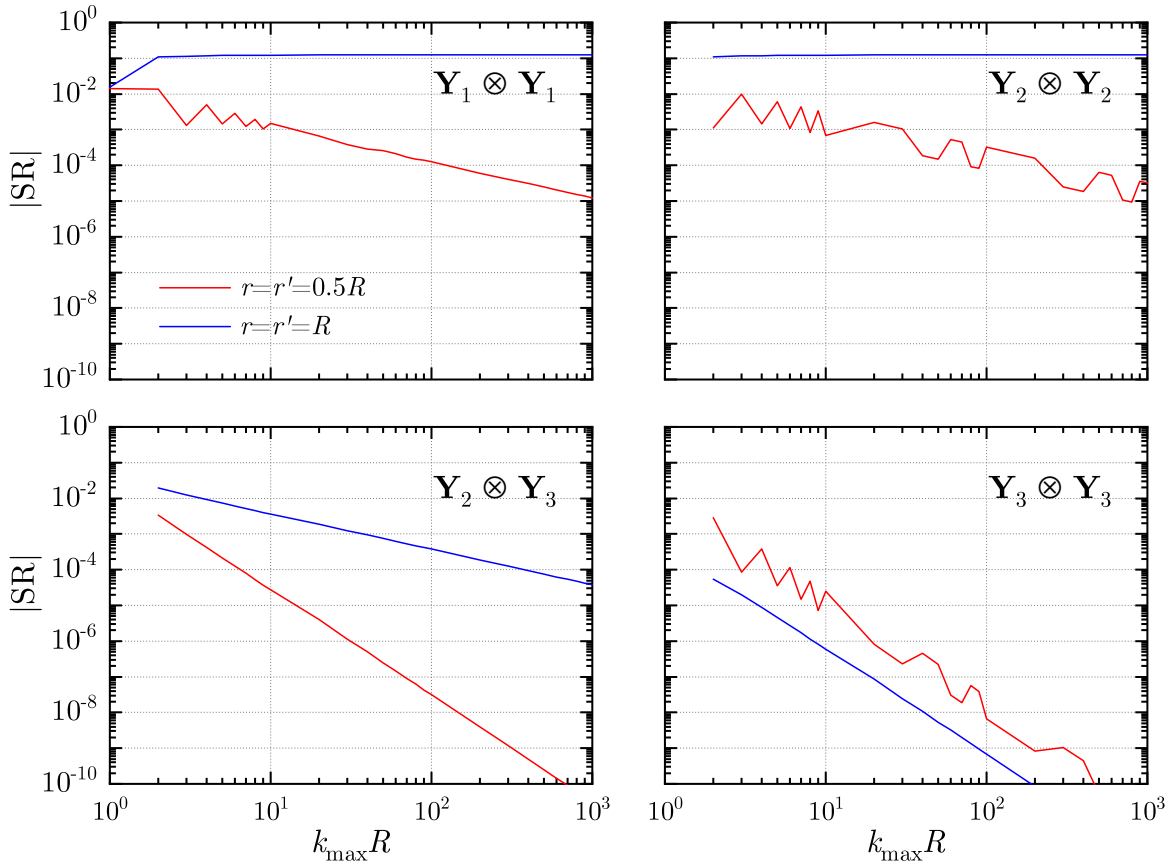

Fig. E.2.1: Convergence rate of Eq. (E.7) for a spherically symmetric basis system, with $\varepsilon_s = 9$, radius R, and $l = 1$.

Scattering matrix

We illustrate the effect of the sum rule on the scattering matrix on Fig. E.2.2. For the case labelled 'ML' we use $\mathbf{G}(\mathbf{r},\mathbf{r}';k) = \sum_n \frac{\mathbf{E}(\mathbf{r})\otimes\mathbf{E}(\mathbf{r})}{k_n(k-k_n)} + \sum_\lambda \frac{\mathbf{E}_\lambda(\mathbf{r})\otimes\mathbf{E}_\lambda(\mathbf{r})}{k^2}$, and for 'ML$_{\text{sr}}$' we use $\mathbf{G}_{\text{sr}}(\mathbf{r},\mathbf{r}';k) = \sum_n \frac{\mathbf{E}(\mathbf{r})\otimes\mathbf{E}(\mathbf{r})}{k(k-k_n)} + \sum_\lambda \frac{\mathbf{E}_\lambda(\mathbf{r})\otimes\mathbf{E}_\lambda(\mathbf{r})}{k^2}$, which we insert into Eq. (6.2), and compare the real part of the scattering matrix with the exact solution. We can see that for both $\mathbf{Y}_{1lm} \otimes \mathbf{Y}_{1lm}$ and $\mathbf{Y}_{2lm} \otimes \mathbf{Y}_{2lm}$ the use of the sum rule leads to an offset in the scattering matrix elements.

Note that the use of the sum rule probably would not significantly affect methods that calculate the scattering matrix via volume integrals (just as the RSE, which also relies on the volume integral, works with both GD versions). This is due to only an infinitesimally thin surface layer being affected by the sum rule, which can be considered to have a vanishing weight in the integral domain.

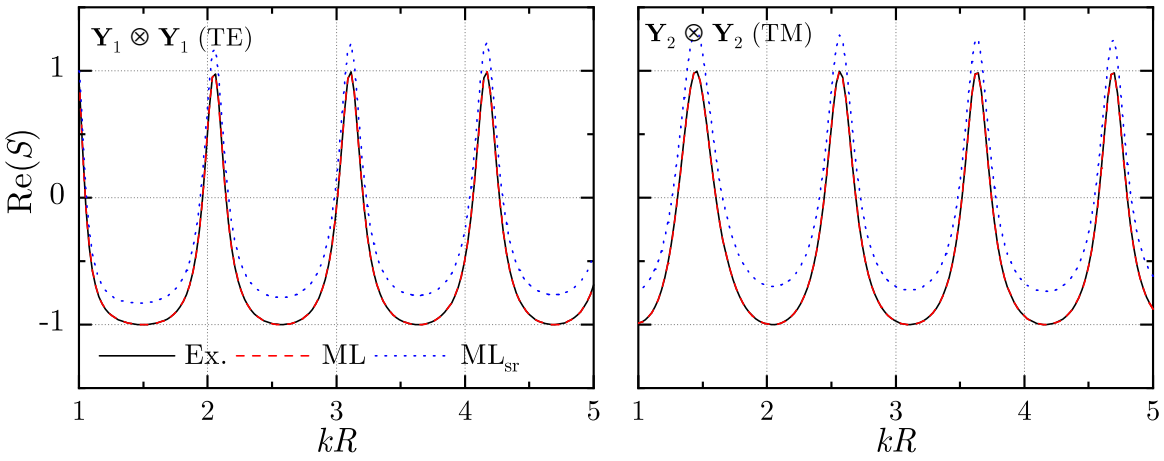

Fig. E.2.2: Comparison of the real part of the scattering matrix, for a sphere with $\varepsilon_s = 9$, radius R, and $l = 1$.

Bibliography

[1] Philip Morse. *Vibration and Sound*. Acoustical Society of Amer. Publications, New York, Oct 1991.

[2] Herbert Goldstein and Charles P. Poole & John Safko. *Classical Mechanics*. Pearson Education, Nov 2011.

[3] Michael Spivak. *Physics for Mathematicians, Mechanics I*. Publish or Perish, Houston, Tex., 1st edition, Dec 2010.

[4] Eugen Merzbacher. *Quantum Mechanics 3E*. John Wiley & Sons, New York, 3rd edition, Dec 1997.

[5] John David Jackson. *Classical Electrodynamics*. Wiley, New York, 3rd edition, Dec 1998.

[6] David J. Griffiths. *Introduction to Quantum Mechanics*. Cambridge University Press, Cambridge, 2nd edition edition, Aug 2016.

[7] A. Tanimu and E. A. Muljarov. Resonant-state expansion applied to one-dimensional quantum systems. *Physical Review A*, 98(2):022127, Aug 2018.

[8] M. B. Doost, W. Langbein, and E. A. Muljarov. Resonant state expansion applied to two-dimensional open optical systems. *Phys. Rev. A*, 87:043827, Apr 2013.

[9] Sam Neale and Egor A. Muljarov. Resonant-state expansion for planar photonic crystal structures. *Phys. Rev. B*, 101(15):155128, Apr 2020.

[10] Yuto Ashida, Zongping Gong, and Masahito Ueda. Non-hermitian physics. *Advances in Physics*, 69(3):249–435, Jul 2020.

[11] R H Cole. *Theory of Ordinary Differential Equations*. Appleton-Century-Crofts, 1st edition, Jan 1968.

[12] A. Baz', Ya. Zel'dovich, and A. Perelomov. *Scattering, Reactions and Decay in Non-relativistic Quantum Mechanics*. U. S. Department of Commerce, Washington, D. C., 1969.

[13] J Humblet and L Rosenfeld. Theory of nuclear reactions: I. resonant states and collision matrix. *Nuclear Physics*, 26(4):529–578, 1961.

[14] E. A. Muljarov, W. Langbein, and R. Zimmermann. Brillouin-wigner perturbation theory in open electromagnetic systems. *Europhys. Lett.*, 92(5):50010, 2010.

[15] LA Khalfin. Contribution to the decay theory of a quasi-stationary state. *Sov. Phys. JETP*, 6(6):1053–1063, 1958.

[16] Subrahmanyan Chandrasekhar and Steven Detweiler. The quasi-normal modes of the schwarzschild black hole. *Proceedings of the Royal Society of London. A. Mathematical and Physical Sciences*, 344(1639):441–452, 1975.

[17] Q. Bai, M. Perrin, C. Sauvan, J-P Hugonin, and P. Lalanne. Efficient and intuitive method for the analysis of light scattering by a resonant nanostructure. *Opt. Express*, 21:27371, 2013.

[18] G. Gamow. Zur quantentheorie des atomkernes. *Z. Physik*, 51(3):204–212, mar 1928.

[19] Ya B. Zel'dovich. On the theory of unstable states. *Sov. Phys. JETP*, 12:542–548, 1961.

[20] Valeria Ferrari and Leonardo Gualtieri. Quasi-normal modes and gravitational wave astronomy. *General Relativity and Gravitation*, 40(5):945–970, May 2008.

[21] H. M. Lai, P. T. Leung, K. Young, P. W. Barber, and S. C. Hill. Time-independent perturbation for leaking electromagnetic modes in open systems with application to resonances in microdroplets. *Phys. Rev. A*, 41:5187–5198, May 1990.

[22] Darrell W. Pepper and Juan C. Heinrich. *The Finite Element Method: Basic Concepts and Applications with MATLAB, MAPLE, and COMSOL, Third Edition*. CRC Press, 3rd edition, Apr 2017.

[23] Elsherbeni. *The Finite-Difference Time-Domain Method for Electromagnetics: With MATLAB Simulations*. Scitech Publishing, Edison, NJ, 2nd edition, Dec 2015.

[24] Max Born and Emil Wolf. *Principles of optics: electromagnetic theory of propagation, interference and diffraction of light*. CUP Archive, 1999.

[25] Kim Hwi, Park Junghyun, and Lee Byoungho. *Fourier Modal Method and Its Applications in Computational Nanophotonics*. CRC Press, Boca Raton, 1st edition, Mar 2012.

[26] M. A. Yurkin and A. G. Hoekstra. The discrete dipole approximation: An overview and recent developments. *Journal of Quantitative Spectroscopy and Radiative Transfer*, 106(1):558–589, Jul 2007.

[27] D. M. Whittaker and I. S. Culshaw. Scattering-matrix treatment of patterned multilayer photonic structures. *Physical Review B*, 60(4):2610–2618, Jul 1999.

[28] S. G. Tikhodeev, A. L. Yablonskii, E. A. Muljarov, N. A. Gippius, and T. Ishihara. Quasi-guided modes and optical properties of photonic crystal slabs. *Phys. Rev. B*, 66:45102, 2002.

[29] F. Hartmann. *Boundary Element Methods*, page 192–202. Elsevier, Oxford, Jan 2001.

[30] Patric Lind. Completeness relations and resonant state expansions. *Physical Review C*, 47(5):1903–1920, May 1993.

[31] P. T. Leung, S. Y. Liu, and K. Young. Completeness and orthogonality of quasinormal modes in leaky optical cavities. *Physical Review A*, 49(4):3057–3067, Apr 1994.

[32] S. V. Lobanov, W. Langbein, and E. A. Muljarov. Resonant-state expansion applied to three-dimensional open optical systems: Complete set of static modes. *Phys. Rev. A*, 100(6):063811, December 2019.

[33] Horst R. Beyer. On the completeness of the quasinormal modes of the pöschl–teller potential. *Communications in Mathematical Physics*, 204(2):397–423, Jul 1999.

[34] Mathias Perrin. Eigen-energy effects and non-orthogonality in the quasi-normal mode expansion of maxwell equations. *Opt. Express*, 24(24):27137–27151, 2016.

[35] T. Weiss and E. A. Muljarov. How to calculate the pole expansion of the optical scattering matrix from the resonant states. *Phys. Rev. B*, 98:085433, Aug 2018.

[36] Wei Yan, Rémi Faggiani, and Philippe Lalanne. Rigorous modal analysis of plasmonic nanoresonators. *Phys. Rev. B*, 97:205422, May 2018.

[37] Christophe Sauvan. Quasinormal modes expansions for nanoresonators made of absorbing dielectric materials: study of the role of static modes. *Optics Express*, 29(6):8268–8282, 2021.

[38] S. V. Lobanov, W. Langbein, and E. A. Muljarov. Resonant-state expansion of three-dimensional open optical systems: Light scattering. *Phys. Rev. A*, 98(3):033820, 2018.

[39] E. M. Purcell. Spontaneous emission probabilities at radio frequencies. *Phys. Rev.*, 69:681, 1946.

[40] C. Sauvan, J. P. Hugonin, I. S. Maksymov, and P. Lalanne. Theory of the spontaneous optical emission of nanosize photonic and plasmon resonators. *Phys. Rev. Lett.*, 110:237401, Jun 2013.

[41] Rong-Chun Ge, Philip Trøst Kristensen, Jeff F Young, and Stephen Hughes. Quasinormal mode approach to modelling light-emission and propagation in nanoplasmonics. *New Journal of Physics*, 16(11):113048, 2014.

[42] Mohsen Kamandar Dezfouli, Reuven Gordon, and Stephen Hughes. Modal theory of modified spontaneous emission of a quantum emitter in a hybrid plasmonic photonic-crystal cavity system. *Physical Review A*, 95(1):013846, Jan 2017.

[43] E. A. Muljarov and W. Langbein. Exact mode volume and purcell factor of open optical systems. *Physical Review B*, 94(23):235438, Dec 2016.

[44] Lin Zschiedrich, Felix Binkowski, Niko Nikolay, Oliver Benson, Günter Kewes, and Sven Burger. Riesz-projection-based theory of light-matter interaction in dispersive nanoresonators. *Physical Review A*, 98(4):043806, Oct 2018.

[45] Jianji Yang, Harald Giessen, and Philippe Lalanne. Simple analytical expression for the peak-frequency shifts of plasmonic resonances for sensing. *Nano Letters*, 15(5):3439–3444, May 2015.

[46] S. Both and T. Weiss. First-order perturbation theory for changes in the surrounding of open optical resonators. *Optics Letters*, 44(24):5917–5920, Dec 2019.

[47] Steffen Both, Martin Schäferling, Florian Sterl, Egor A. Muljarov, Harald Giessen, and Thomas Weiss. Nanophotonic chiral sensing: How does it actually work? *ACS Nano*, 16(2):2822–2832, Feb 2022.

[48] S. F. Almousa and E. A. Muljarov. Varying the medium surrounding an optical resonator: An efficient and rigorous way to calculate its spectral changes. *arXiv:2109.07026 [physics]*, Feb 2022. arXiv: 2109.07026.

[49] Frank Vollmer and Deshui Yu. *Optical Whispering Gallery Modes for Biosensing: From Physical Principles to Applications*. Springer, 1st edition, Oct 2020.

[50] Zoltan Sztranyovszky, Wolfgang Langbein, and Egor A. Muljarov. First-order perturbation theory of eigenmodes for systems with interfaces. *arXiv*, page 10.48550/ARXIV.2205.13041, 2022.

[51] Wei Yan, Philippe Lalanne, and Min Qiu. Shape deformation of nanoresonator: A quasinormal-mode perturbation theory. *Physical Review Letters*, 125(1):013901, Jul 2020.

[52] Rong-Chun Ge and Stephen Hughes. Quantum dynamics of two quantum dots coupled through localized plasmons: An intuitive and accurate quantum optics approach using quasinormal modes. *Physical Review B*, 92(20):205420, Nov 2015.

[53] Sebastian Franke, Stephen Hughes, Mohsen Kamandar Dezfouli, Philip Trøst Kristensen, Kurt Busch, Andreas Knorr, and Marten Richter. Quantization of quasinormal modes for open cavities and plasmonic cavity quantum electrodynamics. *Physical Review Letters*, 122(21):213901, May 2019.

[54] Stephen Hughes, Sebastian Franke, Chris Gustin, Mohsen Kamandar Dezfouli, Andreas Knorr, and Marten Richter. Theory and limits of on-demand single-photon sources using plasmonic resonators: A quantized quasinormal mode approach. *ACS Photonics*, 6(8):2168–2180, Aug 2019.

[55] Luca Carletti, Kirill Koshelev, Costantino De Angelis, and Yuri Kivshar. Giant nonlinear response at the nanoscale driven by bound states in the continuum. *Phys. Rev. Lett.*, 121:033903, Jul 2018.

[56] Carlo Gigli, Tong Wu, Giuseppe Marino, Adrien Borne, Giuseppe Leo, and Philippe Lalanne. Quasinormal-mode non-hermitian modeling and design in nonlinear nano-optics. *ACS photonics*, 7(5):1197–1205, 2020.

[57] Mohsen Kamandar Dezfouli, Christos Tserkezis, N. Asger Mortensen, and Stephen Hughes. Nonlocal quasinormal modes for arbitrarily shaped three-dimensional plasmonic resonators. *Optica*, 4(12):1503–1509, Dec 2017.

[58] Philippe Lalanne, Wei Yan, Kevin Vynck, Christophe Sauvan, and Jean-Paul Hugonin. Light interaction with photonic and plasmonic resonances. *Laser Photonics Rev.*, 12(5):1700113, 2018.

[59] Philip Trøst Kristensen, Kathrin Herrmann, Francesco Intravaia, Kurt Busch, and Kurt Busch. Modeling electromagnetic resonators using quasinormal modes. *Advances in Optics and Photonics*, 12:612–708, Sep 2020.

[60] S Both and T Weiss. Resonant states and their role in nanophotonics. *Semiconductor Science and Technology*, 37(1):013002, 2021.

[61] Mohammed Benzaouia, John D. Joannopoulos, Steven G. Johnson, and Aristeidis Karalis. Quasi-normal mode theory of the scattering matrix, enforcing fundamental constraints for truncated expansions. *Physical Review Research*, 3(3):033228, Sep 2021.

[62] Christophe Sauvan, Jean-Paul Hugonin, Rémi Carminati, and Philippe Lalanne. Modal representation of spatial coherence in dissipative and resonant photonic systems. *Physical Review A*, 89(4):043825, 2014.

[63] M. B. Doost, W. Langbein, and E. A. Muljarov. Resonant-state expansion applied to three-dimensional open optical systems. *Phys. Rev. A*, 90:013834, Jul 2014.

[64] Jakob Rosenkrantz de Lasson, Lars Hagedorn Frandsen, Philipp Gutsche, Sven Burger, Oleksiy S. Kim, Olav Breinbjerg, Aliaksandra Ivinskaya, Fengwen Wang, Ole Sigmund, Teppo Häyrynen, Andrei V. Lavrinenko, Jesper Mørk, and Niels Gregersen. Benchmarking five numerical simulation techniques for computing resonance wavelengths and quality factors in photonic crystal membrane line defect cavities. *Optics Express*, 26(9):11366–11392, Apr 2018.

[65] P. Lalanne, W. Yan, A. Gras, C. Sauvan, J.-P. Hugonin, M. Besbes, G. Demésy, M. D. Truong, B. Gralak, F. Zolla, A. Nicolet, F. Binkowski, L. Zschiedrich, S. Burger, J. Zimmerling, R. Remis, P. Urbach, H. T. Liu, and T. Weiss. Quasinormal mode solvers for resonators with dispersive materials. *J. Opt. Soc. Am. A*, 36(4):686–704, Apr 2019.

[66] K. M. Lee, P. T. Leung, and K. M. Pang. Dyadic formulation of morphology-dependent resonances. i. completeness relation. *JOSA B*, 16(9):1409–1417, Sep 1999.

[67] Masud Mansuripur, Miroslav Kolesik, and Per Jakobsen. Leaky modes of solid dielectric spheres. *Physical Review A*, 96(1):013846, Jul 2017.

[68] E. A. Muljarov and T. Weiss. Resonant-state expansion for open optical systems: generalization to magnetic, chiral, and bi-anisotropic materials. *Opt. Lett.*, 43(9):1978–1981, 2018.

[69] Christophe Sauvan, Tong Wu, Rachid Zarouf, Egor A. Muljarov, and Philippe Lalanne. Normalization, orthogonality, and completeness of quasinormal modes of open systems: the case of electromagnetism [invited]. *Optics Express*, 30(5):6846–6885, Feb 2022.

[70] Lev Alvertovich Weinstein. *Open Resonators and Open Waveguides*. Golem Press, Jan 1969.

[71] L. D. Landau and E. M. Lifshitz. *Quantum Mechanics: Non-Relativistic Theory: 3*. Butterworth-Heinemann, 3rd edition, Jan 1981.

[72] J. Bang, F.A. Gareev, M.H. Gizzatkulov, and S.A. Goncharov. Expansion of continuum functions on resonance wave functions and amplitudes. *Nucl. Phys. A*, 309(3):381–421, oct 1978.

[73] H. M. Lai, C. C. Lam, P. T. Leung, and K. Young. Effect of perturbations on the widths of narrow morphology-dependent resonances in mie scattering. *J. Opt. Soc. Am. B*, 8(9):1962, sep 1991.

[74] PT Leung, SY Liu, and K Young. Completeness and time-independent perturbation of the quasinormal modes of an absorptive and leaky cavity. *Physical Review A*, 49(5):3982, 1994.

[75] P. T. Leung, S. Y. Liu, S. S. Tong, and K. Young. Time-independent perturbation theory for quasinormal modes in leaky optical cavities. *Phys. Rev. A*, 49:3068–3073, Apr 1994.

[76] P. T. Leung and K. M. Pang. Completeness and time-independent perturbation of morphology-dependent resonances in dielectric spheres. *J. Opt. Soc. Am. B*, 13(5):805–817, May 1996.

[77] K. M. Lee, P. T. Leung, and K. M. Pang. Dyadic formulation of morphology-dependent resonances. ii. perturbation theory. *JOSA B*, 16(9):1418–1430, Sep 1999.

[78] Sheung-wah Ng, Pui-tang Leung, and Kai-ming Lee. Dyadic formulation of morphology-dependent resonances. iii. degenerate perturbation theory. *JOSA B*, 19(1):154–164, 2002.

[79] E. A. Muljarov and W. Langbein. Comment on "normalization of quasinormal modes in leaky optical cavities and plasmonic resonators". *Physical Review A*, 96(1):017801, Jul 2017.

[80] L. J. Armitage, M. B. Doost, W. Langbein, and E. A. Muljarov. Resonant-state expansion applied to planar waveguides. *Phys. Rev. A*, 89:053832, May 2014.

[81] S. V. Lobanov, G. Zoriniants, W. Langbein, and E. A. Muljarov. Resonant-state expansion of light propagation in nonuniform waveguides. *Phys. Rev. A*, 95(5):053848, may 2017.

[82] E. A. Muljarov and W. Langbein. Resonant-state expansion of dispersive open optical systems: Creating gold from sand. *Phys. Rev. B*, 93:075417, Feb 2016.

[83] H. S. Sehmi, W. Langbein, and E. A. Muljarov. Applying the resonant-state expansion to realistic materials with frequency dispersion. *Phys. Rev. B*, 101(4):045304, Jan 2020.

[84] Sam Neale and Egor A. Muljarov. Accidental and symmetry-protected bound states in the continuum in a photonic-crystal slab: A resonant-state expansion study. *Physical Review B*, 103(15):155112, Apr 2021.

[85] E. A. Muljarov. Full electromagnetic Green's dyadic of spherically symmetric open optical systems and elimination of static modes from the resonant-state expansion. *Phys. Rev. A*, 101(5):053854, may 2020.

[86] David J. Bergman and D. Stroud. Theory of resonances in the electromagnetic scattering by macroscopic bodies. *Phys. Rev. B*, 22:3527–3539, Oct 1980.

[87] Parry Y. Chen, David J. Bergman, and Yonatan Sivan. Generalizing normal mode expansion of electromagnetic green's tensor to open systems. *Physical Review Applied*, 11(4):044018, Apr 2019.

[88] Parry Y. Chen, Yonatan Sivan, and Egor A. Muljarov. An efficient solver for the generalized normal modes of non-uniform open optical resonators. *J. Comput. Phys.*, 422:109754, 2020.

[89] Parry Y. Chen and Yonatan Sivan. Robust location of optical fiber modes via the argument principle method. *Computer Physics Communications*, 214:105–116, May 2017.

[90] Arnold Sommerfeld. *Partial differential equations in physics*. Academic press, 1949.

[91] Philip Trøst Kristensen, Rong-Chun Ge, and Stephen Hughes. Normalization of quasi-normal modes in leaky optical cavities and plasmonic resonators. *Phys. Rev. A*, 92:053810, 2015.

[92] Philip Trøst Kristensen, Rong-Chun Ge, and Stephen Hughes. Reply to "comment on 'normalization of quasinormal modes in leaky optical cavities and plasmonic resonators' ' '. *Physical Review A*, 96(1):017802, Jul 2017.

[93] Paul A Martin. *Multiple scattering: interaction of time-harmonic waves with N obstacles*. Number 107. Cambridge University Press, 2006.

[94] B. Vial, F. Zolla, A. Nicolet, and M. Commandré. Quasimodal expansion of electromagnetic fields in open two-dimensional structures. *Phys. Rev. A*, 89:023829, 2014.

[95] A. Gras, P. Lalanne, and M. Duruflé. Nonuniqueness of the quasinormal mode expansion of electromagnetic lorentz dispersive materials. *JOSA A*, 37(7):1219–1228, Jul 2020.

[96] Jerrold E. Marsden and Michael J. Hoffman. *Basic Complex Analysis*. W. H. Freeman, New York, 3rd edition, Jan 1999.

[97] Peter Henrici. *Applied and Computational Complex Analysis - Vol 1: Power Series, Integration, Conformal Mapping, Location of Zeros*. John Wiley & Sons Inc, New York, american 1st edition, Jun 1974.

[98] George B. Arfken, Hans J. Weber, and Frank Harris. *Mathematical Methods for Physicists*. Academic Press, 5th edition, Nov 2000.

[99] J. Defrance and T. Weiss. On the pole expansion of electromagnetic fields. *Optics Express*, 28(22):32363–32376, Oct 2020.

[100] Philip Trøst Kristensen, Jakob Rosenkrantz de Lasson, Mikkel Heuck, Niels Gregersen, and Jesper Mørk. On the theory of coupled modes in optical cavity-waveguide structures. *Journal of Lightwave Technology*, 35(19):4247–4259, 2017.

[101] M. B. Doost, W. Langbein, and E. A. Muljarov. Resonant-state expansion applied to planar open optical systems. *Phys. Rev. A*, 85:023835, Feb 2012.

[102] T. Weiss, M. Schäferling, H. Giessen, N. A. Gippius, S. G. Tikhodeev, W. Langbein, and E. A. Muljarov. Analytical normalization of resonant states in photonic crystal slabs and periodic arrays of nanoantennas at oblique incidence. *Phys. Rev. B*, 96:045129, 2017.

[103] Pochi Yeh. *Optical Waves in Layered Media*. Wiley-Interscience, 1st edition, Feb 2005.

[104] Zoltan Sztranyovszky, Wolfgang Langbein, and Egor A Muljarov. Optical resonances in graded index spheres: A resonant-state-expansion study and analytic approximations. *Physical Review A*, 105(3):033522, 2022.

[105] Wei Liu, Andrey E. Miroshnichenko, Dragomir N. Neshev, and Yuri S. Kivshar. Broadband unidirectional scattering by magneto-electric core–shell nanoparticles. *ACS Nano*, 6(6):5489–5497, Jun 2012.

[106] Philip J. Wyatt. Scattering of electromagnetic plane waves from inhomogeneous spherically symmetric objects. *Phys. Rev.*, 127(5):1837–1843, sep 1962.

[107] D. Q. Chowdhury, S. C. Hill, and P. W. Barber. Morphology-dependent resonances in radially inhomogeneous spheres. *J. Opt. Soc. Am. A*, 8(11):1702, Nov 1991.

[108] J. P. Huang, K. W. Yu, G. Q. Gu, and Mikko Karttunen. Electrorotation in graded colloidal suspensions. *Physical Review E*, 67(5):051405, May 2003.

[109] Alexander Shalashov and Egor Gospodchikov. Simple approach to electromagnetic scattering by small radially inhomogeneous spheres. *IEEE Trans. Antennas Propag.*, 64(9):3960–3971, sep 2016.

[110] J. B. Pendry, D. Schurig, and D. R. Smith. Controlling electromagnetic fields. *Science*, Jun 2006.

[111] Lee W. Casperson. Electromagnetic modes of an inhomogeneous sphere. *JOSA*, 65(4):399–403, Apr 1975.

[112] James R. Wait. Electromagnetic scattering from a radially inhomogeneous sphere. *Appl. Sci. Res. B*, 10(5-6):441–450, dec 1962.

[113] Li Kai and Patrizio Massoli. Scattering of electromagnetic-plane waves by radially inhomogeneous spheres: a finely stratified sphere model. *Appl. Opt.*, 33(3):501–511, Jan 1994.

[114] James A. Lock. Electromagnetic scattering of a plane wave by a radially inhomogeneous sphere in the short wavelength limit. *J. Quant. Spectrosc. Radiat. Transfer*, 202:126–135, nov 2017.

[115] F. A. Albini. Scattering of a plane wave by an inhomogeneous sphere under the born approximation. *J. Appl. Phys.*, 33(10):3032–3036, oct 1962.

[116] L. Dong, G. Q. Gu, and K. W. Yu. First-principles approach to dielectric response of graded spherical particles. *Phys. Rev. B*, 67(22):224205, Jun 2003.

[117] Vladimir S. Ilchenko, Anatoliy A. Savchenkov, Andrey B. Matsko, and Lute Maleki. Dispersion compensation in whispering-gallery modes. *J. Opt. Soc. Am. A*, 20(1):157–162, Jan 2003.

[118] Vincent Laquerbe, Romain Pascaud, Thierry Callegari, Laurent Liard, and Olivier Pascal. Analytical model to study the electrostatic resonance of sub-wavelength radially inhomogeneous negative permittivity spheres. *IEEE Antennas Wireless Propag. Lett.*, 16:2894–2897, 2017.

[119] Lee W. Casperson. Electromagnetic modes of an inhomogeneous sphere. *Applied Optics*, 20(15):2738–2741, Aug 1981.

[120] D. W. Vernooy, V. S. Ilchenko, H. Mabuchi, E. W. Streed, and H. J. Kimble. High-q measurements of fused-silica microspheres in the near infrared. *Opt. Lett.*, 23(4):247, feb 1998.

[121] A. Perot and Charles Fabry. On the application of interference phenomena to the solution of various problems of spectroscopy and metrology. *Astrophys. J.*, 9:87, feb 1899.

[122] David J. Griffiths. *Introduction to Electrodynamics*. Cambridge University Press, June 2017.

[123] Günter Roll and Gustav Schweiger. Geometrical optics model of mie resonances. *J. Opt. Soc. Am. A*, 17(7):1301, Jul 2000.

[124] Mehdi Keshavarz Hedayati and Mady Elbahri. Antireflective coatings: Conventional stacking layers and ultrathin plasmonic metasurfaces, a mini-review. *Materials*, 9(6):497, jun 2016.

[125] B. R. Johnson. Theory of morphology-dependent resonances: shape resonances and width formulas. *J. Opt. Soc. Am. A*, 10(2):343–352, Feb 1993.

[126] Philip M. Morse. Diatomic molecules according to the wave mechanics. ii. vibrational levels. *Phys. Rev.*, 34(1):57–64, Jul 1929.

[127] Jens Peder Dahl and Michael Springborg. The morse oscillator in position space, momentum space, and phase space. *J. Chem. Phys.*, 88(7):4535, Apr 1988.

[128] Shoufeng Lan and M. Hossein-Zadeh. Faraday effect in high-q whispering-gallery mode optical cavities. *IEEE Photonics J.*, 3(5):872–880, oct 2011.

[129] Serge Vincent, Xin Jiang, Philip Russell, and Frank Vollmer. Thermally tunable whispering-gallery mode cavities for magneto-optics. *Appl. Phys. Lett.*, 116(16):161110, apr 2020.

[130] http://langsrv.astro.cf.ac.uk/RSESpherical/RSESpherical.html.

[131] Lei Bi, Wushao Lin, Zheng Wang, Xiaoyun Tang, Xiaoyu Zhang, and Bingqi Yi. Optical modeling of sea salt aerosols: The effects of nonsphericity and inhomogeneity. *Journal of Geophysical Research: Atmospheres*, 123(1):543–558, 2018.

[132] I.S. Karanasiou, N.K. Uzunoglu, and C.C. Papageorgiou. Towards functional noninvasive imaging of excitable tissues inside the human body using focused microwave radiometry. *IEEE Transactions on Microwave Theory and Techniques*, 52(8):1898–1908, Aug 2004.

[133] Ying Li, Liyun Rao, Renjie He, Guizhi Xu, Qing Wu, Weili Yan, Guoya Dong, and Qingxin Yang. A novel combination method of electrical impedance tomography inverse problem for brain imaging. *IEEE Transactions on Magnetics*, 41:1848–1851, May 2005.

[134] J. Sun and G. D. Egbert. A thin-sheet model for global electromagnetic induction. *Geophysical Journal International*, 189(1):343–356, Apr 2012.

[135] Werner Koch. Acoustic resonances in rectangular open cavities. *AIAA journal*, 43(11):2342–2349, 2005.

[136] F.A. Dahlen, , and Jeroen Tromp. Theoretical global seismology. In *Theoretical Global Seismology*. Princeton university press, 2021.

[137] Mikhail S Agranovich, Boris Z Katsenelenbaum, Aleksej N Sivov, and Nikolai N Voitovich. *Generalized method of eigenoscillations in diffraction theory*. Wiley-VCH, 1999.

[138] Rong-Chun Ge and S. Hughes. Design of an efficient single photon source from a metallic nanorod dimer: a quasi-normal mode finite-difference time-domain approach. *Optics Letters*, 39(14):4235–4238, Jul 2014.

[139] Philip Morse and Herman Feshbach. *Methods of Theoretical Physics, Part II*. McGraw-Hill Education, 1953.

[140] Alexandre Gras, Wei Yan, and Philippe Lalanne. Quasinormal-mode analysis of grating spectra at fixed incidence angles. *Optics Letters*, 44(14):3494–3497, 2019.

[141] Gastón García-Calderón and Rudolf Peierls. Resonant states and their uses. *Nuclear Physics A*, 265(3):443–460, 1976.

[142] RF Harrington. *Time-harmonic electromagnetic fields*. Weinheim, Brisbane, Singapore, Toronto: John Wiley&Sons. Inc, 2001.

[143] NR Hill. Integral-equation perturbative approach to optical scattering from rough surfaces. *Physical Review B*, 24(12):7112, 1981.

[144] Steven G Johnson, Mihai Ibanescu, MA Skorobogatiy, Ori Weisberg, JD Joannopoulos, and Yoel Fink. Perturbation theory for maxwell's equations with shifting material boundaries. *Physical review E*, 65(6):066611, 2002.

[145] Jianji Yang, Harald Giessen, and Philippe Lalanne. Simple analytical expression for the peak-frequency shifts of plasmonic resonances for sensing. *Nano Letters*, 15(5):3439–3444, May 2015.

[146] Parry Y. Chen and Yonatan Sivan. Resolving the gibbs phenomenon via a discontinuous basis in a mode solver for open optical systems. *Journal of Computational Physics*, 429:110004, 2021.

[147] Chris Kottke, Ardavan Farjadpour, and Steven G. Johnson. Perturbation theory for anisotropic dielectric interfaces, and application to subpixel smoothing of discretized numerical methods. *Physical Review E*, 77(3):036611, Mar 2008.

[148] Attilio Zilli, Wolfgang Langbein, and Paola Borri. Quantitative measurement of the optical cross sections of single nano-objects by correlative transmission and scattering microspectroscopy. *ACS Photonics*, 6(8):2149–2160, jul 2019.

[149] Lukas M Payne, Wiebke Albrecht, Wolfgang Langbein, and Paola Borri. The optical nanosizer–quantitative size and shape analysis of individual nanoparticles by high-throughput widefield extinction microscopy. *Nanoscale*, 12(30):16215–16228, 2020.

[150] Yisu Wang, Attilio Zilli, Zoltan Sztranyovszky, Wolfgang Langbein, and Paola Borri. Quantitative optical microspectroscopy, electron microscopy, and modelling of individual silver nanocubes reveals surface compositional changes at the nanoscale. *Nanoscale Adv.*, 2:2485–2496, 2020.

[151] David A. Powell. Interference between the modes of an all-dielectric meta-atom. *Physical Review Applied*, 7(3):034006, Mar 2017.

[152] Jakob Rosenkrantz de Lasson, Jesper Mørk, and Philip Trøst Kristensen. Three-dimensional integral equation approach to light scattering, extinction cross sections, local density of states, and quasi-normal modes. *JOSA B*, 30(7):1996–2007, 2013.

[153] Mikhail V. Rybin, Kirill L. Koshelev, Zarina F. Sadrieva, Kirill B. Samusev, Andrey A. Bogdanov, Mikhail F. Limonov, and Yuri S. Kivshar. High-q supercavity modes in subwavelength dielectric resonators. *Phys. Rev. Lett.*, 119:243901, Dec 2017.

[154] H. Friedrich and D. Wintgen. Interfering resonances and bound states in the continuum. *Phys. Rev. A*, 32:3231–3242, Dec 1985.

[155] Mikhail Odit, Kirill Koshelev, Sergey Gladyshev, Konstantin Ladutenko, Yuri Kivshar, and Andrey Bogdanov. Observation of supercavity modes in subwavelength dielectric resonators. *Advanced Materials*, 33(1):2003804, 2021.

[156] Vasilii Mylnikov, Son Tung Ha, Zhenying Pan, Vytautas Valuckas, Ramón Paniagua-Domínguez, Hilmi Volkan Demir, and Arseniy I. Kuznetsov. Lasing action in single subwavelength particles supporting supercavity modes. *ACS Nano*, 14(6):7338–7346, Jun 2020.

[157] Mohammad-Ali Miri and Andrea Alù. Exceptional points in optics and photonics. *Science*, 363(6422):eaar7709, 2019.

[158] I. S. Gradshteyn, I. M. Ryzhik, Alan Jeffrey, and Daniel Zwillinger. *Table of Integrals, Series, and Products*. Academic Press, 6th edition, Aug 2000.

[159] Parry Y. Chen and Yonatan Sivan. Resolving the gibbs phenomenon via a discontinuous basis in a mode solver for open optical systems. *Journal of Computational Physics*, 429:110004, Mar 2021.

[160] Lukas M Payne, Francesco Masia, Attilio Zilli, Wiebke Albrecht, Paola Borri, and Wolfgang Langbein. Quantitative morphometric analysis of single gold nanoparticles by optical extinction microscopy: Material permittivity and surface damping effects. *The Journal of Chemical Physics*, 154(4):044702, 2021.

[161] Yisu Wang, Zoltan Sztranyovszky, Attilio Zilli, Wiebke Albrecht, Sara Bals, Paola Borri, and Wolfgang Langbein. Quantitatively linking morphology and optical response of individual silver nanohedra. *Nanoscale*, 14:11028 – 11037, Jul 2022.

[162] COMSOL. https://www.comsol.com/, Accessed: Aug 2022.

[163] Eduardo M. Perassi, Juan. C. Hernandez-Garrido, M. Sergio Moreno, Ezequiel R. Encina, Eduardo A. Coronado, and Paul A. Midgley. Using highly accurate 3d nanometrology to model the optical properties of highly irregular nanoparticles: A powerful tool for rational design of plasmonic devices. *Nano Letters*, 10(6):2097–2104, Jun 2010.

[164] Gustav Mie. Beiträge zur optik trüber medien, speziell kolloidaler metallösungen. *Annalen der Physik*, 330(3):377–445, 1908.

[165] H. C. van de Hulst. *Light Scattering by Small Particles*. Dover Publications Inc., New York, illustrated edition edition, Mar 2003.

[166] Olaf Schubert, Jan Becker, Luigi Carbone, Yuriy Khalavka, Tetyana Provalska, Inga Zins, and Carsten Sönnichsen. Mapping the polarization pattern of plasmon modes reveals nanoparticle symmetry. *Nano Lett.*, 8:2345–2350, 2008.

[167] C. Oubre and P. Nordlander. Finite-difference time-domain studies of the optical properties of nanoshell dimers. *The Journal of Physical Chemistry B*, 109(20):10042–10051, May 2005.

[168] Zhichao Ruan and Shanhui Fan. Temporal coupled-mode theory for light scattering by an arbitrarily shaped object supporting a single resonance. *Physical Review A*, 85(4):043828, Apr 2012.

[169] Jakob Rosenkrantz de Lasson, Jesper Mørk, and Philip Trøst Kristensen. Three-dimensional integral equation approach to light scattering, extinction cross sections, local density of states, and quasi-normal modes. *JOSA B*, 30(7):1996–2007, Jul 2013.

[170] Filippo Alpeggiani, Nikhil Parappurath, Ewold Verhagen, and L. Kuipers. Quasinormal-mode expansion of the scattering matrix. *Phys. Rev. X*, 7:021035, 2017.

[171] Rémi Colom, Ross McPhedran, Brian Stout, and Nicolas Bonod. Modal expansion of the scattered field: Causality, nondivergence, and nonresonant contribution. *Physical Review B*, 98(8):085418, 2018.

[172] M. Ismail Abdelrahman and B. Gralak. Completeness and divergence-free behavior of the quasi-normal modes using causality principle. *OSA Continuum*, 1(2):340–348, Oct 2018.

[173] Frédéric Zolla, André Nicolet, and Guillaume Demésy. Photonics in highly dispersive media: the exact modal expansion. *Optics Letters*, 43(23):5813–5816, Dec 2018.

[174] Minh Duy Truong, André Nicolet, Guillaume Demésy, and Frédéric Zolla. Continuous family of exact dispersive quasi-normal modal (dqnm) expansions for dispersive photonic structures. *Optics Express*, 28(20):29016–29032, Sep 2020.

[175] K. F. Riley, M. P. Hobson, and S. J. Bence. *Mathematical Methods for Physics and Engineering: A Comprehensive Guide*. Cambridge University Press, Cambridge, New York, 3rd edition, Mar 2006.

[176] Grant R. Fowles. *Introduction to Modern Optics*. Dover Publications Inc., New York, new edition, May 1990.

[177] Leslie Hogben. *Handbook of Linear Algebra*. Chapman and Hall/CRC, 2nd edition, Dec 2016.

[178] T. Weiss, M. Mesch, M. Schäferling, H. Giessen, W. Langbein, and E. A. Muljarov. From dark to bright: First-order perturbation theory with analytical mode normalization for plasmonic nanoantenna arrays applied to refractive index sensing. *Phys. Rev. Lett.*, 116(23):237401, jun 2016.

[179] Allan D. Pierce. *Acoustics: An Introduction to Its Physical Principles and Applications*. Springer, Cham, Switzerland, 3rd edition edition, Jun 2019.

[180] John A Roumeliotis and John D Kanellopoulos. Acoustic eigenfrequencies and modes in a soft-walled spherical cavity with an eccentric inner small sphere. *Journal of the Franklin Institute*, 329(4):727–735, 1992.

[181] James B Mehl. Acoustic resonance frequencies of deformed spherical resonators. ii. *The Journal of the Acoustical Society of America*, 79(2):278–285, 1986.

[182] Sebastian Franke, Juanjuan Ren, and Stephen Hughes. Impact of mode regularization for quasinormal mode perturbation theories. Apr 2022. arXiv:2204.03982 [cond-mat, physics:physics].